Advanced Control Strategies for Voltage Source Converters in Microgrids and Traction Networks

THÈSE N^O 5479 (2012)

ÉCOLE POLYTECHNIQUE FÉDÉRALE DE LAUSANNE

POUR L'OBTENTION DU GRADE DE DOCTEUR ÈS SCIENCES

PAR

Behrooz BAHRANI

acceptée sur proposition du jury:

Prof. J. R. Mosig, président du jury
Prof. A. Rufer, directeur de thèse
Dr A. Karimi, rapporteur
Prof. M. Liserre, rapporteur
Dr G. Papafotiou, rapporteur

EPFL

ÉCOLE POLYTECHNIQUE
FÉDÉRALE DE LAUSANNE

Suisse
2012

In the memory of my dear father

and

dedicated to my beloved wife, Fateme, and my family…

Acknowledgements

Abstract

Increasing concerns regarding global warming caused by greenhouse gases, which are mainly generated by conventional energy resources, e.g., fossil fuels, have created significant interest for the research and development in the field of renewable energies. Such interests are also intensified by the finitude availability of conventional energy resources. To take full benefit of renewable energy resources, e.g., wind and solar energy, interfacing power electronics devices are essential, which together with the energy resources form <u>D</u>istributed <u>G</u>eneration (DG) units. If properly controlled and coordinated, the optimal and efficient operation of DG units, which are the main building block of rapidly emerging microgrid technologies, can be ensured. In fact, the optimal and efficient operation of any energy conversion systems, e.g., microgrids, traction networks, etc., necessitates some sorts of control strategies. Being structured into two main parts and exploiting two-level <u>V</u>oltage <u>S</u>ource <u>C</u>onverters (VSCs), this thesis introduces several control strategies in the context of microgrids and electrified traction networks. Although the proposed approaches of this thesis are mainly tailored for two-level VSCs, the methods are equally applicable to other converter technologies.

In the first part, adopting an optimization-based loop shaping approach, a vector current control strategy for three-phase grid-tied VSCs is proposed. The proposed control strategy is able to independently regulate the <u>d</u>irect and <u>q</u>uadrature (dq)-components of the converter currents in a fully decoupled manner and shows very fast dynamic response similar to the existing methods. In order to extend the applicability of the proposed vector control method to single-phase systems, a countermeasure is also proposed. In single-phase systems, to form the orthogonal component of the current needed to create the dq-axes, the converter current is phase-shifted a quarter of a fundamental period. This phase-shift is the reason of strongly coupled dq-axes and oscillatory dynamic response in such systems. To obviate the need for the problematic phase-shifting, adopting a <u>F</u>ictive <u>A</u>xis <u>E</u>mulator (FAE), the orthogonal fictive current is created concurrent to the real one. In such a case, utilizing the proposed decoupled vector control strategy and the FAE, the dq-currents of single-phase converters are also regulated in a fully decoupled manner. Moreover, in this part, using a

generalized version of the optimization-based loop shaping approach, three voltage control schemes are proposed for the voltage regulation of islanded microgrids. Since the dedicated loads of islanded microgrids are not fixed, the loop shaping is simultaneously carried out for various operating points of interests, i.e., for various combinations of the load parameters. Two single-stage control strategies and a cascade one are proposed: (i) a single-stage PI-based Multi-Input Multi-Output (MIMO) controller, (ii) a single-stage PI-based MIMO controller in conjunction with resonant terms, which is able to compensate for the adverse impacts of nonlinear loads, and (iii) a cascade PI-based MIMO controller. The cascade control scheme utilizes the proposed decoupled vector control strategy as its inner loop for regulating the converter current.

In the second part, this thesis focuses on electrified traction networks and addresses a power quality problem in such networks, i.e., catenary voltage fluctuations. The Active Line-side Converter (ALC) of modern locomotives is utilized as STATic COMpensator (STATCOM) in order to inject reactive power to compensate for the adverse effects of catenary line voltage fluctuations. To determine the proper amount of reactive power, several control strategies belonging to the PI-controllers family are proposed: (i) a P-controller, (ii) a PI-controller, and (iii) a gain-scheduled PI-controller. Among the proposed approaches, the gain-scheduled strategy provides the best performance. The gain-scheduling is performed through identifying the catenary inductance at the connection point of the locomotive to that. The inductance identification is carried out by the injection of harmonic current through the ALC and monitoring its effect on the locomotive voltage. Despite its acceptable performance, the gain-scheduled approach shows several shortcomings. Therefore, utilizing the optimization-based loop shaping technique, a high-order voltage support scheme is also proposed. The proposed high-order scheme does not need any online tuning and/or modification while provides excellent performance for various operating points.

Keywords: Active Line-side Converter, Current Control, Grid-connected Mode, Islanded Mode, Identification, Locomotive, Loop Shaping, Low System Voltage, Microgrids, Traction Networks, Vector Control, Voltage Control, Voltage Source Converter

Résumé

Les préoccupations croissantes concernant le réchauffement climatique causé par les gaz à effet de serre ont créé beaucoup d'intérêts pour la recherche et le développement dans le domaine des énergies renouvelables. Ces intérêts sont renforcés par la disponibilité limitée des ressources en énergies fossiles. Afin d'exploiter au mieux ces ressources renouvelables, telles que l'énergie éolienne et l'énergie solaire, des dispositifs de l'électronique de puissance sont essentiels comme interface avec le réseau électrique. Avec les ressources renouvelables, ces interfaces forment des unités de production décentralisées, qui constituent les éléments principaux des micro-réseaux. De manière à garantir le fonctionnent optimal et efficace de ces unités de production décentralisées, des stratégies de contrôle sont nécessaires comme pour tout type de système de conversion d'énergie. Cette thèse est structuré en deux parties principaux et présente plusieurs stratégies de contrôle dans le contexte des micro-réseaux et des réseaux de traction électrifiés. Bien que les approches proposées soient principalement adaptées pour les onduleurs de tension deux niveaux, les méthodes développées sont également applicables aux autres technologies de convertisseurs.

Dans la première partie de cette thèse, une stratégie de commande vectorielle du courant pour l'onduleur de tension triphasé est proposée. Elle repose sur une démarche de synthèse de la boucle basée sur l'optimisation. Cette stratégie est capable de réguler indépendamment les composants directe et quadrature (d et q) des courants des onduleurs de tension triphasés. En outre, elle montre une réponse dynamique au moins aussi rapide que les méthodes existantes, tout en découplant totalement les axes d et q. Afin d'étendre l'applicabilité de la méthode de régulation proposée aux onduleurs monophasés, une adaptation est proposée. De manière traditionnelle, dans des systèmes monophasés, la composante orthogonale du courant nécessaire à la création des axes d et q est formée par un déphasage du courant de l'onduleur d'un quart de période fondamentale. Ceci cause un fort couplage des axes d et q, ainsi q'une réponse dynamique oscillante dans ces systèmes. Afin d'éviter ce couplage problématique, un émulateur d'axe fictif est adopté. Il émule le courant orthogonal simultanément au courant réel. Dans un tel cas, en utilisant le contrôle vectoriel proposé et l'émulateur d'axe fictif, les

courants d et q de l'onduleur monophasé sont également réglés d'une manière totalement découplée. En outre, en utilisant une version généralisée de l'approche à la synthèse de la boucle développé précédemment, trois stratégies de contrôle de tension sont proposées pour la régulation de la tension des micro-réseaux îlotés. Étant donné que les charges dédiées des micro-réseaux îlotés sont variables, la synthèse de la boucle est réalisée simultanément pour des points de fonctionnement d'intérêts différents, c'est à dire, pour diverses combinaisons des paramètres de charge. Trois stratégies sont proposées : (i) un contrôleur de type PI multivariable, (ii) un contrôleur de type PI multivariable en conjonction avec des termes de résonance, qui est capable de compenser les effets néfastes des charges non-linéaires, et (iii) un contrôleur cascadé de type PI mutlivariable. Le système de contrôle en cascade utilise la stratégie de réglage de courant découplé proposée comme boucle interne pour la régulation du courant de l'onduleur.

Dans la deuxième partie, cette thèse se concentre sur les réseaux de traction et traite d'un problème de qualité de puissance dans de tels réseaux. Les convertisseurs 4-quadrants des locomotives modernes sont utilisés comme compensateurs statiques afin d'injecter de la puissance réactive. Ceci doit permettre de compenser les effets néfastes des fluctuations de tension. Pour déterminer la puissance réactive à injecter, plusieurs stratégies de contrôle appartenant à la famille des contrôleurs PI sont proposées : (i) un régulateur de type P, (ii) un régulateur de type PI, et (iii) un régulateur de type PI à gains programmés. Parmi les approches proposées, la stratégie à gains programmés fournit les meilleures performances. Les gains appropriés sont déterminés en identifiant l'inductance de la caténaire au point de raccordement de la locomotive. L'identification de l'inductance est réalisée par l'injection de courant harmonique par le convertisseur 4-quadrants et en mesurant son effet sur la tension d'alimentation de la locomotive. En dépit de performances acceptables, cette approche souffre de plusieurs lacunes. C'est pourquoi un système de contrôle d'ordre élevé est également proposé. Il ne nécessite pas l'identification des paramètres de al ligne de contact et garantit des performances excellentes pour des points de fonctionnement multiples.

Mots clefs : Chute de tension de caténaire, contrôle de courant, contrôle de tension, contrôle vectoriel, convertisseur 4-quadrants, identification, locomotive, micro-réseaux, micro-réseaux îlotés, onduleur de tension, réseaux de traction, synthèse de la boucle

Contents

List of Abbreviations

ALC Active Line-side Converter

CLPI Catenary Line Parameters Identifier

CMPC Cascade Multivariable-PI Controller

DG Distributed Generation

dq direct-quadrature

FACTS Flexible AC Transmission Systems

FAE Fictive Axis Emulator

GVSS Gain-scheduled Voltage Support Scheme

IGBT Insulated Gate Bipolar Transistor

JP Junction Point

LPF Low Pass Filter

MIMO Multi-Input Multi-Output

OMCC Optimization-based Multivariable-PI Current Controller

OVSS Optimization-based Voltage Support Scheme

PC Point of Connection

PCC Point of Common Coupling

PI Proportional Integral

PIVSS Proportional-Integral-based Voltage Support Scheme

PLC Passive Line-side Converter

PLL Phase Locked Loop

PMCC Pseudo-continuous Multivariable-PI Current Controller

PR Proportional Resonant

PRBS Pseudo-Random Binary Sequence

PVSS Proportional-based Voltage Support Scheme

PWM Pulse-Width Modulation

RRF Rotating Reference Frame

SDP Semi-Definite Programming

SIP Semi-Infinite Programming

SISO Single-Input Single-Output

SMPC Single-stage Multivariable-PI Controller

SMPRC Single-stage Multivariable-PI Resonant Controller

SOGI Second Order Generalized Integrator

SRF Stationary Reference Frame

STATCOM STATic COMpensator

THD Total Harmonic Distortion

VSC Voltage Source Converter

List of Symbols

C_f Filter Capacitance

d Catenary Line Length

f System Frequency

f_s Sampling Frequency

f_{sw} Switching Frequency

$\mathbf{G}$ 2 × 2 System Transfer Function Matrix

G_i SISO System Transfer Function at i^{th} Operating Point

$\mathbf{G_i}$ 2 × 2 System Transfer Function Matrix at i^{th} Operating Point

G_{ii} Elements of $\mathbf{G}$

$\mathscr{G}$ Family of G_is or $\mathbf{G_i}$s

i_1 Substation1 Current

i_2 Substation2 Current

i_C Filter Capacitance Current

i_L Load Current

i_t VSC Current

$\mathbf{K}$ 2 × 2 Controller Transfer Function Matrix

K SISO Controller Transfer Function

K_{api} Proportional Gain of Gain-scheduled PI-Controller

K_i Resonance Gain of PR-Controller

K_{ii} Elements of **K**

K_p Proportional Gain of P-Controller

K_{pi} Proportional Gain of PI-Controller

K_{pr} Proportional Gain of PR-Controller

L 2×2 Open Loop Transfer Function Matrix

L_D SISO Desired Open Loop Transfer Function

L_D 2×2 Desired Open Loop Transfer Function Matrix

L_{Dq} Elements of **L_D**

L_f Filter Inductance

L_i SISO Open Loop Transfer Function at i^{th} Operating Point

L_i 2×2 Open Loop Transfer Function Matrix at i^{th} Operating Point

L_{ii} Elements of **L**

$\mathscr{L}$ Family of L_is or **L_i**s

L_l Catenary Inductance per km

L_s Substation Internal Inductance

L_t Transformer Leakage Inductance

n_t Transformer Ratio

P Active Power

Q Reactive Power

R_f Filter Resistance

R_l Catenary Resistance per km

R_s Substation Internal Resistance

R_t Transformer Series Resistance

s Laplace Operator

T_i Integral Time Constant of PI-Controller

T_{pE} Average Value of the Delays

v Grid Voltage

v_{dc} DC-Link Voltage

v_{pc} Voltage at the Point of Connection of Locomotives

v_{SS} Substation Voltage

v_t^* PWM Input Signal

v_t VSC Terminal Voltage

x Locomotive Distance from Substation1

θ Voltage Phase Angle

λ Forgetting Factor

ω_h System Angular Frequency at h^{th} Harmonic

ω_n System Nominal Angular Frequency

ϕ Locomotive Phase Angle

ψ Catenary Impedance Phase Angle

1

Introduction

Global warming mainly caused by greenhouse gases generated by conventional energy resources, e.g., oil and coal, and also the finitude availability of such resources have induced significant research and development in the field of renewable energy resources. Consistent increase in the penetration of $\underline{D}$istributed $\underline{G}$eneration (DG) units, which normally interface renewable energy resources to the grid through $\underline{V}$oltage $\underline{S}$ource $\underline{C}$onverters (VSCs), has created significant interest in the optimal grid integration, control, and operation of DG units in the context of microgrids [1]. Microgrids are considered as a basic feature of active distribution networks and are able to take full advantage of DG units, if controlled, coordinated, and operated efficiently in both grid-connected and islanded modes [2–8]. Moreover, the transport sector, which is the main consumer of energy in the world, is also abandoning fossil fuels for energy generation through electrification. Electrified traction networks and also electric vehicles are attracting significant interest and are expected to hold a significant share of the transport industry in the future. For example, in Switzerland, 99% of the traction network is electrified [9]. To take full benefit of such electrified systems and also for their optimal operation especially in terms of energy efficiency and reliability, they must be properly controlled and operated through state-of-the-art control strategies.

Being structured into two parts, this thesis introduces several control strategies in the context of microgrids and electrified traction networks. In the first part, mainly relying on an optimization-based control design procedure, the thesis proposes several current and voltage control tools for the grid-connected and islanded operation of microgrids. However, the proposed approaches are general and may be utilized in various energy conversion applications where voltage and/or current regulation are required. In the second part, exploiting some ideas and control schemes of the first part, the thesis focuses on electric traction networks and addresses a power quality problem in such networks. To obviate the studied power quality problem, several countermeasures are also proposed.

1.1 Statement of the Problems

1.1.1 Microgrids

In the grid-connected mode of operation of a microgrid, the frequency and voltage at the Point of Common Coupling (PCC) are imposed by the utility grid. In this case, each DG unit controls its real/reactive power exchange based on current control techniques. In the islanded mode of operation, however, the frequency and voltage are no longer imposed by the grid, and the current control techniques used in the grid-connected mode cannot guarantee the sustainable operation of the islanded microgrid. Therefore, subsequent to an islanding event, the islanding must be detected as fast as possible [10], and an appropriate control strategy must be adopted to regulate the voltage and frequency of the microgrid and to manage/share the power among the DG units. Therefore, for the sound operation of DG units, they must be equipped with both voltage regulation schemes for the islanded mode and current control methods for the grid-connected mode.

1.1.2 Traction Networks

AC traction networks can be regarded as special microgrids whose DG units are the locomotives traveling within them. These special microgrids are expected to always operate in the grid-connected mode, and since they are normally supplied by weak single-phase grids, they are susceptible to various distortions. However, benefitting from the control strategies tailored for microgrids and exploiting the line-side converter of locomotives, one can provide traction networks with some ancillary services.

The line-side converters of locomotives, classified into two major classes, i.e., Passive Line-side Converters (PLCs) and Active Line-side Converters (ALCs), are mainly responsible for the adverse effects of locomotives on the network voltage and current. Moreover, they determine how the locomotives themselves are affected by the network voltage distortions. Traditionally, two major types of PLCs have been being employed [11]: (i) diode rectifiers and (ii) phase-angle-controlled thyristor converters. These topologies absorb distorted current polluted with low-order harmonic distortions, which results in two power quality degradation issues [11]: (i) harmonic over-voltage and (ii) loss of average voltage. Thanks to the rapid advancements in the semiconductor technologies, high voltage and current Insulated Gate Bipolar Transistor (IGBT) switches able to commutate at relatively high frequencies, e.g., 1-2 kHz, can be utilized to form Pulse-Width Modulation (PWM) four-quadrant ALCs [12–14]. Adopting such converters at switching frequencies higher than 1 kHz results in the significant reduction of switching harmonics at the catenary AC side, while practically no low-order harmonic current is generated. Therefore, modern locomotives do not have the aforementioned problems of low-order harmonics. However, voltage drop along the catenary line or low system-voltage is another limiting power quality issue in traction networks [11, 15], which is caused by both PLC-based and ALC-based locomotives. Low system-voltage normally occurs at the end of a

heavily loaded line, which is supplied by one substation, or in the middle of a line supplied by two substations at both ends. Note that in other points of the line, this effect also exists. However, in the aforementioned points, the effect of the low system-voltage phenomenon is maximum. Low system-voltage limits the performance of the locomotives fed by the affected line and also limits the maximum transmittable power along the line.

Old thyristor/diode-based locomotives will soon be obsoleted by their ALC-based competitors. This fact alleviates the importance of PLC-related problems. However, the low system-voltage problem is a common issue for both old and modern locomotives. Moreover, the increasing number of high-speed and high-power locomotives being constantly added to traction networks intensifies the importance of the low system-voltage problem. Therefore, necessary countermeasures must be explored and implemented.

1.2 Existing Methods

1.2.1 Microgrids

1.2.1.1 Current Control of Grid-connected VSCs

Various current control approaches have been proposed for grid-tied VSCs in the literature [3, 6, 16–32], which can be categorized into two major classes [21]: (i) linear and (ii) nonlinear controllers. Due to their structural simplicity and fully digital implementability, the linear approaches such as Stationary Reference Frame (SRF)-based and Rotating Reference Frame (RRF)-based controllers are more commonly used. Among SRF-based controllers, Proportional Resonant (PR) regulators [19, 25, 26] are very well known and popular. PR-controllers track AC references in the stationary reference frame with zero steady-state error. However, they suffer from several drawbacks, e.g., sensitivity to grid frequency variations, exponentially decaying transients during step changes, and being pushed toward instability margins even by a small phase shift introduced by the adopted current sensors [25]. Moreover, since PR-controllers have more poles than Proportional Integral (PI)-controllers, they introduce a greater phase lag in the Nyquist plot of the open loop transfer function, which makes their tuning more complicated compared to PI-controllers. Furthermore, the choice of the damping ratio of non-ideal PR-controllers, which are used in practice instead of ideal PR-controllers, is itself another design issue. Therefore, RRF-based controllers are normally preferred in many applications and show acceptable performance. Among RRF-based controllers, PI-based regulators are the most renowned and easy-to-design ones, which provide fulfilling performance. The control scheme proposed in [24] is probably the most well-known and utilized approach in the literature. In this method, two current axes, i.e., direct-quadrature (dq)-axes, are defined, and a control strategy is proposed based on the mathematical model of the system. Using feedforward signals and PI-controllers, the axes are independently controlled. However, due to the imperfect disturbance rejection of PI-controllers, the parametric errors and the mathematical modeling mismatch result in the coupled current axes. That is,

upon a step change in each axis, the other axis experiences a transient, which results in power quality problems and performance degradation.

Another RRF-based approach is proposed in [3, 18] whose structure is similar to that of the controller of [24], however, its axes decoupling capability is more efficient. This current control strategy is based on the pseudo-continuous model of the converter, and hereinafter, it is called the Pseudo-continuous Multivariable-PI Current Controller (PMCC). Although the PMCC results in very sound performance, however, even adopting this approach, the current axes cannot be fully decoupled. The reason is that the PMCC also relies on the mathematical model of the system and the exact values of the system parameters. In this thesis, it is shown that the parametric errors and modeling mismatch deteriorate the dynamic performance of the PMCC and result in the coupling of the dq-axes.

It must be noted that although PI-based approaches can be efficiently used for the current regulation of three-phase VSCs in rotating reference frames, however, they exhibit shortcomings when utilized in single-phase systems. In such systems, the common approach is to create a set of imaginary quantities orthogonal to those of the single-phase system so as to obtain DC quantities by means of a stationary to rotating frame ($\alpha\beta$ to dq) transformation [33, 34]. The orthogonal imaginary current component is obtained by phase shifting the measured real signal by a quarter of the fundamental period. The measured and the shifted current components are then employed in an $\alpha\beta$ to dq transformation, and a conventional dq-currents controller with decoupling strategy is used. The output quantities of the controller are then back-transformed to the $\alpha\beta$-frame to obtain the ac control signals. The α-component of the control signal is employed and fed into the PWM block while the β-component is discarded. This approach is relatively simple and straightforward, however, the introduction of such delay in the system tends to deteriorate the dynamic response, which becomes slower and oscillatory.

1.2.1.2 Voltage Control of Islanded Microgrids

The voltage control of islanded microgrids has been extensively investigated in the literature, and various control strategies have been proposed [2, 35–53]. The most reported strategy is the frequency/real-power and voltage/reactive-power droop-based method for the voltage and frequency control of islanded microgrids with multiple DG units [2, 36–43]. In the context of a single-DG-unit microgrid, several islanded mode control strategies have been proposed and reported [50–53]. The control strategy in [50] is intended for a pre-specified balanced load and cannot accommodate large variations in the load parameters. To enhance the stability and robustness of a microgrid in the presence of balanced linear load conditions, a linear quadratic gaussian controller has been proposed in [51]. Reference [52] presents a multivariable controller for the voltage regulation of a microgrid with its local *RLC* load, with uncertain parameters perturbed around their nominal rated values. The control method proposed in [52] leads to a high-order multivariable controller. Although, the designed controller has robust stability to load parameters variations, the performance is guaranteed only for the nominal

load. To accommodate highly unbalanced loads, a control strategy has been proposed in [53] that utilizes an internal oscillator to maintain the frequency and a feedback control system to regulate the voltage.

In the presence of nonlinear loads and harmonically polluted load currents, the voltages of a microgrid become severely distorted, and the power quality is deteriorated. Consequently, neither of the above-mentioned control strategies can eliminate/minimize the adverse impacts of the harmonics. Furthermore, the robust stability of a microgrid may not be guaranteed for large variations of the load parameters if the above-mentioned methods are utilized.

1.2.2 Voltage Support in Traction Networks

Traditionally, to compensate for the adverse effects of low system-voltage, various compensators, e.g., thyristor-switched reactors and thyristor-switched capacitors, are used [54, 55]. Moreover, several semiconductor-based solutions are proposed [15, 56–60]. For some specific traction systems, supercapacitor-based compensators are also suggested [61]. These solutions, however, are all static and can only locally compensate for low system-voltage. Moreover, in some cases, their initial cost is a prohibitive issue.

1.3 Thesis Objectives

1.3.1 Microgrids

1.3.1.1 Current Control of Grid-connected VSCs

The widespread applicability of dq-currents controllers provides substantial inducements to investigate and propose alternative regulation schemes that can overcome the axis-coupling problem. Using nonparametric models, this thesis proposes a robust current regulation scheme for VSCs in which the d- and q-axes are decoupled. The design procedure consists of an optimization-based loop shaping. The shaping is performed by minimizing the second norm of the error between the system nonparametric transfer function matrix and a desired one. The minimization is subject to a few constraints, which guarantee the stability and the desired performance of the closed-loop system [62, 63]. The structure of the achieved controller is similar to that of the PMCC [3], however, instead of integrators in the transversal arms of the controller, PI-controllers are used. The proposed method provides better dynamic performance compared to its predecessors and is structurally simple.

Moreover, in this thesis, an alternative current regulation scheme for single-phase systems is proposed. In the proposed method, instead of introducing a delay of a quarter of a fundamental period, the β-component of the control signal along with that of the grid voltage are fed into a fictive model of the system to create the imaginary current orthogonal to the converter current. The created orthogonal current and the converter current are then fed into a dq-currents regulator. Therefore, upon step changes in the d- or q-axis reference value, the

actual quantities in the real and imaginary systems react at the same time and in the same way to track the reference quantities. This is in contrast with the common approaches in which the imaginary component reacts a quarter of a cycle after the real component, which is the reason of the relatively poor dynamic response of the conventional dq-currents control strategies in single-phase converters.

1.3.1.2 Voltage Control of Islanded Microgrids

This thesis proposes a general multivariable voltage controller design methodology for islanded single-DG-unit microgrids. The design approach consists of an optimization-based open-loop shaping with a few constraints. The constraints guarantee the desired dynamic performance and the stability of the closed-loop system. To shape the open-loop transfer function matrix, the nonparametric model of the system at several operating points of interest are derived, and the summation of the second norm of the errors between their respective transfer function matrices and a desired one is minimized, while the constraints are respected.

Based on the proposed methodology, three dq-voltages control schemes are proposed: (i) a single-stage PI-based Multi-Input Multi-Output (MIMO) controller, (ii) a single-stage PI-based MIMO controller in conjunction with resonant terms, and (iii) a cascade PI-based MIMO controller. All proposed controllers are able to accommodate large variations in the load parameters of the islanded microgrid, while the single-stage controller with resonant terms and the cascade one are also able to compensate for the adverse effects of nonlinear and/or harmonically polluting loads, e.g., resistors fed by rectifiers.

1.3.2 Voltage Support in Traction Networks

The real and reactive power exchange of ALCs with the catenary are normally regulated through current control schemes [64–71]. In such a case, utilizing a voltage-oriented system, the d-component (q-component) of the ALC current is proportional to the real power (reactive power). The set-point of the d-component is then determined according to the real power demand of the locomotive, while that of the q-component is normally set to zero. However, due to railways speed limits, railways traffic, etc., locomotives normally do not operate at their rated power levels. Therefore, benefiting from the unused capacity of their ALCs, one can utilize locomotives as mobile STATic COMpensators (STATCOMs) and inject reactive power to compensate for low system-voltage. In this thesis, inspiring from the proposed cascade voltage control scheme of islanded microgrids, the set-point of the q-component of the ALC current is determined through a secondary control loop responsible for maintaining the locomotive voltage at its connection point to the network.

Several PI-based approach are proposed for the secondary control loop in this thesis. Since the physical positions of locomotives and also the network architecture are not fixed, a single P- or PI-controller is not able to stabilize the system and/or to provide acceptable performance

for all operating scenarios. Therefore, identifying the parameters of the system in real-time, a gain-scheduled controller is used, whose parameters depend on the catenary inductance. Although, the gain-scheduled PI approach shows acceptable performance, it exhibits several shortcomings, e.g., the pollution of the network with harmonic currents injected for the identification, susceptibility to errors in the identification, etc. To overcome such shortcomings, and since a single PI-controller does not show acceptable dynamic performance for all scenarios, i.e., for all positions of the locomotive in the network and for all network architectures, higher-order controllers must be utilized. In this thesis, utilizing such high-order controllers, another compensation scheme is also presented that does not require any online modifications and does not pollute the network, while shows acceptable performance for all assumed scenarios. To design such high-order controllers, a model of the system is essential. Since a parametric model of the system is not readily achievable, the nonparametric models of the system for various locomotive positions and system architectures are obtained. Then, using an optimization-based loop shaping approach [63], a high-order controller is designed.

1.4 H_∞ Control Design Method for Nonparametric Models

In this thesis, as mentioned in the previous sections, to design controllers for several SISO and MIMO applications, an H_∞ control design method is utilized [62,63]. Contrary to many control design methods, this approach acts on nonparametric or spectral models, and therefore, it does not suffer from drawbacks associated with parametric models. Moreover, this method is able to design fixed-order controllers, which is in contrast with many of its counterparts, e.g., robust control techniques applied to state representation of MIMO models. Another important feature of this design method is that it can treat the case of multimodel uncertainty, which is very useful in various industrial applications.

The core idea of this design procedure is shaping the open-loop and closed-loop transfer functions of the system through convex optimizations. In the following chapters, this design procedure is explained step by step to design controllers for each of the aforementioned applications, i.e., the current control of grid-tied VSCs, the voltage control of islanded microgrids, and voltage support in traction networks.

1.5 Thesis Outline

This thesis consists of two parts. In the first part, several current and voltage control strategies applicable to VSCs are proposed. Although the controllers are proposed in the context of microgrids, they are rather general and can be utilized in various energy conversion applications. In the second part, which is dedicated to traction networks, several ancillary services using the ALC of modern locomotives are proposed. Note that in Part II, some of the ideas and methods of Part I are adopted.

The next two chapters, which constitute Part I, are structured as follows:

- Chapter 2 presents a vector control strategy for regulating the current of three-phase grid-tied VSCs in an RRF. The proposed approach is based on shaping the open-loop and closed-loop transfer function matrices of the system and results in decoupled dq-axes. Moreover, proposing a $\underline{F}$ictive $\underline{A}$xis $\underline{E}$mulator (FAE), this chapter extends the applicability of the decoupled vector current control scheme to single-phase grid-tied VSCs.

- Chapter 3 proposes a multivariable digital control design methodology for the voltage regulation of an islanded single-DG-unit microgrid and its dedicated load. The controller design methodology is based on a family of spectral MIMO models of the microgrid system and performs open-loop and closed-loop shaping simultaneously for the assumed models by a convex optimization approach similar to that of Chapter 2. Adopting the proposed methodology, two single-stage and one cascade voltage control schemes for islanded microgrids are presented.

Chapters 4 to 6 constitute Part II and are organized as follows:

- In Chapter 4, adopting the ALC of modern locomotives, an identification strategy is proposed, which estimates the parameters of the catenary line through the injection of low-order harmonic current and monitoring the corresponding voltage at the connection point of the locomotive to the network.

- Chapter 5 details the low system-voltage problem in traction networks and proposes several voltage support schemes for such systems. The proposed methods are based on the injection of capacitive reactive power through the current-controlled ALC of locomotives. Among the proposed approaches, the gain-scheduled PI-controller shows the best performance. The gain scheduling is carried out through identifying the parameters of the catenary line by the method of Chapter 4.

- Chapter 6 introduces another voltage support scheme to compensate for the adverse effects of low system-voltage, which overcomes the deficiencies of the proposed methods of Chapter 5. Similar to the methods of Chapter 5, the proposed approach is based on the injection of reactive power through the current-controlled ALC of modern locomotives. However, instead of a gain-scheduled PI-controller, a 5th-order controller is utilized, which does not need any online tuning. To design the 5th-order controller, adopting the nonparametric models of the system at various locations, an optimization-based open-loop and closed-loop shaping approach is used. The loop shaping guarantees the stability and the acceptable performance of the closed-loop system for various locomotive positions in the network.

Finally, Chapter 7 concludes the thesis and expresses its contributions and possible future works.

General Control Tools for Microgrids Part I

Introduction to Part I

In this part, several general-purpose control tools for the regulation of the current and voltage of grid-connected and islanded microgrids are proposed. Chapter 2 presents an existing vector current control scheme for grid-tied three-phase VSCs and discusses its deficiencies in terms of axis-coupling. Then, adopting an optimization-base controller design procedure, a vector control scheme for such VSCs is proposed that obviates the axis-coupling problem of the existing one. Moreover, proposing a countermeasure, the applicability of the proposed vector control method is extended to single-phase systems. In Chapter 3, adopting the same design procedure, three voltage control approaches for islanded microgrids and their dedicated loads are proposed. Two of the proposed approaches directly regulate the voltage and consist of only one stage. The third one, however, has a cascade structure and utilizes the developed vector current control scheme of Chapter 2 as its inner current control loop.

It must be noted that the proposed control tools of this part, although primarily developed for microgrids, are equally applicable to various energy conversion systems where current and/or voltage regulation are required.

2

Decoupled Vector Control of Grid-tied VSCs

2.1 Introduction

Using nonparametric models, this chapter proposes a vector control strategy for the current regulation of three-phase grid-tied VSCs, in which the d- and q-axes are decoupled. The design procedure consists of an optimization-based loop shaping, which guarantees the stability and the desired performance of the closed-loop system [62, 63]. The structure of the achieved controller is similar to that of the PMCC [3], however, instead of integrators in the transversal arms of the controller, PI-controllers are used. The proposed method provides better dynamic performance compared to its predecessors and is structurally simple. In this chapter, the design procedure of the decoupled dq-currents control strategy is presented, and its performance is evaluated for three-phase systems based on simulation and experimental results.

Moreover, in this chapter, the applicability of the proposed vector control scheme is extended to single-phase grid-connected VSCs. In such systems, conventionally, to create two orthogonal signals required for extracting the dq-components of the current, the converter current is delayed a quarter of a fundamental period. Such delay results in oscillatory dynamics and strongly coupled axes. In the proposed method of this chapter, the β-component of the control signal along with that of the grid voltage are adopted in order to create the imaginary current orthogonal to the converter current such that the real and imaginary currents concurrently react to set-point changes. The feasibility of the proposed strategy is validated based on time-domain simulation studies and experimental results.

The rest of the chapter is structured as follows. Section 2.2 describes the axis-coupling problem in the dq-currents control of VSCs and also briefly presents the previously proposed PMCC [3]. Section 2.3 presents the proposed dq-currents control strategy for three-phase systems and compares its performance with that of the PMCC. Section 2.4 extends the applicability of the decoupled dq-currents controller to single-phase systems. Section 2.5 concludes the chapter.
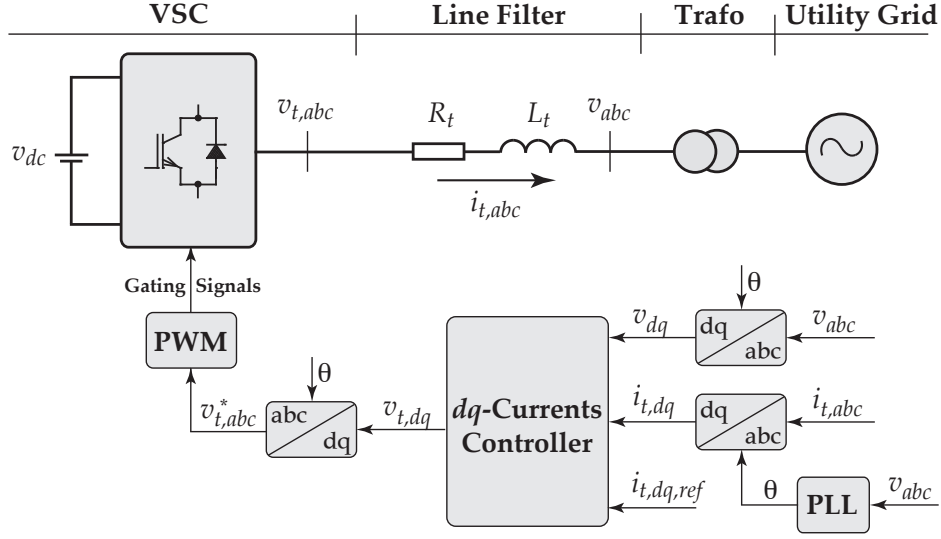
Figure 2.1: The one-line diagram of the three-phase test system

2.2 Statement of Problem and An Existing Current Controller

Grid-tied VSCs are normally interfaced to a utility grid through a line reactor filter comprising an inductor, while their currents are regulated. In this section, adopting a three-phase VSC, a three-phase test system is studied, and its mathematical model is developed. Then, using the model, the axis-coupling problem of dq-currents controllers is detailed. Moreover, an existing dq-currents control method, i.e., the PMCC, is briefly reviewed.

Figure 2.1 shows a one-line schematic diagram of the utilized test system that is a three-phase VSC connected to the utility grid through a series line reactor filter and a coupling transformer. The filter is modeled by an inductor, L_t, and a resistor, R_t. Moreover, the leakage inductance and series resistance of the transformer are added to the corresponding parameters of the filter. Table 2.1 presents the parameters of the test system. Note that the dynamics of the VSC DC-side are neglected, and utilizing a DC source, the DC-link voltage is fixed at 350 V.

It must be noted that in this thesis, all variables in time-domain are represented by minuscules, while variables in z- or s-domain are represented by majuscules. Moreover, all transfer function matrices are depicted by bold characters while transfer functions and the individual entries of transfer function matrices are shown by italic characters. Furthermore, throughout the thesis, the input signals of PWM blocks and the converters outputs are identically labeled. However, the input signals of PWM blocks are accompanied by asterisks in order to emphasize that they are not exactly the same, as the converters outputs contain switching ripples.

Table 2.1: The parameters of the three-phase test system of Figure 2.1

Quantity	Value	Comment
L_t	5 mH (0.18 pu)	Inductance of VSC Filter
R_t	0.3 Ω (0.036 pu)	Resistance of VSC Filter
S_{base}	0.8 kVA (1 pu)	VSC Rated Power
v_{dc}	35 0 V	DC Bus Voltage
v_{abc}	46 V (rms) (1 pu)	VSC-side Ph-G Grid Voltage
n_t	5	Transformer Ratio
f_{sw}	5 kHz	PWM Carrier Frequency
f_s	5 kHz	Sampling Frequency
f	50 Hz	System Nominal Frequency
ω_n	314.15 rad/s	Nominal Angular Frequency

2.2.1 Axis-Coupling Problem

In this section, deriving the mathematical model of the three-phase system of Figure 2.1, the axis-coupling problem is explained. The dynamics of the VSC AC-side variables of Figure 2.1 are described in an abc-frame as follows:

$$v_{t,abc} = R_t i_{t,abc} + L_t \frac{di_{t,abc}}{dt} + v_{abc}, \tag{2.1}$$

in which v_{abc} and $v_{t,abc}$ are the grid voltages and the VSC terminal voltages, respectively. Moreover, $i_{t,abc}$ represents the converter currents. Extracting the phase-angle of v_{abc}, (2.1) is transformed to the dq-frame and is expressed by

$$v_{t,dq} = R_t i_{t,dq} + L_t \frac{di_{t,dq}}{dt} + j\omega_n L_t i_{t,dq} + v_{dq} \tag{2.2}$$

in which ω_n is the nominal angular frequency. Separating the real and imaginary terms, the dynamics of the d- and q-axes are then deduced as

$$R_t i_{t,d} + L_t \frac{di_{t,d}}{dt} = v_{t,d} + \omega_n L_t i_{t,q} - v_d \tag{2.3}$$

and

$$R_t i_{t,q} + L_t \frac{di_{t,q}}{dt} = v_{t,q} - \omega_n L_t i_{t,d} - v_q. \tag{2.4}$$

Equations (2.3) and (2.4) represent the relationship between the control signals and the current of each axis along with the mutual coupling effect of the axes, and confirm that the axes are coupled. Applying Laplace transform to (2.3) and (2.4), the structural diagram of the system in the rotating reference frame is achieved, as shown in Figure 2.2, which contains the coupling terms. However, designing proper controllers, the resulting closed-loop system can
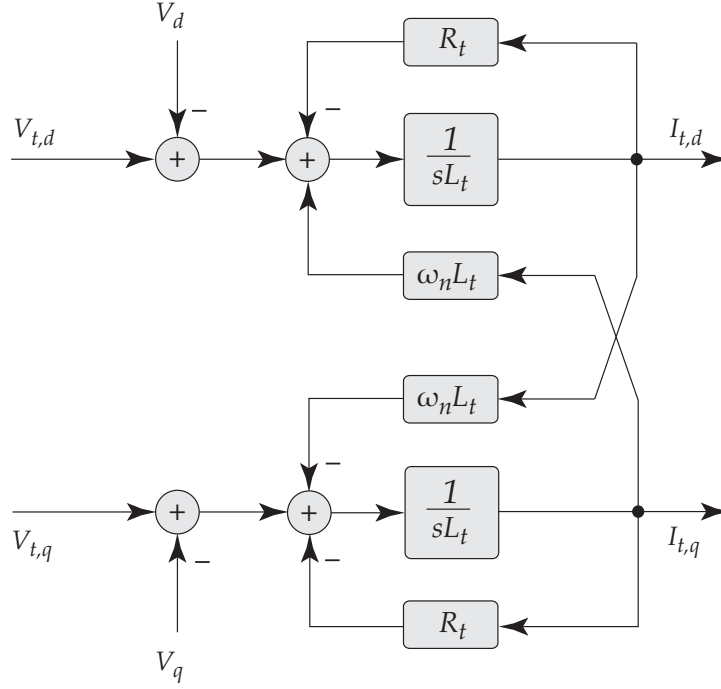
Figure 2.2: The structural diagram of the test system in the RRF

be decoupled. In the following, an existing current control method, i.e., the PMCC, is briefly reviewed, which although reduces the coupling effect, however, it cannot fully decouple the system. Then, adopting an optimization-based loop shaping approach, a controller capable of decoupling the axes is introduced.

2.2.2 Pseudo-continuous Multivariable-PI Current Controller - PMCC

In this section, the PMCC is briefly described, and its structural diagram is provided. To design the PMCC, the system transfer function is essential. Applying Laplace transform to (2.2), the following is derived:

$$V_{t,dq}(s) = R_t I_{t,dq}(s) + L_t s I_{t,dq}(s) + j\omega_n L_t I_{t,dq}(s) + V_{dq}(s) \tag{2.5}$$

in which $V_{t,dq}$, V_{dq}, and $I_{t,dq}$ are vectors represented by $x_d + j x_q$. In the following, for simplicity reason, the Laplace operator (s) of $V_{t,dq}$, V_{dq}, and $I_{t,dq}$ are omitted. Since the system is symmetric, instead of using the matrix representation of the transfer functions for MIMO systems, one can introduce a so-called *Complex Transfer Function*. Therefore, subtracting V_{dq} from both side of (2.5), the complex transfer function of the system from $V_{t,dq} - V_{dq}$ to $I_{t,dq}$ is achieved as

$$G_S(s) = \frac{K_s}{1 + (s + j\omega_n)T_s} \tag{2.6}$$

in which $T_s = \frac{L_t}{R_t}$ and $K_s = \frac{1}{R_t}$. In (2.6), the coupling between the d- and q-axes is represented by the term $j\omega_n T_s$. The PWM block of Figure 2.1 is also modeled by a so-called pseudo-continuous approach [3, 18] as follows:

$$G_P(s) = \frac{1}{1 + (s + j\omega_n)T_{pE}}. \tag{2.7}$$

In (2.7), T_{pE} is the average value of the delays caused by the PWM converter, the measurement devices, the sampling, etc. In case the switching frequency of the converter and the sampling frequency are high enough, the effect of $j\omega_n T_{pE}$ is negligible. Therefore, assuming high switching and sampling frequencies, (2.7) can be approximated by

$$G_P(s) = \frac{1}{1 + sT_{pE}}. \tag{2.8}$$

The open-loop transfer function of the system utilizing the PMCC is then deduced as

$$G_o(s) = G_R(s)G_S(s)G_P(s) \tag{2.9}$$

in which $G_R(s)$ represents the PMCC. Substituting for $G_S(s)$ and $G_P(s)$ from (2.6) and (2.8), respectively, in (2.9), the following open-loop complex transfer function is achieved:

$$G_o(s) = G_R(s)\frac{K_s}{1 + (s + j\omega_n)T_s}\frac{1}{1 + sT_{pE}}. \tag{2.10}$$

In order to obtain a standard transfer function without complex coefficients, $G_R(s)$ is selected as follows:

$$G_R(s) = \frac{1 + (s + j\omega_n)T_s}{sT_i}, \tag{2.11}$$

which leads to the simplification of (2.10) as

$$G_o(s) = \frac{K_s}{sT_i(1 + sT_{pE})}. \tag{2.12}$$

The open-loop transfer function of (2.12) is a standard transfer function without complex coefficients. Therefore, the closed-loop system is decoupled. The remaining parameter to design is T_i, which can be calculated by a usual criterion on the phase margin. Note that since the grid voltages are fixed and imposed by the utility grid, one can add their dq-components to the outputs of the controller as feedforward signals to cancel their effects.

The PMCC defined by (2.11) has a complex transfer function with the real and imaginary terms. Separating the terms, the controller is written as

$$Y_d + jY_q = \left(\frac{1 + sT_s}{sT_i} + j\frac{\omega_n T_s}{sT_i}\right)\left(I_{\varepsilon,d} + jI_{\varepsilon,q}\right) \tag{2.13}$$

in which Y_{dq} and $I_{\varepsilon,dq}$ are the controller outputs and the error signals in the dq-axes, respectively. Therefore,

$$Y_d = \frac{1+sT_s}{sT_i}I_{\varepsilon,d} - \frac{\omega_n T_s}{sT_i}I_{\varepsilon,q} \tag{2.14}$$

and

$$Y_q = \frac{1+sT_s}{sT_i}I_{\varepsilon,q} + \frac{\omega_n T_s}{sT_i}I_{\varepsilon,d}. \tag{2.15}$$

Equations (2.14) and (2.15) represent the control signals in both d- and q-axes, which include cross coupling terms. The structural diagram of the PMCC is shown in Figure 2.3 in which the grid voltages feedforward signals are also depicted.

Note that the PMCC relies on low-order parametric model of the system to decouple the axes. For example, $G_p(s)$ is a low-order parametric model of the PWM converter, which does not fully reflect its dynamic behavior. Since no mathematical model can precisely model a real system, the axis-decoupling achieved by the PMCC is not perfect, although it is superior compared to that of the conventional dq-currents controllers [24]. Moreover, the parametric
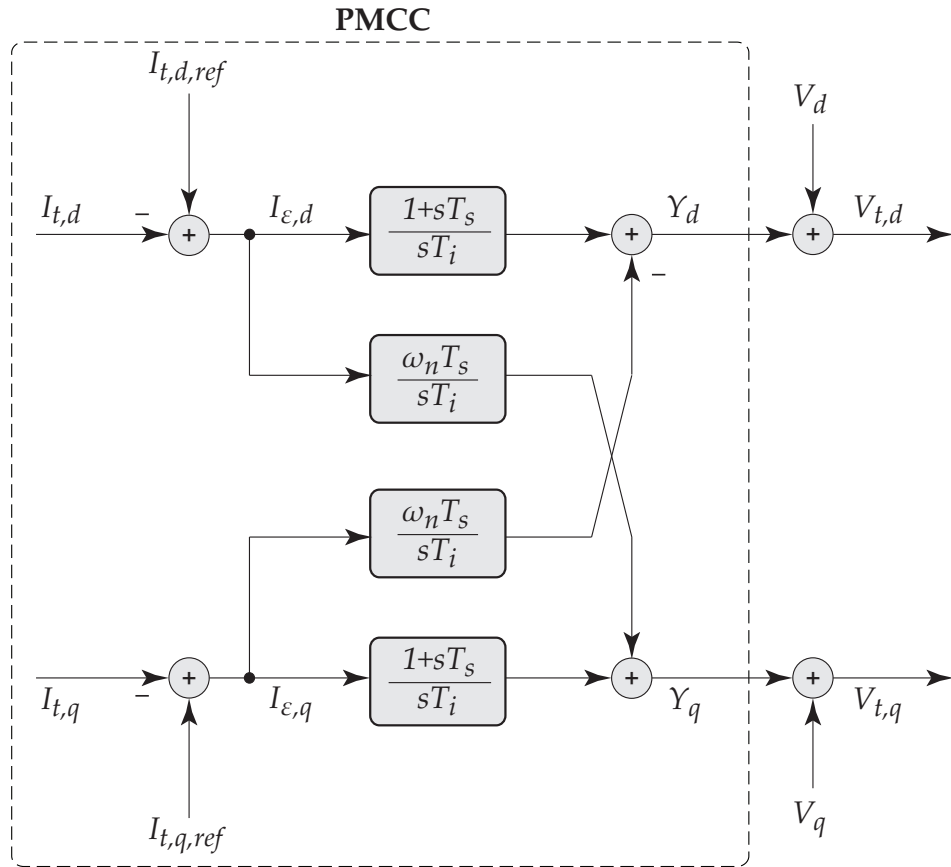
Figure 2.3: The structural diagram of the PMCC with the grid voltage feedforward signals
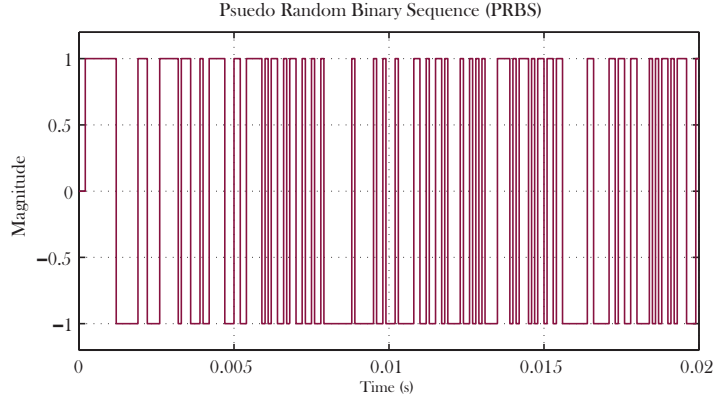
Figure 2.4: Typical PRBS in the time domain

errors, i.e., the errors in determining the parameters of the system, intensify the imperfect decoupling problem. In the following, adopting the nonparametric model of the system, a MIMO controller is designed whose structure is similar to that of the PMCC, however, it provides decoupled current axes and superior dynamic performance.

2.3 Optimization-based Multivariable-PI Current Controller - OMCC

The Optimization-based Multivariable-PI Current Controller (OMCC) design is based on minimizing the difference between the open-loop transfer function matrix of the system and a desired open-loop transfer function matrix. The minimization is subject to some convex constraints and forms a convex optimization problem. In the following, first, the nonparametric model of the system is derived, which is a 2×2 nonparametric model consisting of frequency response functions. Then, the utilized controller structure is explained, and finally, solving the optimization problem subject to some constraints, the optimal coefficients of the controller are determined.

2.3.1 System Nonparametric Model

To achieve the open-loop transfer function matrix, the nonparametric model of the to-be-controlled system is necessary. The 2×2 model of the system can be represented by the transfer function matrix **G** as follows:

$$
\begin{bmatrix} I_{t,d} \\ I_{t,q} \end{bmatrix} = \underbrace{\begin{bmatrix} G_{11} & G_{12} \\ G_{21} & G_{22} \end{bmatrix}}_{\mathbf{G}(s)} \begin{bmatrix} V_{t,d} \\ V_{t,q} \end{bmatrix}.
\tag{2.16}
$$

To achieve the nonparametric model, one can excite the system through applying a Pseudo-Random Binary Sequence (PRBS) as the inputs and monitor the outputs. A PRBS, as depicted in Figure 2.4, is a sequence of pulses with random width and a pre-specified amplitude,

which has the properties of a discrete-time white noise (a flat spectrum) and has special mathematical characteristics that make it attractive as a stimulus signal [72]. In the system of Figure 2.1, exciting $v_{t,d}$ with a PRBS, one can identify the frequency responses of G_{11} and G_{21} as

$$G_{11}(j\omega) = \frac{\mathscr{F}(i_{t,d})}{\mathscr{F}(v_{t,d})} \quad \text{and} \quad G_{21}(j\omega) = \frac{\mathscr{F}(i_{t,q})}{\mathscr{F}(v_{t,d})} \tag{2.17}$$

in which $\mathscr{F}$ stands for Fourier Transform. The same holds for identifying the nonparametric model of G_{22} and G_{12} through exciting $v_{t,q}$. Note that for the system identification, it is recommended that the inputs, i.e., $v_{t,d}$ and $v_{t,q}$, take their steady-states values corresponding to zero VSC currents, and then, the PRBS is superimposed to one of the inputs. Moreover, note that the selection of the PRBS amplitude is of high importance. The reason is that the amplitude must be large enough to sufficiently excite the system, while it does not violate the operating ranges of the system.

Figure 2.5 depicts the identified nonparametric model of the system of Figure 2.1 whose parameters are set according to Table 2.1 for two values of R_t: (i) 0.3 Ω and (ii) 1.1 Ω. Note that $R_t = 0.3$ Ω is the sum of the series resistance of the line filter and the coupling transformer, which is measured by an RLC meter in a real experimental system. However, other resistive elements, e.g., the resistance of the cables and the resistance of the grid, are present in the system and affect the nonparametric model. Assuming such resistive elements, R_t can be as high as 1.1 Ω. These resistive elements are not taken into account in the PMCC design procedure and can be regarded as parametric errors, which together with the modeling mismatch result in the axis-coupling problem. Figure 2.5 shows that the parametric errors and modeling mismatch can lead to substantial discrepancies in the identified nonparametric models. However, since the OMCC utilizes the identified nonparametric model, which precisely reflects the dynamic behavior of the system, the modeling mismatch and/or parametric errors do not deteriorate its performance.

2.3.2 Controller Structure

The test system of Figure 2.2 has two outputs, i.e., $i_{t,d}$ and $i_{t,q}$, which are aimed to be controlled by two inputs, i.e., $v_{t,d}$ and $v_{t,q}$. Therefore, a typical 2×2 multivariable control structure, as shown in Figure 2.6, is used. The matrix representation of the controller is as follows:

$$\begin{bmatrix} V_{t,d} \\ V_{t,q} \end{bmatrix} = \underbrace{\begin{bmatrix} K_{11} & K_{12} \\ K_{21} & K_{22} \end{bmatrix}}_{\mathbf{K}(s)} \begin{bmatrix} I_{\epsilon,d} \\ I_{\epsilon,q} \end{bmatrix}. \tag{2.18}$$

Since the controller to be designed should be the competitor of the PMCC, the PI-controllers are selected as the elements of the controller matrix, i.e., $K_{ij}(s) = \rho_{P,ij} + \frac{\rho_{I,ij}}{s}$ in which $i = 1, 2$ and $j = 1, 2$. Therefore, $K_{ij}(s) = \rho_{ij}^T \phi(s)$ in which $\rho_{ij}^T = [\rho_{P,ij}, \rho_{I,ij}]$ and $\phi^T = [1, \frac{1}{s}]$. This implies that the open-loop transfer function matrix of the system is a function of the vector
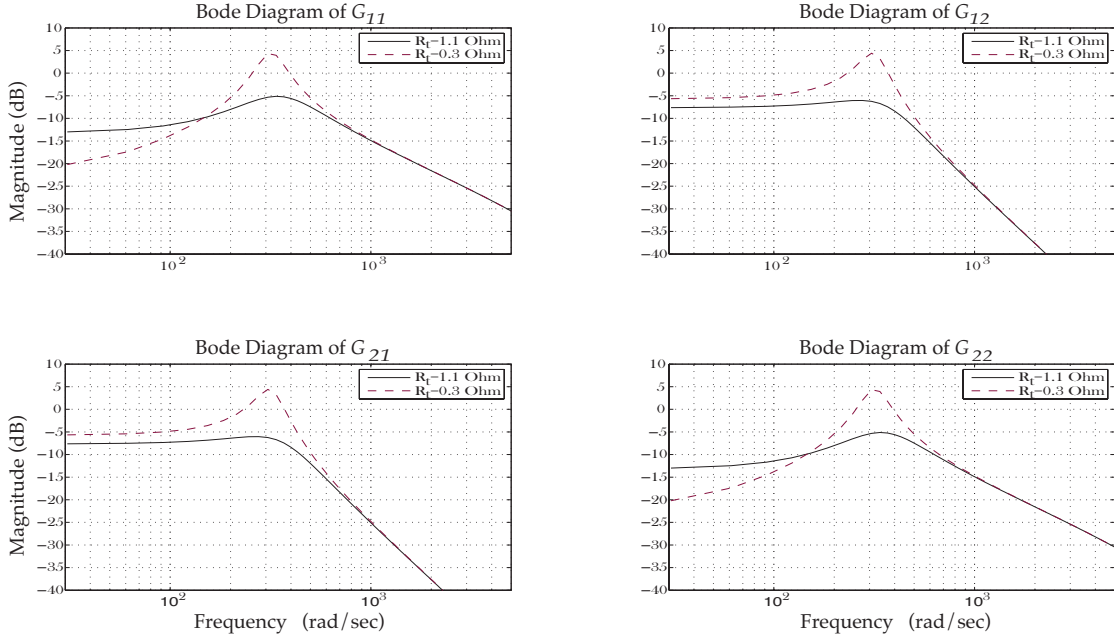
Figure 2.5: The nonparametric models of the system for two values of R_t

$\rho = [\rho_{P,11}, \rho_{I,11}, ..., \rho_{P,22}, \rho_{I,22}]$ and is shown as a function of frequency by

$$\mathbf{L}(j\omega, \rho) = \mathbf{G}(j\omega)\mathbf{K}(j\omega, \rho) = \begin{bmatrix} L_{11} & L_{12} \\ L_{21} & L_{22} \end{bmatrix}. \tag{2.19}$$

In the following, using convex optimization theory and defining some constraints that guarantee the robustness and the stability of the closed-loop system, the optimal coefficients of the controller, i.e., the elements of ρ, are calculated.

2.3.3 Optimization-based Controller Design

Shaping the open-loop transfer function matrix, $\mathbf{L}(s, \rho)$, is performed by minimizing the second norm of the error between $\mathbf{L}(s, \rho)$ and a desired open-loop transfer function matrix, $\mathbf{L_D}(s)$. Therefore, the controller design approach consists of the following optimization problem:

$$\min_{\rho} \| \mathbf{L}(\rho) - \mathbf{L_D} \|^2. \tag{2.20}$$

The primary goals in the dq-currents control are decoupling the axes and showing satisfactory dynamic performance. Therefore, a reasonable desired open-loop transfer function matrix for the dq-currents controlled system of Figure 2.1 is as follows:

$$\mathbf{L_D}(s) = \begin{bmatrix} L_{D1} & 0 \\ 0 & L_{D2} \end{bmatrix} = \begin{bmatrix} \frac{\omega_c}{s} & 0 \\ 0 & \frac{\omega_c}{s} \end{bmatrix}. \tag{2.21}$$
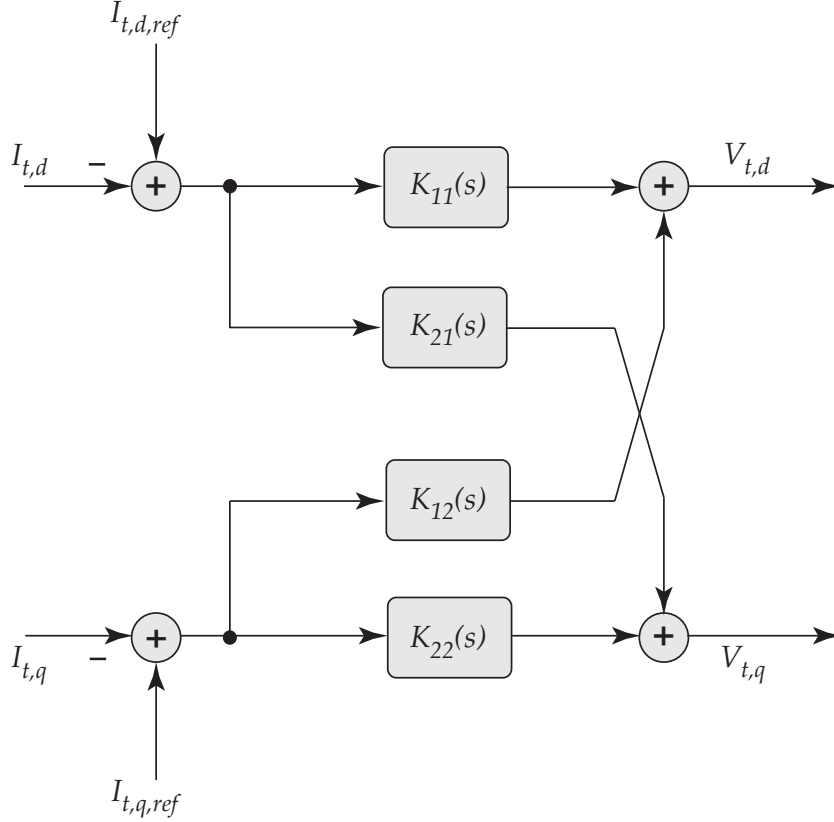
Figure 2.6: The generic structure of a 2×2 **multivariable controller for the system of Figure 2.1**

The transfer function matrix of (2.21) results in the desired decoupled system, while the dynamic performance of each axis, e.g., the system bandwidth and response time, can be manipulated by the choice of ω_c. Moreover, the closed-loop sensitivity function of the diagonal elements, $S_{qq} = (1 + L_{qq})^{-1}$, can be shaped using $|W_1(j\omega)S_{qq}(j\omega)| < 1 \ \forall \omega$, where $W_1(j\omega)$ is a weighting filter, and $q = 1,2$. This is an H_∞ performance condition that guarantees the robustness of the main axes [73]. A convex approximation of this condition can be given by the following linear constraints [62,63]:

$$|W_1(j\omega)[1 + L_{Dq}(j\omega,\rho)]| - \mathcal{R}e\{[1 + L_{Dq}(-j\omega)][1 + L_{qq}(j\omega,\rho)]\} < 0$$

$$\forall \omega \in \mathbb{R} \ \text{for} \ q = 1,2. \quad (2.22)$$

Note that solving the optimization problem of (2.20) constrained to (2.22) results in a decoupled open-loop transfer function matrix that has excellent reference signal tracking capability. However, it does not guarantee the stability of the multivariable closed-loop system. To ensure the stability of the multivariable closed-loop system, the Generalized Nyquist Stability criterion must be respected. This criterion guarantees the stability of the feedback system *if and only if the net sum of anticlockwise encirclements of the critical point* $(-1 + j0)$ *by the set*

of eigenvalues of the matrix $\mathbf{L}(j\omega)$ *is equal to the total number of the right-half plane poles of* $\mathbf{L}(s)$. To satisfy this condition, adopting *Gershgorin bands*, the references [62, 63] prove that assuming the nonparametric model $\mathbf{G}(j\omega)$, the linearly parameterized controller $\mathbf{K}(s)$ defined in (2.18) stabilizes the closed-loop system if

$$r_q(\omega,\rho) - \frac{\mathscr{R}e\{[1+L_{Dq}(-j\omega)][1+L_{qq}(j\omega,\rho)]\}}{|1+L_{Dq}(j\omega)|} < 0 \quad \forall \omega \in \mathbb{R} \text{ for } q = 1,2. \tag{2.23}$$

In (2.23), the diagonal matrix $\mathbf{L_D}(j\omega)$ should be chosen such that the number of counterclockwise encirclements of the critical point by the Nyquist plot of the set of its eigenvalues is equal to the number of unstable poles of $\mathbf{G}(s)$. Therefore, the transfer function matrix of (2.21) is a fulfilling choice. Moreover, $r_1(\omega,\rho)$ and $r_2(\omega,\rho)$ are defined as:

$$r_1(\omega,\rho) = |L_{21}(j\omega,\rho)|, \tag{2.24}$$

and

$$r_2(\omega,\rho) = |L_{12}(j\omega,\rho)|. \tag{2.25}$$

Considering the constraints for the desired performance, as shown in (2.22), and the constraints for the stability of the closed-loop system, as shown in (2.23), the OMCC design is summarized into the following optimization problem:

$$\min_{\rho} \| \mathbf{L}(\rho) - \mathbf{L_D} \|^2,$$

subject to

$$|W_1(j\omega)[1+L_{Dq}(j\omega,\rho)]| - \mathscr{R}e\{[1+L_{Dq}(-j\omega)][1+L_{qq}(j\omega,\rho)]\} < 0$$

and

$$r_q(\omega,\rho) - \frac{\mathscr{R}e\{[1+L_{Dq}(-j\omega)][1+L_{qq}(j\omega,\rho)]\}}{|1+L_{Dq}(j\omega)|} < 0 \quad \forall \omega \in \mathbb{R} \text{ for } q = 1,2. \tag{2.26}$$

The optimization problem of (2.26) includes infinite number of constraints and finite number of variables and is known as a $\underline{\text{S}}$emi-$\underline{\text{I}}$nfinite $\underline{\text{P}}$rogramming (SIP) problem, which is hard to solve. A practical solution to this problem is to neglect the frequencies above a certain frequency, i.e., ω_{max}, for which the gain of the open-loop transfer function matrix is close

to zero. For discrete-time systems, this frequency can be chosen as the Nyquist frequency that is half of the sampling frequency. Then, one can only consider the gridded frequency interval [0 ω_{max}], which contains finite frequency points. Such problems are referred to as Semi-Definite Programming (SDP) problems and are solved utilizing standard SDP-solvers, e.g., SeDuMi [74].

Choosing N linearly spaced frequencies in the interval [0 ω_{max}] $\in \mathbb{R}$, the quadratic objective function is approximated by:

$$\| \mathbf{L}(\rho) - \mathbf{L_D} \|^2 \approx \sum_{k=1}^{N} \| \mathbf{L}(j\omega_k, \rho) - \mathbf{L_D}(j\omega_k) \|_F \qquad (2.27)$$

where $\|.\|_F$ is the Frobenius norm. Therefore, the following optimization problem is deduced:

$$\min_{\rho} \sum_{k=1}^{N} \| \mathbf{L}(j\omega_k, \rho) - \mathbf{L_D}(j\omega_k) \|_F,$$

subject to

$$|W_1(j\omega_k)[1 + L_{Dq}(j\omega_k)]| \mathcal{R}e[1 + L_{Dq}(-j\omega_k)][1 + L_{qq}(j\omega_k, \rho)] < 0$$

and

$$r_q(\omega, \rho) - \frac{\mathcal{R}e\{[1 + L_{Dq}(-j\omega)][1 + L_{qq}(j\omega, \rho)]\}}{|1 + L_{Dq}(j\omega)|} < 0 \quad \text{for } k = 1, ..., N \text{ and } q = 1, 2. \qquad (2.28)$$

2.3.4 Performance Evaluation

The purpose of this section is to evaluate the performance of the OMCC and also to compare it with that of the PMCC both in simulation and experiment. For the simulation part, the system of Figure 2.1, whose parameters are set according to Table 2.1, is simulated in MATLAB/PLECS environment. Using the bilinear method [75], the continuous-time control and signal processing commands are transformed to discrete-time and are developed into a S-function in MATLAB/Simulink. Moreover, for the experimental part, adopting the test system of Figure 2.1 and the corresponding parameters of Table 2.1, a three-phase experimental setup is implemented. To implement the control strategies and signal processing algorithms, an FPGA-based controller, which provides a C programming environment, is used. The adopted FPGA is XC4010PC84 FPGA manufactured by XILINX. The control and signal processing algorithms are first discretized using the bilinear method and then developed into C codes. It should be noted that in order to achieve perfect isolation between the power and
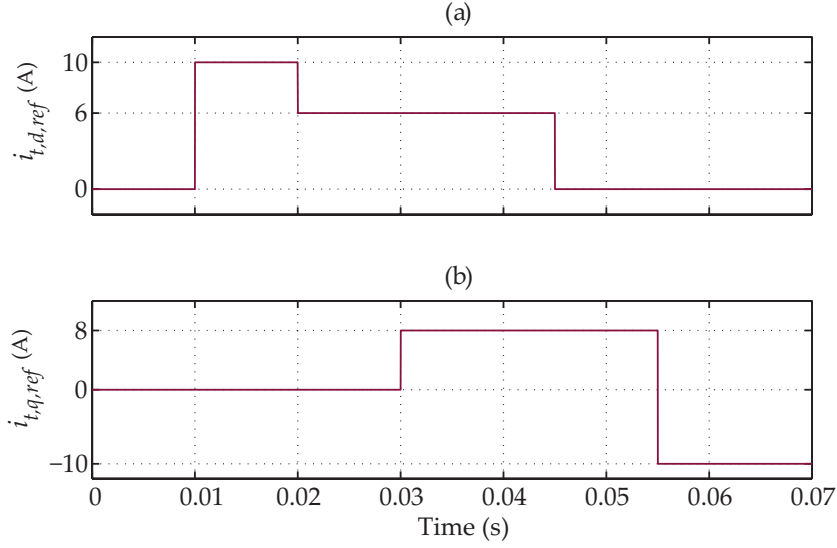
Figure 2.7: The reference values for the inverter currents: (a) the d-component and (b) the q-component

control circuits, optic-based gate drivers are adopted for driving the IGBTs.

For the performance evaluation, a reference tracking test is conducted for each control strategy. Figures 2.7 (a) and (b) depict the reference signals utilized in the conducted tests for the d- and q-axes, respectively. $i_{t,d,ref}$ consists of three step changes, i.e., 0 to 10 A, 10 to 6 A, and 6 to 0 A, at the time instants $t = 0.01$ s, $t = 0.02$ s, and $t = 0.045$ s, respectively. Moreover, $i_{t,q,ref}$ experiences two step changes from 0 to 8 A and from 8 to -10 A, at the time instants $t = 0.03$ s and $t = 0.055$ s, respectively.

To design the PMCC, for the simulation, the parameters of Table 2.1 are adopted. Moreover, for the experimental part, the measured values of the resistance and inductance of the filter along with those of the transformer are used, which are measured by an RLC meter. The experimentally measured values comply with those of Table 2.1. However, Figure 2.8 depicts that the identified model of the experimental setup does not match the nonparametric model of a system whose parameters are set according to Table 2.1, and rather comply with the nonparametric model of a system with $R_t = 1.1$ Ω. The difference between the measured value of $R_t = 0.3$ Ω and the identified value of $R_t = 1.1$ Ω represents the parametric errors and also the unmodeled resistive elements of the system. Therefore, to design the OMCC for the simulation and the experiment, the simulation-based nonparametric model corresponding to $R_t = 1.1$ Ω and the experiment-based nonparametric model of Figure 2.8 are adopted, respectively. Moreover, to mimic the experimental case in the simulation part, although the PMCC is designed for $R_t = 0.3$ Ω, R_t is set to 1.1 Ω in the simulated system. Of course, it must be noted that using a trial-and-error approach, one can tune the PMCC to achieve better results and to reduce the error between the real value of R_t and the value used for the design. However, the purpose of this chapter is to demonstrate the deficiencies of the PMCC, while
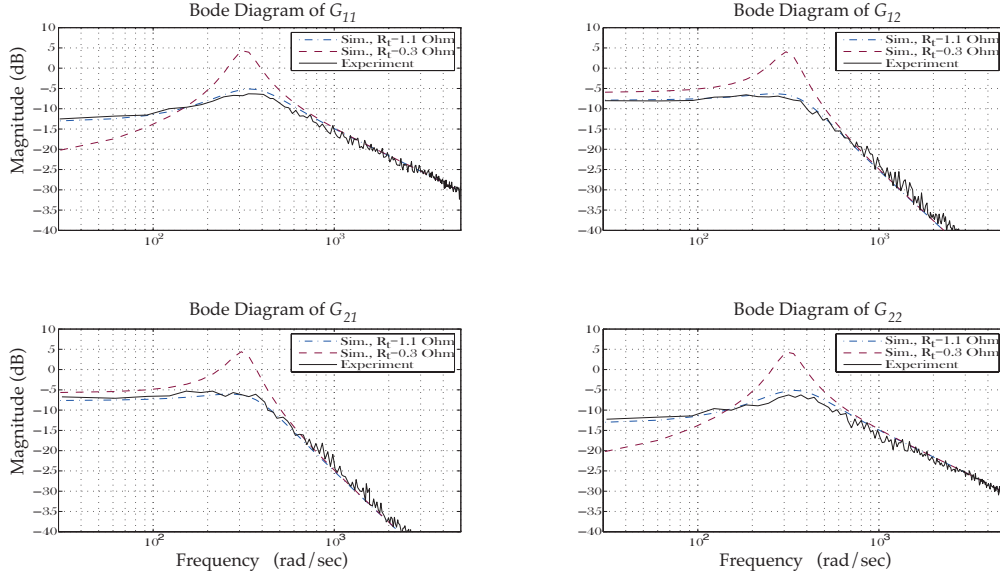
Figure 2.8: The nonparametric models of the simulated system for two values of R_t and the nonparametric model of the experimental system

systematically designed, compared to the OMCC.

To design the controllers in the following sections, the same bandwidth is selected for all cases, which is $\omega_c = 1000\frac{rad}{s}$. Moreover, the weighting filter adopted for the OMCC design is $W_1(j\omega) = 0.5$. This value guarantees a gain margin of at least 2 and a phase margin of greater than 29 degrees [72].

2.3.4.1 Simulation Results

In the simulation part, R_t is set to 1.1 Ω. However, in order to mimic the parametric errors of a real scenario, for the PMCC design, R_t is assumed to be 0.3 Ω. Then, adopting the aforementioned design parameters, the PMCC is designed, and it is represented by

$$\mathbf{K_{PMCC}}(z) = \begin{bmatrix} \frac{5.08z-4.92}{z-1} & -\frac{0.157z+0.157}{z-1} \\ \frac{0.157z+0.157}{z-1} & \frac{5.08z-4.92}{z-1} \end{bmatrix}. \tag{2.29}$$

Moreover, utilizing the simulation-based nonparametric model of Figure 2.8 corresponding to $R_t = 1.1$ Ω and taking the aforementioned design procedure, the OMCC is designed, which is represented by

$$\mathbf{K_{OMCC}}(z) = \begin{bmatrix} \frac{5.089z-4.899}{z-1} & -\frac{0.320z+0.0001}{z-1} \\ \frac{0.320z+0.0001}{z-1} & \frac{5.089z-4.899}{z-1} \end{bmatrix}. \tag{2.30}$$

Figure 2.9: The simulation results of the test system of Figure 2.1 equipped with the PMCC designed for $R_t = 0.3\Omega$ during step changes in the d- and q-axes: (a) the line currents, (b) the dq-components of the currents, and (c) the dq-components of the control signals

In the following, the performance of the designed controllers of (2.29) and (2.30) are respectively evaluated in simulation.

Reference Tracking Test for PMCC   In this section, adopting the aforementioned reference tracking test scenario in MATLAB/PLECS environment, the performance of the PMCC is evaluated. It is shown that due to the parametric errors and modeling mismatch, the dynamic performance of the PMCC deteriorates, and subsequent to step changes in the d-axis (q-axis), a non-negligible transient is experienced in the q-axis (d-axis). This verifies that the PMCC may not fully decouple the current axes.

The test signals of Figures 2.7 (a) and (b) are applied to $i_{t,d,ref}$ and $i_{t,q,ref}$, respectively. Upon each step change, the line currents and their corresponding dq-components, as shown in Figures 2.9 (a) and (b), change to track the reference signals in less than 2 ms with zero steady-state errors. However, Figure 2.9 (b) shows that upon each step change in each axis, the other
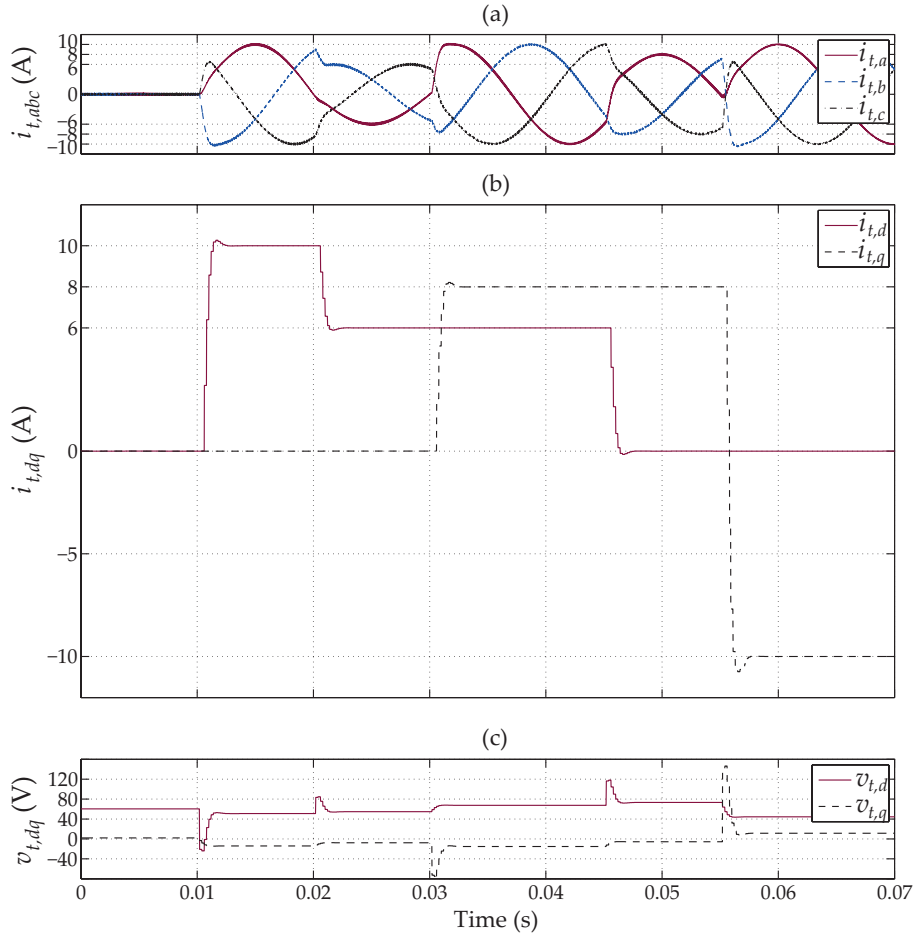
Figure 2.10: The simulation results of the test system of Figure 2.1 equipped with the OMCC during step changes in the d- and q-axes: (a) the line currents, (b) the dq-components of the currents, and (c) the dq-components of the control signals

axis experiences a transient whose magnitude depends on the amount of the step change and verifies that the PMCC suffers from axis-coupling problem. Figure 2.9 (c) depicts the dq-components of the control signals, which subsequent to each step change, are adapted to the new operating points by the PMCC.

Reference Tracking Test for OMCC Utilizing the system of Figure 2.1 equipped with the OMCC of (2.30) and applying the test sequences of Figures 2.7 (a) and (b) to $i_{t,d,ref}$ and $i_{t,q,ref}$, respectively, the same test is conducted for the OMCC to evaluate its performance. After each change in the d- or q-axis reference value, the OMCC regulates the line currents at the desired level in less than 2 ms, as shown in Figures 2.10 (a) and (b). Figure 2.10 (b) depicts the dq-components of the line currents, which subsequent to each step change, are regulated at the desired values as fast as the PMCC case and with zero steady-state errors. Moreover, Figure 2.10 (b) verifies that upon each step change in the d-axis (q-axis), the q-component

(d-component) of the currents does not experience any transient, which confirms the full axis-decoupling capability of the OMCC. Figure 2.10 (c) depicts the dq-components of the control signals.

To numerically compare the decoupling capability of the controllers, the second norm of the error in d-axis during a step change in the q-axis is calculated. The utilized criterion is summarized as $D = \frac{1}{t_2 - t_1} \sqrt{\int_{t_1}^{t_2} i_{\epsilon,q}^2}$. Calculating this norm for $t_1 = 0.055\ s$ and $t_2 = 0.075\ s$, $D = 3.82$ for the PMCC, while $D = 0.001$ for the OMCC, which confirms more effective decoupling capability of the OMCC compared to that of the PMCC. Moreover, although the rise time of both controllers are the same, the OMCC settling time is much less than that of the PMCC. For example, subsequent to the last step change in the q-axis reference value, the OMCC reaches the $\pm 5\%$ steady-state boundary within $2\ ms$ while it takes $20\ ms$ for the PMCC to reach that.

In order to compare the performance of the OMCC with that of the PMCC when designed for the exact values of the system parameters, i.e., filter resistance and inductance, the same reference tracking test is also carried out for a PMCC designed for $R_t = 1.1\Omega$. Figure 2.11 (a) shows the abc-frame currents of the converter. The dq-components of the current are also shown in Figure 2.11 (b), which confirm that even if the parameters of the system are available with no measurement errors, the PMCC is not able to fully decouple the dq-components of the line currents. This is mainly due to the modeling mismatch of the system in the PMCC design procedure, e.g., the modeling mismatch of the PWM converter, which is modeled by a first-order transfer function. The dq-components of the control signal are also shown in Figure 2.11 (c).

2.3.4.2 Experimental Results

In this section, the performance of the OMCC is experimentally evaluated and is compared with that of the PMCC. To design the PMCC, the filter parameters are of most importance and are measured using an RLC meter. The measured inductance and resistance of the line reactor filter and the transformer are $L_t = 5.0\ mH$ and $R_t = 0.3\ \Omega$, which are used to design the PMCC. However, to design the OMCC, the nonparametric model of the system is obtained through a PRBS-based identification on the experimental setup, as shown in Figure 2.8. Note that although the measured R_t is $0.3\ \Omega$, however, the experiment-based identified nonparametric model complies with a theoretical model corresponding to $R_t = 1.1\ \Omega$. A photo of the experimental setup is shown in Figure 2.12.

The designed controllers in discrete-time are represented by

$$\mathbf{K_{PMCC}}(z) = \begin{bmatrix} \frac{5.080z - 4.920}{z-1} & -\frac{0.157z + 0.157}{z-1} \\ \frac{0.157z + 0.157}{z-1} & \frac{5.080z - 4.920}{z-1} \end{bmatrix} \tag{2.31}$$
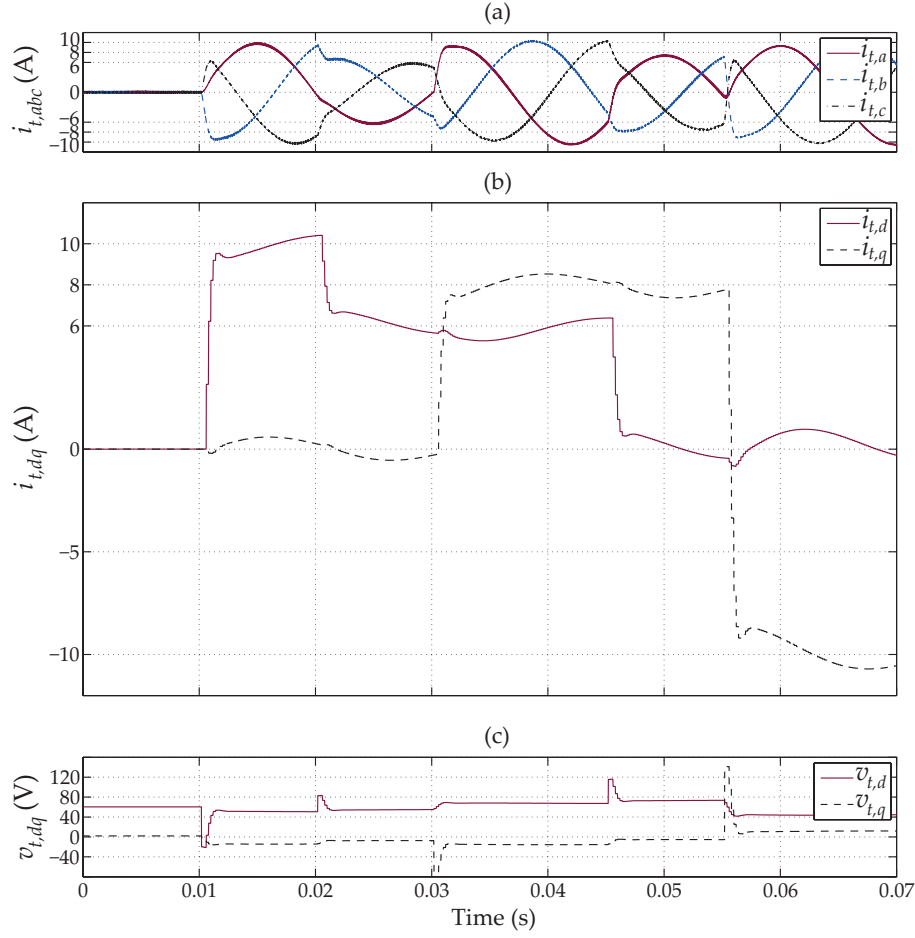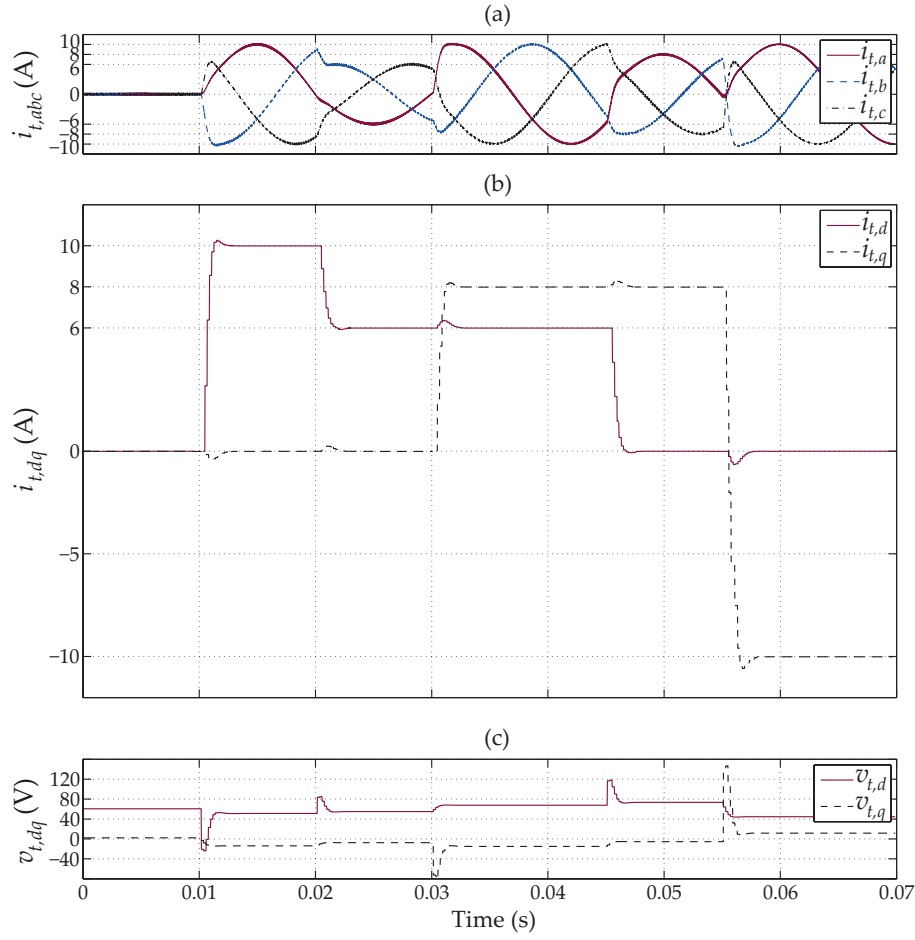
Figure 2.11: The simulation results of the test system of Figure 2.1 equipped with the PMCC designed for $R_t = 1.1\Omega$ during step changes in the d- and q-axes: (a) the line currents, (b) the dq-components of the currents, and (c) the dq-components of the control signals

and

$$\mathbf{K_{OMCC}}(z) = \begin{bmatrix} \frac{5.140z-4.851}{z-1} & -\frac{0.324z-0.0004}{z-1} \\ \frac{0.324z-0.0005}{z-1} & \frac{5.140z-4.850}{z-1} \end{bmatrix}. \tag{2.32}$$

In the following, using the aforementioned reference tracking test, the performance of the designed controllers of (2.31) and (2.32), respectively, are experimentally evaluated.

Reference Tracking Test for PMCC In this section, the performance of the PMCC is experimentally evaluated in terms of tracking reference signals. It is shown that in accordance with the simulation results, utilizing the PMCC, the dq-axes of the currents are not fully decoupled, mainly due to the parametric errors and modeling mismatch.
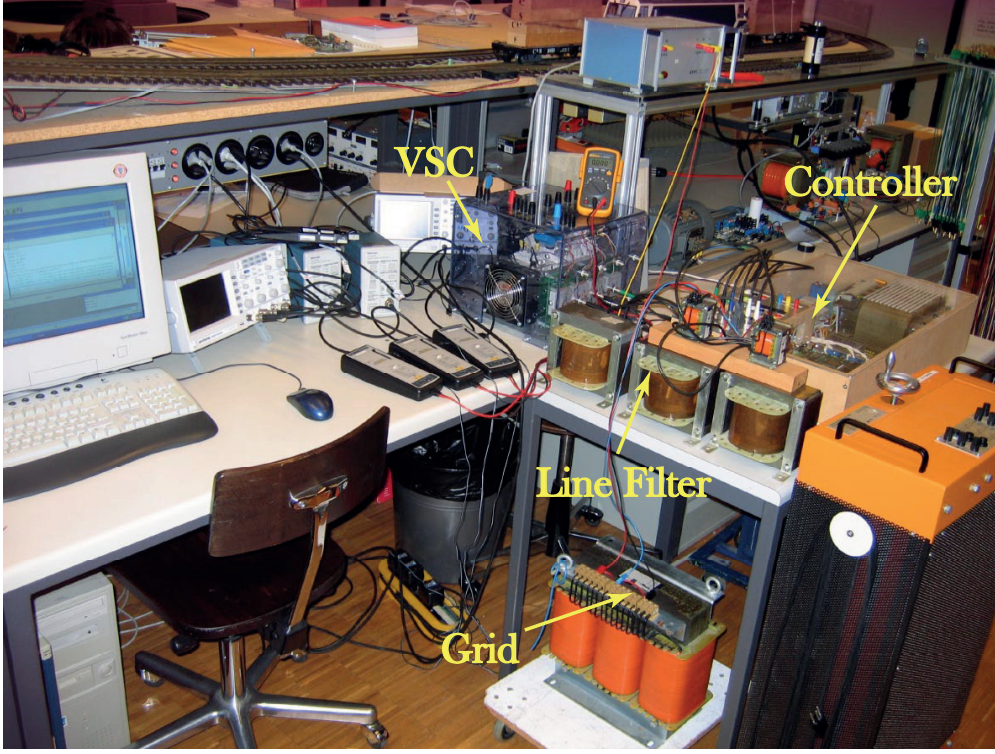
Figure 2.12: The three-phase experimental setup

To experimentally evaluate the performance of the PMCC, the reference tracking test is conducted. Figures 2.13 (a) and (b) show the inverter currents and their dq-components, respectively, which follow the step changes in the reference values in less than 2 ms. However, subsequent to each step change in the reference value of the d-axis (q-axis) current, the q-axis (d-axis) current experiences a non-negligible transient. Note that the dq-components of the currents contain 300 Hz ripples, which are caused by the lag-time of the PWM strategy [76]. Figure 2.13 (c) shows the dq-components of the control signals that upon each step change, vary to accommodate the requested change. The results confirm that the PMCC may not fully decouple the axes due to the parametric errors and modeling mismatch.

Reference Tracking Test for OMCC Utilizing the implemented experimental setup equipped with the OMCC and applying the same reference tracking test, the performance of the OMCC is experimentally evaluated. Figure 2.14 (a) and (b) depict the line currents and their corresponding dq-components, respectively. Figure 2.14 (b) shows that after each step change in the reference value of the d- or q-axis, the OMCC regulates the line currents at the desired level in less than 2 ms. Moreover, it confirms that upon a step change in each axis, the current of the other one remains unchanged. Figure 2.14 (c) depicts the dq-components of the control signals, which subsequent to each step change, are adapted to the new operating points by the OMCC.
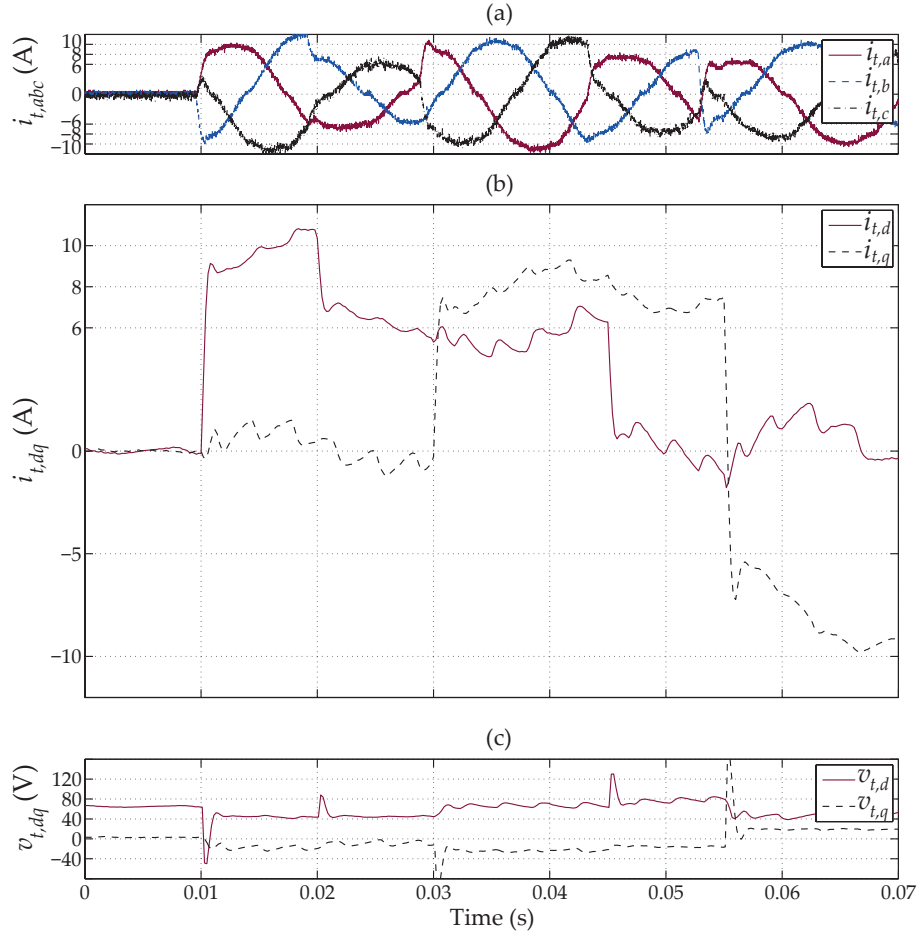
Figure 2.13: The experimental results of the test system of Figure 2.1 equipped with the PMCC during step changes in the d- and q-axes: (a) the line currents, (b) the dq-components of the currents, and (c) the dq-components of the control signals

The presented test results confirm the simulation results and show that the proposed controller, i.e., the OMCC, (i) is capable of tracking reference signals with zero steady-state errors, (ii) has fast dynamics, and (iii) contrary to the PMCC, provides fully decoupled d- and q-axes of currents.

2.4 Extension to Single-Phase VSCs

The control strategy of the previous section necessitates a stationary to rotating reference frame transformation, which in three-phase systems is viable through an abc to $\alpha\beta$ and then an $\alpha\beta$ to dq transformation. Since the transformation to a rotating reference frame requires two orthogonal signals, i.e., α and β, such a transformation cannot be directly applied to single-phase systems as variables in a single-phase system contains only one component.

To obviate the aforementioned shortcoming, one solution is to generate fictive orthogonal
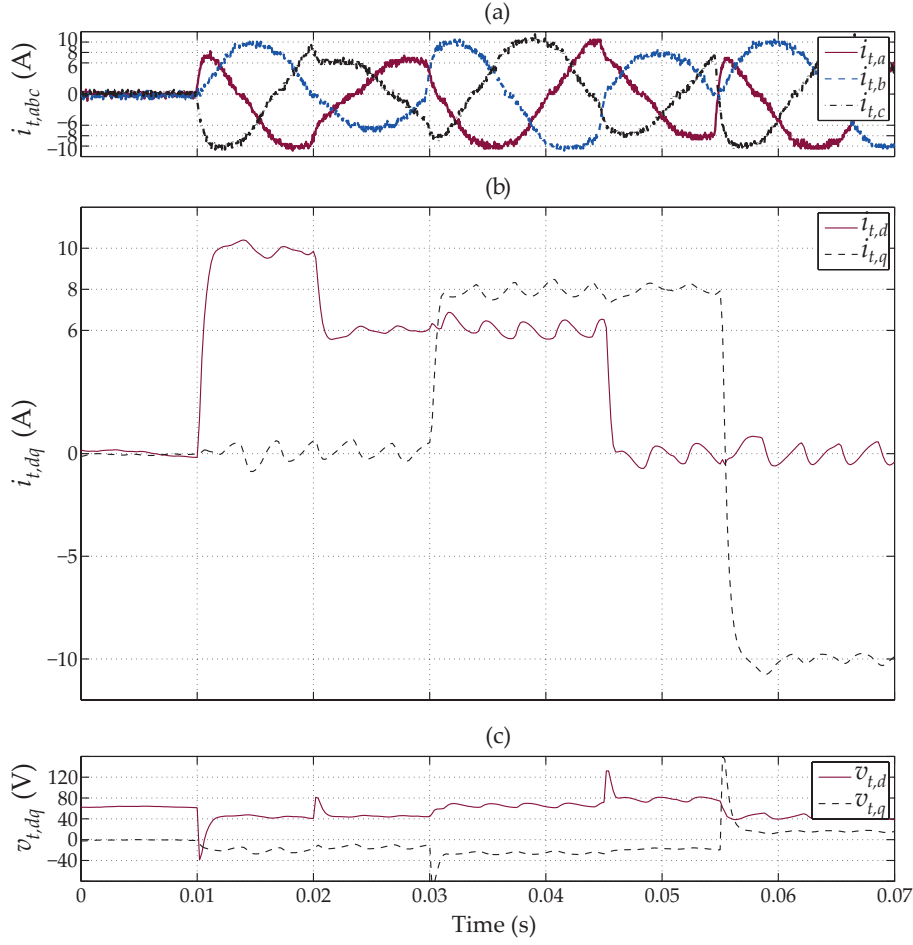
Figure 2.14: **The experimental results of the test system of Figure 2.1 equipped with the OMCC during step changes in the** d**- and** q**-axes: (a) the line currents, (b) the** dq**-components of the currents, and (c) the** dq**-components of the control signals**

components of the current and voltage by phase shifting the physical ones a quarter of a fundamental period [33,34]. In such a case, the physical single-phase variables form the α-axis while the fictive variables represent the β-axis. The α- and β-axes are then transformed to a rotating reference frame in which the dq-currents controller is implemented. The resulting control signals in the dq-reference frame are transferred back to the $\alpha\beta$-frame, and the α-component of the control signals is fed into the PWM block while its β-component is discarded. The structural diagram of this controller is depicted in Figure 2.15. However, phase shifting the current and voltage to create the required orthogonal signals deteriorates the dynamics of the system and makes it slow and oscillatory as the physical and fictive axes do not run concurrently. Therefore, any transient in the physical axis is also experienced in the fictive axis a quarter of fundamental period later. To obviate this shortcoming, the orthogonal component of the current must be concurrently generated with the physical axis current.

To generate the reference phase angle for the stationary to rotating reference frame transforma-
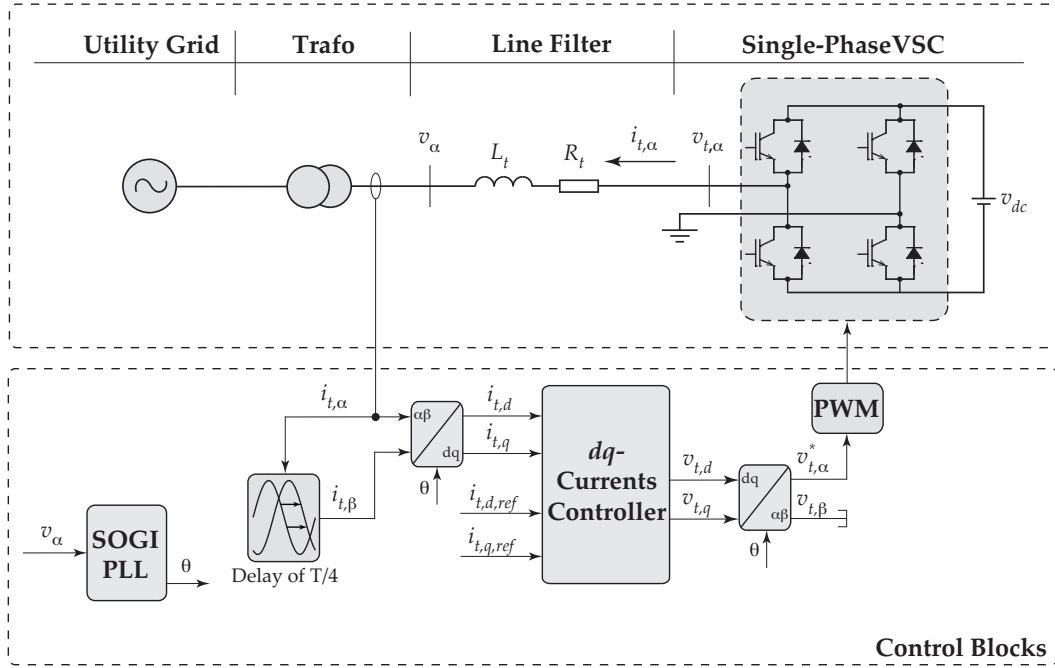
Figure 2.15: A single-phase test system consisting of a grid-tied VSC and the grid along with the conventional single-phase current regulation scheme

tion, a single-phase Phase Locked Loop (PLL) based on a Second Order Generalized Integrator (SOGI) [77] is used. Using the SOGI, the utilized PLL generates the required orthogonal component of the voltage concurrently with the physical axis and prevents the introduction of the delay to create that.

2.4.1 Fictive Axis Emulator - FAE

To concurrently generate the required orthogonal current, one can use a fictive model of the system, which is the transfer function of the real system in a SRF, hereinafter called the FAE. The detailed structural diagram of the FAE is represented in Figure 2.16. In such a case, the orthogonal component of the grid voltage created by the SOGI and the orthogonal component of the control signal created by the dq-currents controller are fed to the FAE. The orthogonal current component is emulated as a fictive one with the FAE block of the controller system. Then, the classical $\alpha\beta$ to dq transformation is used, followed by a dq-currents controller as described in Section 2.2 or Section 2.3. The link to the system is made through a dq to $\alpha\beta$ transformation. The real component path is closed through the physical system, and the imaginary path is closed through the FAE. Figure 2.17 shows the proposed control strategy in which the FAE is used to generate the orthogonal component of the current. In the following, the performance of the FAE-based single-phase dq-currents control strategy is evaluated based on simulation studies and is compared to that of the delay-based method, and the findings are verified by experimental results.
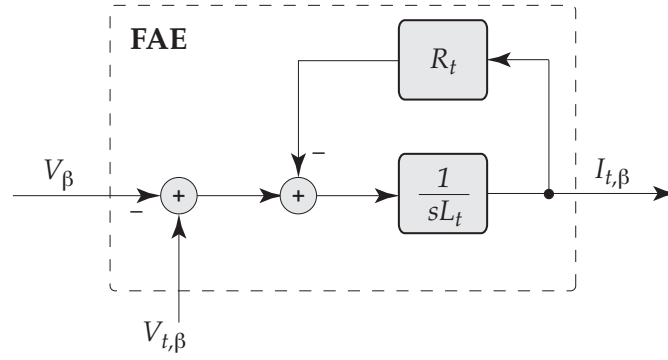
Figure 2.16: The detailed structural diagram of the FAE
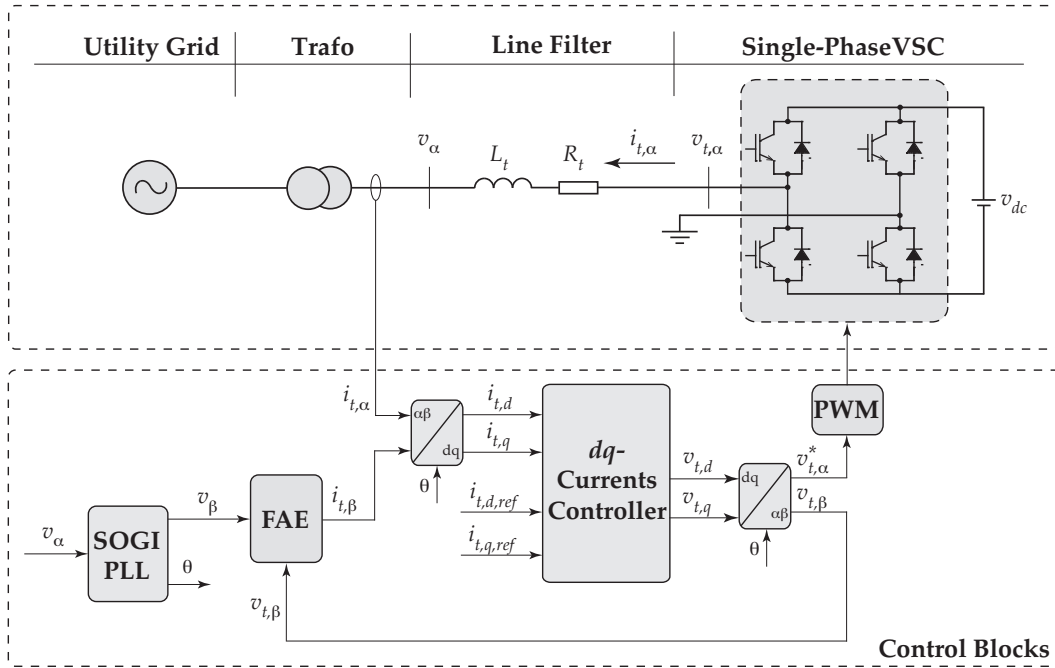
Figure 2.17: The single-phase test system along with the proposed current control scheme based on the FAE

2.4.2 Performance Evaluation

The purpose of this section is to evaluate the performance of the FAE-based regulator based on simulation and experiment and also to compare it with that of the delay-based control strategy. For the comparison, in a simulation test bench, a reference tracking test is conducted for each controller. Moreover, for the experimental performance evaluation of the FAE-based method, the same reference tracking test is carried out. To implement the control strategy and the FAE, a 16-bit digital signal controller developed by Microchip, i.e., dsPIC30F6010A, which provides a C programming environment, is used. The control and the signal processing algorithms are first discretized by using the bilinear method and then developed into C codes.

Table 2.2: The parameters of the system of Figures 2.15 and 2.17

Quantity	Value	P.U.	Comment
L_t	5 mH	0.023 pu	Inductance of VSC Filter
R_t	0.15 Ω	0.002 pu	Resistance of VSC Filter
S_{base}	0.8 kVA	1 pu	VSC Rated Power
v	230 V (rms)	1 pu	Grid Nominal Voltage
v_{dc}	300 V		DC Bus Voltage
f_{sw}	10 kHz		PWM Carrier Frequency
f_s	5 kHz		Sampling Frequency
f	50 Hz		System Nominal Frequency

2.4.2.1 Simulation Results

To evaluate the performance of the proposed current control scheme and to compare it with that of the delay-based method, a simulation test bench is developed in Simulink/MATLAB software environment. The test systems of Figures 2.15 and 2.17 are utilized, and their parameters are set based on Table 2.2. In the following, a reference tracking test is conducted for each controller, and their performances are contrasted.

Delay-based Controller   Adopting the control strategy of Figure 2.15 with the bandwidth of 200 Hz, the inverter is initially injecting zero current. At time instant $t = 0.343$ s, the reference value of the q-axis steps up to 1 pu. Moreover, at time instant $t = 0.357$ s, the reference values of both d- and q-axes are changed to 0.8 pu and 0.6 pu, respectively. As shown in Figure 2.18 (a), since the grid is stiff enough, the grid voltage, i.e., the α-component, and accordingly, the generated orthogonal voltage, i.e., the $\beta-$component, do not change during the step changes. However, subsequent to the step changes in the d- and/or q-axes reference values, the controller tries to regulate the $\alpha-$current at the desired value. However, due to excessive transients caused by the delay, there is an overshoot in the regulated current, as depicted in Figure 2.18 (b). Moreover, as shown in Figure 2.18 (c), the d- and q-axes of the currents experience non-negligible transients for even more than a quarter of a cycle due to the delay used in the controller. Therefore, it takes more than a quarter of a cycle for the d- and q-components of the current to track the requested reference values. The conducted study demonstrates that the delay-based control scheme suffers from excessive transients subsequent to step changes in its d- and/or q-axes.

Note that in the steady-state, the controller can regulate the current with zero steady-state error. Moreover, the measured Total Harmonic Distortion (THD) of the current in the steady-state is 3.9%.
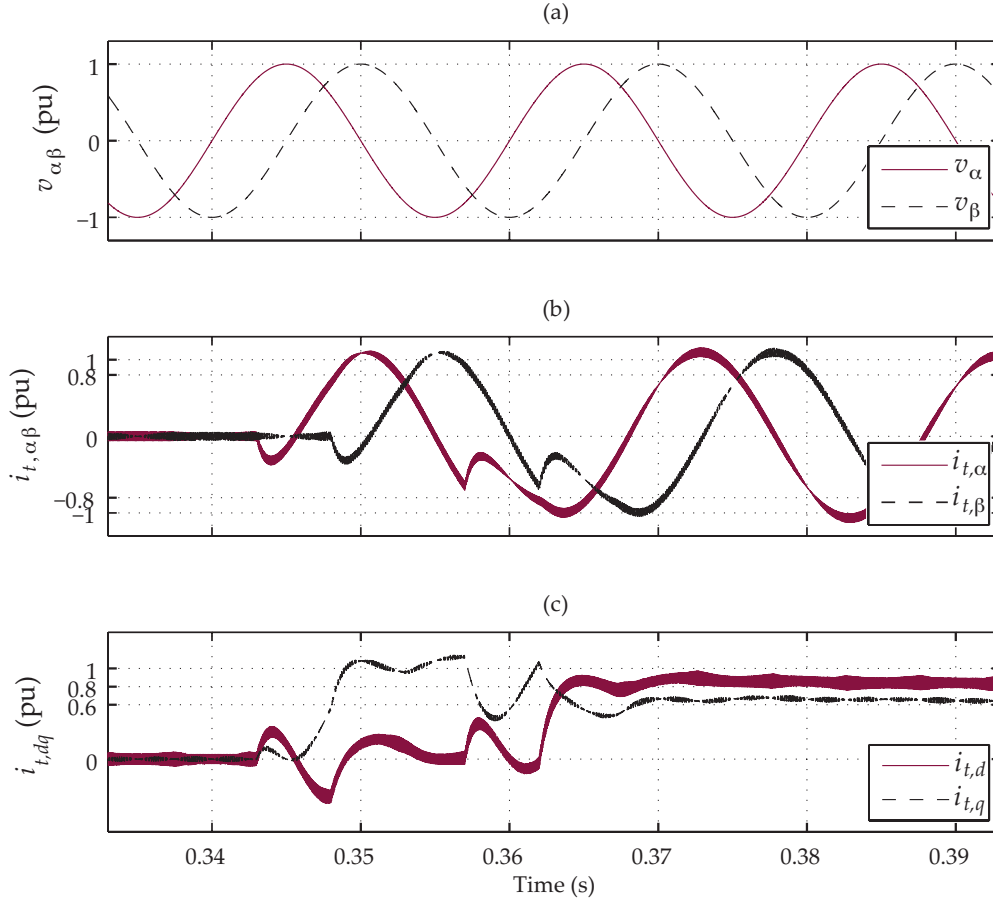
Figure 2.18: The simulation results of the test system of Figure 2.15 equipped with the conventional delay-based current controller: (a) the grid voltage and its orthogonal component, (b) the converter current and its orthogonal component, and (c) the d- and q-components of the converter current

FAE-based Controller In order to fairly compare the performance of the methods, exactly the same test as the previous section is conducted for the FAE-based approach, and also the same PI-controllers with the same bandwidth of 200 Hz are utilized. The inverter of Figure 2.17 is initially injecting zero current. At time instant $t = 0.343\ s$, the reference value of the q-axis steps up to 1 pu. Moreover, at time instant $t = 0.357\ s$, the reference values of both d- and q-axes are changed to 0.8 pu and 0.6 pu, respectively. The grid voltage and its orthogonal component generated by the SOGI PLL are shown in Figure 2.19 (a), which do not experience any transient during the test due to the stiffness of the grid. Subsequent to the step changes in the d- and q-axes references, both α-and β-currents track the desired reference values in almost 2 ms with zero steady-state error, Figure 2.19 (b). Moreover, as shown in Figure 2.19 (c), the d- and q-axes of the currents track the reference values in almost 2 ms with zero steady-state error. The conducted study demonstrates that the proposed vector control scheme works as if the system is with multiple phases represented by space-phasors, however, the components of the fictive space-phasors correspond to a physical quantity for the real
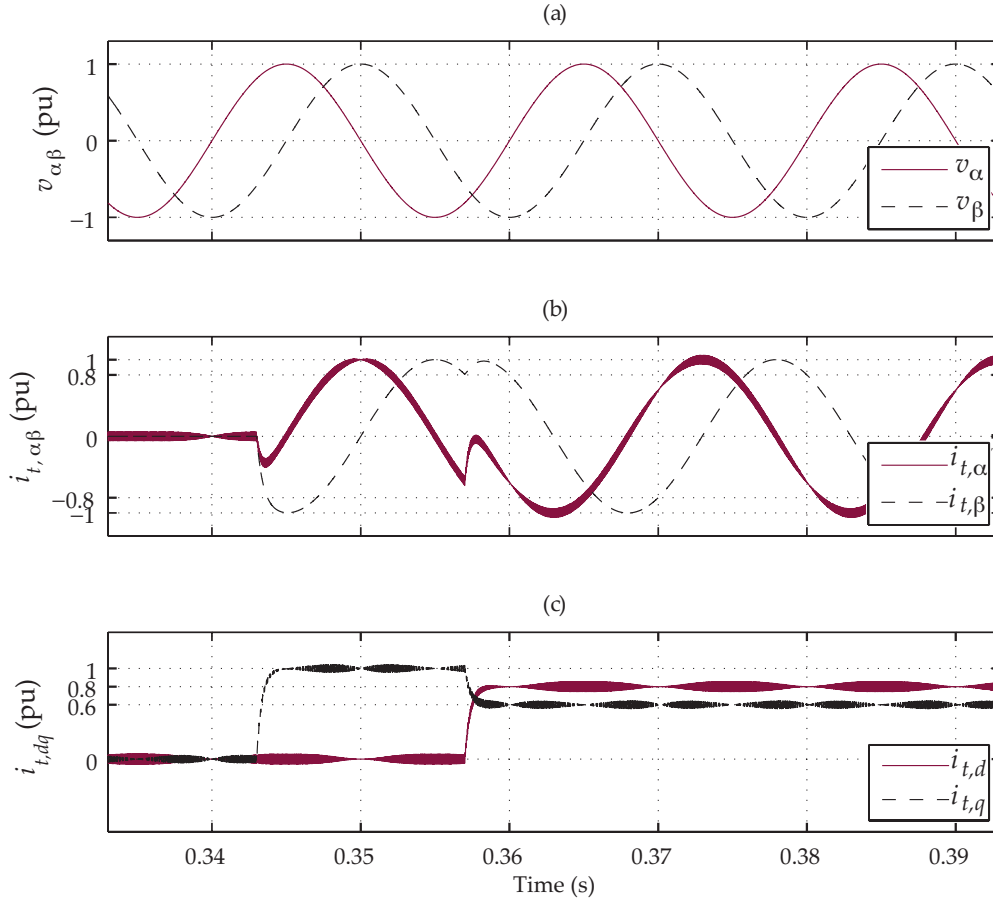
Figure 2.19: The simulation results of the test system of Figure 2.17 equipped with the FAE-based controller: (a) the grid voltage and its orthogonal component, (b) the converter current and its emulated orthogonal component, and (c) the d- and q-components of the converter current

part and to a fictive quantity for the imaginary part.

Note that similar to the delay-based controller, the FAE-based controller is capable of regulating the current with zero steady-state error, and the measured THD of the current in the steady-state is 4%, which verifies that the performances of the controllers in the steady-states are quite similar. However, the reported studies verify that the proposed FAE-based method has superior dynamics performance compared to that of the conventional delay-based approach upon step changes in the set-points. In the following, the performance of the proposed FAE-based controller is also experimentally evaluated.

2.4.2.2 Experimental Results

In this test, the performance of the proposed FAE-based current control scheme is experimentally evaluated. The test system of Figure 2.17 is adopted, and a prototype, as shown in
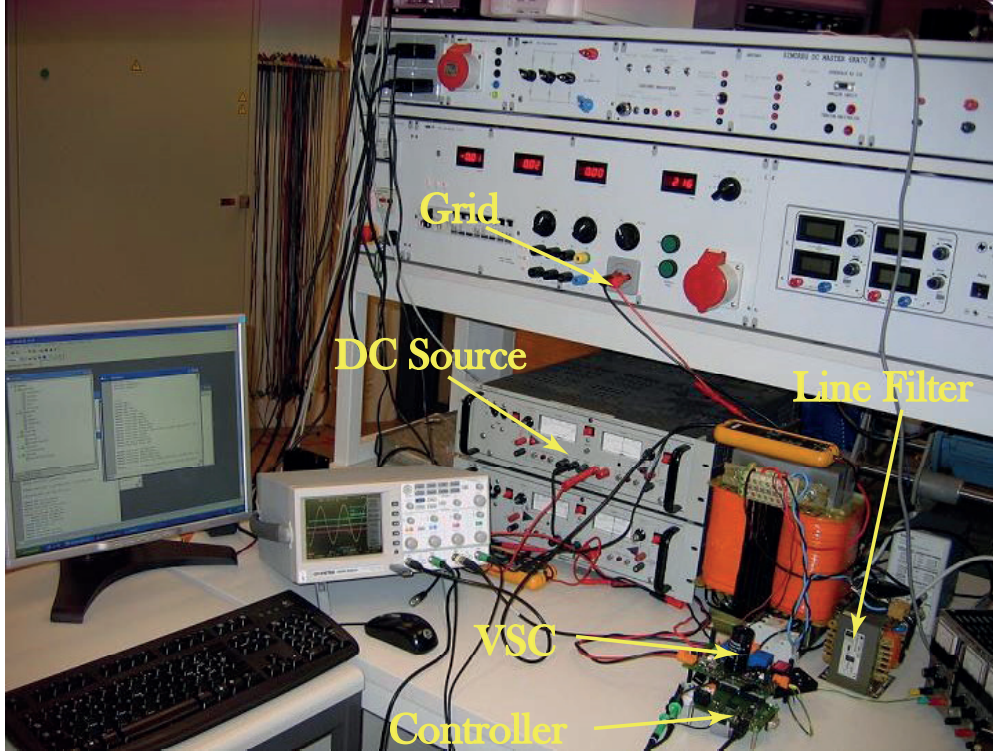
Figure 2.20: The single-phase FAE-based experimental setup

Figure 2.20, is implemented based on that. The VSC initially injects zero current as both d- and q-reference values are set to zero. At time instant $t = 0.343\ s$, the reference value of the q-axis steps up to 1 pu, and also at time instant $t = 0.357\ s$, the reference values for both d- and q-axes are changed to 0.8 and 0.6 pu, respectively. The grid regulates its voltage and consequently, its orthogonal component at the rated value during the transients, as depicted in Figure 2.21 (a). However, upon each step change, the α-current, i.e., the converter current, and the β-current, i.e., the fictive axis current, and also their corresponding d- and q-components change to track the reference value step changes in almost 2 ms, as shown in Figures 2.21 (b) and (c). Note that the simulation and the experimental results of the FAE-based controller do agree, which verifies the validity of the proposed control scheme.

It must be noted that inconsistencies between the resistance and the inductance of the fictive axis and those of the real one may result in slightly oscillatory dynamic responses. However, as shown in [6], the method is robust with respect to such inconsistencies, especially if the bandwidth of the closed loop system is high enough.

2.5   Conclusions

A vector control strategy for the decoupled dq-currents regulation of grid-tied VSCs is proposed. The proposed method can be utilized in various grid-tied applications for regulating
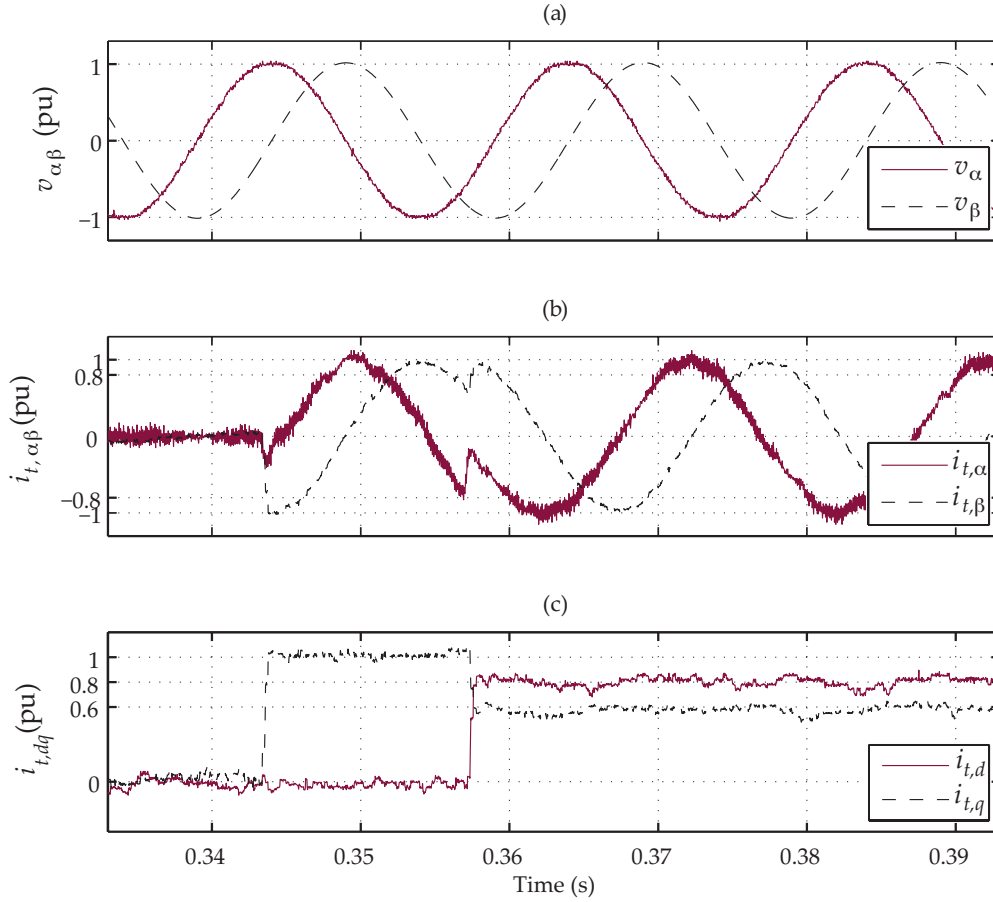
Figure 2.21: The experimental results of the test system of Figure 2.17 equipped with the FAE-based controller: (a) the grid voltage and its orthogonal component, (b) the converter current and its emulated orthogonal component, and (c) the d- and q-components of the converter current

the current and consequently the power exchange with the grid. The method relies on shaping the nonparametric open-loop and closed-loop transfer function matrices of the system through constrained convex optimization. The adopted constraints ensure the stability of the closed-loop system and also result in the desired performance. The nonparametric model is obtained through system identification, and therefore, the proposed method is immune to the modeling mismatch and/or parametric errors.

Similar to the previously proposed current regulation schemes [18, 24], the proposed method independently regulates the dq-components of the currents while it does not impose excessive structural complexity. However, contrary to the previously proposed methods, the proposed approach fully decouples the current axes, i.e., the dq-axes. The performance of the proposed method is evaluated in MATLAB/PLECS environment, and the findings are confirmed by the experiments. It is concluded that the proposed optimization-based method:

- tracks the reference signals with zero steady-state errors,

- has better dynamic performance compared to the previously proposed approaches,

- results in decoupled current axes.

Moreover, the applicability of the proposed decoupled dq-currents control strategy is extended to single-phase grid-tied VSCs. In such systems, in order to form a stationary and also a synchronous frame, orthogonal components are required for both voltage and current. The orthogonal component of the voltage is generated by a SOGI-based PLL. In the conventional approaches phase shifting is adopted in order to create the orthogonal current, which results in strongly coupled axes. However, the proposed control strategy generates the required orthogonal current concurrently with the physical system. The proposed countermeasure generates the required orthogonal current component by the FAE, which results in fast non-oscillatory dynamics and decoupled dq-axes. The performance of the proposed control strategy is evaluated based on simulation and experiment, and moreover, it is compared with that of the conventional delay-based approach. The conducted studies conclude that the proposed method:

- can maintain the stability of the system and track reference values with zero steady-state error,

- has superior dynamic response compared to the conventional approach.

<div style="text-align: right;">*3*</div>

Voltage Control of Islanded Microgrids

3.1 Introduction

This chapter proposes a general digital multivariable controller design methodology for the voltage control of an islanded single-DG-unit microgrid with large variations of the load parameters. The proposed method is based on the system open-loop shaping with some constraints to ensure the stability of the closed-loop system. It uses MIMO nonparametric or spectral models of the system for an arbitrary number of desired operating points along with a linearly parameterized MIMO controller to form a set of open-loop transfer function matrices. Based on the dynamic performance and decoupling requirements, a desired open-loop transfer function matrix is also formed, and its diagonal and off-diagonal elements are determined. Minimizing the summation of the errors between the open-loop transfer function matrices and the desired one, the coefficients of the controller are optimally determined. The diagonal elements of the controller are tuned to satisfy the desired dynamic performance, while simultaneously, the off-diagonal elements are designed to decouple the dq-axes components. To ensure the stability of the designed controller, the minimization problem is subject to some constraints. The salient feature of the proposed design methodology, as compared with the existing multivariable controllers, is its capability to accommodate multi-model uncertainties and to achieve robustness with respect to the uncertainties in the load parameters [62].

Based on the proposed design methodology, three novel MIMO dq-voltages control methods, to regulate the voltages of an islanded single-DG-unit microgrid, are presented: (i) a single-stage PI-based MIMO controller, (ii) a single-stage PI-based MIMO controller in conjunction with resonant terms, which is able to compensate for the adverse impacts of nonlinear loads, and (iii) a cascade PI-based MIMO controller. The cascade control strategy consists of an inner dq-currents control loop, which is realized by the approach of Chapter 2, and an outer loop responsible for providing the set-points of the inner loop. The proposed controllers guarantee the robust stability and provide satisfactory performance of the islanded microgrid, despite load uncertainties. The performances of the proposed controllers are evaluated based on
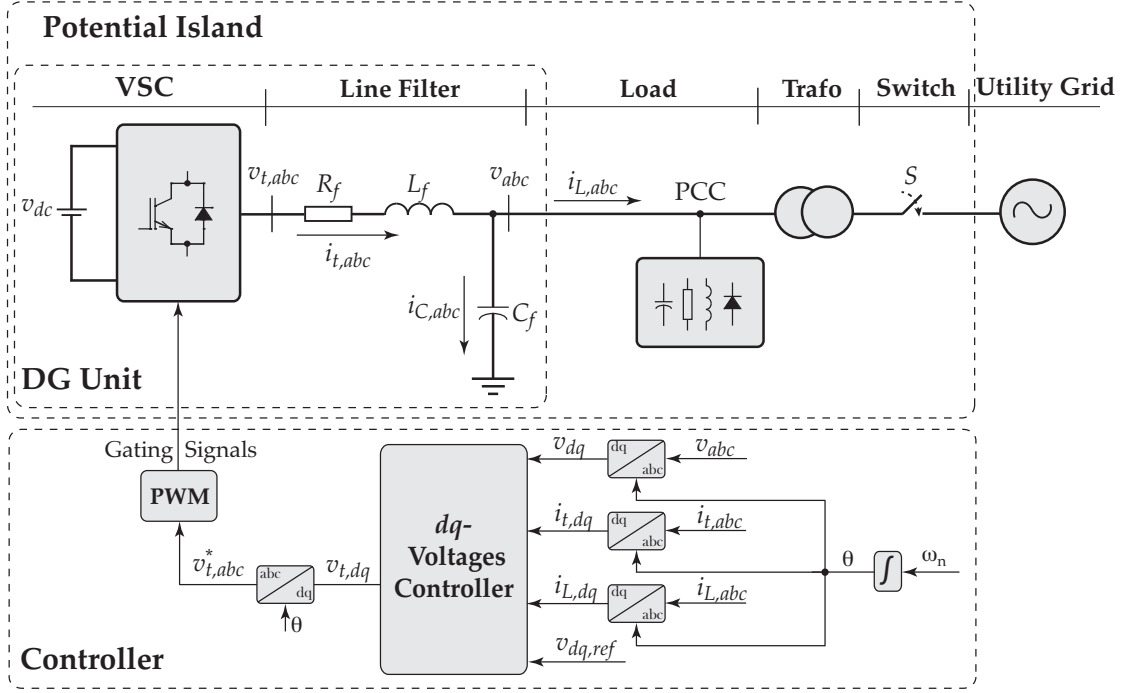
Figure 3.1: The single-line diagram of the three-phase single-DG-unit microgrid

time-domain simulation studies and are experimentally validated.

The rest of this chapter is organized as follows. Section 3.2 describes the single-DG-unit microgrid study system. Section 3.3 presents the proposed multivariable controller design methodology. Section 3.4 presents the details of three designed dq-based voltage controllers for the islanded system. The performance evaluation of the proposed voltage controllers, under various operating scenarios, is reported in Section 3.5. Section 3.6 concludes the chapter.

3.2 Study System Description

Figure 3.1 shows a schematic single-line diagram of the study microgrid system. The microgrid system comprises a single DG unit, which is connected to its dedicated load and the utility grid at the PCC. The DG unit is represented by a DC voltage source, a VSC, and a series LC filter. The filter is realized by an inductor, L_f, and a capacitor, C_f. The inductor has a series internal resistance, R_f. The load can be any combination of a three-phase parallel RLC load and a three-phase diode rectifier. The microgrid can be connected to the utility grid through a coupling transformer and a switch. The parameters of the study system of Figure 3.1 are summarized in Table 3.1.

In the grid-connected mode of the operation of the system of Figure 3.1, the switch S is closed, and the grid imposes the amplitude and the frequency of the PCC voltages. However, In the

Table 3.1: The parameters of the study system of Figure 3.1

Quantity	Value	PU	Comment
R_f	0.3 Ω	0.11	Resistance of VSC Filter
L_f	1.5 mH	0.18	Inductance of VSC Filter
C_f	100 μF	0.074	Capacitance of VSC Filter
S_{base}	0.6 kVA	1	VSC Rated Power
v_{dc}	200 V		DC Bus Voltage
v	40 V (peak)	1	Ph-G Nominal Voltage
f_{sw}	10 kHz		PWM Carrier Frequency
f_s	50 kHz		Sampling Frequency
f	50 Hz		System Nominal Frequency
ω_n	314.15 rad/s		Nominal Angular Frequency

islanded mode, which is the main focus of this chapter, the switch S is open, and the voltages at the PCC are no longer imposed by the utility grid. Thus, the primary purpose of the controller block of Figure 3.1 is to regulate the amplitude and frequency of the load voltages, v_{abc}. This is achieved by a controller that regulates the dq-components of the load voltages, i.e., v_{dq}, at their desired values. The dq-components of the load voltages, converter currents, and load currents along with the reference values of the dq-voltages are fed into the controller. The controller then generates the control signals, i.e., the dq-components of the VSC terminal voltages, $v_{t,dq}$. The dq-voltages controller block along with the required input signals and their associated output signals are depicted in Figure 3.1. As shown in Figure 3.1, the frequency of the islanded microgrid is set at the system nominal frequency, ω_n, in an open loop manner.

In the next section, a general multivariable design methodology for the voltage control of the system of Figure 3.1 is proposed. Then, in the following sections, using the presented design methodology, three dq-voltages control strategies are proposed.

3.3 Proposed Multivariable Control Design Methodology

This section proposes a general methodology to design a voltage controller for a VSC-based system. The proposed methodology originates from the MIMO controller design approach in [62], which based on a family of spectral MIMO models of the system, develops a convex optimization-based control method. The basic idea of this approach is to shape the open-loop transfer function matrix of the system by minimizing the absolute errors between a family of the open-loop transfer function matrices of the system, obtained for various operating points of interest, i.e., $\mathscr{L} = \{\mathbf{L_i}(j\omega); i = 1, ..., m; \forall \omega \in \mathbb{R}\}$, and a desired open-loop transfer function matrix, i.e., $\mathbf{L_D}(s)$. The system open-loop transfer function matrix at the ith operating point of the system is $\mathbf{L_i}(j\omega) = \mathbf{G_i}(j\omega)\mathbf{K}(j\omega)$, where $\mathbf{G_i}(j\omega)$ represents the system transfer function matrix at the ith operating point of the system, and $\mathbf{K}(j\omega)$ represents the controller transfer function matrix. Since this loop shaping approach does not necessarily guarantee the desired

performance and stability of the closed-loop system, to meet performance and robustness specifications, the minimization problem is subject to some constraints. The design procedure includes the following main steps: (i) the determination of a family of the nonparametric models of the system at various operating points, (ii) the determination of the class of the controller, and (iii) system open-loop shaping by the minimization of the summation of the square second norm of the errors between the system open-loop transfer function matrices and a desired open-loop transfer function matrix.

It must be noted that the following design procedure is basically a generalization of the design approach presented in Chapter 2. Therefore, some part of the following discussions are similar to those of Chapter 2.

3.3.1 Determination of a Family of Nonparametric Models

Assuming a system with two inputs and two outputs, the transfer function matrix of the system at each operating point, based on nonparametric models, is given by

$$\begin{bmatrix} y_1 \\ y_2 \end{bmatrix} = \underbrace{\begin{bmatrix} G_{i,11} & G_{i,12} \\ G_{i,21} & G_{i,22} \end{bmatrix}}_{\mathbf{G_i}(j\omega)} \begin{bmatrix} u_1 \\ u_2 \end{bmatrix}, \tag{3.1}$$

where the index i represents the ith operating point of the system. Moreover, u_1 and u_2 represent the inputs while y_1 and y_2 represent the outputs. The elements of the matrix $\mathbf{G_i}(j\omega)$ are determined by frequency response measurements of the system, i.e., the estimation of the frequency response of the system in the range of the frequencies of interest. To achieve this, a potential approach is to stimulate the system by using a PRBS generator at its input ports [72] and measure the response at the output ports as explained in Section 2.3.1. Applying a PRBS with a sufficient amplitude, within the operating range of the system, to u_1, two elements of the matrix $\mathbf{G_i}(j\omega)$ can be identified as follows:

$$G_{i,11}(j\omega) = \frac{\mathscr{F}(y_1)}{\mathscr{F}(u_1)} \quad \text{and} \quad G_{i,21}(j\omega) = \frac{\mathscr{F}(y_2)}{\mathscr{F}(u_1)}, \tag{3.2}$$

where $\mathscr{F}$ represents the Fourier transform. Likewise, by applying a PRBS to u_2, the other two elements of the matrix $\mathbf{G_i}(j\omega)$ are identified as

$$G_{i,12}(j\omega) = \frac{\mathscr{F}(y_1)}{\mathscr{F}(u_2)} \quad \text{and} \quad G_{i,22}(j\omega) = \frac{\mathscr{F}(y_2)}{\mathscr{F}(u_2)}. \tag{3.3}$$

Repeating the same procedure for m operating points, a family of the nonparametric models of the system is determined as

$$\mathscr{G} = \{\mathbf{G_i}(j\omega); i = 1, ..., m; \forall \omega \in \mathbb{R}\}. \tag{3.4}$$

The family of the nonparametric models of the system, represented by (3.4), are used as a basis to design the voltage controllers. It must be noted that if the parametric model of the system is available, one can extract the frequency response of the parametric model for various operating points to form the required spectral model family. However, since parametric models do not precisely reflect the dynamic behavior of the system, the PRBS-based identification approach is preferred.

3.3.2 Determination of the Class of Controller

To form the open-loop transfer function matrix of the overall system including the controller, the class of the to-be-designed controller is required. Since the objective is to design a linearly parameterized multivariable digital controller, the class of the controller is determined in the z-domain. A generic form of such a multivariable discrete-time controller in the z-domain is given by

$$\mathbf{K}(z) = \left[\begin{array}{cc} K_{11} & K_{12} \\ K_{21} & K_{22} \end{array} \right]. \tag{3.5}$$

Each element of the controller matrix of (3.5) is then given by

$$K_{ij}(z,\rho) = \rho^T \phi(z), \tag{3.6}$$

where

$$\rho^T = [\rho_1, \rho_2, \ldots, \rho_n] \tag{3.7}$$

and

$$\phi^T(z) = [\phi_1(z), \phi_2(z), \ldots, \phi_n(z)]. \tag{3.8}$$

In (3.7) and (3.8), n is the controller order for each element of the controller matrix, and $\phi_m(z)$, $m = 1, \ldots, n$, are stable transfer functions possibly with poles on the imaginary axis. Therefore, the 2×2 controller of (3.5) has $4 \times n$ controller parameters, which must be determined.

Replacing $z = e^{-j\omega}$ in (3.5), the frequency response of the controller, i.e., $\mathbf{K}(j\omega)$, is deduced. Then, having the family of the nonparametric models of the system from (3.4) and the frequency response of the controller class of (3.5), a family of the open-loop transfer function matrices of the overall system is concluded by

$$\mathcal{L} = \{\mathbf{L_i}(j\omega); i = 1, \ldots, m; \forall \omega \in \mathbb{R}\}, \tag{3.9}$$

in which $\mathbf{L_i}(j\omega) = \mathbf{G_i}(j\omega)\mathbf{K}(j\omega)$.

3.3.3 Loop Shaping by Convex Optimization

The loop shaping of the open-loop transfer function matrix of a system with a family of nonparametric models like $\mathscr{L}$ is carried out by minimizing the summation of the square second norm of the errors between the individual entries of $\mathscr{L}$ and a desired open-loop transfer function matrix, $\mathbf{L_D}(s)$. Consequently, the control design procedure turns to an optimization problem as follows [62]:

$$\min_{\rho} \sum_{i=1}^{m} \parallel \mathbf{L_i}(\rho) - \mathbf{L_D} \parallel^2, \tag{3.10}$$

where m is the number of the open-loop transfer function matrices that form the family of $\mathscr{L}$. The desired open-loop transfer function matrix, $\mathbf{L_D}$, is chosen to meet the system requirements, e.g., satisfactory dynamic response and reduced coupling between the inputs and the outputs. As an example, for a 2×2 MIMO system, a potential desired open-loop transfer function matrix is

$$\mathbf{L_D}(s) = \left[\begin{array}{cc} L_{D1} & 0 \\ 0 & L_{D2} \end{array} \right] = \left[\begin{array}{cc} \frac{\omega_c}{s} & 0 \\ 0 & \frac{\omega_c}{s} \end{array} \right]. \tag{3.11}$$

In the transfer function matrix of (3.11), the off-diagonal elements are set at zero to decouple the system while the diagonal elements are tuned to provide the required dynamic response by adjusting ω_c. Furthermore, the closed-loop sensitivity function of the diagonal elements, $S_{i,qq} = (1 + L_{i,qq})^{-1}$, can be shaped using $|W_1(j\omega)S_{i,qq}(j\omega)| < 1 \ \forall \omega$, where $W_1(j\omega)$ is a weighting filter, $q = 1, 2$, and $i = 1, ..., m$. This is an H_∞ performance condition that guarantees the robustness of the main axes [73]. A convex approximation of this condition can be given by the following linear constraints [62]:

$$|W_1(j\omega)[1 + L_{Dq}(j\omega, \rho)]| - \mathcal{R}e\{[1 + L_{Dq}(-j\omega)][1 + L_{i,qq}(j\omega, \rho)]\} < 0$$
$$\forall \omega \in \mathbb{R}, \ i = 1, ..., m, \text{ and } q = 1, 2. \tag{3.12}$$

Solving the optimization problem of (3.10) constrained to (3.12) results in a decoupled open-loop transfer function matrix, which provides satisfactory reference tracking capability. However, it does not guarantee the stability of the multivariable closed-loop system. To ensure the stability of the multivariable closed-loop system, the Generalized Nyquist Stability criterion must be respected. This criterion guarantees the stability of the feedback system *if and only if the net sum of counterclockwise encirclements of the critical point* $(-1 + j0)$ *by the set of eigenvalues of the matrix* $\mathbf{L_i}(j\omega)$ *is equal to the total number of the right-half plane poles of* $\mathbf{L_i}(s)$. To satisfy this condition, adopting *Gershgorin bands*, reference [62] proves that assuming the nonparametric model $\mathbf{G_i}(j\omega)$, the linearly parameterized controller $\mathbf{K}(z)$ defined in (3.5)

stabilizes the closed-loop system if

$$r_{i,q}(\omega, \rho) - \frac{\mathcal{R}e\{[1 + L_{Dq}(-j\omega)][1 + L_{i,qq}(j\omega, \rho)]\}}{|1 + L_{Dq}(j\omega)|} < 0$$
$$\forall \omega \text{ for } i = 1, ..., m \text{ and } q = 1, 2. \tag{3.13}$$

In (3.13), the diagonal matrix $\mathbf{L_D}(j\omega)$ should be chosen such that the number of counterclockwise encirclements of the critical point by the Nyquist plot of the set of its eigenvalues is equal to the number of unstable poles of $\mathbf{G_i}(s)$. For example, the transfer function matrix of (3.11) is a fulfilling choice. Moreover, $r_{i,1}(\omega, \rho)$ and $r_{i,2}(\omega, \rho)$ are defined as

$$r_{i,1}(\omega, \rho) = |L_{i,21}(j\omega, \rho)| \tag{3.14}$$

and

$$r_{i,2}(\omega, \rho) = |L_{i,12}(j\omega, \rho)|. \tag{3.15}$$

Considering the constraints for the desired performance given by (3.12) and the constraints for the stability of the closed-loop system given by (3.13), the design procedure is summarized into the following optimization problem:

$$\min_{\rho} \sum_{i=1}^{m} \| \mathbf{L_i}(\rho) - \mathbf{L_D} \|^2, \tag{3.16}$$

subject to

$$|W_1(j\omega)[1 + L_{Dq}(j\omega, \rho)]| - \mathcal{R}e\{[1 + L_{Dq}(-j\omega)][1 + L_{i,qq}(j\omega, \rho)]\} < 0$$
$$\forall \omega \in \mathbb{R} \text{ for } i = 1, ..., m \text{ and } q = 1, 2. \tag{3.17}$$

and

$$r_{i,q}(\omega, \rho) - \frac{\mathcal{R}e\{[1 + L_{Dq}(-j\omega)][1 + L_{i,qq}(j\omega, \rho)]\}}{|1 + L_{Dq}(j\omega)|} < 0$$
$$\forall \omega \in \mathbb{R} \text{ for } i = 1, ..., m \text{ and } q = 1, 2. \tag{3.18}$$

The optimization problem of (3.16), known as a SIP problem, includes infinite number of constraints and finite number of variables, which is difficult to solve. A practical solution to this problem is to neglect the frequencies above a certain frequency, i.e., ω_{max}, for which the

gain of the open-loop transfer function matrix is close to zero. For discrete-time systems, this frequency can be chosen as the Nyquist frequency. Then, one can only consider the gridded frequency interval $[0 \ \omega_{max}]$, which contains finite frequency points. Such problems are referred to as SDP problems and are solved utilizing standard SDP-solvers, e.g., SeDuMi [74].

Choosing N linearly spaced frequencies within the range of $[0 \ \omega_{max}] \in \mathbb{R}$, the quadratic objective function is approximated by

$$\sum_{i=1}^{m} \| \mathbf{L_i}(\rho) - \mathbf{L_D} \|^2 \approx \sum_{i=1}^{m} \sum_{k=1}^{N} \| \mathbf{L_i}(j\omega_k, \rho) - \mathbf{L_D}(j\omega_k) \|_F, \tag{3.19}$$

where $\|.\|_F$ is the Frobenius norm. Therefore, the following optimization problem is deduced:

$$\min_{\rho} \sum_{i=1}^{m} \sum_{k=1}^{N} \| \mathbf{L_i}(j\omega_k, \rho) - \mathbf{L_D}(j\omega_k) \|_F, \tag{3.20}$$

subject to

$$|W_1(j\omega_k)[1 + L_{Dq}(j\omega_k)]| - \mathcal{Re}[1 + L_{Dq}(-j\omega_k)][1 + L_{i,qq}(j\omega_k, \rho)] < 0$$
$$\text{for } k = 1, \dots, N, \ i = 1, \dots, m, \text{ and } q = 1, 2 \tag{3.21}$$

and

$$r_{i,q}(\omega_k, \rho) - \frac{\mathcal{Re}\{[1 + L_{Dq}(-j\omega_k)][1 + L_{i,qq}(j\omega_k, \rho)]\}}{|1 + L_{Dq}(j\omega_k)|} < 0$$
$$\text{for } k = 1, \dots, N, \ i = 1, \dots, m, \text{ and } q = 1, 2. \tag{3.22}$$

The optimization problem of (3.20) in conjunction with the constraints in (3.21) and (3.22) is then used as a basis to determine the optimal coefficients of the proposed MIMO controllers in the following section.

3.4   Proposed dq-Augmented Voltage Controllers

In this section, the spectral-model-based multivariable control design approach of Section 3.3 is used to propose three dq-based voltage control strategies for the single-DG-unit islanded microgrid of Figure 3.1: (i) a Single-stage Multivariable-PI Controller (SMPC) comprising four PI-controllers to regulate the load voltages in the presence of linear balanced three-phase loads, (ii) a Single-stage Multivariable-PI Resonant Controller (SMPRC), which uses resonant terms in conjunction with the PI-controllers of the SMPC to regulate the load voltages in the presence of linear and/or nonlinear loads, and (iii) a Cascade Multivariable-PI Controller
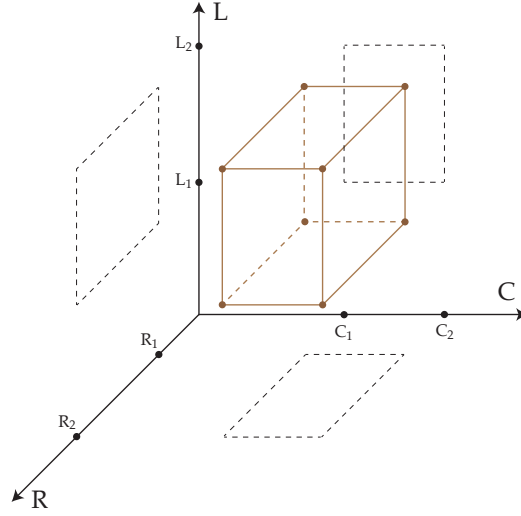
Figure 3.2: The cube formed by the intervals of (3.23) in the three-dimensional RLC space

(CMPC) that utilizes four PI-controllers to form an outer voltage control loop, which generates the set-points of an inner current control loop. In the following, the controllers are detailed.

3.4.1 Single-stage Multivariable-PI Controller - SMPC

Based on the design methodology of Section 3.3, the first step is to obtain the nonparametric models of the system at the operating points for which the controller is designed, and form a family of models. To form the family, it is assumed that the load parameters may change within some uncertainty ranges as presented by

$$
\begin{aligned}
6\ \Omega &\le R \le 600\ \Omega, \\
25\ mH &\le L \le 50\ mH, \\
200\ \mu F &\le C \le 400\ \mu F,
\end{aligned}
\tag{3.23}
$$

which form a cube in the three-dimensional RLC space, as shown in Figure 3.2. Then, eight models corresponding to the vertices of the cube are taken to form the family of models and are utilized in the optimization problem. Figure 3.3 depicts two of the assumed models corresponding to $RLC = [6\ \Omega,\ 25\ mH, 200\ \mu F]$ and $RLC = [600\ \Omega,\ 50\ mH, 400\ \mu F]$. Therefore, the family of spectral model is determined as follows:

$$
\mathscr{G} = \{\mathbf{G_i}(j\omega); i = 1, ..., 8; \forall \omega \in \mathbb{R}\}.
\tag{3.24}
$$

In the single-stage controllers, the inputs of the to-be-controlled system are the dq-components of the VSC terminal voltages, $v_{t,dq}$, while the system outputs are the dq-components of the load voltages, v_{dq}. Therefore, applying a PRBS to $v_{t,q}$, two elements of the matrix $\mathbf{G_i}(j\omega)$ for
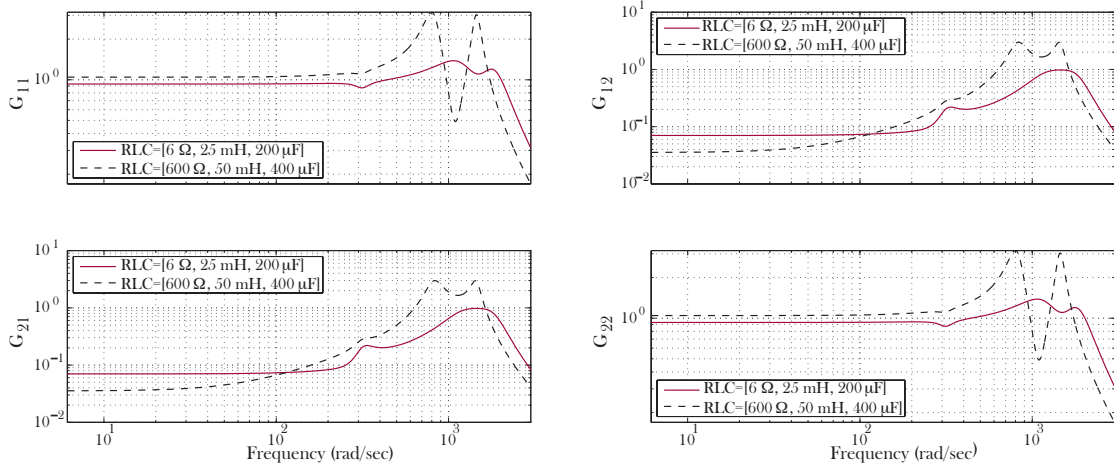
Figure 3.3: Two spectral models of the system corresponding to RLC = [6 Ω, 25 mH, 200 μF] and RLC = [600 Ω, 50 mH, 400 μF]

the ith operating point can be identified as follows:

$$G_{i,11}(j\omega) = \frac{\mathscr{F}(v_d)}{\mathscr{F}(v_{t,d})} \quad \text{and} \quad G_{i,21}(j\omega) = \frac{\mathscr{F}(v_q)}{\mathscr{F}(v_{t,d})}, \tag{3.25}$$

where $\mathscr{F}$ represents the Fourier transform. Likewise, by applying a PRBS to $v_{t,q}$, the other two elements of the matrix $\mathbf{G_i}(j\omega)$ are identified as

$$G_{i,12}(j\omega) = \frac{\mathscr{F}(v_d)}{\mathscr{F}(v_{t,q})} \quad \text{and} \quad G_{i,22}(j\omega) = \frac{\mathscr{F}(v_q)}{\mathscr{F}(v_{t,q})}. \tag{3.26}$$

It must be noted that even if the to-be-designed controller stabilizes the closed-loop system for the assumed points, it does not necessarily guarantee the stability of all points within the assumed cube. However, taking more points within the assumed cube and solving the optimization problem for all of them, the resulting controller more likely stabilize the system for all points. It should be noted that as far as the optimization problem is feasible and has a solution, any desired number of models can be utilized in the optimization problem.

The second step is to determine the class of the controller. The primary goal of the SMPC is to stabilize the system and to regulate the voltages in the presence of linear balanced three-phase loads. Therefore, four PI-controllers are selected for the individual elements of the transfer function matrix of the MIMO controller. Figure 3.4 depicts the structure of the SMPC. The coefficients of the individual PI-controllers are determined in the third step of the control design methodology, i.e., solving the constrained minimization problem. To solve the constrained minimization problem of (3.20), a desired open-loop transfer function matrix is
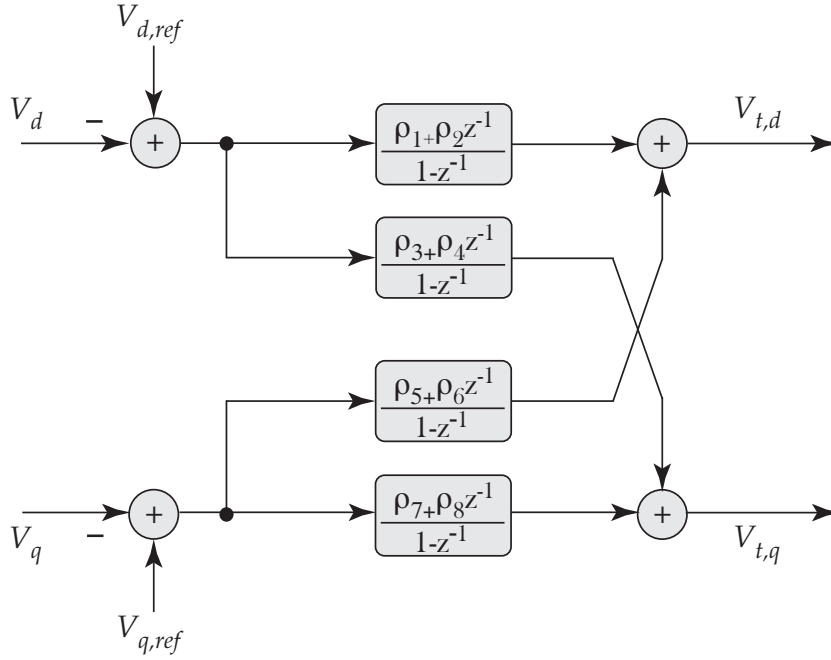
Figure 3.4: The structural diagram of the SMPC

required. A reasonable open-loop transfer function matrix for this application is chosen as

$$\mathbf{L_D}(s) = \begin{bmatrix} \frac{\omega_c}{s} & 0 \\ 0 & \frac{\omega_c}{s} \end{bmatrix},$$

(3.27)

where $\omega_c = 150 \frac{rad}{s}$. The zero off-diagonal elements of $\mathbf{L_D}$ are to decouple the $d-$ and $q-$axes. Solving the minimization problem of (3.20), the controller transfer function matrix is calculated as

$$\mathbf{K}(z) = \begin{bmatrix} \frac{\rho_1+\rho_2 z^{-1}}{1-z^{-1}} & \frac{\rho_5+\rho_6 z^{-1}}{1-z^{-1}} \\ \frac{\rho_3+\rho_4 z^{-1}}{1-z^{-1}} & \frac{\rho_7+\rho_8 z^{-1}}{1-z^{-1}} \end{bmatrix} = \begin{bmatrix} \frac{0.061-0.058z^{-1}}{1-z^{-1}} & \frac{-0.048+0.048z^{-1}}{1-z^{-1}} \\ \frac{0.048-0.048z^{-1}}{1-z^{-1}} & \frac{0.061-0.059z^{-1}}{1-z^{-1}} \end{bmatrix}.$$

(3.28)

3.4.2 Single-stage Multivariable-PI-Resonant Controller - SMPRC

The SMPC in Section 3.4.1 is designed based on the assumption of having linear, balanced three-phase loads. In the presence of nonlinear loads where the currents are significantly polluted with low-order harmonics, e.g., 5th and 7th harmonics, the designed SMPC does not provide satisfactory performance. The objective of this section is to improve the performance of the SMPC by modifying the class of the controller and adding additional resonant terms to the individual PI-controllers and also to the desired open-loop transfer function matrix. The structure of the modified SMPC in conjunction with the resonant terms, i.e., the so-called
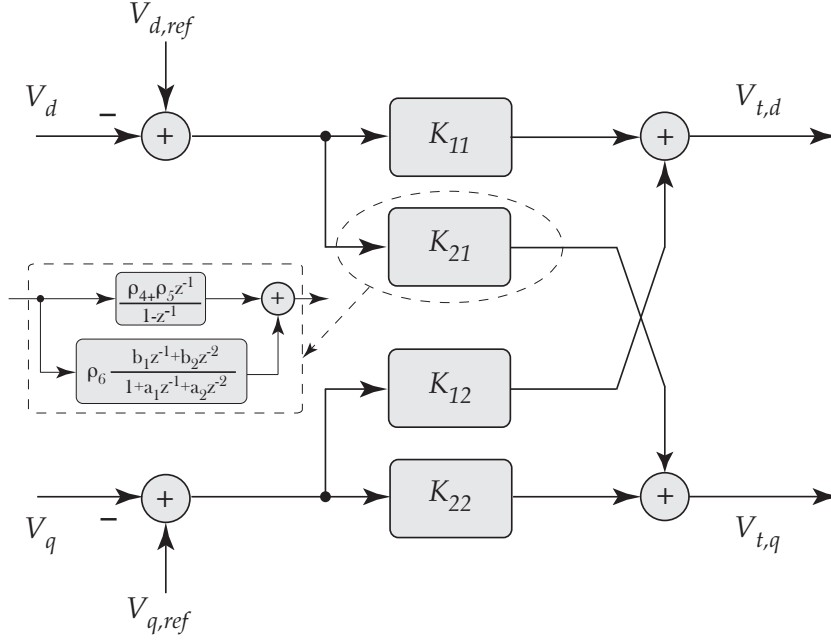
Figure 3.5: The structural diagram of the SMPRC

SMPRC, is depicted in Figure 3.5. The harmonics of the order of 5 and 7 in the abc-frame both appear at the frequency of 300 Hz in the dq-frame. Therefore, adding a single resonant term tuned at the frequency of 300 Hz to the elements of the controller matrix can eliminate both 5th and 7th voltage harmonics. As an example, the second diagonal element of the controller transfer function matrix, i.e., $K_{21}(z)$, is expressed as

$$K_{21}(z) = \frac{\rho_4 + \rho_5 z^{-1}}{1 - z^{-1}} + \rho_6 \frac{b_1 z^{-1} + b_2 z^{-2}}{1 + a_1 z^{-1} + a_2 z^{-2}}. \tag{3.29}$$

The term $\frac{b_1 z^{-1} + b_2 z^{-2}}{1 + a_1 z^{-1} + a_2 z^{-2}}$ in (3.29) represents an equivalent term for $\frac{\omega_h^2}{s^2 + 2\zeta\omega_h s + \omega_h^2}$ in discrete-time domain, in which $\omega_h = 2\pi300$, and $\zeta = \frac{3}{\omega_h}$ is the damping ratio. Moreover, $a_1 = -2\alpha\beta$ and $a_2 = \alpha^2$, and the coefficients b_1 and b_2 are determined as follow:

$$b_1 = 1 - \alpha(\beta + \frac{\zeta\omega_h}{\omega_b}\eta) \quad \text{and} \quad b_2 = \alpha^2 + \alpha(\frac{\zeta\omega_h}{\omega_b}\eta - \beta), \tag{3.30}$$

in which $\omega_b = \omega_h\sqrt{1 - \zeta^2}$ for $\zeta < 1$, $\alpha = e^{\frac{-\zeta\omega_h}{f_s}}$, $\beta = cos(\frac{\omega_b}{f_s})$, $\eta = sin(\frac{\omega_b}{f_s})$, and f_s represents the sampling frequency. Note that in the presence of highly nonlinear loads, the most significant harmonics are the low-order harmonics of the order of 5 and 7, which both appear at the frequency of 300 Hz in the dq-frame. Therefore, using only one resonant term tuned at the frequency of 300 Hz is enough to eliminate the low-order harmonics generated by such nonlinear loads. However, in case the elimination of higher-order harmonics, e.g., 11th and

13th harmonic voltage components, is also of interest, additional resonant terms can be added to the existing terms.

To determine the coefficients of the SMPRC, similar to the design procedure of the SMPC, the identified spectral models of the system are required. Similar to the SMPC, eight spectral models as expressed in(3.24), corresponding to the vertices of the cube formed by the intervals of (3.23), are obtained and utilized in the design procedure. Moreover, the desired open-loop transfer function matrix is determined by adding resonant terms tuned at 300 Hz to the diagonal elements of the transfer function matrix of (3.27). Therefore, the desired open-loop transfer function matrix is:

$$\mathbf{L_D}(s) = \begin{bmatrix} \frac{\omega_{c1}}{s} + \frac{\omega_{c2}}{s^2+2\zeta\omega_h s+\omega_h^2} & 0 \\ 0 & \frac{\omega_{c1}}{s} + \frac{\omega_{c2}}{s^2+2\zeta\omega_h s+\omega_h^2} \end{bmatrix} \tag{3.31}$$

in which $\omega_{c1} = 70 \frac{rad}{s}$. Moreover, ω_{c2} for the models with $R = 6\ \Omega$ is $90000\ \frac{rad}{s}$ and for the models with $R = 600\ \Omega$ is $80000\ \frac{rad}{s}$. Then, solving the optimization problem of (3.20), the coefficients of the SMPRC are determined and expressed by

$$\begin{aligned}\mathbf{K}(z) &= \begin{bmatrix} \frac{\rho_1+\rho_2 z^{-1}}{1-z^{-1}} + \frac{\rho_3(b_1 z^{-1}+b_2 z^{-2})}{1+a_1 z^{-1}+a_2 z^{-2}} & \frac{\rho_4+\rho_5 z^{-1}}{1-z^{-1}} + \frac{\rho_6(b_1 z^{-1}+b_2 z^{-2})}{1+a_1 z^{-1}+a_2 z^{-2}} \\ \frac{\rho_7+\rho_8 z^{-1}}{1-z^{-1}} + \frac{\rho_9(b_1 z^{-1}+b_2 z^{-2})}{1+a_1 z^{-1}+a_2 z^{-2}} & \frac{\rho_{10}+\rho_{11} z^{-1}}{1-z^{-1}} + \frac{\rho_{12}(b_1 z^{-1}+b_2 z^{-2})}{1+a_1 z^{-1}+a_2 z^{-2}} \end{bmatrix} \\ &= \begin{bmatrix} \frac{0.061-0.060 z^{-1}}{1-z^{-1}} + \frac{-0.013(b_1 z^{-1}+b_2 z^{-2})}{1+a_1 z^{-1}+a_2 z^{-2}} & \frac{0.032-0.032 z^{-1}}{1-z^{-1}} + \frac{-0.002(b_1 z^{-1}+b_2 z^{-2})}{1+a_1 z^{-1}+a_2 z^{-2}} \\ \frac{-0.032+0.032 z^{-1}}{1-z^{-1}} + \frac{0.002(b_1 z^{-1}+b_2 z^{-2})}{1+a_1 z^{-1}+a_2 z^{-2}} & \frac{0.061-0.06 z^{-1}}{1-z^{-1}} + \frac{-0.013(b_1 z^{-1}+b_2 z^{-2})}{1+a_1 z^{-1}+a_2 z^{-2}} \end{bmatrix}. \end{aligned} \tag{3.32}$$

3.4.3 Cascade Multivariable-PI Controller - CMPC

Cascade control or multi-loop control strategies have been extensively utilized and reported in the literature [78] for the islanded operation of inverters. In such methods, an inner loop is responsible for the regulation of the inverter current, while the set-points of the current controller are delivered by an outer voltage control loop. The main advantage of cascade control is the capability of load disturbance rejection by adding feedforward signals to the set-points of the current loop.

Reference [78] utilizes Proportional-Resonant controllers to realize the inner and outer loops. However, in this chapter, the controllers are implemented in rotating reference frame, and therefore, a dq-currents controller realized by PI-controllers, i.e., the OMCC as explained in Chapter 2, is utilized to form the inner loop. Figure 3.6 depicts the structure of the controller, in which the OMCC is used as the inner loop. To design the outer voltage loop, which consists of four PI-controllers, the spectral model-based multivariable control design of this chapter is used. It is assumed that the load currents are directly measurable, and may be used as
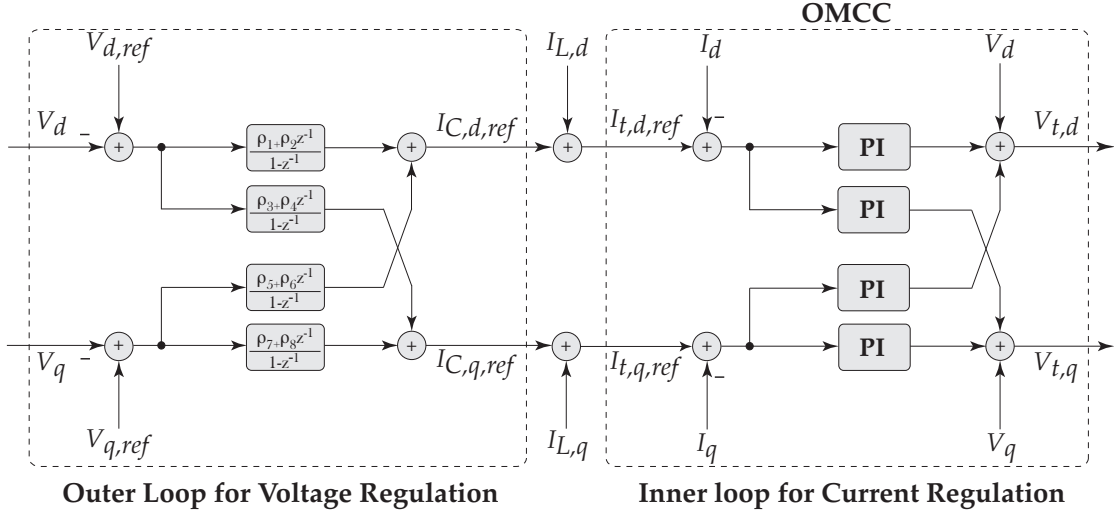
Figure 3.6: The structural diagram of the CMPC

feedforward to reduce the adverse effects of load changes. Therefore, the dq-components of the load currents are added to the outputs of the voltage loop, as shown in Figure 3.6. Thus, the outputs of the voltage loop may be regarded as the set-points of the dq-components of the filter capacitance currents.

To design the outer loop, the first step is to determine the spectral models family. Since the goal of the outer loop is to provide the inner loop with its set-points, the spectral models utilized to design the outer loop are different from those utilized for the SMPC and the SMPRC. The inputs of the to-be-controlled system by the outer loop are the set-points of the dq-currents controller, while the outputs are the dq-components of the load voltages. Therefore, exciting $i_{t,d,ref}$ with a PRBS at the ith operating point, one can identify the frequency response of $G_{i,11}$ and $G_{i,21}$ as

$$G_{i,11}(j\omega) = \frac{\mathcal{F}(v_d)}{\mathcal{F}(i_{t,d,ref})} \quad \text{and} \quad G_{i,21}(j\omega) = \frac{\mathcal{F}(v_q)}{\mathcal{F}(i_{t,d,ref})}. \tag{3.33}$$

The same holds for obtaining $G_{i,22}$ and $G_{i,12}$ through exciting $i_{t,q,ref}$. Two spectral models of the system are identified: (i) the spectral model corresponding to the full load and (ii) the model corresponding to the no load.

PI-controllers are selected as the elements of the controller matrix. Therefore, to design the controller, eight coefficients must be determined for the four PI-controllers of the multivariable control structure. The desired open loop transfer function is also selected as

$$\mathbf{L_D}(s) = \begin{bmatrix} \frac{\omega_c}{s} & 0 \\ 0 & \frac{\omega_c}{s} \end{bmatrix} \tag{3.34}$$

in which $\omega_c = 300 \frac{rad}{s}$. Note that the bandwidth of the voltage loop can be manipulated by the

choice of ω_c. Solving the minimization problem of (3.22), the control matrix is calculated as

$$\mathbf{K}(z) = \left[\begin{array}{cc} \frac{\rho_1+\rho_2 z^{-1}}{1-z^{-1}} & \frac{\rho_5+\rho_6 z^{-1}}{1-z^{-1}} \\[2ex] \frac{\rho_3+\rho_4 z^{-1}}{1-z^{-1}} & \frac{\rho_7+\rho_8 z^{-1}}{1-z^{-1}} \end{array} \right] = \left[\begin{array}{cc} \frac{0.06+64.69 z^{-1}}{1-z^{-1}} & \frac{-0.01+7.85 z^{-1}}{1-z^{-1}} \\[2ex] \frac{0.01-7.89 z^{-1}}{1-z^{-1}} & \frac{0.06+64.68 z^{-1}}{1-z^{-1}} \end{array} \right]. \tag{3.35}$$

Note that taking the design procedure of Chapter 2, an OMCC is designed and used to form the inner current loop. The bandwidth of the designed OMCC is 500 Hz.

In the following, the performance of the designed SMPC, SMPRC, and CMPC are evaluated for several inductive, capacitive, and resistive load changes.

3.5   Performance Evaluation

This section presents a set of simulation and experimental results to evaluate and validate the performance of the proposed controllers for the microgrid system of Figure 3.1.

3.5.1   Simulation Results

The simulation studies of the single-DG-unit microgrid system of Figure 3.1, based on the proposed SMPC, SMPRC, and CMPC, in the MATLAB/PLECS environment are reported in this section. The simulation studies are conducted to demonstrate the performance of the proposed controllers under two load change scenarios: (i) inductive-capacitive load changes and (ii) linear and nonlinear resistive load changes. For the former, the *RLC* load parameters as well as their arrangement are chosen based on the three-phase balanced *RLC* load of Figure 3.7 while for the latter, the three-phase load of Figure 3.8, which includes both linear and nonlinear resistive loads, is used.

3.5.1.1   Inductive-Capacitive Load Changes

Initially, the system of Figure 3.1 operates in the islanded mode, and the three-phase load of Figure 3.7 is connected at the PCC. One of the above-mentioned controllers is in service, and the dq-components of the load voltages are respectively regulated at 40 V and 0 V. The switches S_1 and S_2 in Figure 3.7 are closed at $t = 0.05$ *s* and $t = 0.1$ *s*, respectively. This corresponds to two load changes, i.e., an inductive and a capacitive load change.

SMPC: Figure 3.9 shows the dynamic response of the islanded system to the load changes while the SMPC is in service. The load voltages are depicted in Figure 3.9 (a). The corresponding d- and q-components of the load voltages are shown in Figure 3.9 (b), which during and subsequent to the load changes are regulated at 40 V and 0 V, respectively, by the SMPC. The $d-$ and q-components of the VSC ac-side currents are shown in Figure 3.9 (c), which after
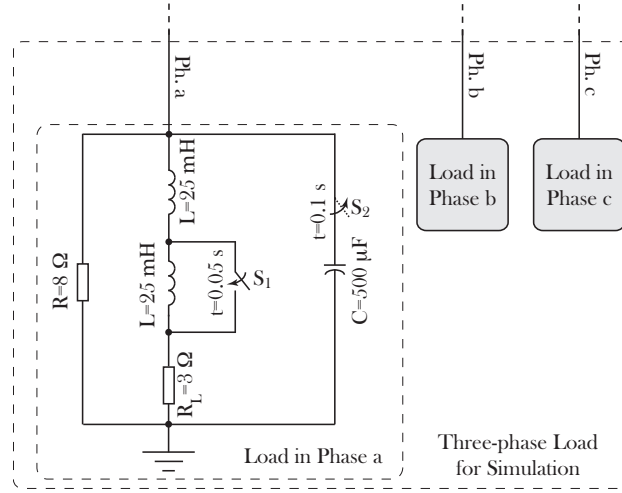
Figure 3.7: The three-phase load for the simulation studies of the inductive-capacitive load change scenarios

each load change, are changed accordingly to accommodate the load demand requirements. Subsequent to each load change, the SMPC adjusts the d- and q-components of the VSC terminal voltages at their corresponding new values, as depicted in Figure 3.9 (d).

SMPRC: The simulation results of a similar case study, when the SMPRC is in service, are also shown in Figure 3.10. The load voltages and their respective dq-components are depicted in Figures 3.10 (a) and (b), respectively. Moreover, the dq-components of the load currents are shown in Figure 3.10 (c), which subsequent to each change in the load parameters, change to accommodate the requested load power demand. The dq-components of the VSC terminal voltages are also shown in Figure 3.10 (d), which are determined by the controller to keep the
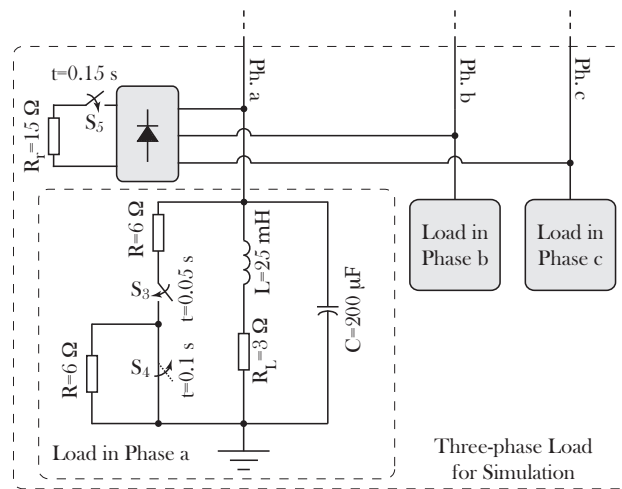
Figure 3.8: The three-phase load for the simulation studies of the resistive-load change scenarios

Figure 3.9: **The simulation response of the islanded system of Figure 3.1 to the inductive-capacitive load change of Figure 3.7 when the SMPC is in service: (a) the three-phase load voltages, (b), (c), and (d) the** d- **and** q-**components of the load voltages, the VSC ac-side currents, and the VSC terminal voltages**

dq-voltages at the requested set-points.

CMPC: To evaluate the performance of the CMPC under the inductive-capacitive load change scenario, the test system of Figure 3.1 is adopted, which operates in an islanded mode, and the CMPC regulates the dq-voltages of the load. Figures 3.11 (a) and (b) show the load voltages and their corresponding dq-components, respectively, which are regulated at their respective set-points. The dq-components of the load currents are also shown in Figure 3.10 (c), and the outputs of the outer loop are depicted in Figure 3.10 (d). Note that the outputs of the outer loop can be regarded as the set-points for the currents of the capacitors

Figure 3.10: The simulation response of the islanded system of Figure 3.1 to the inductive-capacitive load change of Figure 3.7 when the SMPRC is in service: **(a)** the three-phase load voltages, **(b)**, **(c)**, and **(d)** the d- and q-components of the load voltages, the VSC ac-side currents, and the VSC terminal voltages

of the VSC filter. The reason is the load currents are fed to the inner loop as a portion of the reference currents.

The presented results show that in the presence of three-phase linear loads, all controllers act in a similar way in steady-state. However, upon a change in the load parameters, the CMPC manages to reject load disturbance faster than the single-stage controllers. The reason is that the CMPC benefits from the load currents feedforward signals to reject the imposed disturbances. Moreover, the single-stage controllers act similarly in this regard, which is due to the absence of any harmonic distortion in the system. The difference between the performance of the SMPC and the SMPRC is highlighted in Section 3.5.1.2, where significant

Figure 3.11: The simulation response of the islanded system of Figure 3.1 to the inductive-capacitive load change of Figure 3.7 when the CMPC is in service: (a) the three-phase load voltages, (b), (c), and (d) the d- and q-components of the load voltages, the VSC ac-side currents, and the set-points of the inner loop

low-order harmonic currents and consequently voltages flow in the system. The simulation results of Figures 3.9, 3.10, and 3.11 verify the robust stability and the acceptable performance of all proposed controllers with respect to the balanced linear load parameter uncertainties.

3.5.1.2 Resistive Load Changes

To evaluate the performance of the proposed controllers upon resistive load changes, the system is loaded with the three-phase load of Figure 3.8. As shown in Figure 3.8, the system is subject to three resistive load changes. At $t = 0.05$ s, a three-phase purely resistive load of 6 Ω is connected in parallel to the load. This resistive load is stepped up from 6 Ω to 12 Ω at
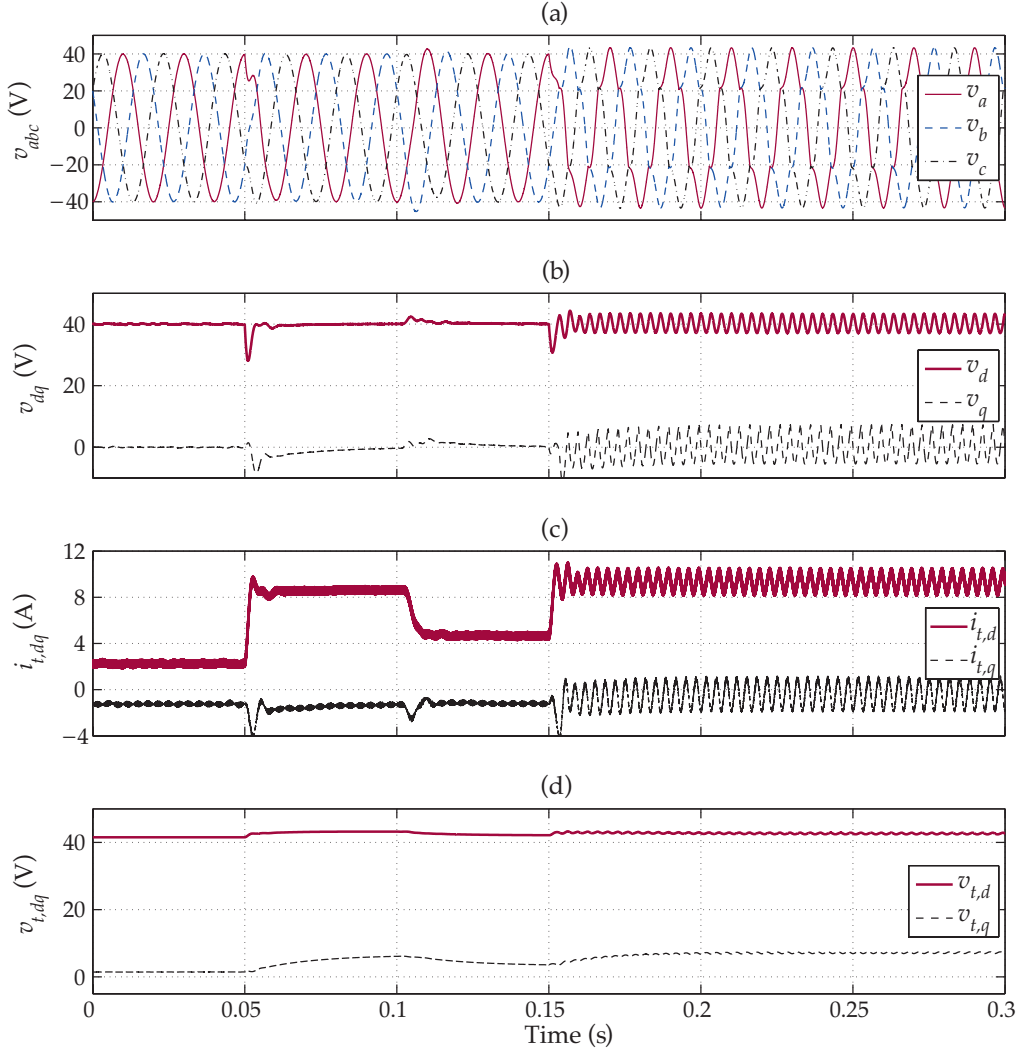
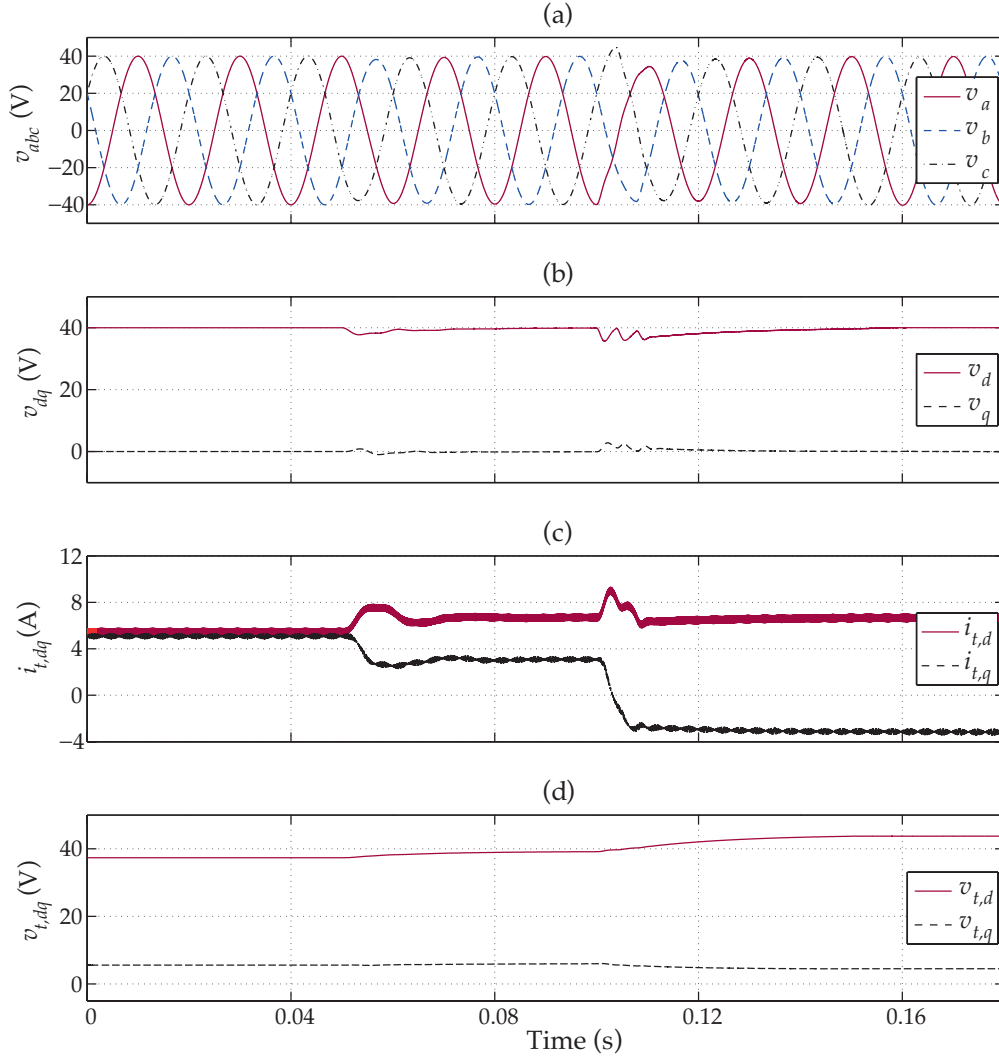**Figure 3.12: The simulation response of the islanded system of Figure 3.1 to a three-step resistive load change of Figure 3.8 when the SMPC is in service: (a) the three-phase load voltages, (b), (c), and (d) the d- and q-components of the load voltages, the VSC ac-side currents, and the VSC terminal voltages**

$t = 0.1\ s$. Then, at $t = 0.15\ s$, a three-phase rectifier, with a resistive load of 15 Ω, is paralleled to the *RLC* load. Note that to create the worst case scenario in terms of generated harmonic components, the rectifier is directly connected to the network, and no interfacing inductance is utilized.

SMPC: Figure 3.12 shows the responses of the system to the load changes when the SMPC is in service. Figure 3.12 (a) shows the instantaneous load voltages, which are regulated at their reference values during and subsequent to the linear resistive load changes. As shown in Figure 3.12 (a), upon the connection of the nonlinear load with the SMPC, significant low-order harmonics of the order of 5 and 7 appear on the voltages, and the THD of the
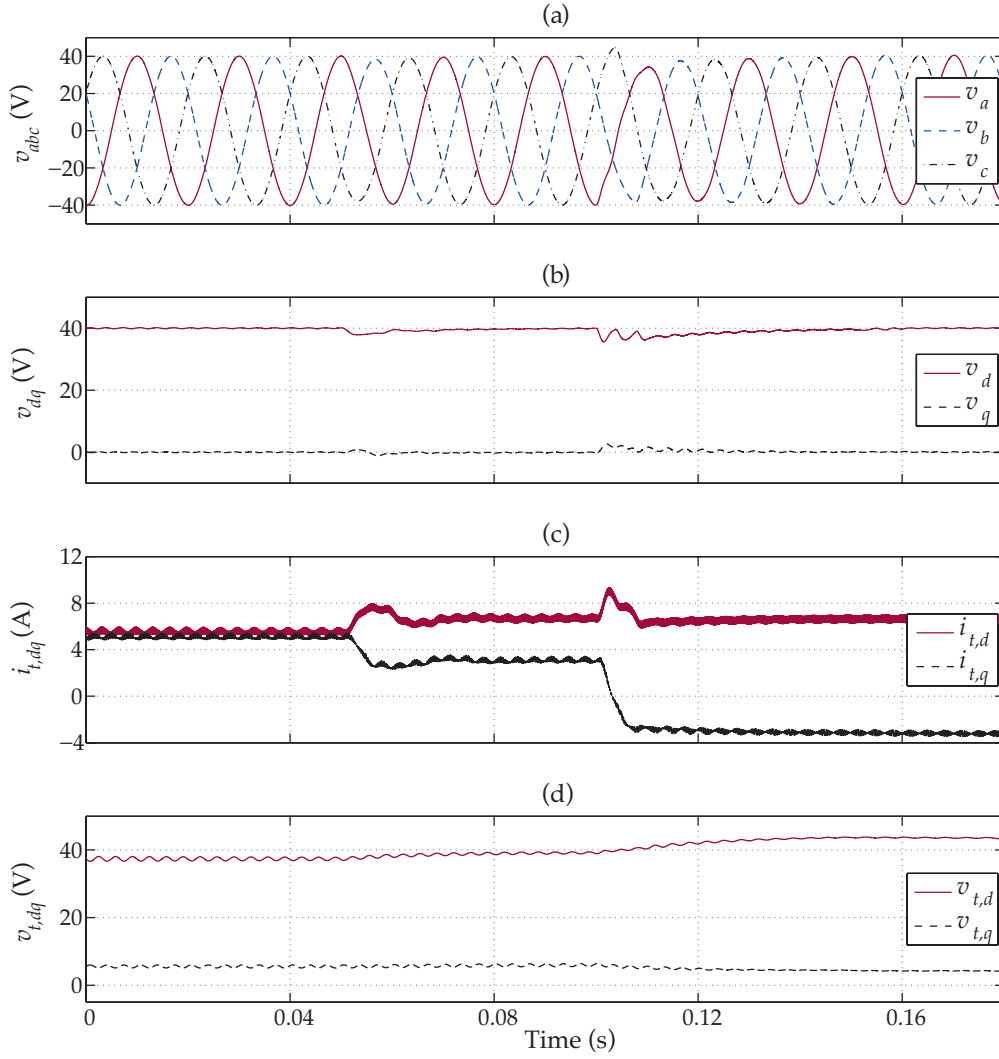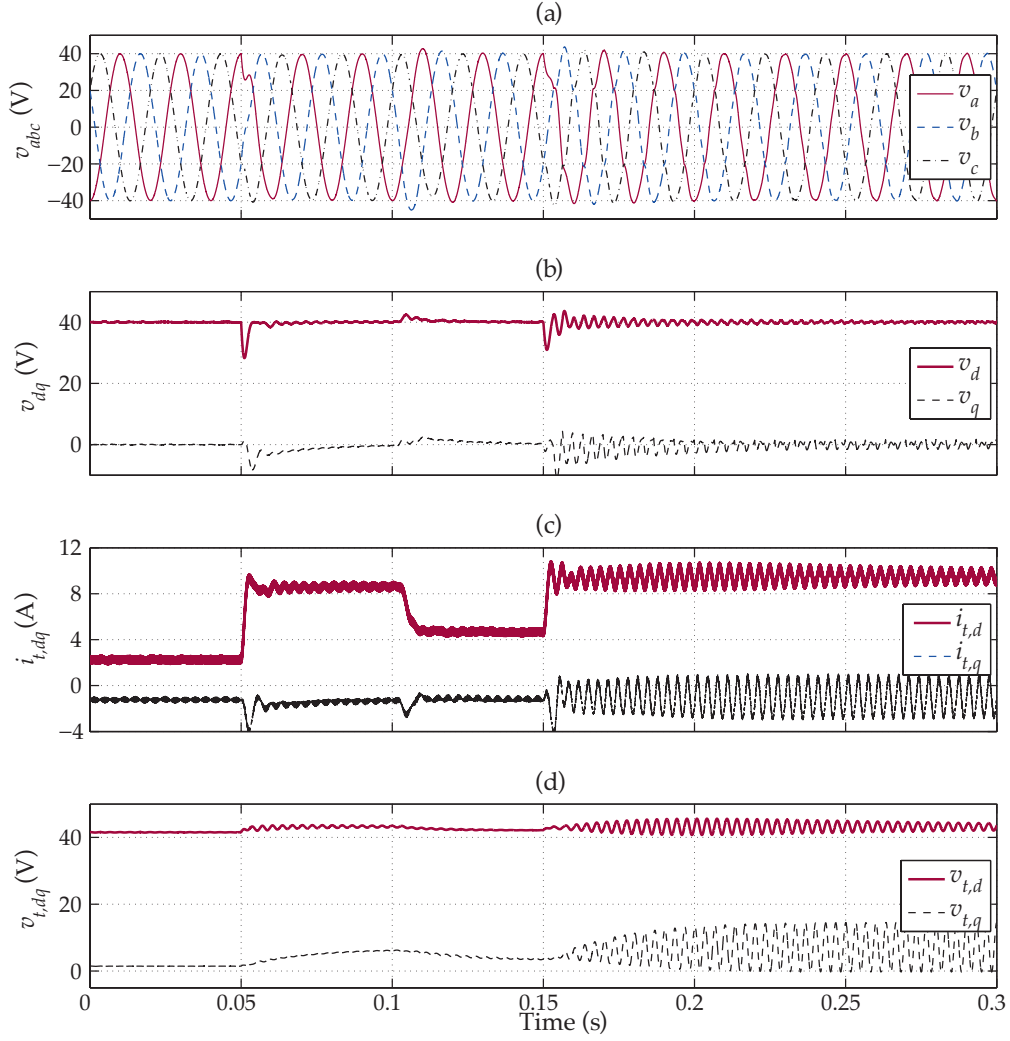
Figure 3.13: The simulation response of the islanded system of Figure 3.1 to a three-step resistive load change of Figure 3.8 when the SMPRC is in service: (a) the three-phase load voltages, (b), (c), and (d) the d- and q-components of the load voltages, the VSC ac-side currents, and the VSC terminal voltages

instantaneous load voltages increases significantly to about 12%. This is due to the inability of the SMPC to reject harmonic disturbances. Figures 3.12 (b) to (d) show the corresponding d- and q-components of the load voltages, the ac-side VSC currents, and the controller outputs, when the SMPC is in service, prior, during, and subsequent to the resistive load changes.

SMPRC: The instantaneous load voltages regulated by the SMPRC are depicted in Figure 3.13 (a). Thanks to its resonant terms, the SMPRC is able to eliminate the 5th and 7th harmonics. Therefore, upon the nonlinear load change, after a transient, the THD of the voltages remains within an acceptable range, i.e., less than 2%. Figure 3.13 (b) shows the dq-components of the load voltages regulated at 40 V and 0 V, respectively. The dq-currents
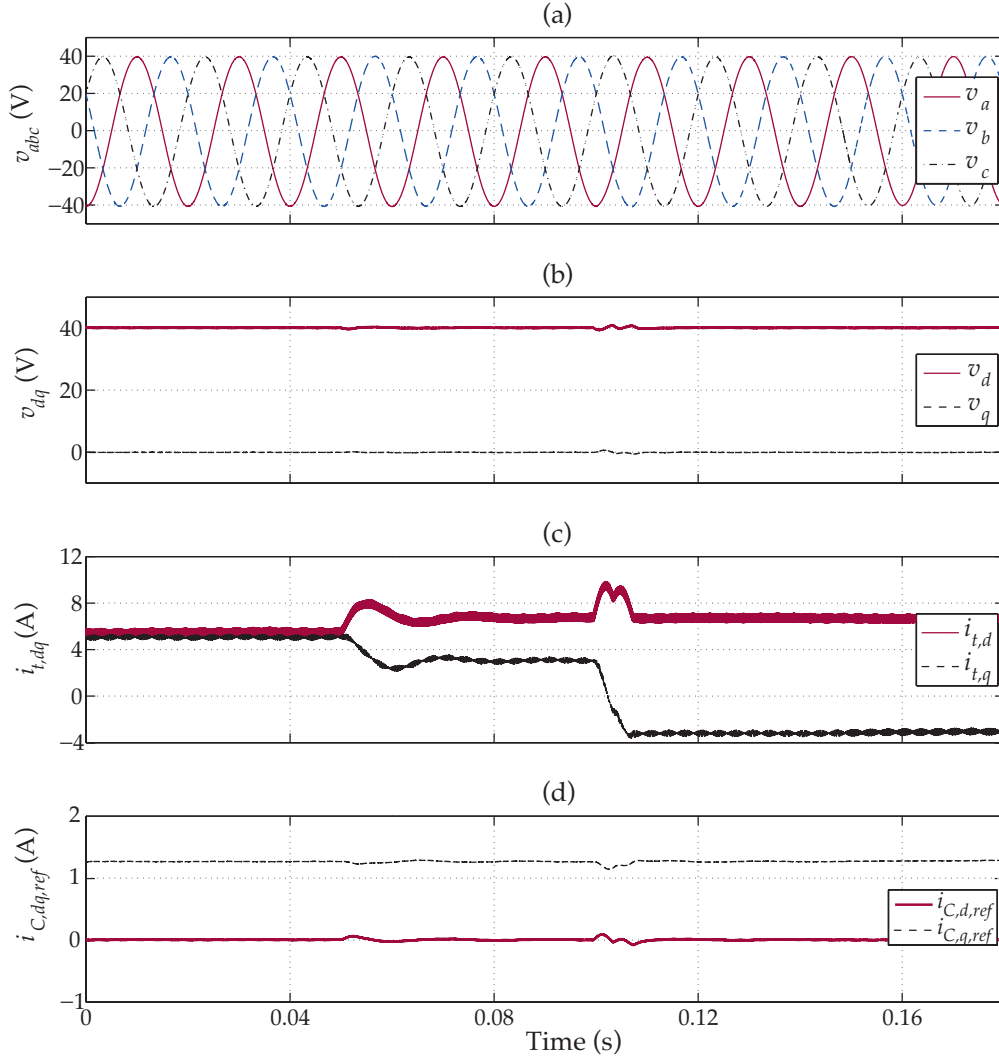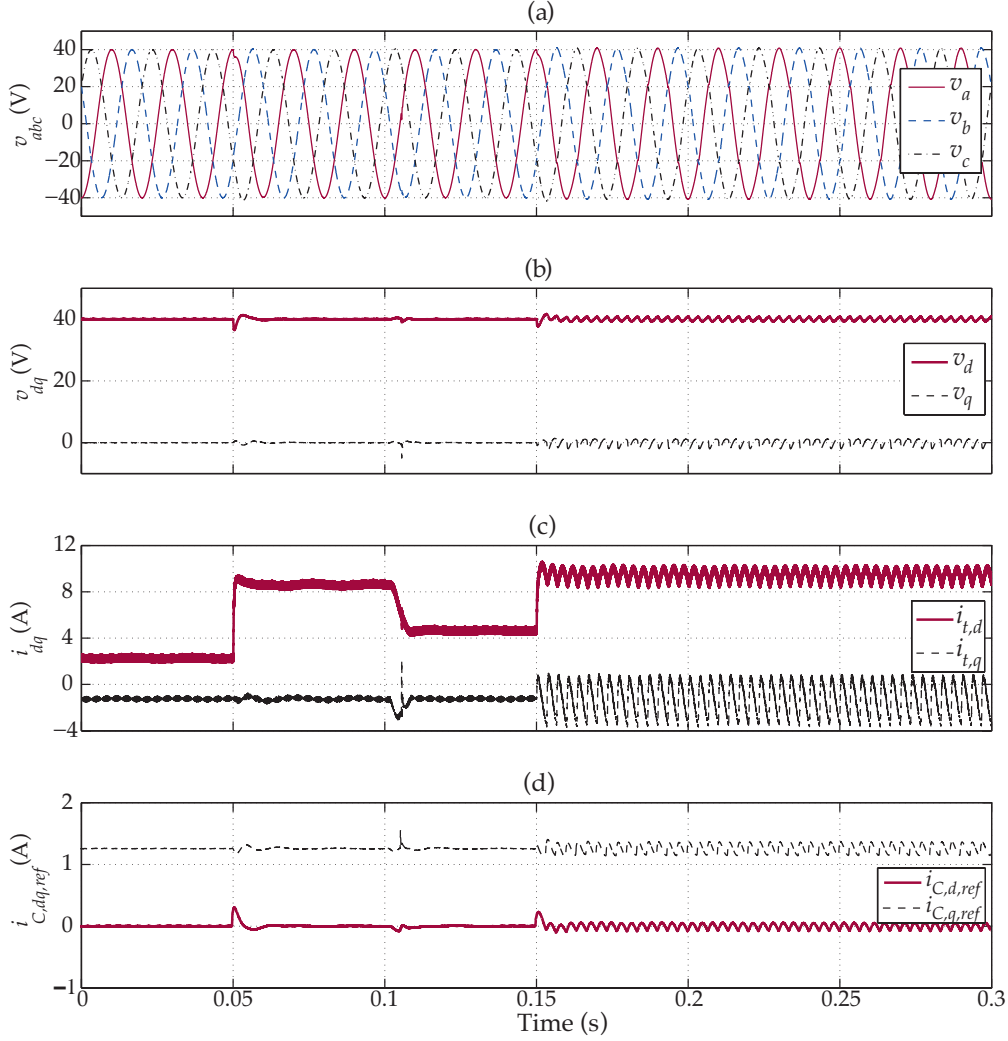
Figure 3.14: The simulation response of the islanded system of Figure 3.1 to a three-step resistive load change of Figure 3.8 when the CMPC is in service: (a) the three-phase load voltages, (b), (c), and (d) the d- and q-components of the load voltages, the VSC ac-side currents, and the set-points of the inner loop

of the load and the controller outputs are presented in Figures 3.13 (c) and (d), respectively. As shown in Figure 3.13 (d), subsequent to the connection of the nonlinear load, the d- and q-components of the VSC terminal voltages, which are the control signals generated by the SMPRC, contain a ripple component with the frequency of 300 Hz. This ripple component is generated by the SMPRC to eliminate the harmonic voltage distortions of the rectifier load.

CMPC: To evaluate the performance of the CMPC, the above-mentioned resistive test scenario is used. Figure 3.14 depicts the responses of the system to the load changes when the load voltages are regulated by the CMPC. The instantaneous load voltages and their corresponding dq-components are shown in Figures 3.14 (a) and (b), respectively. Upon each
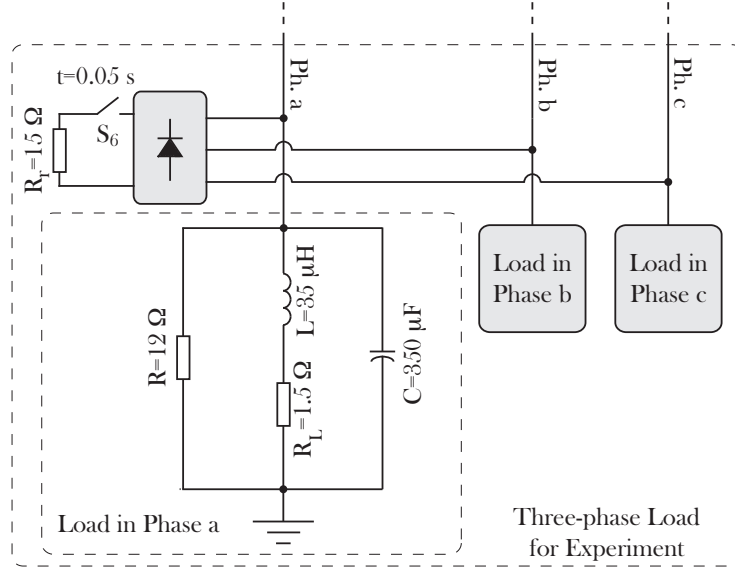
Figure 3.15: **The three-phase load for the experimental investigation of resistive-load change scenarios**

transient, thanks to the utilized feedforward signals of the CMPC, the disturbance is quickly rejected. Moreover, the adverse effects of the nonlinear load are also obviated by the CMPC, and the THD of the load voltages is below 2%, subsequent to the connection of the nonlinear load. The dq-currents of the load are also depicted in Figure 3.14 (c). Moreover, the outer loop outputs are shown in Figure 3.14 (d).

The comparison of Figures 3.12 (a), 3.13 (a), 3.14 (a) confirms the identical performance of the controllers in the presence of linear loads, in steady-state. However, in the presence of nonlinear loads and/or harmonically polluted loads, only the CMPC and the SMPRC have the capability of rejecting the imposed disturbances. Moreover, thanks to its feedforward signals, the CMPC can reject the disturbances caused by load changes more rapidly compared to the other controllers. It must be noted this is achieved at the cost of utilizing current sensors for measuring the load and the converter currents, which means more cost compared to the SMPC or the SMPRC.

3.5.2 Experimental Results

The experimental evaluation and comparison of the performance of the proposed controllers are performed using an experimental test system with the same layout of the system of Figure 3.1. The parameters of the experimental setup are the same as those given in Table 3.1. The setup is loaded with the three-phase load configuration shown in Figure 3.15. The proposed controllers are implemented in a fully digital control platform based on DSP/FPGA called *Boombox*, designed and developed in the Laboratory of Industrial Electronics at the EPFL, with a sampling frequency of up to 100 kHz. A photograph of the experimental setup,
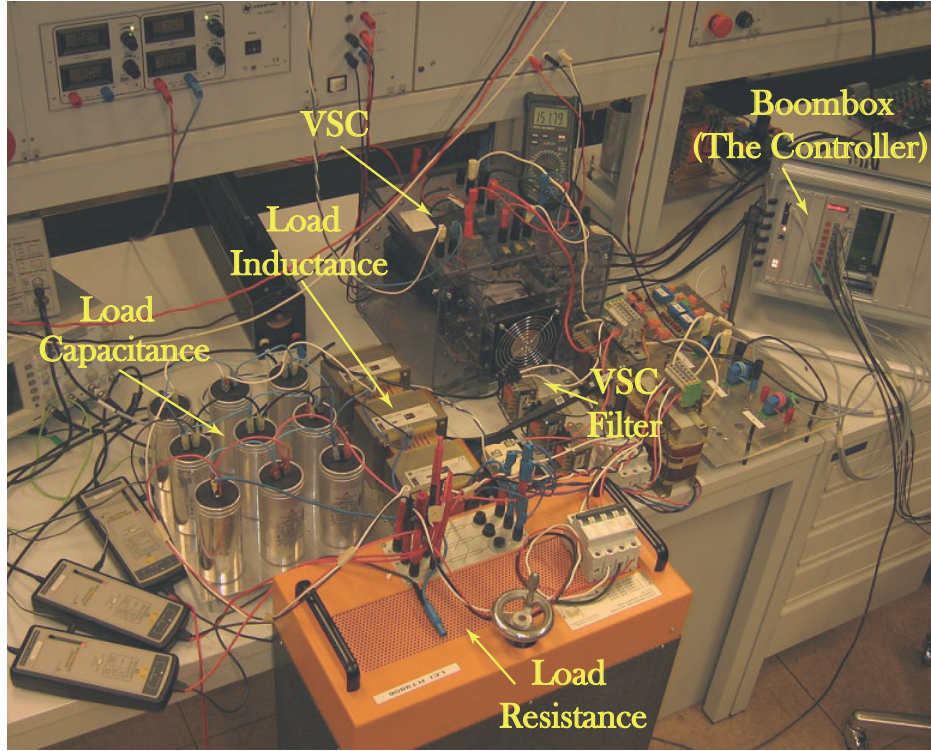
Figure 3.16: The experimental setup

with the highlighted main components, is shown in Figure 3.16. It must be noted that since *Boombox* can accept up to six inputs, only two sets of three-phase variables may be fed to that. Therefore, it is not possible to implement the CMPC with *Boombox*. Thus, in the following, just the performance of the SMPC and the SMPRC are evaluated and compared.

Initially, the system operates based on the SMPC, and the islanded test system is supplying a three-phase RLC load. The SMPC regulates the dq-components of the load voltages at 40 V and 0 V, respectively. At $t = 0.05\ s$, as a nonlinear load, a three-phase full bridge rectifier with a 15 Ω resistive load is paralleled with the RLC load. Figure 3.15 depicts the utilized load. Figure 3.17 shows the dynamic response of the system to the rectifier energization. Figures 3.17 (a) and (b) depict the instantaneous load voltages and the VSC ac-side currents, respectively. Figures 3.17 (c) and (d) show the dq-components of the load voltages and the VSC ac-side currents, respectively. As opposed to the simulation results of Figure 3.12, prior to the nonlinear load energization, the load voltages contain the 5th and 7th order harmonics, and have a THD of about 5.5%. This is due to the 4 μs dead-time of the VSC, which pollutes the VSC terminal voltages, and consequently, the VSC currents and the load voltages with low-order harmonics. This dead-time distortion is created dominantly by the 5th and the 7th order harmonics [79]. Subsequent to the nonlinear load energization, as shown in Figure 3.17 (b), the VSC currents become further distorted due to the rectifier operation, and consequently, the load voltages are also further distorted, i.e., their THD increases to 15.5%.
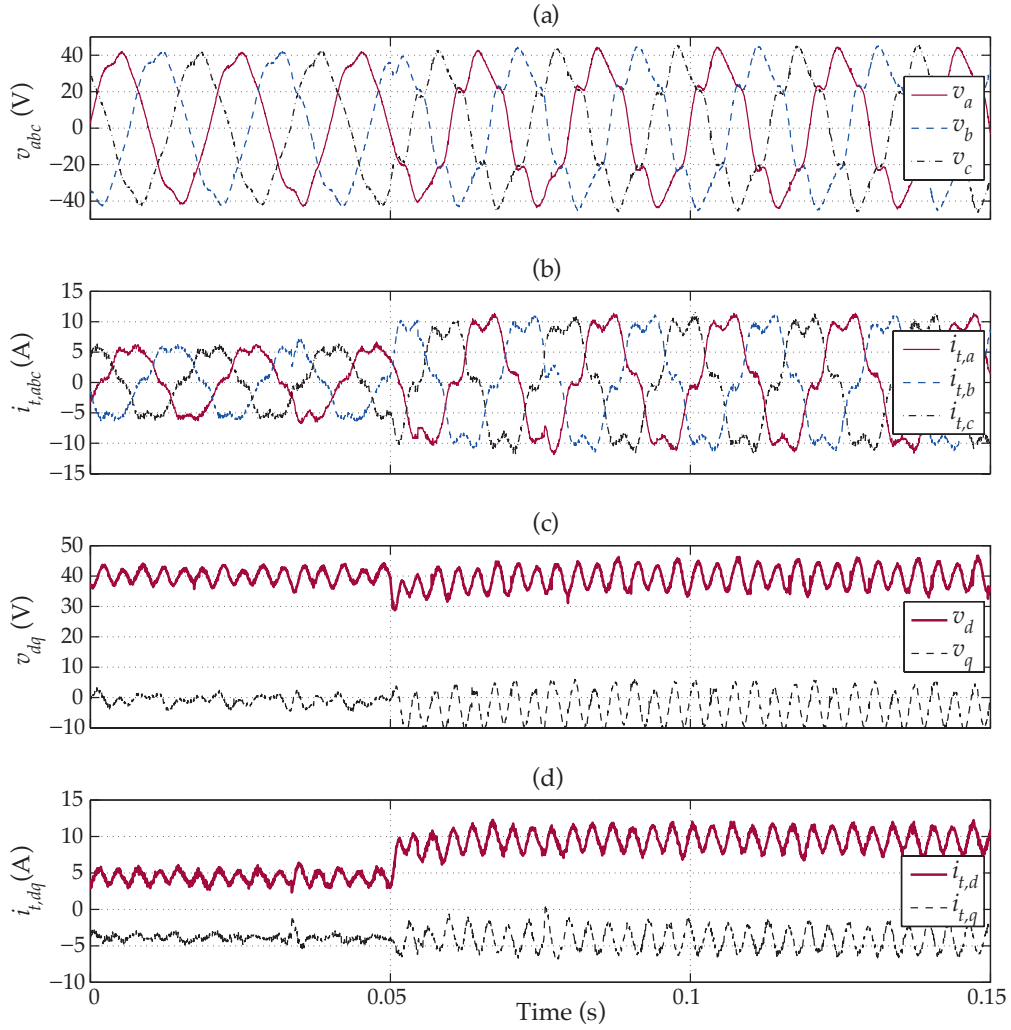
Figure 3.17: The experimental response of the test system of Figure 3.16 with respect to a nonlinear load energization when the SMPC is in service: (a,b) the instantaneous load voltages and the VSC currents, and (c,d) the d- and q-components of the load voltages and control signals

As expected, the SMPRC provides a unique capability to eliminate the adverse impacts of the harmonically polluting nonlinear loads. To demonstrate this capability, the same load change test is carried out when the system operates based on the SMPRC. Figure 3.18 shows the dual waveforms of Figure 3.17 when the SMPRC is in service. As Figure 3.18 (a) shows, prior to the nonlinear load energization, the load voltages, even with the dead-time effect, are harmonic free. This is due to the resonant terms of the SMPRC, which are tuned to, specifically, eliminate the harmonic components of the order of 5 and 7. Subsequent to the nonlinear load energization, due to the residual harmonic terms, the load voltages are slightly distorted. Nevertheless, the THD of the load voltages remains within the acceptable range, about 2.5%, which is mainly due to the residual harmonic components of the order 11 and 13.
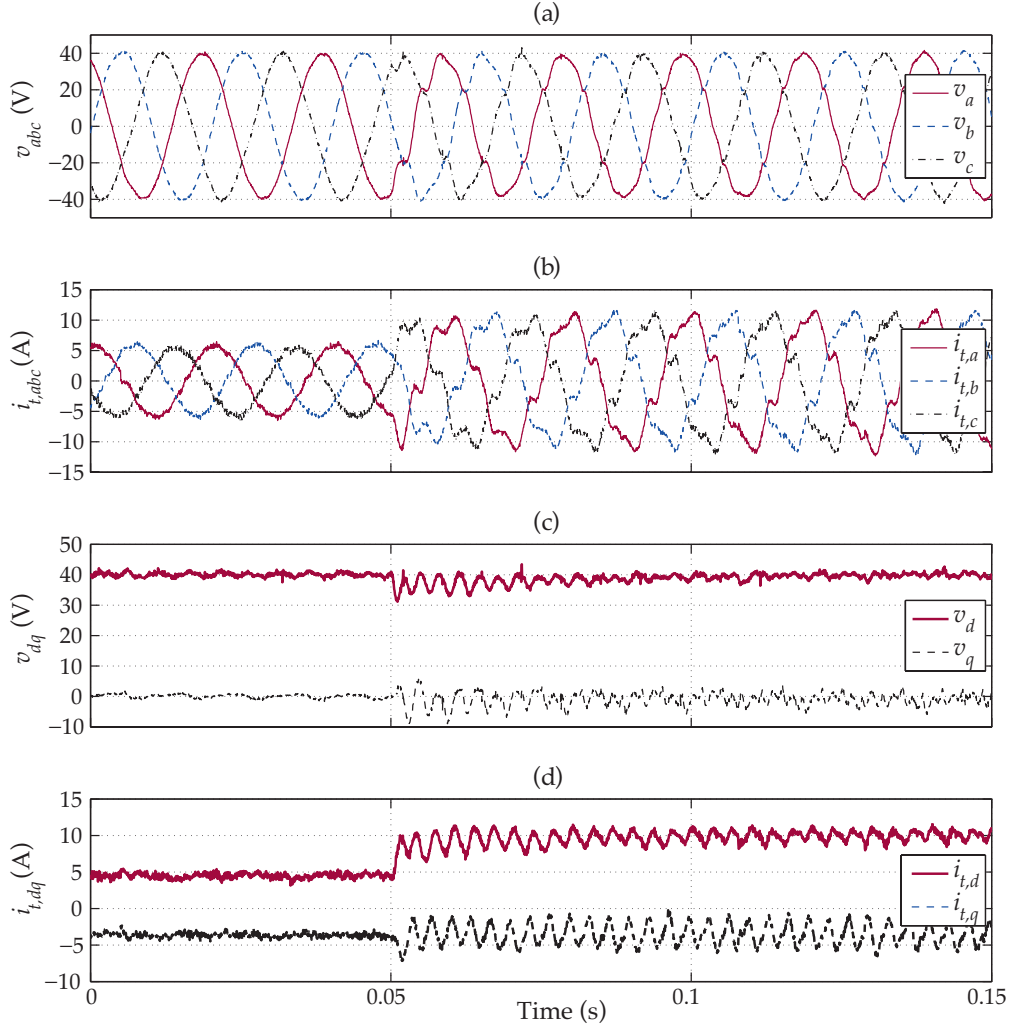
Figure 3.18: The experimental response of the test system of Figure 3.1 with respect to a nonlinear load energization when the SMPRC is in service: (a,b) the instantaneous load voltages and the VSC currents, and (c,d) the d- and q-components of the load voltages and control signals

The experimental results of Figures 3.17 and 3.18 show that both single-stage controllers successfully regulate the load voltages despite the imposed nonlinear dynamics. In addition, the SMPRC is able to counteract the adverse impacts of the low-order harmonic components and provide harmonic-free voltages.

3.6 Conclusions

A multivariable digital design methodology for voltage control of a single-DG-unit microgrid is proposed in this chapter. The proposed methodology is based on shaping the open-loop MIMO transfer function matrix of the system by (i) attaining a family of nonparametric models

of the system at various operating points, (ii) the determination of the class of the to-be-designed controller, and (iii) solving a convex optimization problem. The proposed controller design methodology is fully investigated in the context of voltage control of a single-DG-unit microgrid and its dedicated load. Three digital controllers are designed for the voltage regulation of the studied single-DG-unit microgrid system, i.e., SMPC, SMPRC, and CMPC. The performance of the designed controllers is evaluated for various operating scenarios. Based on the simulation and experimental results, the following conclusions are made:

- All proposed controllers show satisfactory dynamic performance in terms of load voltages regulation and robustness, upon step changes in linear loads.

- The CMPC has faster dynamic response compared to that of the SMPC and the SMPRC in terms of rejecting the disturbances in the load voltages caused by load changes.

- Compared with the SMPC, the SMPRC and the CMPC provide superior performance in the presence of nonlinear loads as they eliminate/minimize the adverse impacts of the low-order harmonics on the load voltages and system operation.

Although the proposed voltage control strategies have been investigated for a single-DG-unit microgrid, they are applicable to multi-DG-unit microgrids as well. In a multi-DG-unit microgrid, one of the DG units can act as a master controller. In such a case, the master DG-unit takes control over the voltage and frequency based on the proposed SMPC, SMPRC, or CMPC, and the rest of the DG units will be equipped with dq-currents controllers, e.g., an OMCC, as if they are connected to the grid.

Traction-System-Related Applications Part II

Introduction to Part II

In the previous part, several current and voltage regulation schemes are developed for VSCs. In this part, exploiting the ALC of modern locomotives and inspiring from the proposed approaches of Part I, several ancillary services are proposed for electrified traction networks. Inspiring form the cascade voltage control of islanded microgrids, a cascade voltage support scheme is proposed whose outer loop consists of a SISO controller and only delivers the reference value of the q-component of the locomotive current. Note that this is in contrast with the outer loop of the CMPC, which determines the reference values of both $d-$ and $q-$components of the current. To realize the outer or secondary loop of the proposed catenary voltage support scheme, several possibilities are proposed. Among the proposed approaches, a gain-scheduled and a high-order controller show better performance, while that of the high-order one is superior. To perform the gain-scheduling, a catenary line inductance identification method is also developed in this part, which relies on the harmonic current injection through the ALC of modern locomotives. Moreover, the high-order controller is designed through a SISO version of the optimization-based design procedure of Chapter 3.

This part is structured as follows. Chapter 4 presents a catenary parameters identification strategy that is able to estimate the parameters of the catenary at the connection point of the locomotive to the line. Chapter 5 proposes several voltage support schemes, which belong to the PI-family, and Chapter 6 proposes the high-order voltage support scheme.

Catenary Parameters Identification

4.1 Introduction

Thanks to the rapid advancements in the semiconductor technologies, currently, modern locomotives with IGBT-based ALCs are extensively manufactured and utilized in traction networks [80]. Adopting IGBTs in the ALCs results in (i) the elimination of previously used snubber circuits in old locomotives, which reduces the cost and weight, (ii) less low-order harmonic distortions, (iii) better controllability of power, etc. Traditionally, to overcome various existing shortcomings in traction networks [11, 81], Flexible AC Transmission Systems (FACTS) devices have been utilized to improve the power quality [15, 82]. However, unlike their passive predecessors, modern locomotives can exploit their ALCs for various contributions toward the network. For example, the ALC of locomotive drive system can be adopted as a reactive power source to compensate for voltage drop along the catenary line, which is the subject of the two next chapters. To optimally determine the required reactive power, adaptive control strategies may be utilized, which depend on the parameters of the line at each time instant.

In this chapter, in addition to its primary function, the ALC is exploited to identify the catenary line parameters at the connection point of the locomotive to the network. The identification is carried out through the periodic injection of low-order harmonic current and monitoring the corresponding voltage at the PC. The adopted current control scheme is a PR-controller-based strategy [19, 68], which is able to inject currents at various harmonics provided at each target harmonic frequency, a resonant term is added in parallel to the rest of the PR-controller. In order to accurately estimate the line parameters, an identification strategy is adopted, which acts in real-time and uses a *forgetting factor* to incorporate the most recent measurements in the estimation process. The utilized identification approach is a real-time recursive least squares identification method [83].

The rest of this chapter is structured as follows. Section 4.2 describes the adopted test system
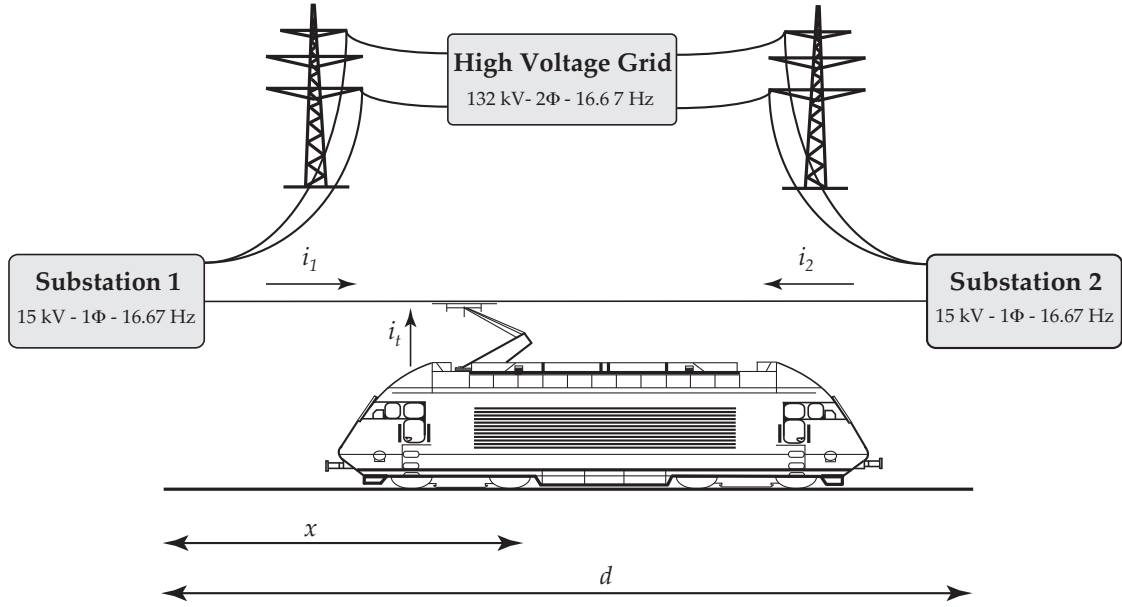
Figure 4.1: A simple traction network consisting of two substations and one locomotive

and details the control strategy utilized for the fundamental and also harmonic current injection. Section 4.3 presents the identification strategy taken for the estimation of the catenary parameters. Section 4.4 evaluates the performance of the proposed identification scheme, and Section 4.5 concludes the chapter.

4.2 Study System and Its Current Control Strategy

In this section, the adopted test system, which is an AC single-phase traction network as shown in Figure 4.1, is presented. Then, the utilized current control strategy of this chapter for both fundamental and harmonic frequency current is detailed.

4.2.1 Study System

The study system consists of a locomotive connected to the catenary through a coupling transformer, which can be modeled by an ideal transformer plus its leakage inductance and series resistance. The catenary is fed by two substations (the SS1 and the SS2), which are 60 km away from each other. The line connecting two substations is represented by its resistance and inductance. The ALC of the drive system of the locomotive is implemented by a single-phase IGBT-based inverter whose DC-link consists of an ideal DC source, and the dynamics of the locomotive motor and its driver are neglected. The schematic diagram of the test system is depicted in Figure 4.2. Note that the line impedance is segmented into two portions according to the position of the locomotive. The segmentation is shown in Figure 4.2 in which each segment is represented by a variable impedance, i.e., $Z_1 = R_1 + j\omega_n L_1$ and $Z_2 = R_2 + j\omega_n L_2$. Table 4.1 presents the parameters of the system.
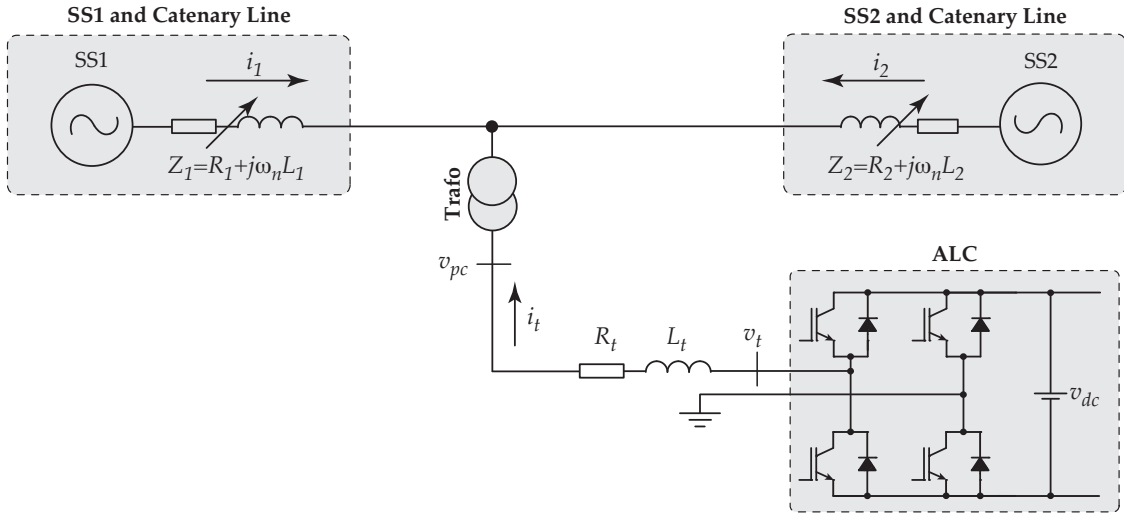
Figure 4.2: The schematic diagram of the traction network of Figure 4.1

4.2.2 Current Control Strategy of Locomotive

The conventional practice for the ALC of locomotives is utilizing current control schemes for the regulation of the input current, which itself results in the active and reactive power regulation. The conventional approaches for the current regulation of single-phase converters are PI-based and PR-based methods [6, 68]. In this chapter, the PR-based current control scheme is adopted for the current regulation. The reason is that injecting harmonic currents, which is needed for identification, is more straightforward with the PR-based current controllers. For the synchronization purposes a single-phase PLL is adopted, which acts on the PC voltage and

Table 4.1: The parameters of the system of Figure 4.2

Quantity	Value	P.U.	Comment
S_{base}	0.625 MVA	1 pu	Base Value of Locomotive Power
v_{pc}	385 V (rms)	1 pu	Locomotive Nominal Voltage
v_{dc}	840 V		DC Bus Voltage
L_t	0.4 mH	0.14 pu	Inductance of Coupling Trafo
R_t	0.019 Ω	0.06 pu	Resistance of Coupling Trafo
n_t	38.961		Transformer Ratio
f_{sw}	2 kHz		PWM Carrier Frequency
f_s	5 kHz		Sampling Frequency
v_{SS}	15000 V (rms)	1 pu	Substation Nominal Voltage
ω_n	$2\pi \times 16.67$ rad/s		System Angular Frequency
R_l	0.08 Ω		Line Resistance/km
L_l	1.2 mH		Line Inductance/km
d	60 km		Line Length
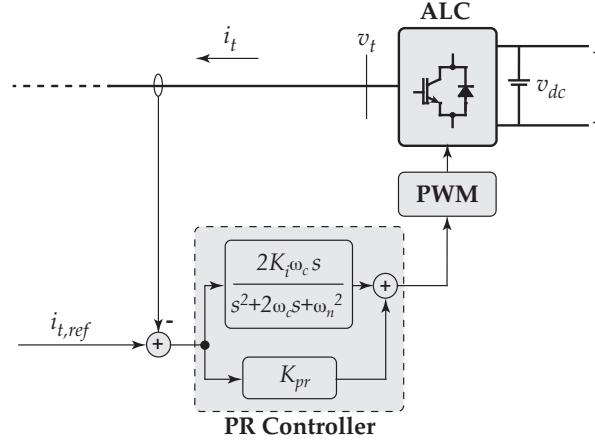
Figure 4.3: PR-controller for the fundamental frequency

its orthogonal component to extract the phase-angle. The orthogonal component is achieved through a SOGI [77]. In the following, the adopted PR-control strategy of the locomotive is briefly explained for both fundamental and harmonic frequency.

4.2.2.1 PR-Control for Fundamental Frequency Current

Contrary to RRF-based controllers [3, 5, 6], which exhibit very high gains at DC, SRF-based controllers act on AC quantities and therefore, must have theoretically infinite gains at target frequencies. PR-controllers are among the best SRF-based controllers, which can inject harmonic currents in parallel with the fundamental frequency current. The transfer function of an ideal PR-controller is as follows [19]:

$$G_{PR}(s) = K_{pr} + \frac{2K_i s}{s^2 + \omega_n^2}, \tag{4.1}$$

where ω_n is the nominal angular frequency of the system, and K_{pr} and K_i are the coefficients of the controller to be designed. The ideal PR-controller of (4.1) shows an infinite gain at the AC frequency of ω_n and no phase shift and gain at other frequencies. Similar to PI-based approaches, the proportional part is tuned for the desired dynamics of the system in terms of bandwidth, and phase and gain margins. Note that in order to avoid instability issues related to the infinite gain of the controller, non-ideal PR-controllers are more practical, which have finite, however, still very high gains at the target frequency in order to ensure perfect tracking in steady-states. A typical non-ideal PR-controller is described as

$$G_{PR}(s) = K_{pr} + \frac{2K_i \omega_c s}{s^2 + 2\omega_c s + \omega_n^2}. \tag{4.2}$$

Proper ω_c tuning is exploited for manipulating the bandwidth of the controller, which eventually results in the reduction of the controller sensitivity to grid voltage frequency deviations. Moreover, K_i can be tuned for shifting the magnitude response [19]. Figure 4.3 shows a simple
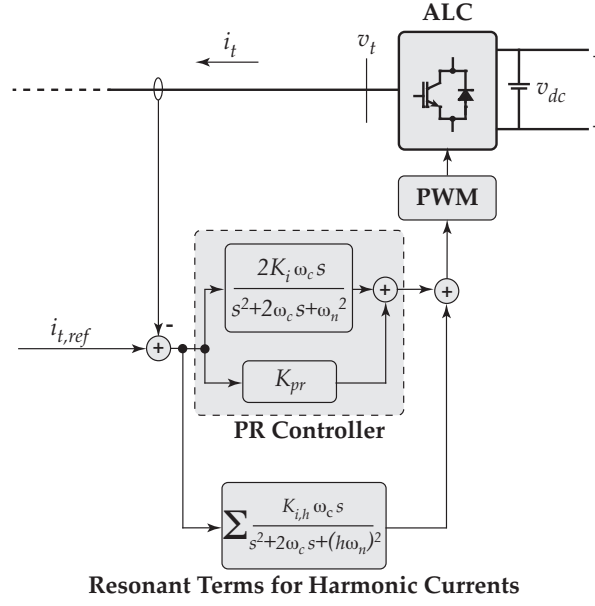
Figure 4.4: PR-controller for the fundamental and harmonic frequencies

schematic diagram of the non-ideal PR-controller along with a ALC whose current is regulated.

4.2.2.2 PR-Control for 7th Harmonic Current

Utilizing PR-controllers offers an interesting advantage in terms of harmonic current injection compared to other methods. In order to regulate any harmonic current, one resonant term associated with that harmonic frequency should be added in parallel to the resonant term of the fundamental frequency current controller. Figure 4.4 depicts a schematic diagram of the PR-controller along with the harmonic resonant terms. Note that similar to the controller for the fundamental frequency current, the resonant terms responsible for harmonic current injection show very high gains at their target harmonic frequencies while they do not change the gain and phase at other frequencies [19].

4.2.2.3 Determination of Reference Signal

The ultimate goal of many input-current-regulated grid-tied VSCs is to control the power flow between the converter and the grid. Therefore, the selection of the reference current is of high importance. In RRF-based controllers, the active and reactive power are regulated by manipulating the reference values of the d- and q-axes of the current. In such systems, extracting the phase-angle of the grid voltage, the currents are transformed to a dq-frame. Utilizing the PLL for phase-angle extraction, the q-component of the grid voltage is forced to zero. Therefore, the d-component of the current is responsible for the active power regulation, while the q-component of the current determines the reactive power, i.e., $P = \frac{1}{2} v_{pc,d} i_{t,d}$ and $Q = \frac{1}{2} v_{pc,d} i_{t,q}$. The same procedure can be taken for the determination of the reference
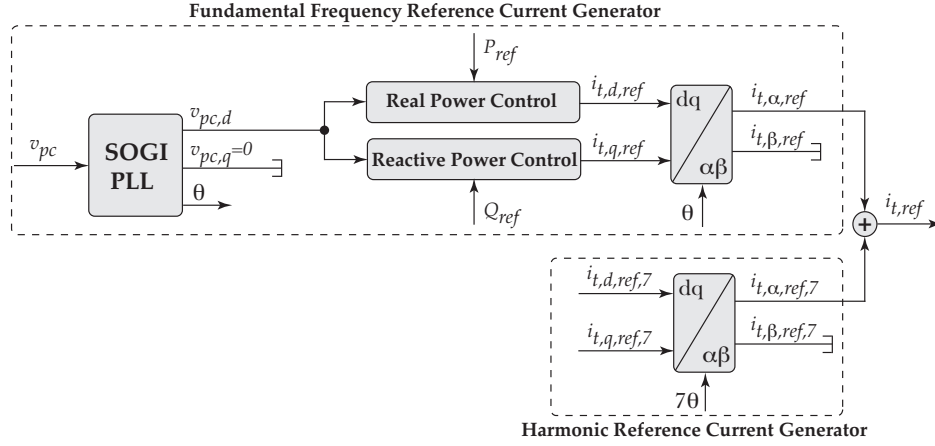
Figure 4.5: The reference current generator

currents for PR-controllers in a SRF. In the single-phase system of Figure 4.2, the SOGI PLL is adopted [77], which extracts the phase-angle of the grid voltage. Assuming reference values for the real and reactive power, i.e., P_{ref} and Q_{ref}, one can determine the required d- and q-axes currents as $i_{d,ref} = \frac{2P_{ref}}{v_{pc,d}}$ and $i_{q,ref} = \frac{2Q_{ref}}{v_{pc,d}}$. Transferring the calculated reference currents to an $\alpha\beta$-frame and discarding the β-component, the α-component is the reference value for the PR-controller, which results in the injection of the required real and reactive power.

To determine the reference value for the harmonic currents, the same procedure is taken. However, the required phase-angle for the transformations is generated by multiplying the phase-angle of the fundamental frequency by the rank of the target harmonic. The schematic diagram of the reference current generator is shown in Figure 4.5.

4.3   Catenary Line Parameters Identifier - CLPI

In this section, the C̲atenary L̲ine P̲arameters I̲dentifier (CLPI) adopted to estimate the inductance and the resistance of the catenary line at the PC is detailed. Note that the impedance measured/estimated at the PC is the parallel combination of the two line segments shown in Figure 4.2, i.e., Z_1 and Z_2. Therefore, the estimated parameters are the inductance and the resistance of $Z = R + jL\omega_n = \frac{Z_1 Z_2}{Z_1 + Z_2}$.

The identification is carried out through the injection of low-order harmonic current through an extra resonant term tuned to the 7th harmonic current, and monitoring the corresponding harmonic voltage at the PC. Note that the injected harmonic current for the identification should not necessarily be low-order harmonic. It can be of any frequency, e.g., 220 Hz, provided the selected frequency is within the viable range of the ALC. For example, with a switching frequency of 2000 Hz and the nominal frequency of 16.67 Hz, one can easily inject the 11th harmonic, however, the injection of the 40th harmonic is not viable. Moreover, the harmonic frequency selection is dependent on the standards adopted by railway companies.
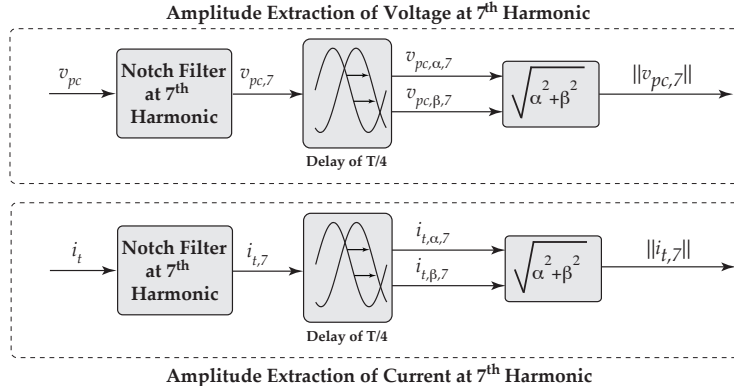
Figure 4.6: The amplitude extraction of the 7th harmonic of the PC voltage and inverter current

The reason is that the injected harmonic must not affect the signals used for signaling or other applications in the network. For example, in the Swiss Federal Railways, the injection of the 7th is permitted provided its amplitude is not beyond a pre-determined threshold, i.e., 100 A.

4.3.1 Identification Through Injection of 7th Harmonic Current

The first step of the identification is the excitation of the system. The system of Figure 4.2 is excited through the injection of the 7th harmonic current. In order to inject the 7th harmonic current, the first step is to determine the required reference signal, which is generated using the block of Figure 4.5. The next step of the identification process is analyzing the consequences of the injected current on the PC voltage at the 7th harmonic. Using notch filters, the 7th harmonic components of the PC voltage and the ALC current are extracted. Then, applying a delay of a quarter of the period of 7th harmonic, the orthogonal components of the PC voltage and the converter current are generated, which are used to calculate their amplitude. Figure 4.6 depicts the blocks responsible for the amplitude generation of the 7th harmonic current and voltage. Using the calculated voltage and current amplitudes corresponding to the 7th harmonic, one can estimate the magnitude of the line impedance at the 7th harmonic as follows:

$$\| Z \| = \frac{\| v_{pc,7} \|}{\| i_{t,7} \|}. \tag{4.3}$$

In the frequencies enough higher than the fundamental one, e.g., the 7th harmonic frequency, the impedance is mainly inductive. Therefore, the magnitude of the impedance of (4.3) divided by the angular frequency at the 7th harmonic, i.e., ω_7, is a fair approximation of the line inductance. Thus, the estimated inductance is

$$L \simeq \frac{\| Z \|}{\omega_7}. \tag{4.4}$$
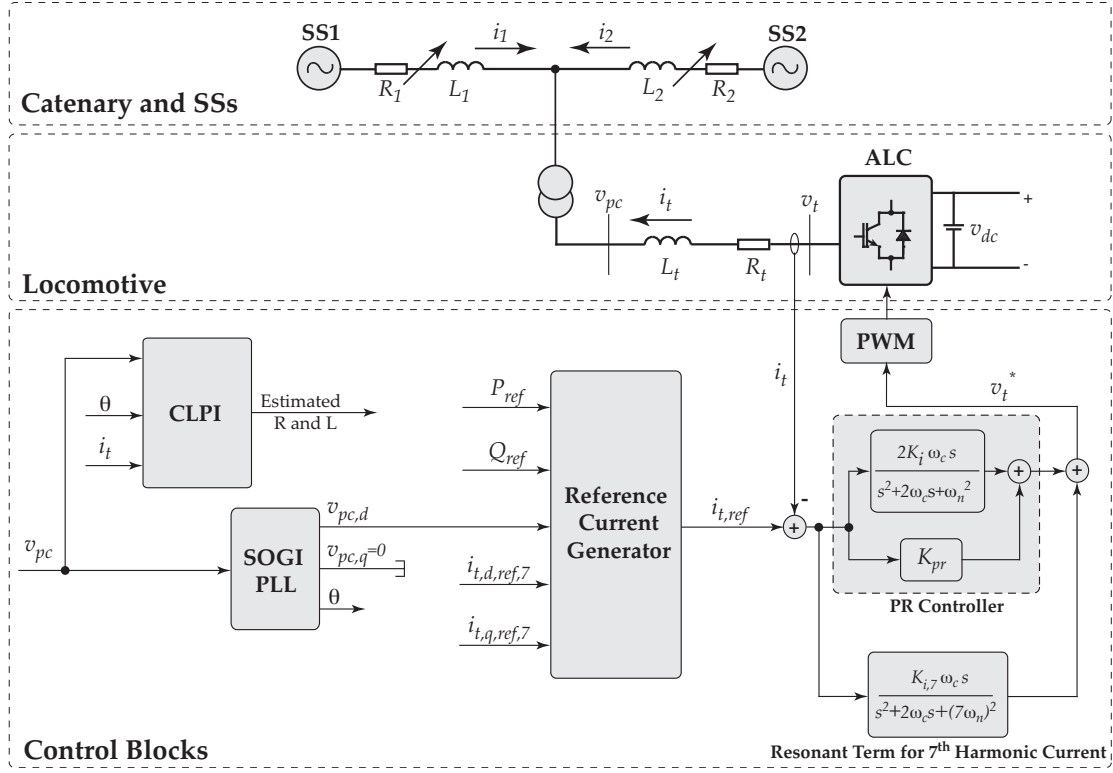
Figure 4.7: The block diagram of the control strategy of the system of Figure 4.2 and the CLPI

Since the inductance and the resistance of a line are normally proportional to each other, one can estimate the line resistance through the estimated inductance. Therefore, in this chapter, only the line inductance identification is discussed. Figure 4.7 depicts the complete diagram of the adopted controller along with the identification blocks.

To more precisely estimate the parameters of the line, one can benefit from the injection of several harmonics at the same time. For example, the concurrent injection of the 7th and the 11th harmonic, and estimating the parameters of the line independently for each harmonic, one can more precisely estimate the parameters as the average of the two identified values.

4.3.2 Recursive Least Squares Real-time Identification

In real systems, measurements are subject to noise and may not be precise. To accurately estimate the line parameters, a real-time identification method [83] is adopted. The method is based on a recursive least squares scheme, which utilizes a forgetting factor to emphasize on the most recent measurements.

4.3.2.1 Offline Least Squares Identification

Assume that the system to be identified has a parametric model as follows:

$$y(t) = \varphi^T(t)\gamma + e(t) \tag{4.5}$$

in which $y(t)$ is a measurable quantity, $\varphi(t)$ is an n-dimensional vector of known quantities, γ is an n-dimensional vector of parameters to be identified, and $e(t)$ is the measurement noise. To better clarify the adopted model, a polynomial, $y(t) = a_0 + a_1 t + ... + a_n t^r$, is expressed by the model of (4.5) through defining

$$\varphi(t) = (1 \ t \ ... \ t^n)^T \text{ and } \gamma = (a_0 \ a_1 \ ... \ a_n)^T. \tag{4.6}$$

Note that the model defined by (4.6) can be used to express a measured constant if $n = 0$.

Assuming N measurements of the output, the least squares estimation of γ is then the vector $\widehat{\gamma}$ that minimizes the following loss function:

$$V(\gamma) = \frac{1}{2} \sum_{t=1}^{N} \varepsilon^2(t) \tag{4.7}$$

in which $\varepsilon(t)$ can be interpreted as the prediction error, as it represents the error between the measured value at time t, i.e., $y(t)$, and the output of the predicted model of one step before the measurement. Reference [83] proves that the following recursive equation minimizes the loss function of (4.7):

$$
\begin{aligned}
\widehat{\gamma}(t) &= \widehat{\gamma}(t-1) + H(t)\varepsilon(t), \\
H(t) &= M(t)\varphi(t), \\
\varepsilon(t) &= y(t) - \varphi^T(t)\widehat{\gamma}(t-1),
\end{aligned} \tag{4.8}
$$

where $M(t)$ can be calculated as follows:

$$M(t) = \frac{M(t-1) - M(t-1)\varphi(t)\varphi^T(t)M(t-1)}{1 + \varphi^T(t)M(t-1)\varphi(t)}, \tag{4.9}$$

and $H(t)$ at each time step is calculated as

$$H(t) = \frac{M(t-1)\varphi(t)}{1 + \varphi^T(t)M(t-1)\varphi(t)}. \tag{4.10}$$

Note that to accurately estimate γ, M and $\widehat{\gamma}$ must be properly initialized.

4.3.2.2 Real-time Recursive Least Squares Identification

For the real-time identification, the derived equations of (4.8) should be manipulated such that the most recent measurements are paid more attention to. Introducing a forgetting factor,

the loss function of (4.7) can be written as

$$V(\gamma) = \frac{1}{2} \sum_{s=1}^{t} \lambda^{t-s} \varepsilon^2(s). \tag{4.11}$$

Selecting $0 < \lambda < 1$, as time passes, older measurements are given less importance. If λ is close to one, the past measurements are not forgotten so quickly. Note that the loss function of (4.7) is a special case of (4.11) in which $\lambda = 1$. Utilizing a forgetting factor is very crucial in real-time identification since the parameters to be identified can change with time. Therefore, the old measurements reflect the information associated with the old parameters of the system, which can mislead the identification process. Note that the selection of λ depends on the rate of change of system parameters, e.g., a rapidly changing system needs a smaller λ compared to a system with very slow rate of parameters change. Introducing the forgetting factor, the derived recursive equations of (4.8) are changed to the following equations [83]:

$$\begin{aligned}
\widehat{\gamma}(t) &= \widehat{\gamma}(t-1) + H(t)\varepsilon(t), \\
H(t) &= M(t)\varphi(t) = \frac{M(t-1)\varphi(t)}{\lambda + \varphi^T(t)M(t-1)\varphi(t)}, \\
\varepsilon(t) &= y(t) - \varphi^T(t)\widehat{\gamma}(t-1).
\end{aligned} \tag{4.12}$$

4.3.3 Real-time Recursive Least Squares Identification of Catenary Parameters

Equation (4.3) calculates the inductance of the catenary line through the injection of harmonic current. This calculation can be regarded as the measurement. In such a case, the measured output of the system is basically the parameter to be estimated. Assuming a model, the measured value for the inductance, i.e., L_m, is

$$L_m(t) = L + e(t) \tag{4.13}$$

in which L and $L_m(t)$ are the real and measured inductance, respectively, and $e(t)$ is the measurement error. Using the model of (4.13), one can apply the real-time identification approach of the previous section, and estimate the inductance in real time. Note that in the model of (4.13), $\varphi(t) = 1$, $\gamma = L$, and $y(t) = L_m$. Therefore, the identification algorithm of (4.12) for the inductance estimation is

$$\begin{aligned}
\widehat{L}(t) &= \widehat{L}(t-1) + H(t)\varepsilon(t), \\
H(t) &= M(t) = \frac{M(t-1)}{\lambda + M(t-1)}, \\
\varepsilon(t) &= L_m(t) - \widehat{L}(t-1).
\end{aligned} \tag{4.14}$$

Since the identification is implemented in discrete-time domain, in (4.14), t denotes the current sampling period, and $t-1$ corresponds to the previous sampling period. Moreover, the selection of $M(0)$ and $\widehat{L}(0)$ are of high importance. In the problem of catenary line inductance identification, $\widehat{L}(0)$ can be selected as the inductance of a line with the length of 15 km. Moreover, $M(0)$ in the inductance estimation problem can be a small number, e.g., 0.5.
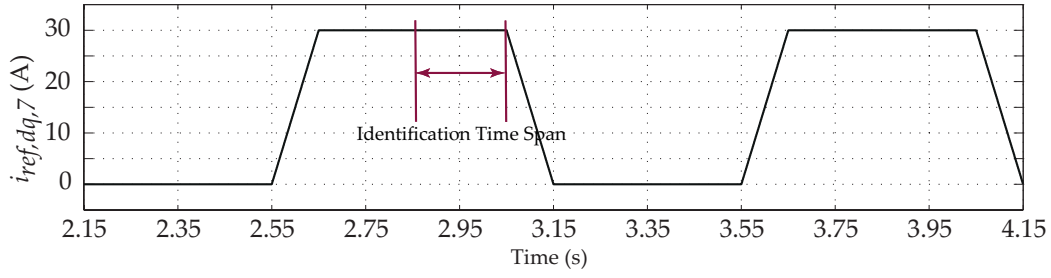
Figure 4.8: The reference value of the injected harmonic current in the $d-$ and q-axes

Note that locomotives normally operate with speeds of less than or around 200 km/h. Therefore, for example, a locomotive traveling at 200 km/h moves almost one kilometer every 20 Seconds. Therefore, the change of the line parameters is not so rapid. Due to this gradual change versus time, the permanent harmonic current injection and parameters estimation are not necessary. Moreover, in a traction network, there are many locomotives traveling at the same time. If they concurrently inject harmonic currents, not only they pollute the network, but also the interaction of the locomotives on each other may render their identifications invalid. Therefore, traction companies must formulate some guidelines and standards for the current injection and identification of the locomotives. For example, the locomotives can be obliged to perform the identification every 15 seconds, and at some specific times. In this case, assuming the network consists of 15 locomotives, each locomotive can perform its identification in a time frame of 1000 ms, at a specific instant in each 15 second period, meaning that Locomotive #1 can start injecting the harmonic current at hh:mm:00, Locomotive #2 at hh:mm:01, etc.

4.4   Performance Evaluation

In this section, the performance of the CLPI is evaluated in MATLAB/PLECS environment. The system of Figure 4.1 is adopted in which the position of the locomotive is not fixed. The initial position is 1 km away from the SS1, and it moves toward the SS2. The final position is 1 km away from the SS2, i.e., 59 km away from the SS1. The simulation time is 120 s corresponding to a locomotive average speed of 1740 km/h. In order to have the same identification samples as in a locomotive traveling along a 60 km railway with the speed of 180 km/h, the number of performed identifications are increased. Assuming the identification process takes place every half a kilometer, in a 60 km railway, 120 identification processes are needed. Therefore, traveling along a 60 km railway with the speed of 1740 km/h, the identifications are repeated every seconds in the simulation. Note that this unrealistic locomotive speed, which is chosen due to the shortcomings of the simulation software, does not affect the validity of the studies.

The reference value for both d- and q-components of the injected harmonic current during a time span of 2 seconds is depicted in Figure 4.8. The reference values for the d- and q-components of the injected current are the same. To prohibit the dynamics of the notch

Figure 4.9: The simulation results of the test system of Figure 4.2 while the locomotive travels from the SS1 to the SS2: (a) the amplitude of the locomotive-side catenary voltage, (b) the locomotive current, (c) the zoomed version of the locomotive-side catenary voltage, and (d) the zoomed version of the locomotive current

filters affecting the identification process, the identification is performed only during 0.2 s of the injection period. The sampling frequency for the identification in the example of this chapter is chosen to be 1 kHz. Therefore, during 0.2 s, 200 samples are taken and fed to the identification algorithm of (4.14). It should be noted that the initial point for the identification process at every second is the last point of the previous second.

During the locomotive movement, it periodically absorbs -2000 A of the locomotive-side d-component current, corresponding to 0.5445 MW of real power, from the catenary, while the q-component of the current is regulated at zero. In order not to impose unacceptable acceleration on the locomotive, the d-component reference value smoothly decreases from zero to -2000 A. Figures 4.9 (a) and (b) depict the PC voltage and the locomotive current during the whole simulation process, respectively. The zoomed version of the PC voltage and the locomotive current are shown in Figures 4.9 (c) and (d), respectively, which include the data between the time instant 47.4. s until 48.9 s.
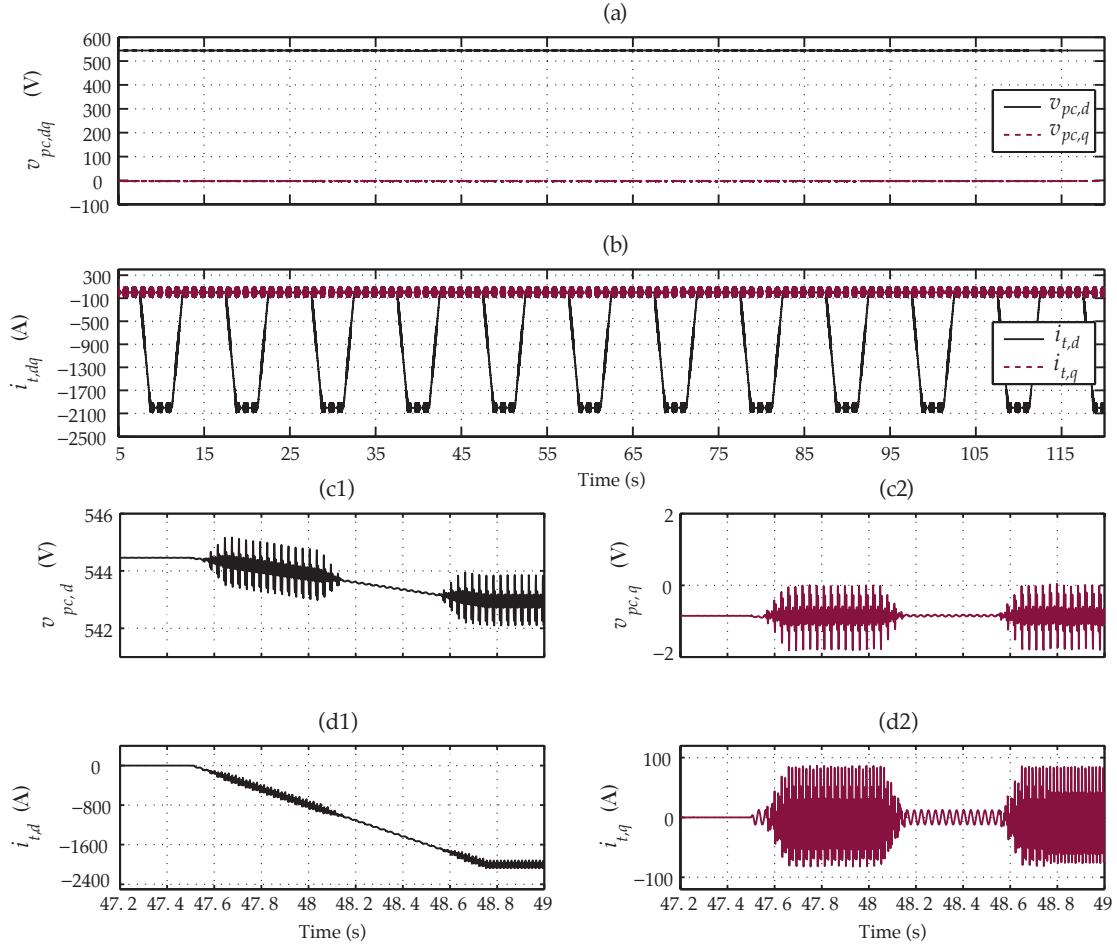
Figure 4.10: The simulation results of the test system of Figure 4.2 while the locomotive travels from the SS1 to the SS2: (a) the dq-components of the locomotive-side catenary voltage, (b) the dq-components of the locomotive current, (c) the zoomed dq-components of the locomotive-side catenary voltage, and (d) the zoomed dq-components of the locomotive current

Figures 4.10 (a) and (b) show the dq-components of the PC voltage and the locomotive current, respectively. The zoomed version of the dq-components of the PC voltage are depicted in Figures 4.10 (c1) and (c2), respectively. The zoomed version of the d-component of the PC voltage shows that before the injection of the d-component of the locomotive current at the time instant 47.52 s, the PC voltage is at its nominal value, i.e., 544.5 V. However, subsequent to the injection of the d-component locomotive current and due to the voltage drop along the line, the d-component of the voltage drops. Moreover, subsequent to the injection of the harmonic current at the time instant 47.54 s, the d-component and also the q-component of the voltage are polluted with the injected harmonic component, as shown in Figures 4.10 (c1) and (c2). The zoomed version of the dq-components of the locomotive current are also depicted in Figures 4.10 (d1) and (d2). The d-component of the locomotive current in the zoomed version is initially set to zero, and at the time instant 47.52 s, it smoothly decreases
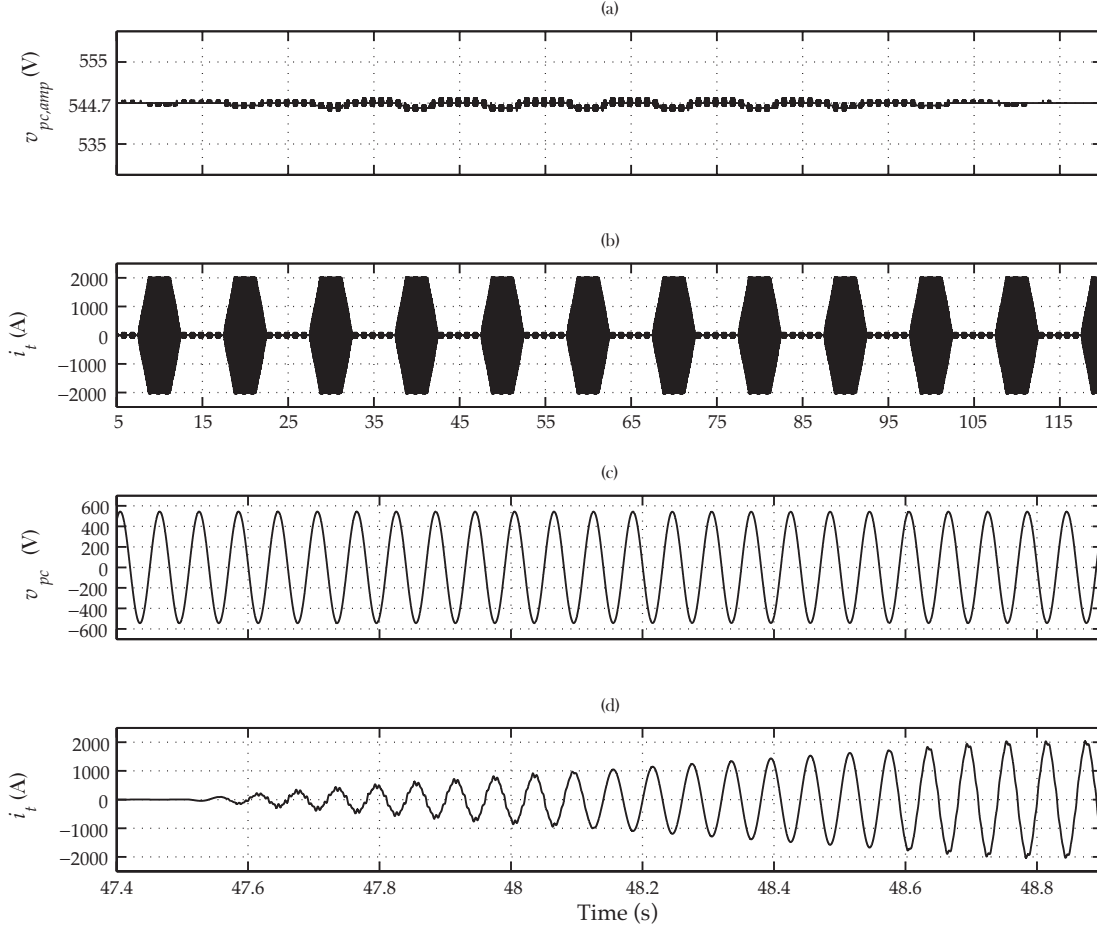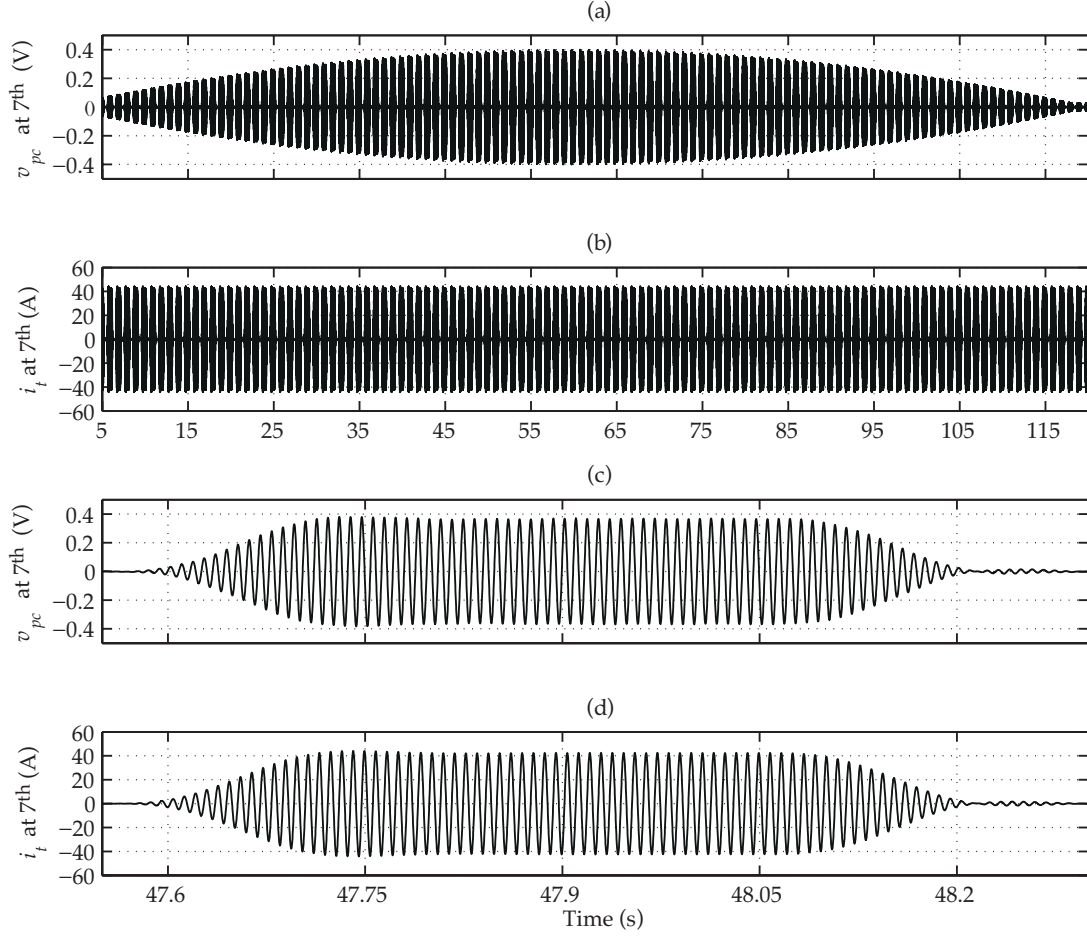
Figure 4.11: The simulation results of the test system of Figure 4.2 while the locomotive travels from the SS1 to the SS2 at the 7th harmonic: (a) the locomotive-side catenary voltage, (b) the locomotive current, (c) the zoomed version of the locomotive-side catenary voltage, and (d) the zoomed version of the locomotive current

from zero to -2000 A. Note that the q-component of the locomotive current at the fundamental frequency is constantly kept at zero, in order not to inject any reactive power.

For the identification, 30 A (rms) of the 7th harmonic current, i.e., $i_{t,d,7} = 30$ A and $i_{t,q,7} = 30$ A, is injected, and its consequence on the PC voltage is analyzed. That is, the corresponding amplitudes of the PC voltage and the injected current at the 7th harmonic are extracted, as shown in Figure 4.6, and used for the identification. In order to extract the amplitudes of the injected current and its corresponding voltage at the PC at the 7th harmonic, the notch filters tuned to the 7th harmonic are utilized. Figures 4.11 (a) and (b) depicts the extracted PC voltage and the locomotive current at the 7th harmonic, respectively. Although the amplitude of the injected current during the simulation time is constant, however, the amplitude of the resulting voltage changes due to the change of the line impedance. The zoomed versions of the PC voltage and the locomotive current from the time instant 47.55 *s* to 48.3 *s* are also
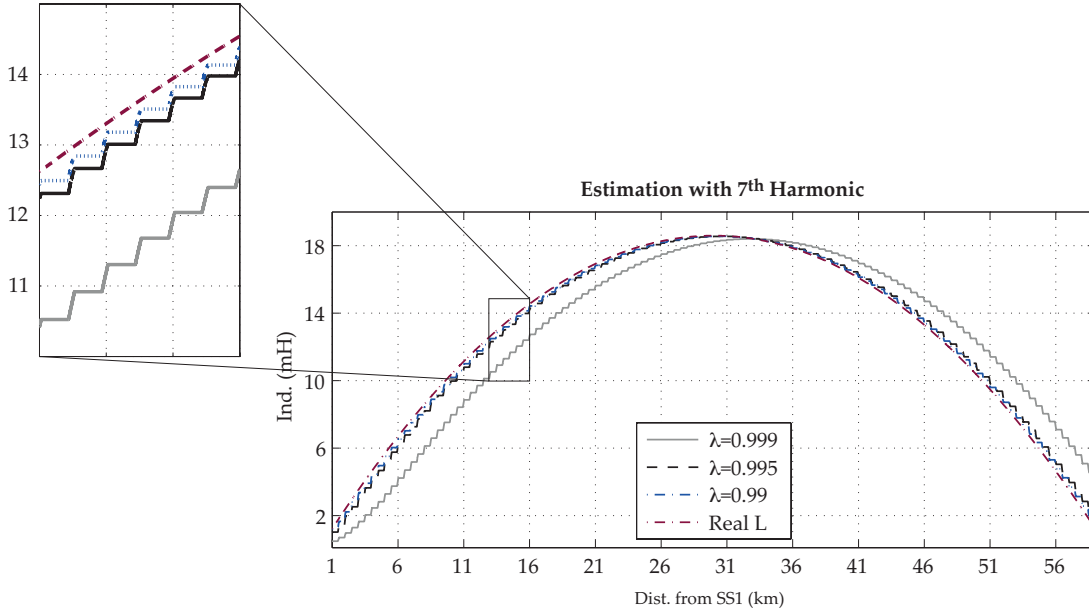
Figure 4.12: The identified line inductance and its real value estimated by the 7th harmonic current injection for several forgetting factors

presented in Figures 4.11 (c) and (d), respectively. Note that due to the smooth injection of the harmonic current, the extracted voltage and current at the 7th harmonic smoothly increase from zero to their final values.

After extracting the amplitudes of the PC voltage and the locomotive current at the 7th harmonic, they are fed to the CLPI in order to estimate the inductance of the catenary line as explained in Section 4.3. Figure 4.12 (a) depicts the estimated inductance for three different forgetting factors and also shows the real value of the inductance versus the distance from the SS1, which verifies that the CLPI is able to effectively estimate the inductance of the line. The results show that for the forgetting factors close to one, the estimation might not be very accurate. The reason is that the forgetting factors very close to one result in forgetting old measurements very slowly, which itself results in inaccurate estimation. However, for locomotives with low speed, forgetting factors close to one can be helpful. In the presented simulation case study, the forgetting factor of 0.99 shows satisfactory results.

4.5   Conclusions

An identification strategy for the estimation of the catenary line parameters is proposed. The method is based on the injection of harmonic current through the ALC of the locomotive drive system, and monitoring the corresponding low-order harmonic voltage at the connection point of the locomotive to the catenary. Adopting the 7th harmonic current injection, the test results show that the estimation through the current injection is viable and can be adopted for the parameter estimation. It must be noted that the injected current can be of any frequency

provided the frequency is within the viable range of the ALC of the locomotive drive system.

Note that the choices of the identification sampling time, the forgetting factor, and the pattern of harmonic injection determine the quality of the estimated inductance, which can be selected according to the system specifications, e.g., the number of locomotives in the system, their speeds, the distance between substations, etc.

ALC-based Catenary Voltage Support

5.1 Introduction

The adoption of reactive power in power systems for voltage support has been largely investigated and studied in the literature [37, 84–88]. In traction networks, utilizing the same concept, to compensate for the adverse effects of low system-voltage, various compensators have been proposed and utilized, e.g., thyristor-switched reactors and thyristor-switched capacitors [54, 55], semiconductor-based solutions [15, 56–60], and supercapacitor-based compensators [61]. These solutions, however, are generally costly and can only locally compensate for low system-voltage. A potential solution for obviating the low system-voltage problem is to take advantage of the ALC of modern locomotives in order to support the catenary voltage.

In this chapter, the ALC is utilized as a STATCOM to provide the network with capacitive reactive power to compensate for the voltage drop along the line. Inspiring from the CMPC of Chapter 3, a cascade catenary voltage support scheme is proposed whose outer or secondary loop is realized by a Single-Input Single-Output (SISO) controller that just delivers the set-point of the q-component of the locomotive current. Note that the set-point of the d-component is generated by another secondary loop realized by another SISO controller responsible for maintaining the DC-link voltage. To realize the voltage support secondary loop, three types of controllers are utilized, which all belong to PI-controllers family: (i) a Proportional-based Voltage Support Scheme (PVSS), (ii) a Proportional-Integral-based Voltage Support Scheme (PIVSS), and (iii) a Gain-scheduled Voltage Support Scheme (GVSS). The difference between the filtered d-component of the catenary voltage and its rated value is fed to the controllers whose outputs are the set-point of the q-axis of the ALC current, which determines the injected reactive power.

The rest of this chapter is structured as follows. Section 5.2 describes the adopted traction network. Section 5.3 details the low system-voltage problem. Adopting the ALC, three controllers for overcoming the low system-voltage problem are described in Section 5.4, and their
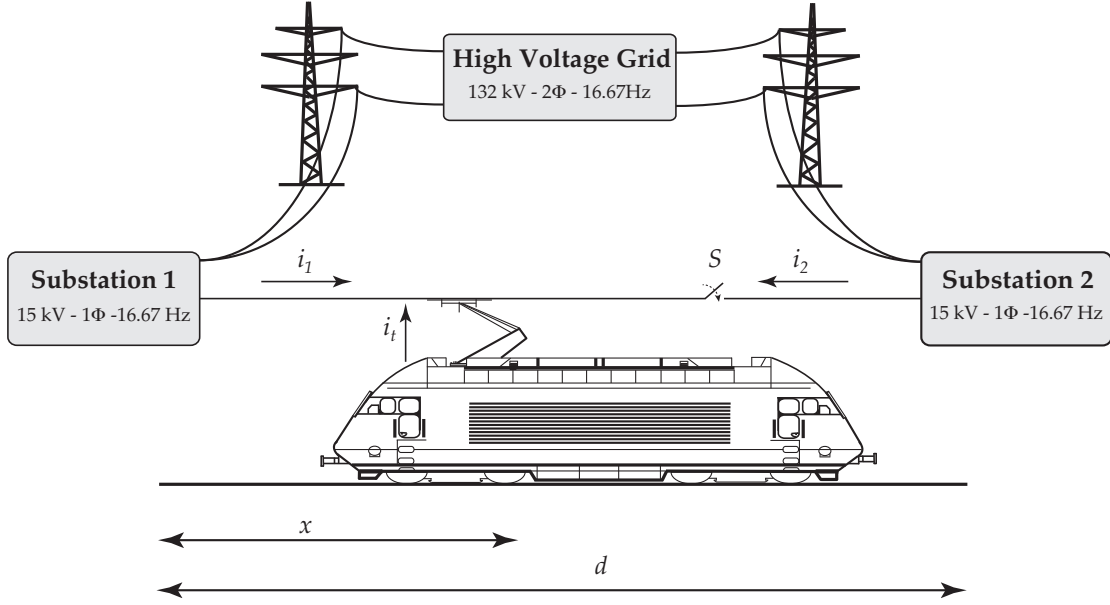
Figure 5.1: The single-locomotive test system

performances are evaluated. Section 5.5 concludes the chapter.

5.2 System Descriptions

In this section, the adopted test system is presented, which is an AC single-phase traction network, as shown in Figure 5.1. The system consists of two substations (the SS1 and the SS2) and a locomotive connected to the catenary through its pantograph. The test system is similar to that of Figure 4.1, however, a switch is added to the test system, which is responsible for disconnecting the SS2 from the rest of the network. The schematic diagram of the system is also depicted in Figure 5.2 along with its dedicated control blocks. The line connecting two substations is represented by its resistance and inductance. Moreover, the locomotive is connected to the catenary through a coupling transformer, which is modeled by an ideal transformer plus its leakage inductance and series resistance represented by L_t and R_t, respectively. The ALC of the locomotive drive system is implemented by a full-bridge single-phase IGBT-based inverter. Note that the DC-link of the inverter consists of a DC voltage source whose voltage is regulated at 840 V, and the dynamics of the locomotive motor and its driver are neglected. The parameters of the test system of this chapter are similar to those of Chapter 4 and are presented in Table 4.1.

Note that there is no line reactor filter added for harmonic switching filtering. The reason is that the leakage inductance of the adopted transformer is large enough and is exploited for switching harmonic filtering.
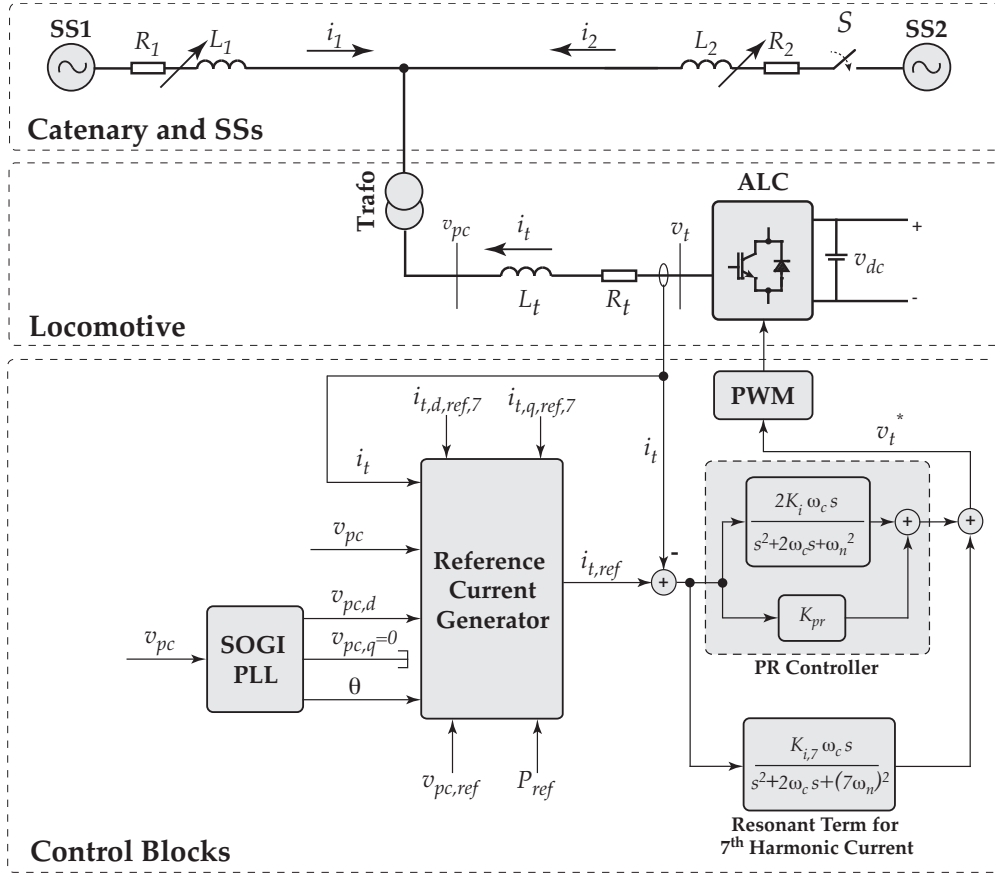
Figure 5.2: The schematic diagram of the test system of Figure 5.1 with its dedicated control blocks

5.2.1 ALC Current Control Strategy

The common practice for the ALC of locomotives is utilizing current control schemes for the regulation of the input current, which itself results in the active and reactive power regulation. In this chapter, the PR-based current control scheme, which is detailed in Chapter 4, is adopted for current regulation. Figure 5.2 depicts the complete schematic diagram of the test system. Similar to the control system of Chapter 4, the utilized PR-based control strategy consists of resonant terms to regulate the fundamental frequency and also harmonic frequency current components. The fundamental frequency component is responsible for controlling the power exchange of the locomotive with the catenary, while the harmonic frequency component is injected for catenary parameters identification. The utilized harmonic frequency is 116.7 Hz corresponding to the 7th harmonic. Note that the identified catenary parameters are utilized in the following sections to implement a gain-scheduled low system-voltage compensation scheme.

In the single-phase system of Figure 5.2, extracting the phase-angle of the catenary voltage through the SOGI PLL, the q-component of the voltage is forced to zero. Therefore, the d-
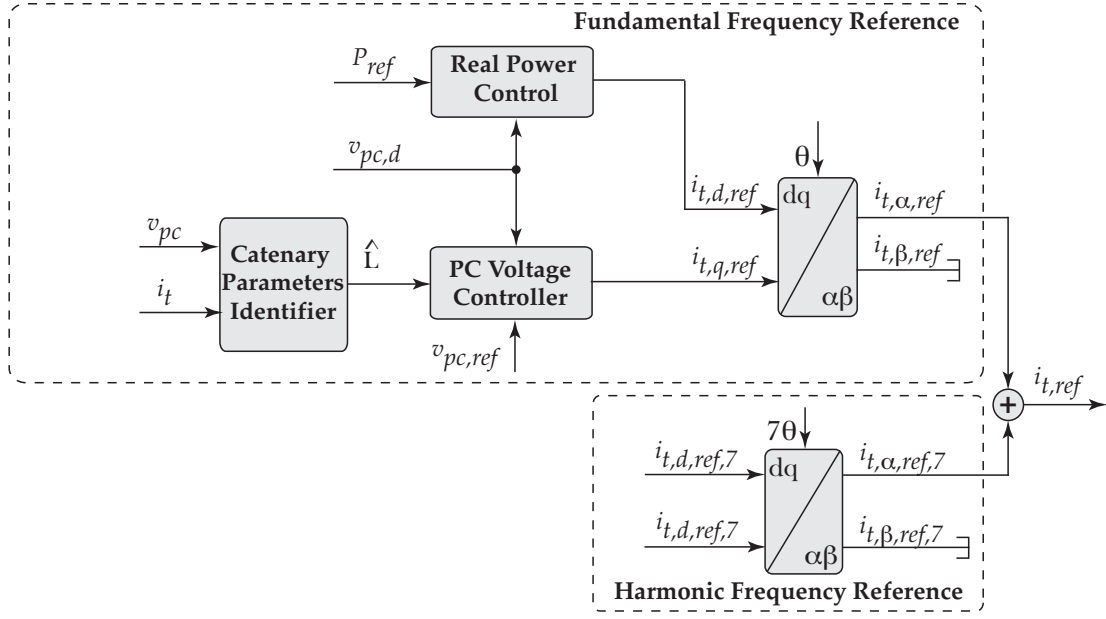
Figure 5.3: The reference current generator for PR-controller

component of the current is responsible for the active power regulation, while its q-component determines the reactive power, i.e., $P = \frac{1}{2}v_{pc,d}i_{t,d}$ and $Q = \frac{1}{2}v_{pc,d}i_{t,q}$. To determine the reference values in the SRF, the reference signals are first determined in the RRF synchronized with the PC voltage. That is, the required d- and q-components of the reference current are determined according to the demanded real and reactive power of the locomotive as if the system is in a RRF. Then, adopting the extracted phase-angle of the PC voltage, the dq-reference values are transferred to an $\alpha\beta$-frame. Discarding the β-component, the α-component is the reference value for the SRF, which results in the injection of the required real and reactive power. Figure 5.3 shows the blocks responsible for generating the reference signal for the current controller. Note that the q-axis reference value is determined through *PC Voltage Controller* block of Figure 5.3, which is explained in the following. This controller, if implemented in an adaptive way, requires the inductance of the line to schedule its parameters, which is identified through the identification strategy of Chapter 4. Therefore, the reference signal of the ALC must contain the 7th harmonic components for identification, as explained in Chapter 4.

5.3   Low System-Voltage

In this section, adopting the system model of Figure 5.2, the low system-voltage problem is detailed. Note that in the following, first, the low system-voltage is explained in the traction system of Figure 5.2, in which the switch S is closed, and both substations are in service. Then, assuming an open switch, the results are extended to a single-substation system.

Assume that the locomotive of Figure 5.2 is consuming P watts of real power and is located
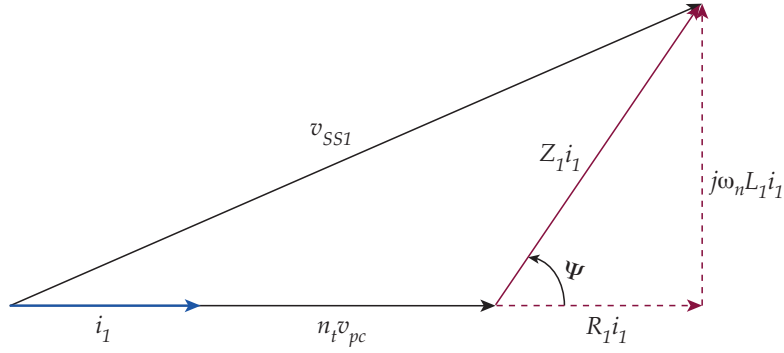
Figure 5.4: The phasors of the system voltages and currents corresponding to the SS1 while the locomotive operates at unity power factor

x kilometers away from the SS1. The length of the line is d kilometers. Applying KVL to the system of Figure 5.2, the following is deduced:

$$v_{SS1} = n_t v_{pc} + Z_1 i_1 \tag{5.1}$$

in which n_t is the turn ratio of the transformer, and $Z_1 = R_1 + j\omega_n L_1$. Moreover, R_1 and L_1 are the resistance and inductance of a segment of the line whose length is x km. Figure 5.4 depicts a vector diagram of (5.1). Adopting the diagram, one can deduce

$$v_{SS1}^2 = (n_t v_{pc} + R_1 i_1)^2 + (\omega_n L_1 i_1)^2. \tag{5.2}$$

Assuming the impedance of the line per kilometer is $Z_l = R_l + j\omega_n L_l$ and $v_{SS1} = v_{SS2}$, the current of the SS1, i.e., i_1, is expressed in terms of the locomotive current as follows:

$$n_t i_1 = \frac{Z_2}{Z_1 + Z_2}(-i_t) = \frac{(d-x)Z_l}{dZ_l}(-i_t) = \left(1 - \frac{x}{d}\right)(-i_t). \tag{5.3}$$

Moreover, the locomotive current is expressed in terms of its real power consumption and the catenary voltage as

$$-i_t = \frac{P}{v_{pc}}. \tag{5.4}$$

Substituting for i_t from (5.4) in (5.3), the following is deduced:

$$i_1 = (1 - \frac{x}{d})\frac{P}{n_t v_{pc}}. \tag{5.5}$$

Moreover, substituting for i_1 from (5.5) in (5.2), the following is derived:

$$\left(n_t v_{pc}\right)^4 + \left(2R_1 P\left(1 - \frac{x}{d}\right) - v_{SS1}^2\right)\left(n_t v_{pc}\right)^2 + \left(R_1^2 + (L_1\omega_n)^2\right)P^2\left(1 - \frac{x}{d}\right)^2 = 0. \tag{5.6}$$

Figure 5.5: The catenary voltage versus the distance of the locomotive from the SS1 for three different locomotive power levels

Substituting xR_l and xL_l for R_1 and L_1, respectively, in (5.6), the following is achieved:

$$\left(n_t v_{pc}\right)^4 + \left(2R_l P\left(x - \frac{x^2}{d}\right) - v_{SS1}^2\right)\left(n_t v_{pc}\right)^2 + \left(R_l^2 + (L_l \omega_n)^2\right)P^2\left(x - \frac{x^2}{d}\right)^2 = 0. \tag{5.7}$$

Solving (5.7) for $n_t v_{pc}$, the voltage of the catenary at the connection point of the locomotive to the network is then determined as

$$n_t v_{pc} = \sqrt{\sqrt{\left(\frac{v_{SS1}^2}{2} - R_l P\left(x - \frac{x^2}{d}\right)\right)^2 - \left(\|Z_l\| P\left(x - \frac{x^2}{d}\right)\right)^2} + \frac{v_{SS1}^2}{2} - R_l P\left(x - \frac{x^2}{d}\right)}. \tag{5.8}$$

Figure 5.5 shows the voltage of the catenary as a function of the locomotive physical position, i.e., x, for several power demand levels. Figure 5.5 confirms that absorbing real power from the catenary results in the voltage drop along the line.

The conducted studies for two-substation networks can be extended to single-substation systems. If the switch S in the system of Figure 5.1 is open, the system is a single-substation one. This situation is similar to a system with a closed switch, in which the length of the catenary line is close to infinity, i.e., $d \simeq \infty$. Therefore, taking the limit of (5.8) as $d \to \infty$ for $x \ll d$, the voltage of the catenary at the connection point of the locomotive to a single-substation network is determined as

$$n_t v_{pc} = \sqrt{\sqrt{\left(\frac{v_{SS1}^2}{2} - R_l P x\right)^2 - \left(\|Z_l\| P x\right)^2} + \frac{v_{SS1}^2}{2} - R_l P x}. \tag{5.9}$$
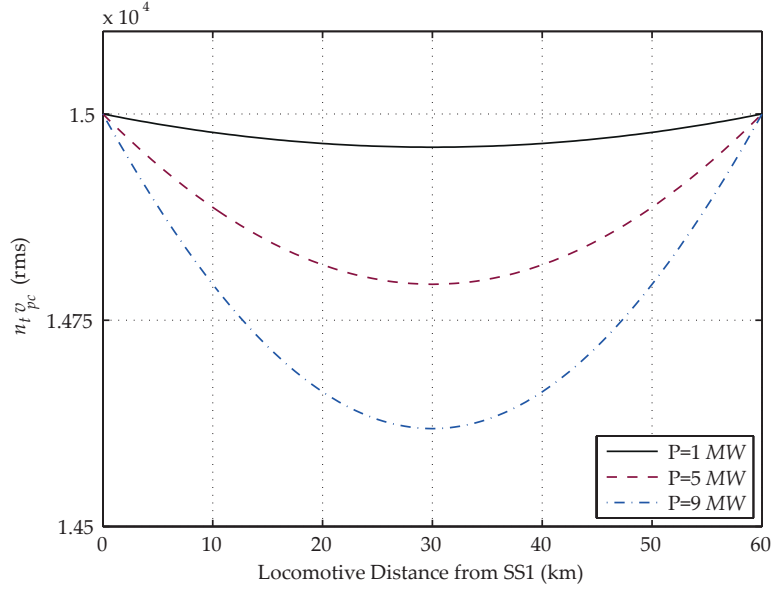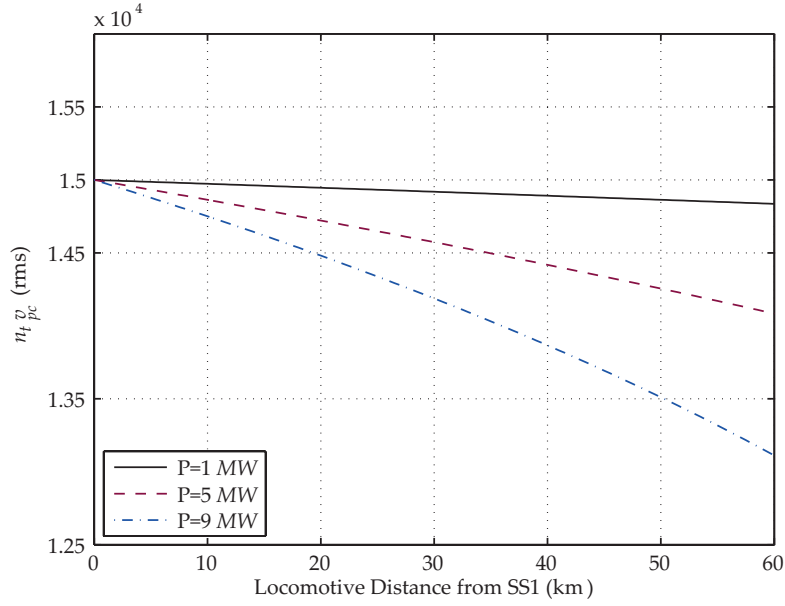
Figure 5.6: **The catenary voltage versus the distance of the locomotive from the SS1 for three different locomotive power levels in a single-substation system**

Figure 5.6 shows the voltage of the catenary as a function of the locomotive physical position, i.e., x, for several power demand levels, in a single-substation network.

To show the effect of real power absorption on the catenary voltage, a simple test is conducted in MATLAB/PLECS environment. The test system of Figure 5.1 is adopted in which the locomotive moves from the proximity of the SS1 toward the SS2 while the switch S is closed. The parameters of the locomotive, the line, and the substations are set according to Table 4.1. The real power demand of the locomotive periodically changes between zero and 544 kW to simulate deceleration and acceleration along the line. However, no reactive power is injected. Figure 5.7 depicts the simulation results. Figure 5.7 (a) shows the filtered PC voltage amplitude, which drops upon absorbing real power by the ALC. The voltage drop depends on the amount of absorbed real power and also on the impedance of the catenary. Figure 5.7 (b) depicts the dq-components of the locomotive current. Note that the maximum amount of voltage drop in Figure 5.7 (a) is 0.3%, which is not significant. However, the voltage drop in this case corresponds to the absorbed power of only one small locomotive. Assuming several more powerful locomotives with the power of ten times larger than that of the studied one, the voltage drop can be 15% or even more. Such voltage drop can result in shut down or power decrement of the locomotives fed by the affected line.

5.4   Low System-Voltage Compensation

Having lower voltage in the middle of the line not only limits the performance of the locomotives fed by the affected line but also limits the capacity of the line. That is, less real power can
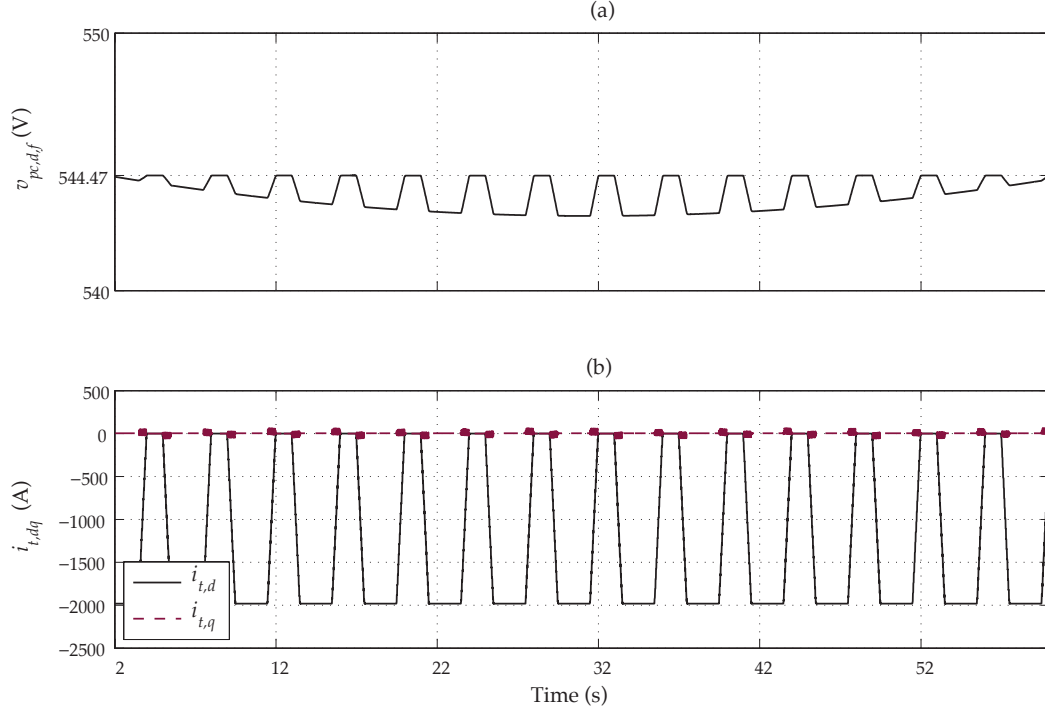
Figure 5.7: **The simulation results of the single-locomotive system of Figure 5.1 without compensation: (a) the filtered PC voltage amplitude and (b) the dq-components of the locomotive current**

be transmitted through the affected line. However, injecting reactive power through the ALC of the locomotive, one can compensate for the voltage drop along the line without installing new infrastructure. In the system of Figure 5.2, assuming the phase-angle between the locomotive voltage and current is ϕ, the phasors corresponding to the locomotive voltage, the SS1 voltage, and the current flowing from the SS1 to the locomotive are as depicted in Figure 5.8.

Taking the same procedure as explained for calculating the locomotive voltage working with $cos(\phi) = 1$ in the two-substation system, one can determine the voltage of the locomotive, which operates at the power factor of $cos(\phi)$, as follows:

$$n_t v_{pc} = \sqrt{\sqrt{\left(\frac{v_{SS1}^2}{2} - \frac{\|Z_l\|P}{cos(\phi)}cos(\psi - \phi)\left(x - \frac{x^2}{d}\right)\right)^2 - \left(\frac{\|Z_l\|P}{cos(\phi)}\left(x - \frac{x^2}{d}\right)\right)^2} + \frac{v_{SS1}^2}{2} - \frac{\|Z_l\|P}{cos(\phi)}cos(\psi - \phi)\left(x - \frac{x^2}{d}\right)}.$$
(5.10)

Assuming a real power demand of $9\ MW$, Figure 5.9 shows the catenary voltage as a function of x for three different levels of reactive power injection, i.e., three different power factors, in a two-substation system. Figure 5.9 verifies that injecting capacitive reactive power, the voltage drop along the line is compensated.

To compensate for the low system-voltage in single-substation systems, similar to the two-
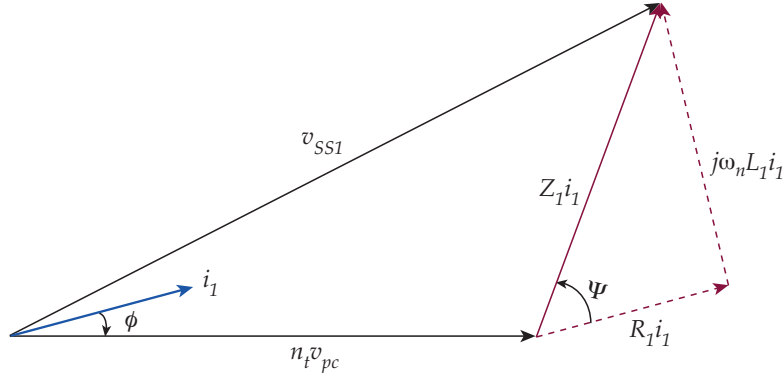
Figure 5.8: The phasors of the system voltages and currents corresponding to the SS1 while the locomotive operates at an arbitrary power factor $cos(\phi)$

substation system, the locomotive can inject reactive power. Assuming the locomotive is operating at the power factor of $cos(\phi)$, the voltage of the locomotive at its connection point to the single-substation system can be determined by taking the limit of (5.10) as $d \rightarrow \infty$ for $x \ll d$ and can be presented as

$$n_t v_{pc} = \sqrt{\sqrt{\left(\frac{v_{SS1}^2}{2} - \frac{\|Z_l\|P}{cos(\phi)}cos(\psi - \phi)x\right)^2 - \left(\frac{\|Z_l\|P}{cos(\phi)}x\right)^2} + \frac{v_{SS1}^2}{2} - \frac{\|Z_l\|P}{cos(\phi)}cos(\psi - \phi)x}. \quad (5.11)$$

Figure 5.10 shows the voltage of a 9 MW locomotive at its connection point to the catenary as a function of the locomotive physical position, i.e., x, for several power factors, in a single-substation network.

Note that the capacity of the ALC in terms of injecting real and reactive power must be considered. Figure 5.11 shows the capacity of a typical converter with the maximum apparent power of S_{max} in which the locomotive always operate in the motor mode. If the converter works at the unity power factor, i.e., $cos(\phi) = 1$, the maximum injectable real power is 1 p.u. while no reactive power is injected. However, sacrificing for 10% of the maximum real power, 43.5% of reactive power can be injected corresponding to a power factor of 0.9. Note that due to various reasons, e.g., the speed limit of railways, locomotives normally travel with speeds and power levels less than their nominal values. Therefore, operating at power factors less than one and injecting reactive power are feasible.

Operating at a fixed power factor may efficiently compensate for the voltage drop at a given point for which the power factor is calculated. However, due to several reasons, e.g., nonuniform impedance of the line in the network, fluctuations in the substation voltages, etc., the required reactive power levels for the compensation in various locations in the network are different. Therefore, a fixed power factor may not efficiently compensate for the voltage drop in the whole network. In the following, using a closed-loop approach, which dictates the reference value of the locomotive current in the q-axis, several low system-voltage compensation schemes are proposed.
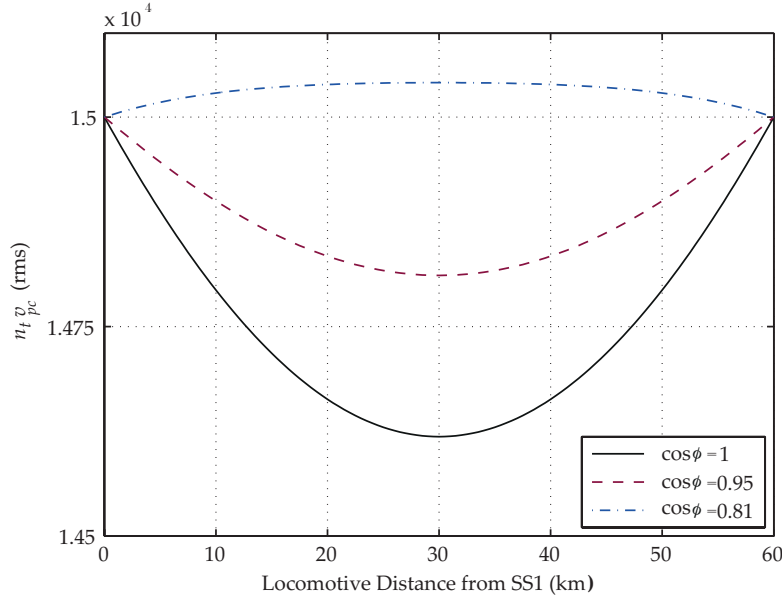
Figure 5.9: The catenary voltage versus the distance of a $9\ MW$ **locomotive from the SS1 for three different levels of compensation in a two-substation system**

5.4.1 PI-Family-based Compensators

In this section, several simple closed-loop approaches are investigated, which are based on feeding the error between the filtered d-component of the PC voltage and its reference value to various controllers of the PI family. Since the adopted PLL forces the q-component of the voltage to zero, the d-component of the PC voltage is equal to its amplitude in steady-state, i.e., $v_{pc,d} = v_{pc,amp}$. In transients, v_{amp} might be slightly different from $v_{pc,d}$. If the difference is significant, one can calculate the amplitude of the PC voltage as follows $v_{pc,amp} = \sqrt{v_{pc,d}^2 + v_{pc,q}^2}$. In this thesis, however, it is assumed that $v_{pc,d} = v_{pc,amp}$ even during transients. In the following, three PI-based techniques are taken and described in the following: (i) the PVSS, (ii) the PIVSS, and (iii) the GVSS. Note that these controllers replace the *PC Voltage Controller* of Figure 5.1. Moreover, note that to filter out various distortions of the network, the PC voltage is first filtered through a <u>L</u>ow-<u>P</u>ass <u>F</u>ilter (LPF) whose cutoff frequency is set to $100\frac{rad}{s}$.

To evaluate the performance of the proposed closed-loop methods, a simulation test is performed. The test is similar for the three aforementioned closed-loop approaches. The test system of Figure 5.1 is taken in which only one locomotive travels from the proximity of the SS1 toward the SS2. The parameters of the system are selected according to Table 4.1. The reference signal of the locomotive d-component current, and consequently the absorbed real power, increase and decrease with a predetermined slope to mimic acceleration and deceleration. The maximum absorbed power is $544\ kW$. Due to the limited capacity of the simulation software, the simulation time span is selected to be 60 s, which corresponds to an unrealistic locomotive speed of almost 3600 km/hour. However, this unrealistic speed does
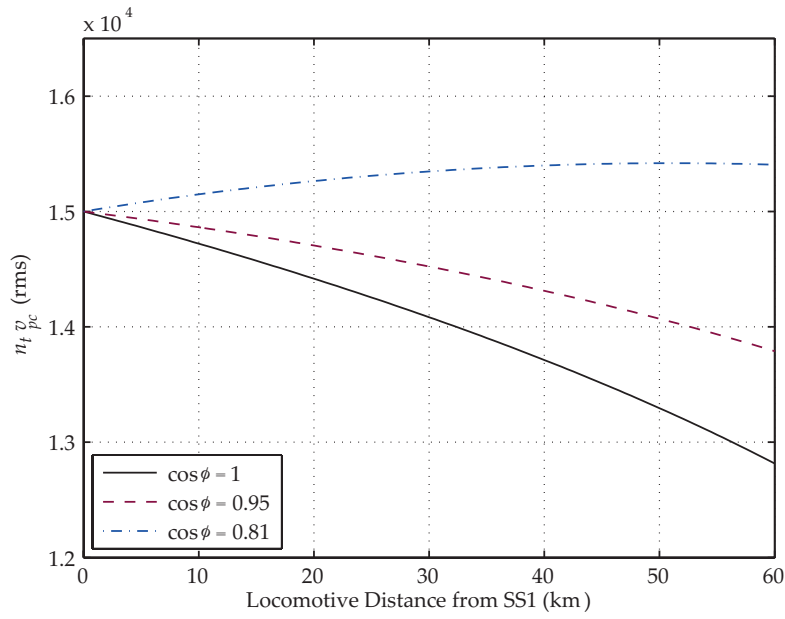
Figure 5.10: The catenary voltage versus the distance of a $9\ MW$ **locomotive from the SS1 for three different levels of compensation in a single-substation system**

not affect the validity of the analysis.

5.4.1.1   Proportional-based Voltage Support Scheme - PVSS

The simplest controller of the PI family is P-controller, which multiplies the error by a gain to generate the control signal. Reference [89] introduces a voltage support scheme through the
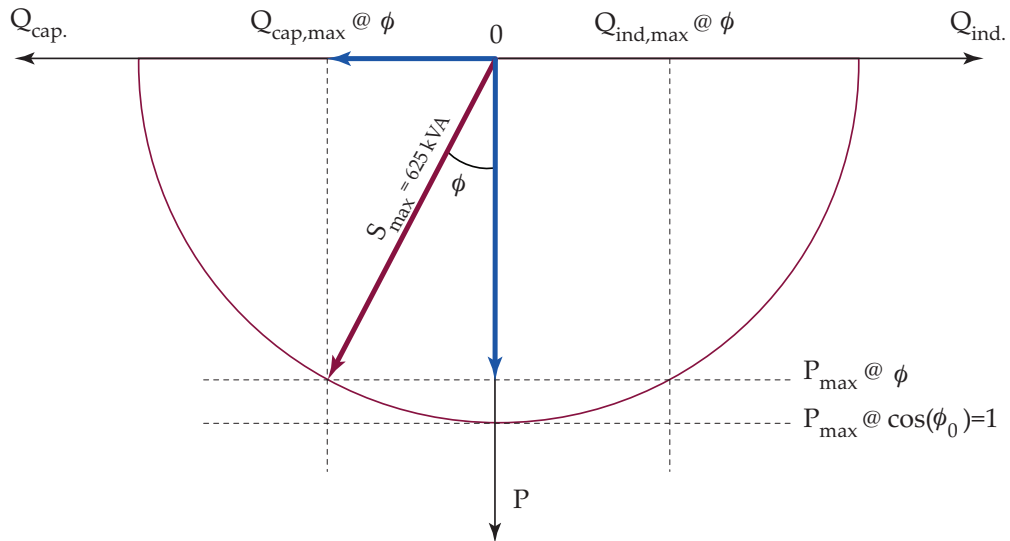
Figure 5.11: The ALC capacity
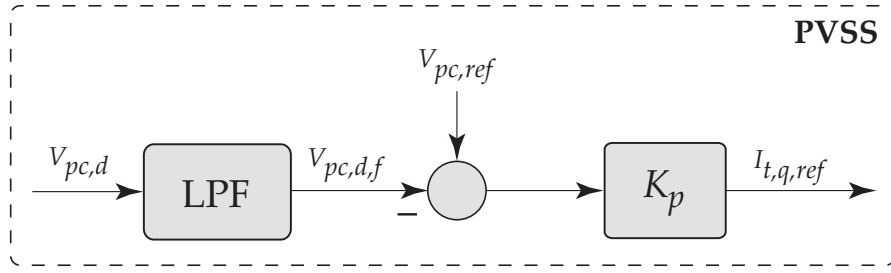
Figure 5.12: The *PC Voltage Controller* of Figure 5.3 realized by the PVSS

ALC, which utilizes a proportional controller. In the technical literature, P-controllers are also known as droop controllers. In the case of voltage compensation, the error is the the difference between the filtered d-component of the catenary voltage and its reference value, and the control signal is the reference value of the q-component of the locomotive current. Figure 5.12 depicts the PVSS block diagram. This controller is simple to implement, however, since it does not show infinite gain at DC, it is not able to eliminate the error in the steady-state. Note that increasing the gain of the P-controller in order to reduce the steady-state error, destabilizes the closed-loop system, and therefore, the gain must be limited. The gain of the P-controller in the PVSS must be selected such that it stabilizes the system for all operating scenarios. The gain that destabilizes the closed-loop system is inversely proportional to the line inductance seen from the PC. Therefore, the location at which the locomotive sees the largest line inductance must be identified, and the PVSS must be designed for that operating scenario. This scenario corresponds to a single-substation system in which the locomotive is at the end of the line. The gain for this point is selected 0.8 of the gain that destabilizes the closed-loop system. Therefore, the gain of the designed PVSS, i.e., K_p, equals 0.8×400.

To evaluate the performance of the designed PVSS, the aforementioned test scenario is conducted. Figure 5.13 (a) shows the filtered amplitude of the locomotive voltage, and verifies that the controller practically fails to regulate the voltage. Figure 5.13 (b) depicts the dq-components of the locomotive current. The P-controller output, i.e., the reference value of the q-component of the locomotive current, is shown in Figure 5.13 (c).

5.4.1.2 Proportional-Integral-based Voltage Support Scheme - PIVSS

In this section, the performance of the PIVSS in terms of low system-voltage compensation is evaluated. Figure 5.14 depicts the PIVSS block diagram in which the error between the filtered d-component of the catenary voltage and its reference value is fed to a PI-controller. Similar to the PVSS design procedure, the PIVSS is designed for the operating scenario in which the line inductance is maximum in the system of Figure 5.1. Applying the Ziegler-Nichols method [90] to this operating point, the designed controller is

$$G_{PI}(s) = K_{pi} + \frac{1}{T_i s} \tag{5.12}$$

98

Figure 5.13: **The simulation results of the test system of Figure 5.1 in which the locomotive equipped with the PVSS travels from the SS1 to the SS2: (a) the filtered amplitude of the locomotive voltage, (b) the dq-components of the locomotive current, and (c) the controller output**
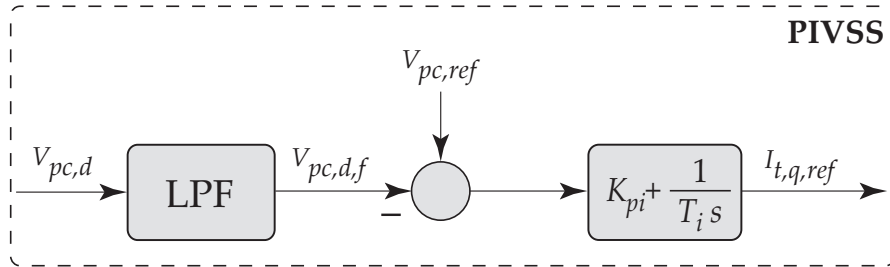
Figure 5.14: **The *PC Voltage Controller* of Figure 5.3 realized by the PIVSS**

in which $K_{pi} = 200$ and $T_i = 0.07$.

The aforementioned test scenario is performed to evaluate the performance of this controller in terms of regulating the PC voltage at its rated value. Figure 5.15 (a) depicts the filtered amplitude of the PC voltage, which is regulated at its rated value by the PIVSS without steady-state error. Figure 5.15 (b) shows the dq-components of the locomotive current, and the reference value of the q-component is shown in Figure 5.15 (c), which is the output of the
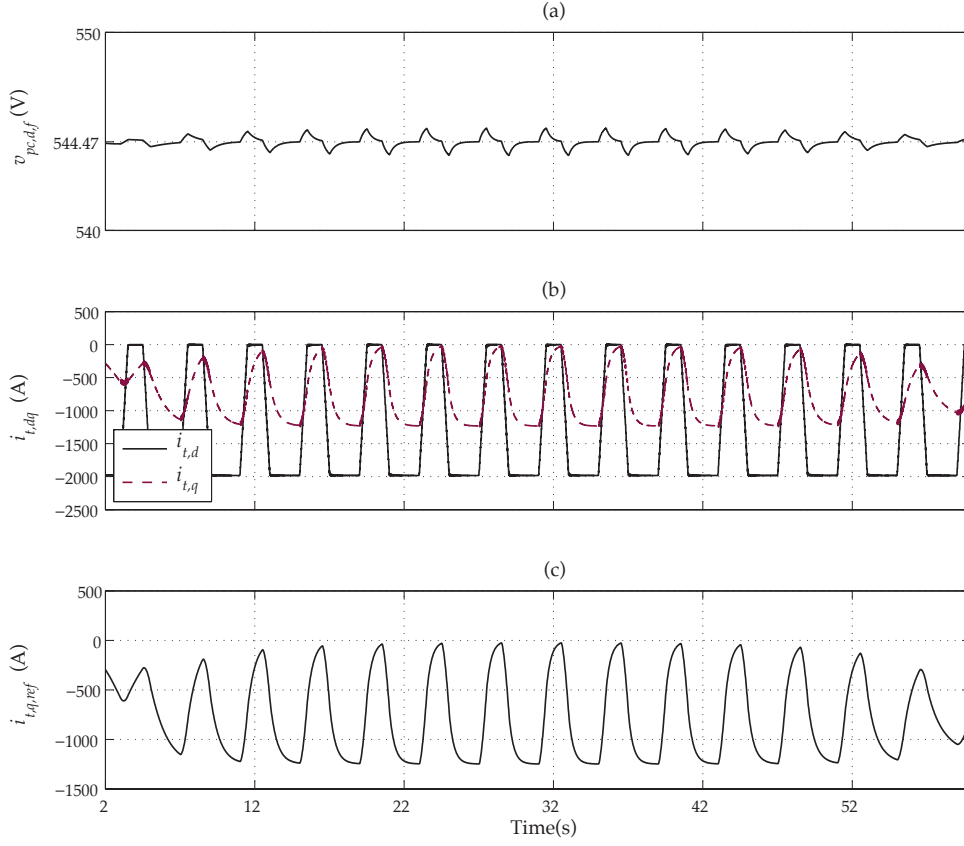
Figure 5.15: The simulation results of the test system of Figure 5.1 in which the locomotive equipped with the PIVSS travels from the SS1 to the SS2: (a) the filtered amplitude of the locomotive voltage, (b) the dq-components of the locomotive current, and (c) the controller output

PIVSS. Note that although the PIVSS regulates the PC voltage, however, its performance in the vicinity of substations is not flawless. The reason is that the PIVSS is designed to achieve the desired performance only for the operating scenario with maximum line inductance, while it only stabilizes the closed-loop system for other cases. To have superior performance for all cases, a gain-scheduled PI-controller is proposed in the following section.

5.4.1.3 Gain-scheduled Voltage Support Scheme - GVSS

Since the physical position of the locomotive is changing in the network, a single PI-controller may not achieve acceptable performance for all possible scenarios. In the following, identifying the line inductance seen from the connection point of the locomotive to the catenary, a gain-scheduled PI-controller, i.e., the GVSS, is proposed.

As explained in the previous section, the PIVSS of (5.12) provides acceptable dynamic performance for the operating scenario in which the locomotive is far from the substations. However,
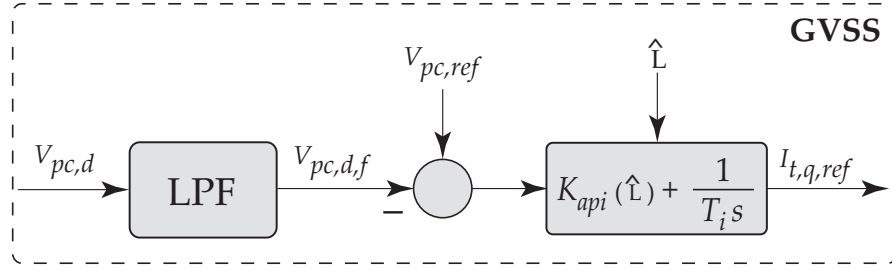
Figure 5.16: The *PC Voltage Controller* of Figure 5.3 realized by the GVSS

as the locomotive moves toward the SS1 or the SS2, the performance of the PIVSS is not excellent. Exploiting the catenary parameters identification of Chapter 4, one can adapt the parameters of the the PIVSS of (5.12) according to the identified inductance. Applying the Ziegler-Nichols frequency response method for various points in the test system of Figure 5.1 and designing PI-controllers, i.e., $G_{PI} = K_{pi} + \frac{1}{T_i s}$, it is concluded that the parameter T_i for all points is the same. However, the parameter K_{pi} changes inversely proportional to the identified inductance, $\widehat{L}$. Therefore, assuming the designed controller of (5.12) and a gain K_{api}, a gain-scheduled PI-controller is designed as

$$G_{PI}(s) = K_{api} + \frac{1}{T_i s},$$

(5.13)

in which $T_i = 0.07$, and the gain K_{api} is determined as follows. Defining several intervals for the estimated inductance and assigning a single gain K_{api} to each interval, the gain K_{api} can only take predetermined values corresponding to the interval to which $\widehat{L}$ belongs. The intervals are selected based on the network specifications, e.g., the length of the line, locomotives speed, etc. Note that the number of the intervals must be finite, and the last interval must be right-bounded. The reason is that in case of the failure of the identification scheme and the divergence of $\widehat{L}$, the voltage regulation strategy should still be in service. Figure 5.16 shows the block diagram of the GVSS, on which the gain of the PI-controller, i.e., K_{api}, depends on the identified line inductance, i.e., $\widehat{L}$.

In the following, using MATLAB/PLECS, the performance of the GVSS is evaluated. Two scenarios are taken: (i) the aforementioned single-locomotive test scenario and (ii) a new test scenario in which the traction network consists of two locomotives and three substations.

Scenario #1   To schedule the gain of the GVSS, the proposed identification scheme of Chapter 4 is active and identifies the inductance of the line every second through the injection of 50 A (rms) of the 7th harmonic corresponding to $0.035 pu$. Note that the harmonic current is injected for 500 ms in each identification period.

Figure 5.17 (a) depicts the filtered amplitude of the catenary voltage during the travel time span of the locomotive, which is well regulated at the rated value by the GVSS with acceptable performance and zero steady-state error. The dq-components of the locomotive current and
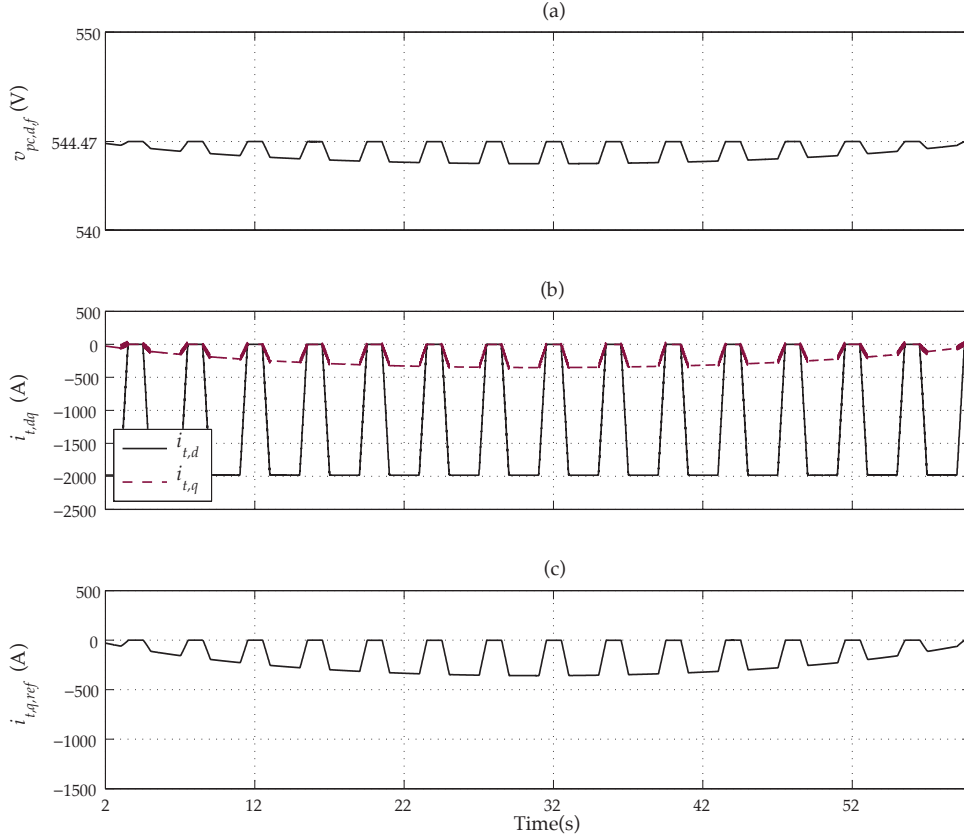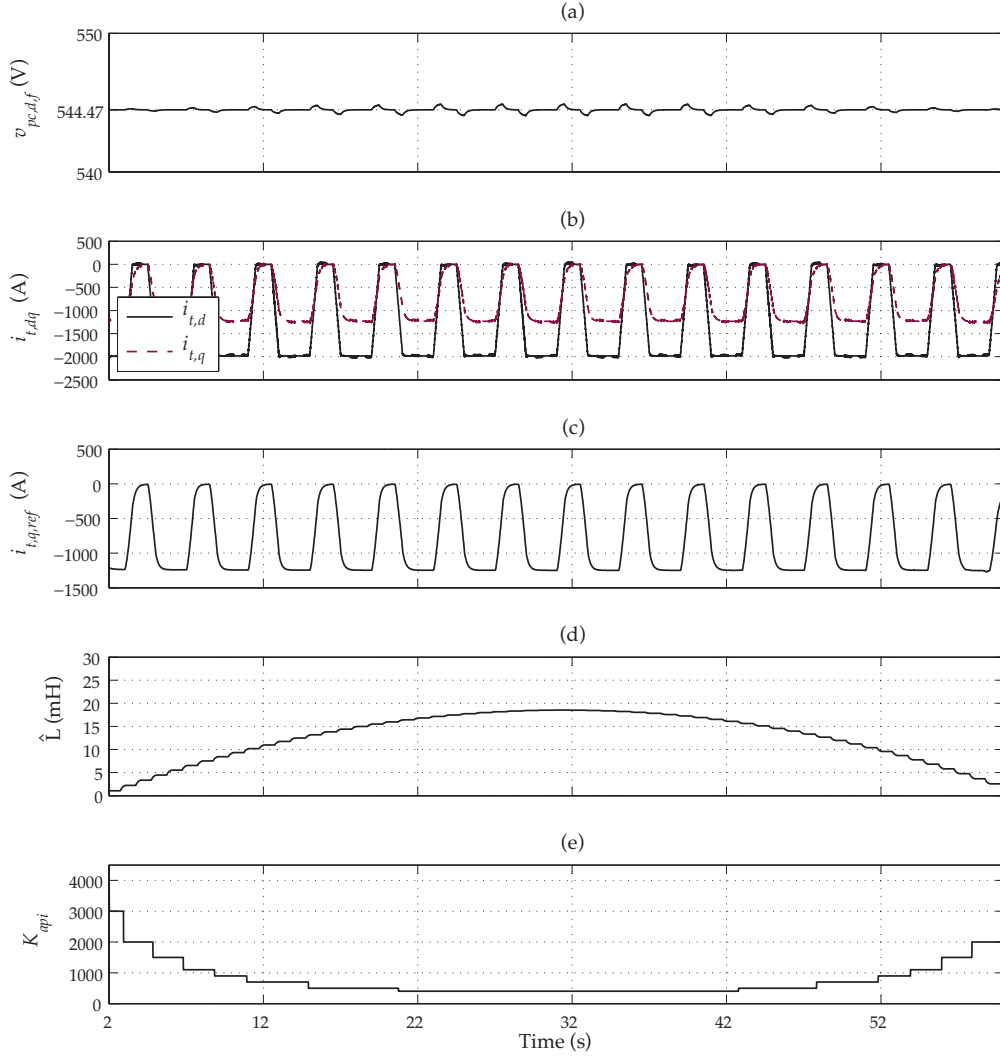
Figure 5.17: The simulation results of the test system of Figure 5.1 in which the locomotive equipped with the GVSS travels from the SS1 to the SS2: (a) the filtered PC voltage amplitude, (b) the dq-components of the locomotive current, (c) the reference value of the locomotive q-component current, (d) the estimated catenary inductance, and (e) the GVSS gain

also the reference signal of the q-component current are shown in Figures 5.17 (b) and (c), respectively. The d-component current rises and falls with a predetermined steepness to resemble the acceleration and deceleration. The injected harmonic current for the identification is also visible in the dq-currents of Figure 5.17 (b). To tune the parameters of the GVSS, the inductance of the line is estimated as shown in Figure 5.17 (d). Using the estimated inductance, the gain of the PI-controller of the GVSS is adaptively scheduled, as depicted in Figure 5.17 (e).
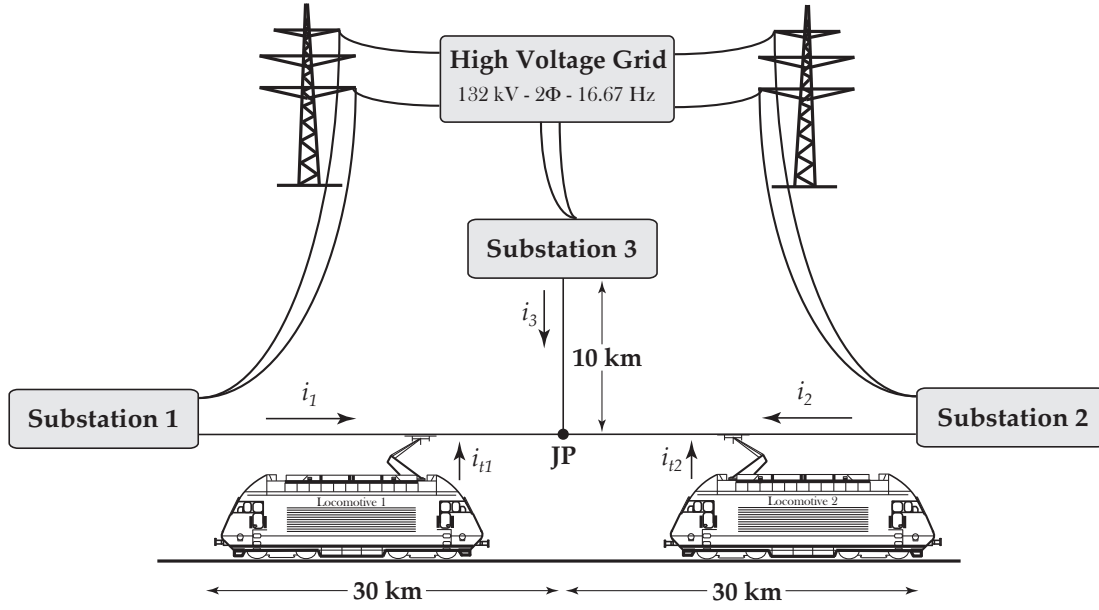
Figure 5.18: The double-locomotive test system

Scenario #2   In order to test the feasibility of the GVSS in more complex systems, a traction network consisting of two locomotives and three substations is assumed as shown in Figure 5.18. Both locomotives are equipped with the proposed voltage support scheme. As shown in Figure 5.18, the lines connecting the SS1 and the SS2 to the Junction Point (JP) are both 30 km long, and the length of the line connecting SS3 to the JP is 10 km. Locomotive 1 and 2 are initially in the proximity of the SS1 and the SS2, respectively. The parameters of the locomotives are the same and are chosen according to Table 4.1.

During the simulation time, Locomotive 1 travels 20 km toward the JP, while Locomotive 2 moves 30 km toward the JP, i.e., its final position is the JP. Similar to the previous single-locomotive test scenario, the locomotives periodically absorb real power to mimic acceleration and deceleration. Figure 5.19 (a) and Figure 5.20 (a) depict the filtered amplitude of the PC voltages of Locomotive 1 and 2, respectively, which are regulated at the reference value with zero steady-state error. Figure 5.19 (b) and Figure 5.20 (b) show the dq-components of the currents of Locomotive 1 and 2, respectively. Moreover, the q-component reference value for the current of Locomotive 1 and 2 are shown in Figure 5.19 (c) and Figure 5.20 (c), respectively. Note that when the locomotives are close to each other, they mutually impact their voltage regulation schemes. However, every locomotive is mainly responsible for compensating for the voltage drop caused by itself. In order not to render the identification process invalid, each locomotive utilizes a unique harmonic frequency to identify the line inductance. Locomotive 1 uses the 7th harmonic while Locomotive 2 adopts the 8th harmonic. Note that each locomotive injects $0.05\,pu$ of harmonic current, which is below the permitted limits. Figure 5.19 (d) and Figure 5.20 (d) show the identified inductances at the connection point of Locomotive 1 and Locomotive 2, respectively. The identified inductances are then used by the locomotives to
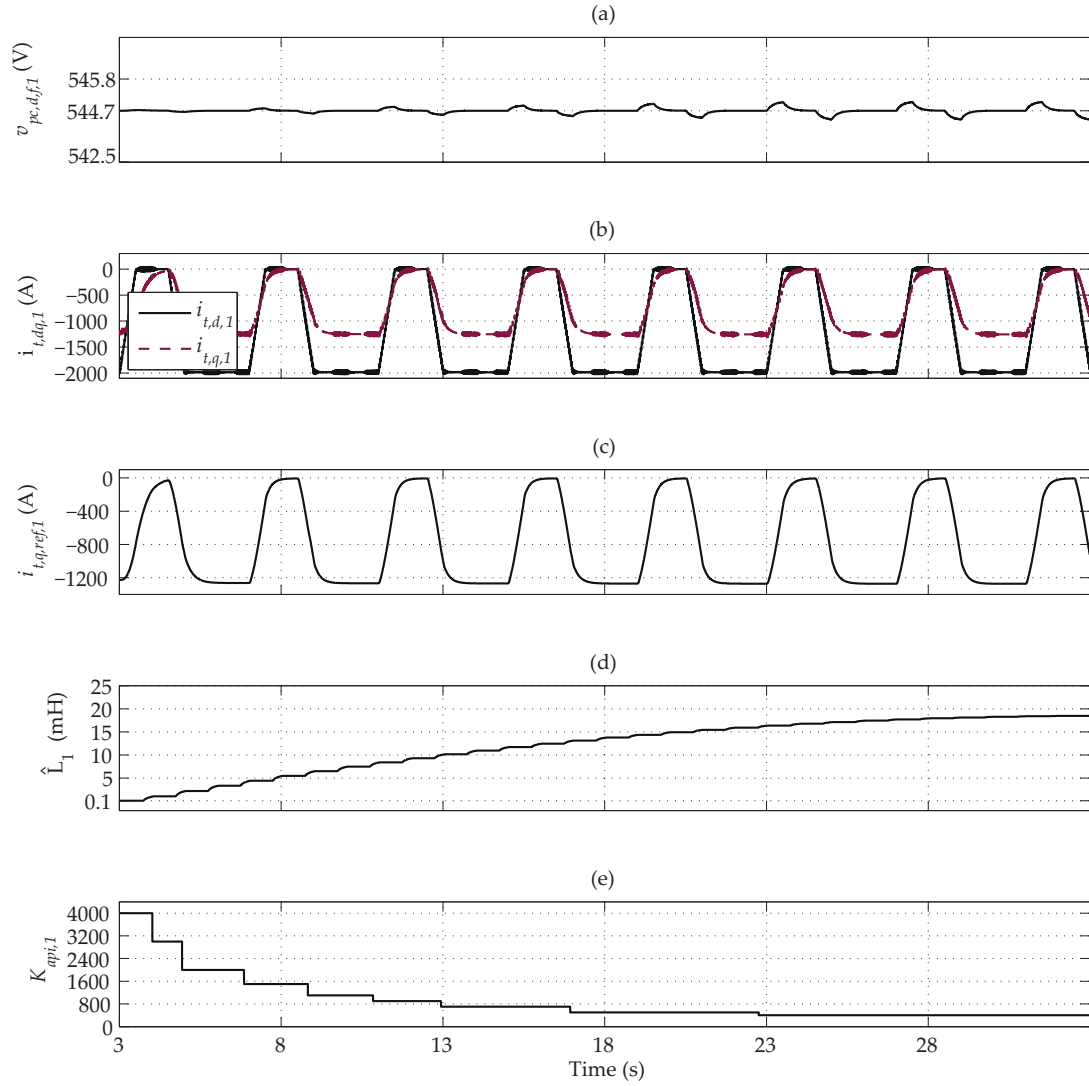
Figure 5.19: The simulation results of Locomotive 1 **in the system of Figure 5.18 equipped with the GVSS: (a) the filtered PC voltage amplitude, (b) the** dq**-components of the locomotive current, (c) the reference value of the locomotive** q**-component current, (d) the estimated catenary inductance, and (e) the GVSS gain**

schedule the gains of their GVSSs responsible for the voltage support. Figure 5.19 (e) and Figure 5.20 (e) show the gains of the GVSSs of Locomotive 1 and 2, respectively.

The presented simulation test studies confirm that the GVSS provides the best dynamic performance among the proposed methods.
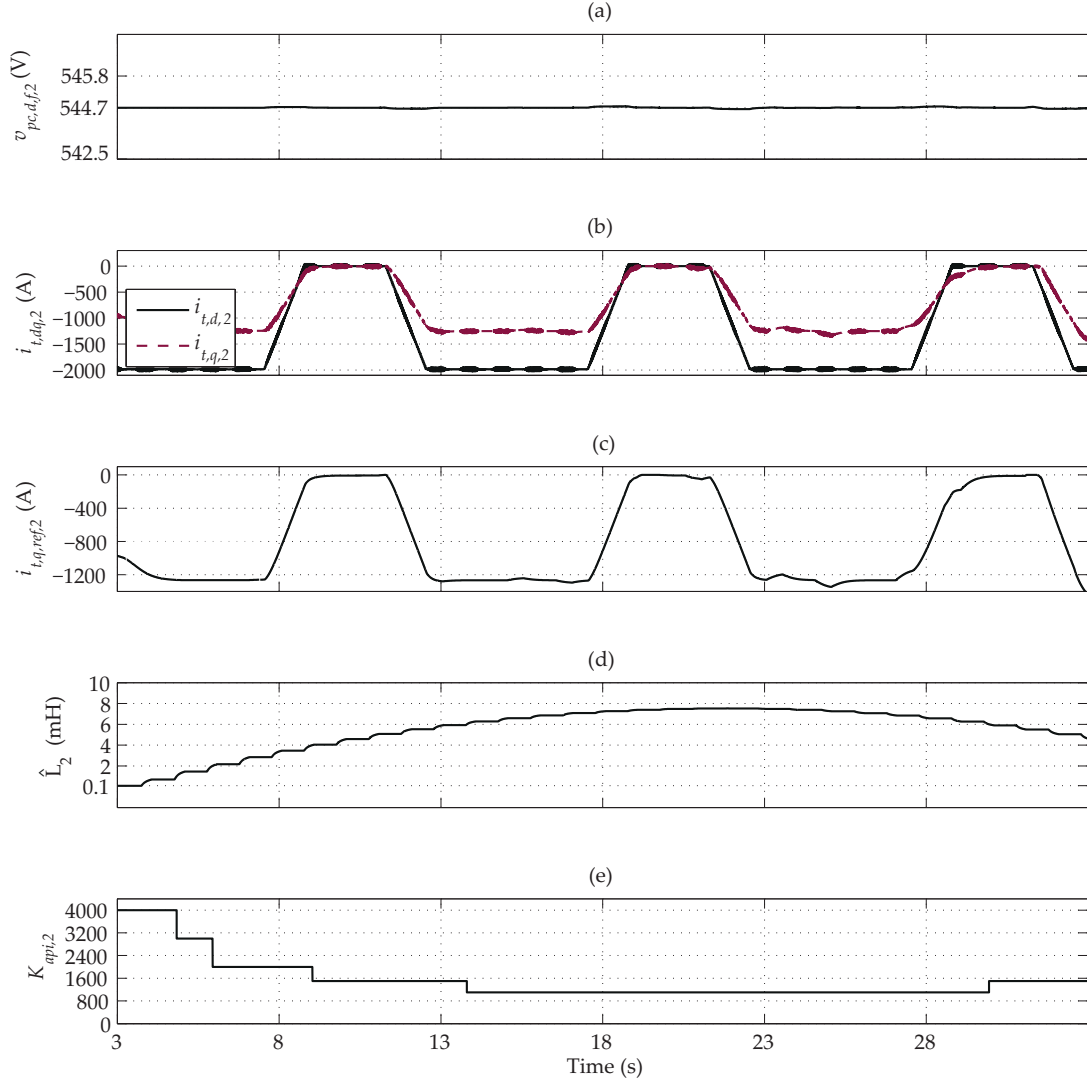
Figure 5.20: The simulation results of Locomotive 2 in the system of Figure 5.18 equipped with the GVSS: (a) the filtered PC voltage amplitude, (b) the dq-components of the locomotive current, (c) the reference value of the locomotive q-component current, (d) the estimated catenary inductance, and (e) the GVSS gain

5.5 Conclusions

The low system-voltage problem is studied in traction networks. Adopting the ALC of modern locomotives, three low system-voltage compensation schemes are also proposed: (i) a P-controller-based method, i.e., PVSS (ii) a PI-controller-based method, i.e., PIVSS, and (iii) a gain-scheduled PI-controller-based method, i.e., GVSS. Among the proposed approaches, the GVSS shows the best performance. In this approach, employing a gain-scheduled PI-controller fed by the voltage error, the compensation scheme injects capacitive reactive power through the current-controlled ALC of locomotives. The gain-scheduling for the PI-controller

is performed through the identification of the line inductance. The identification is carried out by the injection of harmonic frequency current.

The performance of the proposed compensation schemes are evaluated in MATLAB/PLECS environment, and it is concluded that

- among the proposed approaches, the GVSS has the best performance and fully compensate for the voltage drops with acceptable dynamics provided the capacity of the ALC permits,

- the GVSS can also be successfully used in networks consisting of more than one locomotives provided the locomotives are equipped with identification strategies operating at different frequencies.

6

ALC-based Catenary Voltage Support Using High-order Controllers

6.1 Introduction

Among the proposed compensation schemes of Chapter 5, the GVSS provides the best dynamic performance. However, this compensation approach exhibits several shortcomings: (i) it pollutes the network with harmonic currents injected for the identification, (ii) the method is susceptible to errors in the identification, (iii) the method is not easy to implement as it requires additional regulators for harmonic current injection and also extra signal processing efforts for the identification, (iv) the design procedure of the GVSS is not systematic and is based on Ziegler-Nichols method, and therefore, no robustness margin is guaranteed, and (v) sudden changes in the network architecture, e.g., failure of a substation, might destabilize the closed-loop system. The reason of the latter is that upon sudden changes, the parameters of the catenary also suddenly change, which may not be immediately followed by the identification strategy to adapt the parameters of the GVSS.

In this chapter, to overcome the above-mentioned shortcomings, higher-order controllers are utilized to form the secondary control loop, which do not require online tuning and/or modifications. To design such high-order controllers, the nonparametric models of the system for various locomotive positions and system architectures are obtained. Then, using an optimization-based loop shaping approach [63], a high-order controller is designed whose performance for all assumed operating points is satisfactory. In the following, using a simple traction test system, the design procedure of the method is detailed. Then, designing a 5th-order controller, the performance of the proposed method is evaluated in MATLAB/PLECS environment. Moreover, implementing a scaled-down experimental setup, the performance of the method is experimentally evaluated.

The rest of this chapter is structured as follows. Section 6.2 describes the utilized test system and explains the current control strategy used for the locomotive. Section 6.3 presents the
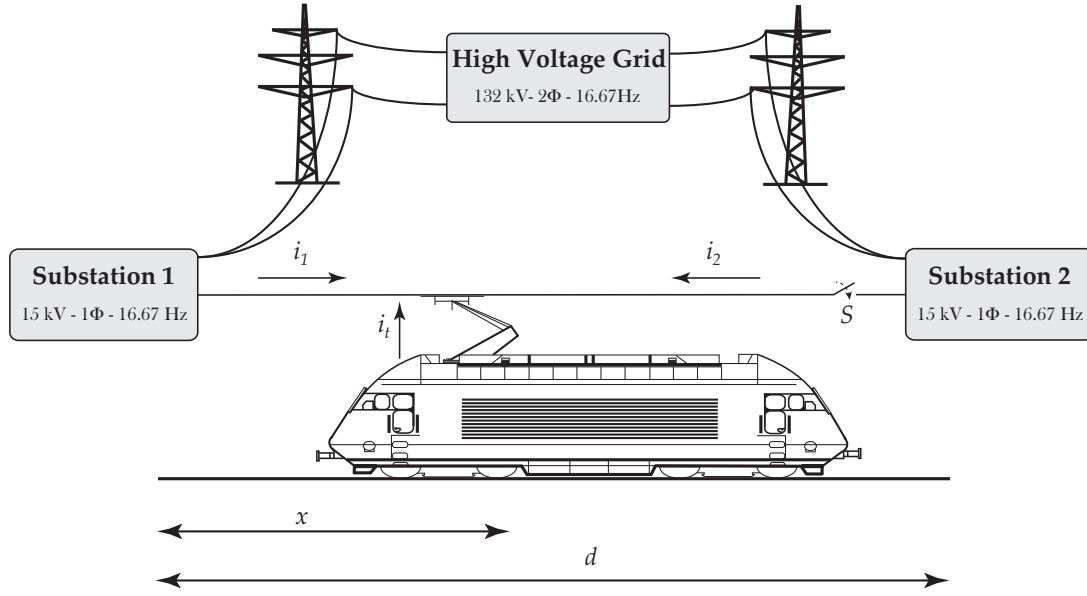
Figure 6.1: A simple traction system consisting of one locomotive and two substations

design procedure of the optimization-based compensation scheme. Section 6.4 evaluates the performance of the designed controller, and Section 6.5 concludes the chapter.

6.2   System Descriptions

In this section, a traction network, based on which the low system-voltage compensation scheme of this chapter is proposed, is explained. A simplified model of the system along with its parameters are also presented. Moreover, the utilized current control strategy of the locomotive is briefly reviewed.

6.2.1   Traction Network

The adopted traction network is an AC single-phase system consisting of two substations connected through a catenary line. The catenary line has an inductive/resistive behavior and can be modeled by an inductor and a resistor. In the utilized system, only one locomotive travels along the line. The architecture of the system is shown in Figure 6.1. Note that Substation2 can be disconnected from the rest of the network by the switch S. This switch is used in the performance evaluation section in order to change the architecture of the system from a two-substation network to a single-substation one.

The simplified schematic diagram of the traction network of Figure 6.1 is depicted in Figure 6.2. The substations are modeled by AC voltage sources, a resistor, and an inductor. The resistor and inductor represent the internal impedance of the substation. The catenary line is modeled by two variable inductors and two variable resistors whose inductance and resistance change

Table 6.1: The parameters of the system of Figure 6.2

Quantity	Value	P.U.	Comment
S_{base}	0.5 MVA	1 pu	Base Value of Locomotive Power
v_{pc}	385 V (rms)	1 pu	Locomotive Nominal Voltage
v_{dc}	840 V		DC Bus Voltage
L_t	0.4 mH	0.14 pu	Leakage Inductance of Transformer
R_t	0.019 Ω	0.06 pu	Resistance of Transformer
n_t	38.961		Transformer Ratio
f_{sw}	2 kHz		PWM Carrier Frequency
f_s	5 kHz		Sampling Frequency
v_{SS}	15000 V (rms)	1 pu	Substation Nominal Voltage
R_s	0.6 Ω	0.0012 pu	Substation Internal Resistance
L_s	8 mH	0.0016 pu	Substation Internal Inductance
ω_n	$2\pi \times 16.67$ rad/s		System Nominal Frequency
R_l	0.08 Ω	0.00016 pu	Line Resistance/km
L_l	1.2 mH	0.00025 pu	Line Inductance/km
d	60 km		Line Length

according to the position of the locomotive. The locomotive is connected to the catenary at the PC through its coupling transformer. The transformer is modeled by an ideal transformer plus its leakage inductance and series resistance. The parameters of the transformer are represented by L_t and R_t. The ALC of the locomotive drive system is implemented by a single-phase IGBT-based inverter whose DC-link consists of an ideal DC source. Since just the control at the AC-side of the line-side converter of the locomotive is of interest of this chapter, the dynamics of the ALC DC-side, including the locomotive motor, is neglected, and the ALC DC-side is implemented by a dc-source. Table 6.1 presents the parameters of the system.

6.2.2 Current Control Strategy of Locomotive

The conventional practice for the ALC of locomotives is utilizing current control schemes for the regulation of the input current, which itself results in the active and reactive power regulation. Various control strategies for the ALCs are proposed in the literature [9, 64–71]. However, the common approaches for the current regulation of single-phase converters are PI-based and PR-based methods [6, 68]. In this chapter, a PI-based current control scheme is adopted for the current regulation that consists of two parts: (i) an FAE, and (ii) a decoupled dq-currents controller, as explained in Chapter 2. Figure 6.2 depicts the block diagram of the adopted control strategy of the locomotive. For the synchronization purposes, a single-phase SOGI-based PLL [77] is adopted. The SOGI PLL generates an orthogonal component for the PC voltage, $v_{pc,\beta}$, and then acts on the PC voltage and its orthogonal component to extract the phase-angle, i.e, θ. The obtained phase-angle is then used for the transformation of the $\alpha\beta$ signals into dq ones or vice versa. Note that if offset is present in the measured PC voltage, a SOGI PLL with offset rejection capability as presented in [91] can be utilized.
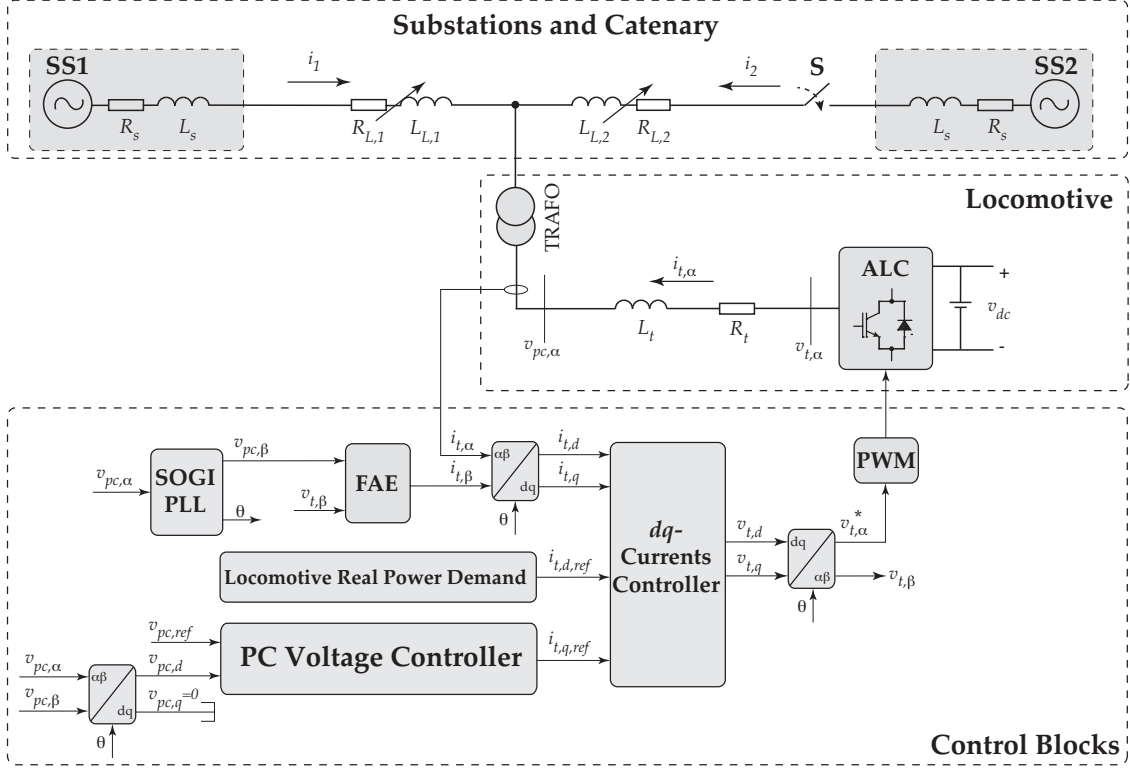
Figure 6.2: The schematic diagram of the traction network

The FAE is responsible for the generation of the required orthogonal component of the current, $i_{t,\beta}$. To generate $i_{t,\beta}$, the difference between the β-component of the control signal, $v_{t,\beta}$, and the β-component of the PC voltage, $v_{pc,\beta}$, is fed to a fictive model of the plant, i.e., $G_s(s) = 1/(L_t s + R_t)$. The converter current and its orthogonal component form the $\alpha\beta$-currents, which are then transferred to a dq-frame. The achieved dq-currents, $i_{t,dq}$, are then fed to the utilized dq-currents controller, which is responsible for the regulation of the converter dq-currents. The outputs of the decoupled dq-currents controller are the dq-components of the control signal, $v_{t,dq}$, which are transformed to an $\alpha\beta$-frame. The α-component, $v_{t,\alpha}$, is fed to the PWM block, while $v_{t,\beta}$ is fed back to the FAE block to generate $i_{t,\beta}$.

The reference values of the dq-currents are determined as follows. The reference value of d-component, $i_{t,d,ref}$, is determined according to the real power demand of the locomotive. Moreover, $i_{t,q,ref}$ is generated through the secondary control loop responsible for compensating for the voltage drop and even over-voltage along the catenary line. In the following, adopting the test system of this section, an Optimization-based Voltage Support Scheme (OVSS) is designed as the secondary loop, which contrary to the approach of Chapter 5, does not need any online modification.

6.3   Optimization-based Voltage Support Scheme - OVSS

The GVSS of Chapter 5 can compensate for the voltage drop along the line, however, it requires online tuning, which results in the pollution of the network. Moreover, the line parameter identification required for adapting the parameters of the GVSS might fail, which results in very poor dynamics. An alternative approach for the compensation is utilizing controllers that are fixed and are not adaptive. However, low-order controllers, e.g., the PVSS and the PIVSS, do not exhibit acceptable dynamic performance for all locomotive positions in the network. Therefore, higher-order controllers must be explored and designed. Designing such controllers is not a trivial task and needs either parametric or nonparametric model of the plant. Since a parametric model of the plant to be controlled is not readily available, one can utilize nonparametric models and design higher-order controllers based on them.

In this section, adopting nonparametric models and convex optimization, the design procedure of a high-order H_∞ controller capable of supporting the PC voltage along the catenary line is detailed. This optimization-based control approach is originally presented in [63] and is basically a SISO version of the design procedure utilized in Chapter 3. The main idea of this method is to minimize the error between a family of the system open-loop transfer functions, i.e., $\mathscr{L} = \{L_i(j\omega); i = 1, ..., m; \forall \omega \in \mathbb{R}\}$, and a desired open-loop transfer function, i.e., $L_D(s)$. Note that in the example of this chapter, $L_i(j\omega) = G_i(j\omega)K(j\omega)$, while $G_i(j\omega)$ and $K(j\omega)$ represent the plant transfer function at the ith position for the locomotive and the controller, respectively. Since shaping the open-loop transfer function does not guarantee the required performance and stability, the minimization is subject to some constraints, which ensure the desired performance and stability of the closed-loop system.

The design procedure of the OVSS consists of three main steps: (i) obtaining the required family of nonparametric models of the system at various locomotive positions, (ii) defining the class of the controller, and (iii) minimizing the summation of the second norm of the errors between the system open-loop transfer functions and a desired open-loop transfer function subject to the constraints ensuring the excellent performance and the stability. In the following, first, the family of the models is derived. Then, the utilized class of controller is explained, and finally, solving the optimization problem subject to some constraints, the optimal coefficients of the controller are determined. Note that the designed controller replaces the *PC Voltage Controller* block of Figure 6.2.

6.3.1   Nonparametric Models

For the PC voltage control strategy of the system of Figure 6.2, the output is the reference value of the q-axis of the locomotive current, i.e., $i_{t,q,ref}$, and the input is the d-component of the PC voltage. Since the adopted PLL forces the q-component of the voltage to zero, the d-component of the PC voltage is equal to its amplitude in steady-state, i.e., $v_{pc,d} = v_{pc,amp}$. Therefore, the transfer function of the system to be controlled is $G(j\omega) = \frac{v_{pc,d}(j\omega)}{i_{t,q,ref}(j\omega)}$. Note that since in traction networks, the PC voltage is normally polluted with various distortions, using

an LPF, $v_{pc,d}$ is filtered to achieve a clean DC signal. In this chapter, a second-order LPF with the cutoff frequency of $100\frac{rad}{s}$ is utilized.

The nonparametric model of the system at the ith position, i.e., $G_i(j\omega)$, is achieved by determining the magnitude and phase of $G_i(j\omega)$ at all frequencies of interest, e.g., frequencies smaller than the system bandwidth. To do so, one can excite the system through applying a PRBS [83] as the input and monitor the output. The PRBS is a sequence of rectangular pulses with random width, which has the properties of a discrete-time white noise (a flat spectrum). In the system of Figure 6.2, exciting $i_{t,q,ref}$ with a PRBS, one can identify $G_i(j\omega)$ as

$$G_i(j\omega) = \frac{\mathscr{F}(v_{pc,d,f})}{\mathscr{F}(i_{t,q,ref})} \tag{6.1}$$

in which $\mathscr{F}$ stands for the Fourier transform, and $v_{pc,d,f}$ is the filtered d-component of the PC voltage. Note that the selection of the PRBS amplitude is of high importance. The reason is that the amplitude must be large enough to sufficiently excite the system, while it does not violate the operating ranges of the system.

To achieve the required family of models $\mathscr{G} = \{G_i(j\omega); i = 1,...,m; \forall \omega \in \mathbb{R}\}$, one can excite the system at various locomotive locations in the network. Note that in the studied system of this chapter, the system transfer function is mainly dependent on the parameters of the catenary line, i.e., its inductance and resistance. Moreover, the resistance is fairly proportional to the inductance. Therefore, at any point in the network, the transfer function is mainly dependent on the inductance seen from the PC. Assuming several typical scenarios for the locomotive position and the switch status, the corresponding nonparametric models are achieved, which form the family of models. The obtained models are similar in pattern and are only different in a gain, which is not frequency dependent. Therefore, one can take the extreme points of the network and derive the corresponding models. The minimum inductance seen by the locomotive is 8 mH, which corresponds to the internal inductance of a typical substation, while the locomotive is very close to one substation. Moreover, assuming the switch S is open, 80 mH is the maximum inductance seen by the locomotive in the network. This value corresponds to the inductance of a 60 km catenary line plus the internal inductance of the substation, while the locomotive is at the end of the line. Thus, the family of models utilized to design the controller consists of two models and is described as follows:

$$\mathscr{G} = \{G_8(j\omega), G_{80}(j\omega); \forall \omega \in \mathbb{R}\}, \tag{6.2}$$

in which G_8 and G_{80} correspond to the model for the inductance of 8 and 80 mH, respectively. The corresponding bode diagrams of G_8 and G_{80} are shown in Figure 6.3. It must be noted that the models are achieved for the points of interest just once, and the locomotives do not require to perform the identification online and during their normal operation.
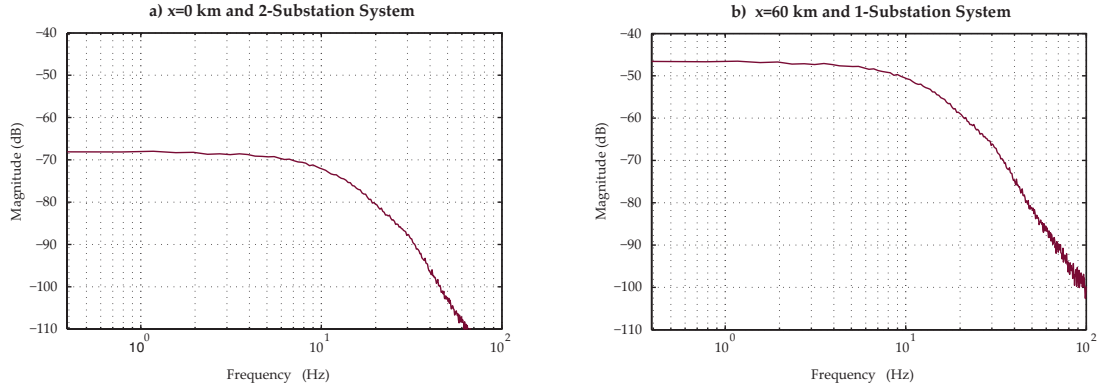
Figure 6.3: The nonparametric models for two locations: (a) $L = 8$ **mH and (b)** $L = 80$ **mH**

6.3.2 Class of Controller

In order to form the open-loop transfer function, in addition to the obtained nonparametric models, the class of the controller to be utilized is needed. Since the controller is implemented in the discrete-time, the class of the controller is defined in z-domain. A generic discrete-time controller in z-domain is of the form of

$$K(z,\rho) = \frac{K_0 + K_1 z^{-1} + K_2 z^{-2} + \cdots + K_n z^{-n}}{1 - z^{-1}} \tag{6.3}$$

in which $\rho = [K_0, K_1, K_2, \ldots, K_n]$. Such a controller includes an integrator, which results in zero steady-state error. The control strategy is then implemented as follows:

$$i_{t,q,ref} = K(z,\rho) \times (v_{pc,ref} - v_{pc,d,f}), \tag{6.4}$$

where $v_{pc,ref}$ is the reference value of the PC voltage. Figure 6.4 depicts the schematic diagram of the controller along with its dedicated low-pass filter, which replaces the *PC Voltage Controller* block of Figure 6.2.

Adopting the obtained nonparametric family of models and the defined controller class, the family of the open-loop transfer functions is

$$\mathscr{L} = \mathscr{G}K(j\omega,\rho) = \{L_8(j\omega), L_{80}(j\omega); \forall \omega \in \mathbb{R}\}. \tag{6.5}$$

$L_8(j\omega,\rho)$ and $L_{80}(j\omega,\rho)$ are linear functions of the controller parameters, ρ. In the following, using convex optimization theory and defining some constraints that guarantee the robustness and the stability of the closed-loop system, the optimal coefficients of the controller, i.e., the elements of ρ, are calculated.

It must be noted that the minimum value for n is dependent on the required dynamics response for the point in which locomotives experience the minimum line inductance and also on the maximum inductance seen by locomotives in the network. The reason is that for the point with the minimum inductance, the controller shows the slowest dynamic response,
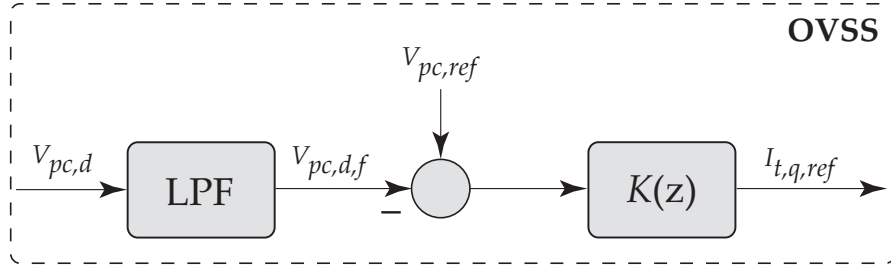
Figure 6.4: The structure of the *PC Voltage Controller* block of Figure 6.2 realized by the OVSS

and therefore, for this point, the controller must be fast enough. Moreover, for the point with the maximum inductance, the controller must be stable. For example, in the studied test system of this chapter, choosing $n = 5$ results in satisfactory dynamic response for $L_{min} = 8$ mH and a stable system for $L_{max} = 80$ mH. Therefore, in the following, $n = 5$.

6.3.3 Loop Shaping and Minimization Problem

Assuming the obtained family of the nonparametric models, shaping their corresponding open-loop transfer functions, $\mathscr{L}$, is performed by minimizing the summation of the second norm of the errors between them and a desired open-loop transfer function, $L_D(s)$. Thus, the OVSS design consists of the following optimization problem:

$$\min_{\rho} \sum_{i=1}^{m} \parallel L_i(\rho) - L_D \parallel^2 . \tag{6.6}$$

Note that in (6.6), m is the number of open-loop transfer functions that form the family $\mathscr{L}$. In this chapter, only two models are assumed, and therefore, $m = 2$. However, in the following, to keep the generality of the discussions, the number of assumed open-loop models is kept at m.

The primary goal of the OVSS is showing satisfactory dynamic performance and zero steady-state error. Therefore, a reasonable desired open-loop transfer function is as follows:

$$L_D(s) = \frac{\omega_c}{s} . \tag{6.7}$$

Manipulating ω_c in (6.7), one can achieve the required dynamic performance, e.g., the system bandwidth. Moreover, to guarantee the robustness of the system, one can shape the closed-loop sensitivity function of each model, i.e, $S_i = (1 + L_i)^{-1}$, using the following constraints:

$$W_1(j\omega)S_i(j\omega) < 1 \quad \forall \omega \in \mathbb{R} \text{ and } i = 1,...,m, \tag{6.8}$$

in which $W_1(j\omega)$ is a weighting filter. This is an H_∞ performance condition that guarantees the robustness of the system [73]. The set of constraints given in (6.8) is non-convex. Reference [63]

approximates the set of constraints of (6.8) by the following linear and convex set as follows:

$$|W_1(j\omega)[1 + L_D(j\omega, \rho)]| - \mathcal{R}e\{[1 + L_D(-j\omega)][1 + L_i(j\omega, \rho)]\} < 0$$
$$\forall \omega \in \mathbb{R} \text{ and } i = 1, ..., m. \tag{6.9}$$

Note that the adopted weighting filter is $W_1(j\omega) = 0.5$. This value guarantees a gain margin of at least 2 and a phase margin of greater than 29 degrees [72]. Considering the constraints for the desired performance, as shown in (6.9), the controller design is summarized into the following optimization problem:

$$\min_{\rho} \sum_{i=1}^{m} \parallel L_i(\rho) - L_D \parallel^2,$$

subject to

$$|W_1(j\omega)[1 + L_D(j\omega, \rho)]| - \mathcal{R}e\{[1 + L_D(-j\omega)][1 + L_i(j\omega, \rho)]\} < 0 \tag{6.10}$$
$$\forall \omega \in \mathbb{R} \text{ and } i = 1, ..., m.$$

The optimization problem of (6.10) is referred to as SIP problem, since it has infinite number of constraints and finite number of variables. To solve such problems, one can neglect the frequency points beyond a threshold, ω_{max}, e.g., the Nyquist frequency for discrete systems, and utilize the gridded frequency interval $[0\ \omega_{max}]$. Therefore, the number of the constraints is also finite, which results in a SDP problem. Such problems are solved by standard SDP-solvers, e.g., SeDuMi [74].

Choosing N linearly spaced frequencies in the interval $[0\ \omega_{max}] \in \mathbb{R}$, the quadratic objective function is approximated by

$$\sum_{i=1}^{m} \parallel L_i(\rho) - L_D \parallel^2 \approx \sum_{i=1}^{m} \sum_{\omega} \parallel L_i(j\omega, \rho) - L_D(j\omega) \parallel_F \tag{6.11}$$

where $\|.\|_F$ is the Frobenius norm. Therefore, the OVSS design is summarized into the following convex optimization problem:

$$\min_{\rho} \sum_{i=1}^{m} \sum_{k=1}^{N} \parallel L(j\omega_k, \rho) - L_D(j\omega_k) \parallel_F,$$

subject to

$$|W_1(j\omega_k)[1 + L_D(j\omega_k)]| - \mathcal{R}e[1 + L_D(-j\omega_k)][1 + L_i(j\omega_k, \rho)] < 0$$
$$\text{for } k = 1, \ldots, N \text{ and } i = 1, ..., m. \tag{6.12}$$

6.4   Performance Evaluation

In this section, the performance of the OVSS is evaluated by using (i) two simulated test systems in MATLAB/PLECS environment and (ii) a scaled-down experimental setup. For the simulation part, the system of Figure 6.1 and a multi-locomotive system are simulated in MATLAB/PLECS environment. For the experimental part, a scaled-down system according to that of Figure 6.1 is implemented, which has only one substation, i.e., the switch S is open.

6.4.1   Simulation Results

In the simulation part, to design the OVSS, the two extreme points in the network, whose associated bode diagrams are depicted in Figure 6.3, are assumed. Taking the procedure detailed in the previous sections, a 5th-order controller for the catenary voltage support is designed. Assuming a desired open-loop transfer function $L_D(s) = \frac{30}{s}$, the designed controller is as follows:

$$K_{5^{th}} = \frac{K_0 + K_1 z^{-1} + K_2 z^{-2} + K_3 z^{-3} + K_4 z^{-4} + K_5 z^{-5}}{1 - z^{-1}}, \tag{6.13}$$

where, $K_0 = -0.99036e6$, $K_1 = 2.49542e6$, $K_2 = -1.71387e6$, $K_3 = 0.01908e6$, $K_4 = 0.07289e6$, and $K_5 = 0.11683e6$.

To evaluate the performance of the OVSS, two test scenarios are defined. The first scenario adopts the test system of Figure 6.1 and evaluates the performance of the proposed controller in a single-locomotive network. Moreover, utilizing a multi-locomotive traction network, as shown in Figure 6.6, and equipping all locomotives with the proposed controller, the effectiveness of the method in more sophisticated networks is validated. The parameters of both systems are set according to Table 6.1. It must be noted that due to the limitations of the simulation software, the locomotive speeds in the conducted simulation tests are not realistic and are up to ten times more than maximum speed of normal locomotives. However, such unrealistic speeds do not affect the validity of the analysis and just impose harsher conditions to the controller in terms of variations in the network parameters.

6.4.1.1   Single-locomotive System

In the system of Figure 6.1, the locomotive is initially at rest absorbing no real and reactive power and is situated close to Substation1, while the switch S is closed. At time instant
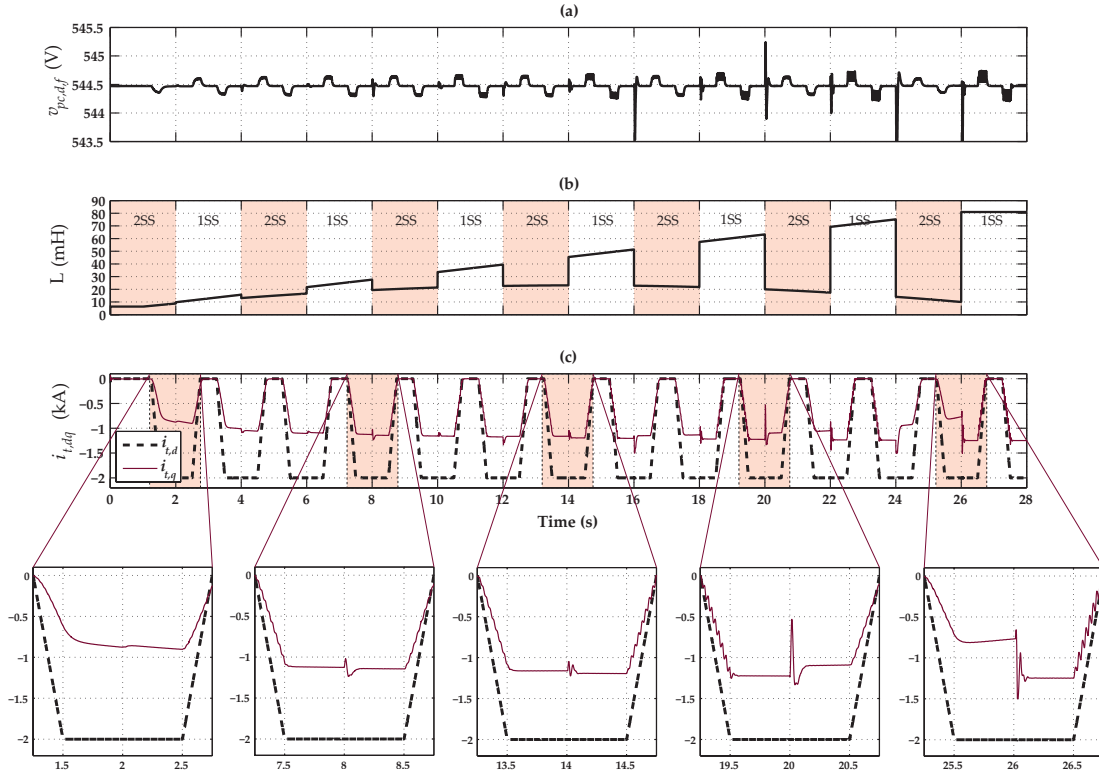
Figure 6.5: The simulation results of the single-locomotive system of Figure 6.1 in which the locomotive travels from the SS1 to the SS2 and the OVSS is in service: (a) the filtered amplitude of the locomotive voltage, (b) the inductance of the line seen by the locomotive, and (c) the dq-components of the locomotive current

$t = 0.25$ s, the locomotive starts traveling along the line toward Substation2. Note that during the locomotive travel time span, it periodically absorbs the d-component of the current, which results in the absorption of real power. Furthermore, the switch S is periodically opened and re-closed during the locomotive travel to mimic Substation2 tripping out and reconnection. That is, when the switch S is closed, the network is a two-substation network, and when the switch S is open, the system of Figure 6.1 is a single-substation network. Moreover, during the locomotive travel, the OVSS is in service and injects the required reactive power for the voltage support.

Figure 6.5 (a) depicts the filtered PC voltage amplitude that is regulated at the rated value, i.e., 544.5 V, during the locomotive travel time span by the 5th-order compensator. However, note that subsequent to each change in $i_{t,d,ref}$, a negligible transient period is experienced in the PC voltage amplitude, which corresponds to the controller response time. Figure 6.5 (b) shows the catenary line inductance seen by the locomotive from the PC, which varies according to the position of the locomotive and the status of the switch S. Figure 6.5 (c) shows the dq-components of the locomotive current. The d-component periodically increases/decreases to resemble locomotive acceleration/deceleration. Upon each reference change in the d-axis, the q-axis is manipulated by the OVSS to compensate for the voltage drop/over-voltage.
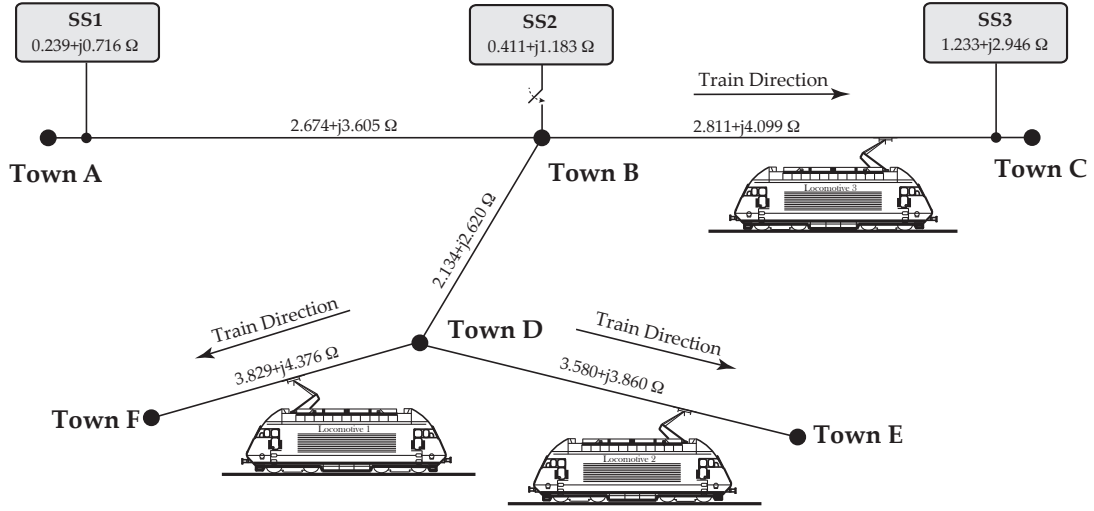
Figure 6.6: The schematic diagram of a multi-locomotive traction network

The zoomed versions of several intervals during the locomotive movement are also shown. The zoomed versions show that the 5th-order OVSS has various response times in various locations, and the controller response time is inversely proportional to the inductance seen by the locomotive. However, the controller is able to stabilize the system for all scenarios, which confirms that there is no need for any online tuning, identification, etc. Note that thanks to the decoupled dq-currents controller, the transients of the d-component (q-component) of the ALC current have no impacts on its q-component (d-component).

6.4.1.2 Multi-locomotive System - A More Realistic Scenario

In this section, the performance of the OVSS in a multi-locomotive traction network, as shown in Figure 6.6, is evaluated. In order to mimic the limitations of a practical scenario, the current limitations of the ALC is taken into account. It is assumed that the apparent power of each ALC is limited to $S_{max} = 1.25$ MVA, as depicted in Figure 6.7. Moreover, in the control strategy of the ALC, the priority is always given to the active power. That is, the maximum injectable reactive power at any instant is determined according to the real power consumption at that instant. Therefore, at any instant the maximum injectable reactive power is $Q_{max}(t) = \sqrt{S_{max}^2 - P(t)^2}$.

As shown in Figure 6.8, locomotives are allowed to operate with full power capacity in a range of the PC voltage. Therefore, it is more beneficial to regulate the PC voltage in a given interval around the rated value, e.g., $V_{pc} = [15kV - \epsilon_1 \quad 15kV + \epsilon_2]$. In such a case, less reactive power is needed to keep the PC voltage in the assumed interval. In the multi-locomotive scenario, while $v_{pc} < 15kV - \epsilon_1$ ($v_{pc} > 15kV + \epsilon_2$,), the OVSS is active and its reference value is $15kV - \epsilon_1$ ($15kV + \epsilon_2$). Moreover, while the PC voltage is within the interval, the OVSS is inactive and is in anti-windup mode. Furthermore, while the anti-windup mode is active, the output of the OVSS is gradually forced to zero, in order not to inject unnecessary reactive power.
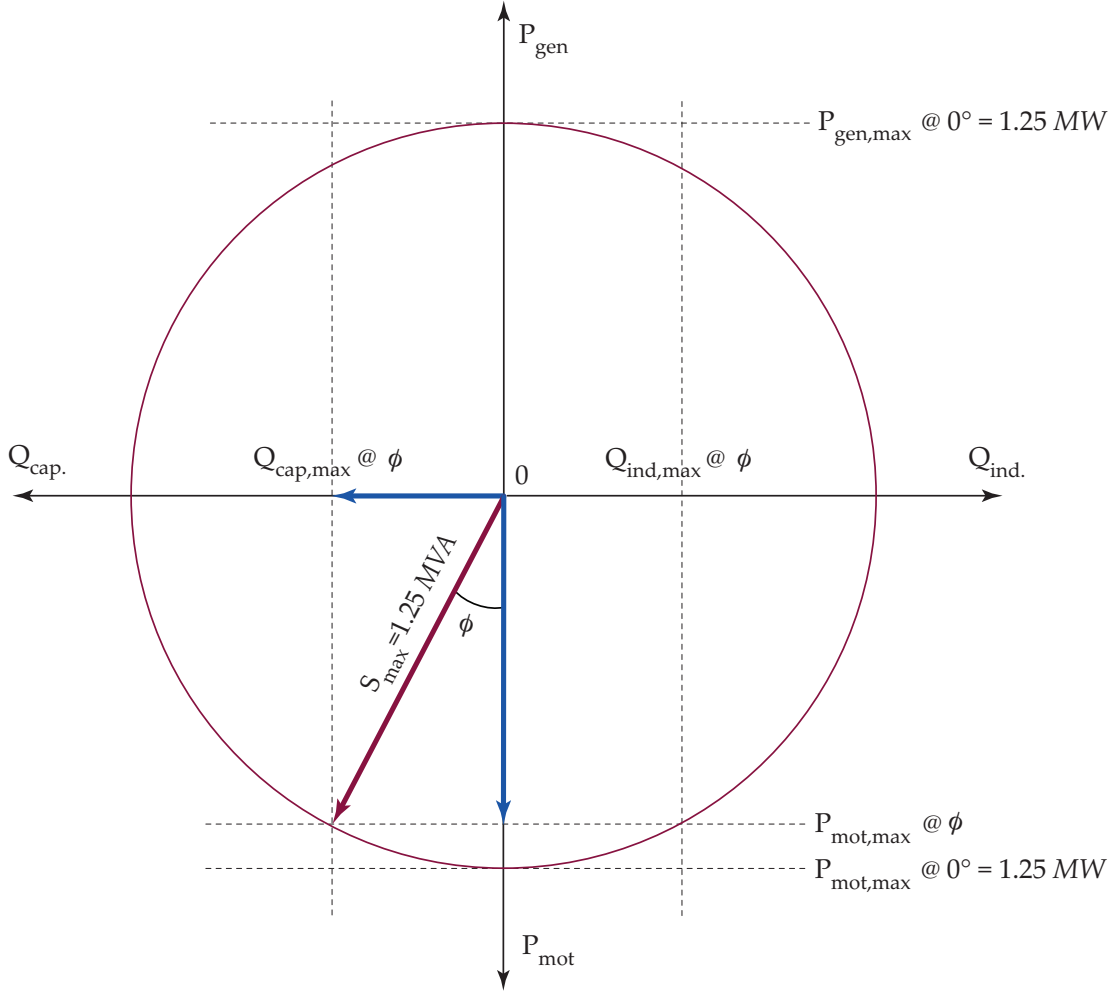
Figure 6.7: The ALC power capacity

It must be noted that other limitations also exist in the control strategy of commercial locomotives and can be taken into account in order to limit the maximum injectable reactive power. However, each supplier of traction converters has its own design approach and consequently its own current limitations, and therefore, discussing other limitations are out of scope of this chapter.

In the multi-locomotive system of Figure 6.6, initially, Locomotive 1 and Locomotive 2 are in Town D, and Locomotive 1 is in Town B. At time instant $t = 1\ s$, Locomotive 1 and Locomotive 2 start traveling toward Town F and Town E, respectively, and Locomotive 3 starts traveling toward Town C. During their travel time span, the locomotives periodically absorb and regenerate real power, to mimic acceleration and braking. Moreover, their 5th-order OVSSs are active, and inject proper amount of reactive power to maintain the voltages at the connection points of the locomotives to the network within $v_{pc} = [15kV - 300V \quad 15kV + 300V]$. Moreover, Substation2 is connected and disconnected during the travel time span of the locomotives, as shown in Figure 6.9.
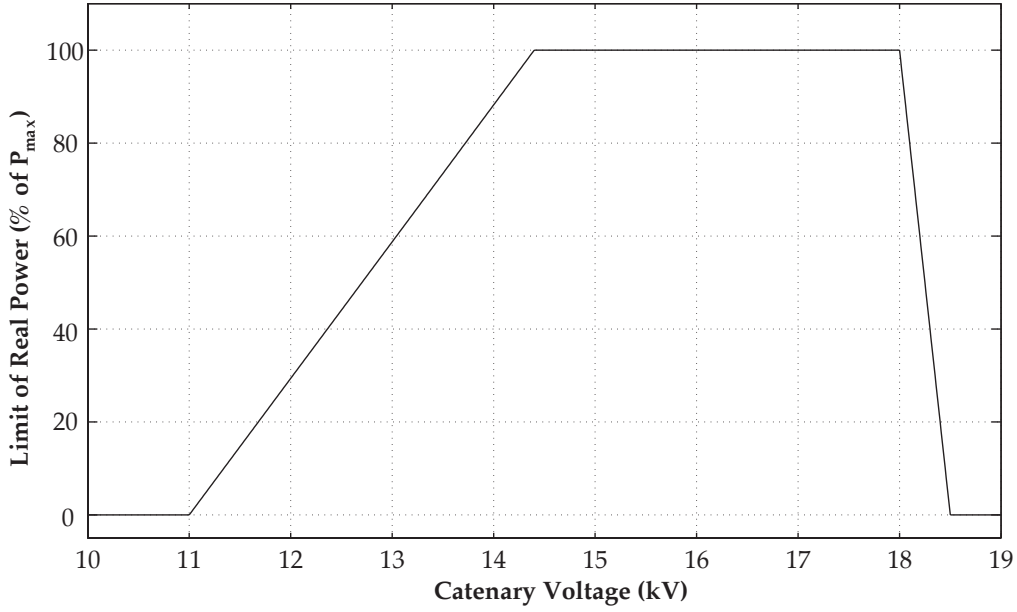
Figure 6.8: The ALC power limits versus the catenary voltage

Figures 6.9 (a), (c), and (e) depict the catenary filtered voltages at the connection points of Locomotive 1, 2, and 3, respectively, which are all well maintained within the assumed interval. Moreover, Figures 6.9 (b), (d), and (f) show the dq-components of the currents of Locomotive 1, Locomotive 2, and Locomotive 3, respectively. Note that since Locomotive 3 is traveling in the electrical proximity of two substations, its voltage is less affected by its real power absorption/regeneration. Therefore, as shown in Figures 6.9 (e) and (f), at the connection point of Locomotive 3, the catenary is maintained within the pre-specified limits with no reactive power injection. However, Locomotive 1 and 2 must inject reactive power to maintain their voltage within the interval. Moreover, note that the current limitation of Locomotive 1 is reached after $t = 11$ s and therefore, the set-point of the q-component of the current is saturated at -2500 A for 0.7 s. The same happens for Locomotive 2 after time instant $t = 10.9$ s for 0.8 s.

To show the improvement achieved by the OVSS, a similar test for the multi-locomotive network of Figure 6.6 is conducted in which no OVSSs are in service. Figures 6.10 (a), (b), and (c) depict the catenary voltages at the connection point of Locomotive 1, 2, and 3, respectively, to the network, which are not within the assumed interval during the travel time spans of the locomotives.

6.4.2 Experimental Results

To experimentally evaluate the performance of the OVSS, a scaled-down version of the test system is implemented. The test system of Figure 6.11 is adopted, and it is assumed that the

Figure 6.9: The simulation results of the multi-locomotive system of Figure 6.6 while the OVSSs of all locomotives are in service: (a) the filtered catenary voltage at the connection point of Locomotive 1, (b) the dq-components of the Locomotive 1 current, (c) the filtered catenary voltage at the connection point of Locomotive 2, (d) the dq-components of the Locomotive 2 current, (e) the filtered catenary voltage at the connection point of Locomotive 3, (f) the dq-components of the Locomotive 3 current

system consists of only one substation, i.e., the switch S is always open. The parameters of the implemented test system are selected according to Table 6.2. To design the OVSS for the experimental test system, two extreme points are identified, i.e., the operating point very close to the substation and the operating point at the end of the line. Then, assuming $L_D(s) = \frac{30}{s}$, the optimization problem of (6.12) is solved, and the coefficients of the 5th-order controller are determined as $K_0 = -7.95930e3$, $K_1 = 19.78095e3$, $K_2 = -13.11031e3$, $K_3 = 0.00000e3$, $K_4 = -0.00000e3$, and $K_5 = 1.28865e3$. Figure 6.11 depicts a photo of the experimental setup.
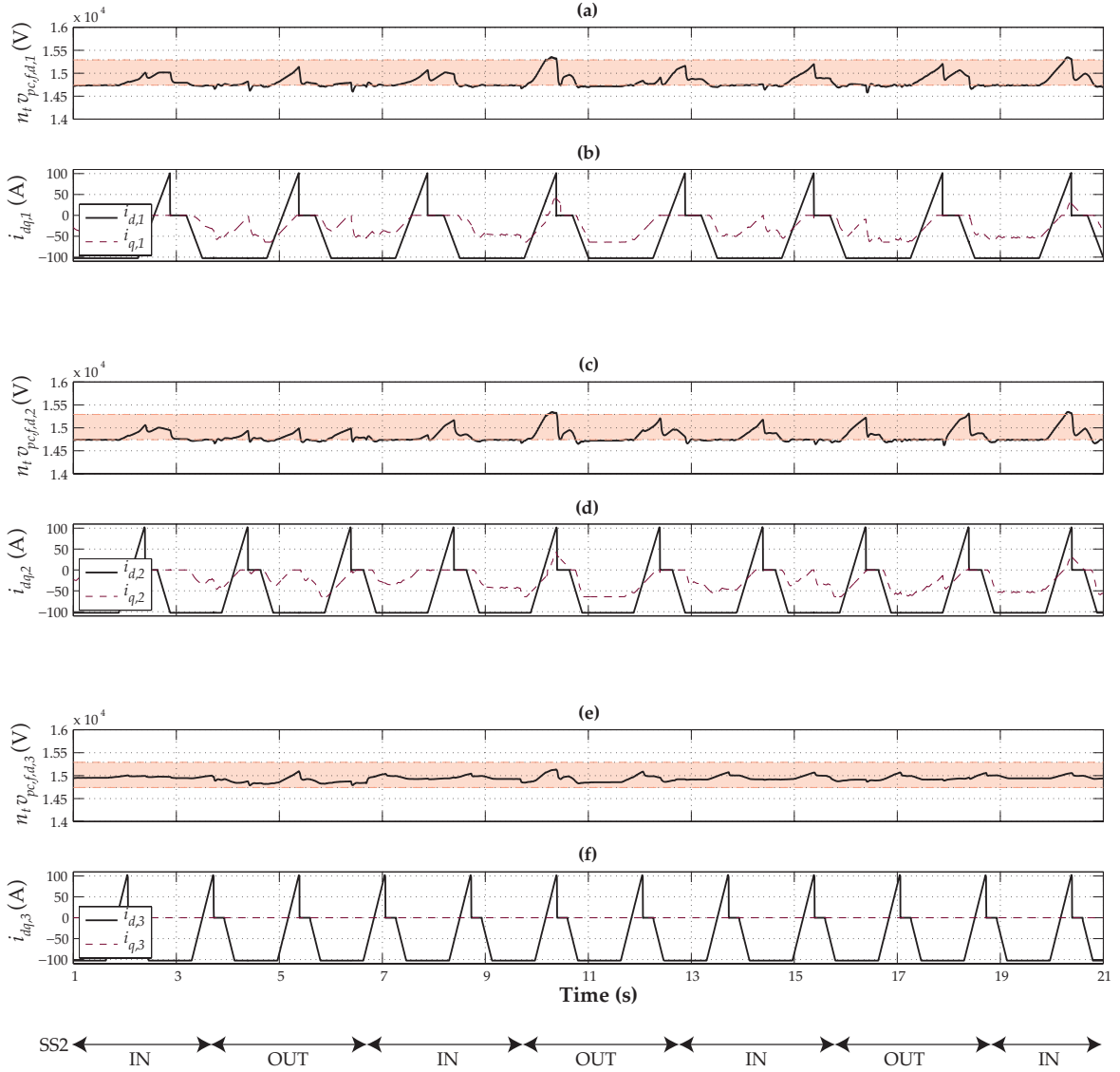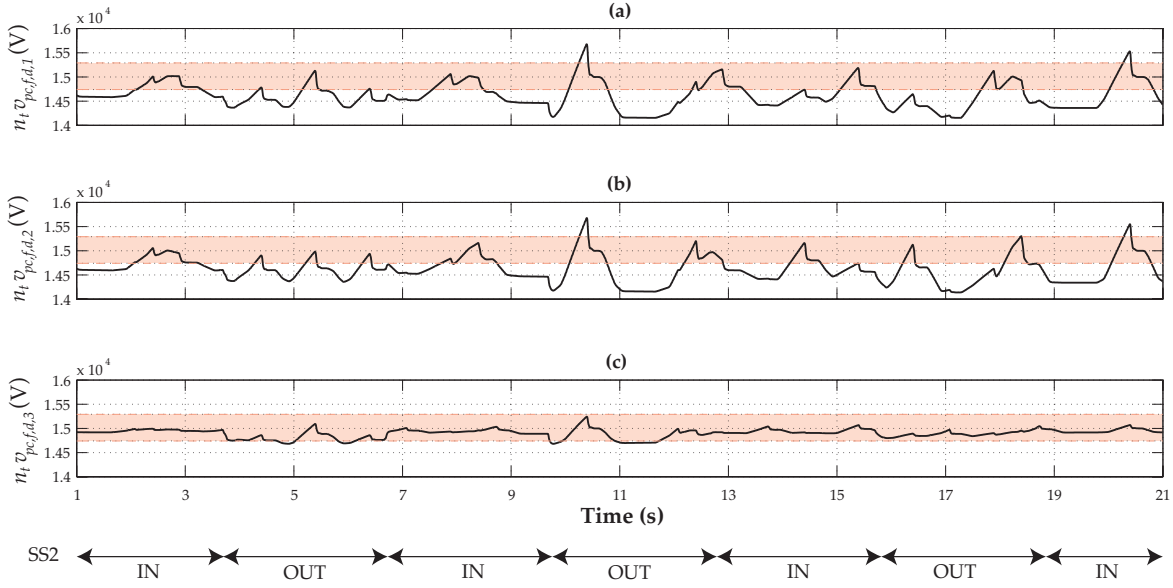
Figure 6.10: The simulation results of the multi-locomotive system of Figure 6.6 while the OVSSs are not in service: (a) the filtered amplitude of the Locomotive 1 PC voltage, (b) the filtered amplitude of the Locomotive 2 PC voltage, and (e) the filtered amplitude of the Locomotive 3 PC voltage

Note that to implement the substation, a PWM converter connected to an LC filter is adopted that utilizes a PR-controller [92] to regulate its output voltage at the rated value. However, the details of the adopted voltage control strategy of the substation are out of the scope of this chapter and are not further discussed.

To implement the control strategies and signal processing algorithms of the locomotive, an FPGA-based controller, which provides a C programming environment, is used. The adopted FPGA is XC4010PC84 FPGA manufactured by XILINX. The control and signal processing algorithms are first discretized using the bilinear method and then developed into C codes. It should be noted that in order to achieve perfect isolation between the power and control circuits, optic-based gate drivers are adopted for driving IGBTs

For the experimental performance evaluation, two test scenarios are assumed: (i) the d-component of the current gradually increases/decreases to mimic the locomotive acceleration/deceleration and (ii) the substation voltage is changed suddenly to mimic sudden drop in the network voltage. These tests are conducted for two extreme points in the network, i.e., (i) close to the substation and (ii) at the end of the line.

6.4.2.1 Locomotive Acceleration/Deceleration

In this test, the performance of the OVSS during and subsequent to changes in the reference value of the d-component of the locomotive current is evaluated. The reference value of

Table 6.2: The parameters of the scaled-down experimental setup of Figure 6.11

Quantity	Value	P.U.	Comment
S_{base}	150 VA	1 pu	Base Value of Locomotive Power
v_{pc}	30 V (peak)	1 pu	Locomotive Nominal Voltage
v_{dc}	100 V		DC Bus Voltage
L_t	27 mH	0.9 pu	Inductance of Locomotive Filter
R_t	1 Ω	0.33 pu	Resistance of Locomotive Filter
n_t	3		Transformer Ratio
f_{sw}	10 kHz		PWM Carrier Frequency
f_s	10 kHz		Sampling Frequency
v_{SS}	90 V (rms)	1 pu	Substation Nominal Voltage
R_s	0.6 Ω	0.023 pu	Substation Internal Resistance
L_s	8 mH	0.029 pu	Substation Internal Inductance
ω_n	$2\pi \times 16.67$ rad/s		System Nominal Frequency
R_l	0.08 Ω	0.00296 pu	Line Resistance/km
L_l	1.2 mH	0.00456 pu	Line Inductance/km
d	60 km		Line Length
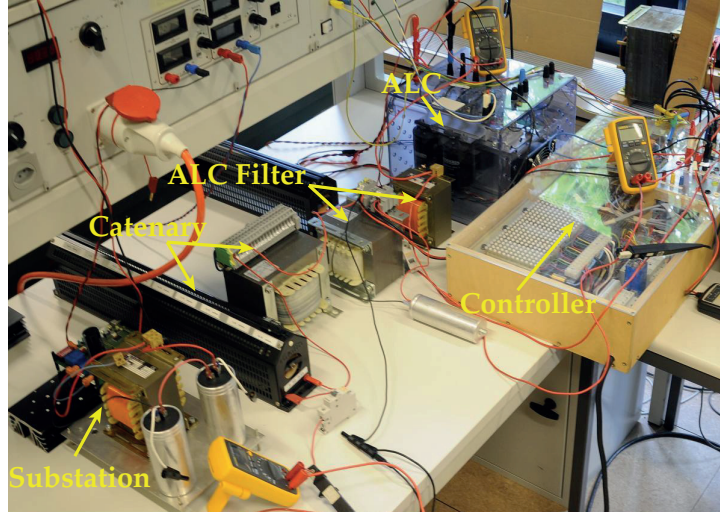
Figure 6.11: The experimental setup

the d-component of the current is initially zero, and at time instant $t = 0.2$ s, $i_{t,d,ref}$ starts decreasing with a slope of 16 $\frac{A}{s}$, and is saturated at $i_{t,d,ref} = -8$ A. 0.5 s after the saturation, $i_{t,d,ref}$ increases with the same slope and reaches zero. During the d-axis reference current change, the OVSS is active and injects proper amount of reactive power to maintain the voltage at its rated value.

Locomotive Close to the Substation   The locomotive is close to the substation and the inductance between the PC and the substation is 8 mH, which corresponds to the internal inductance of the substation. $i_{t,d,ref}$ changes according to the aforementioned scenario, and
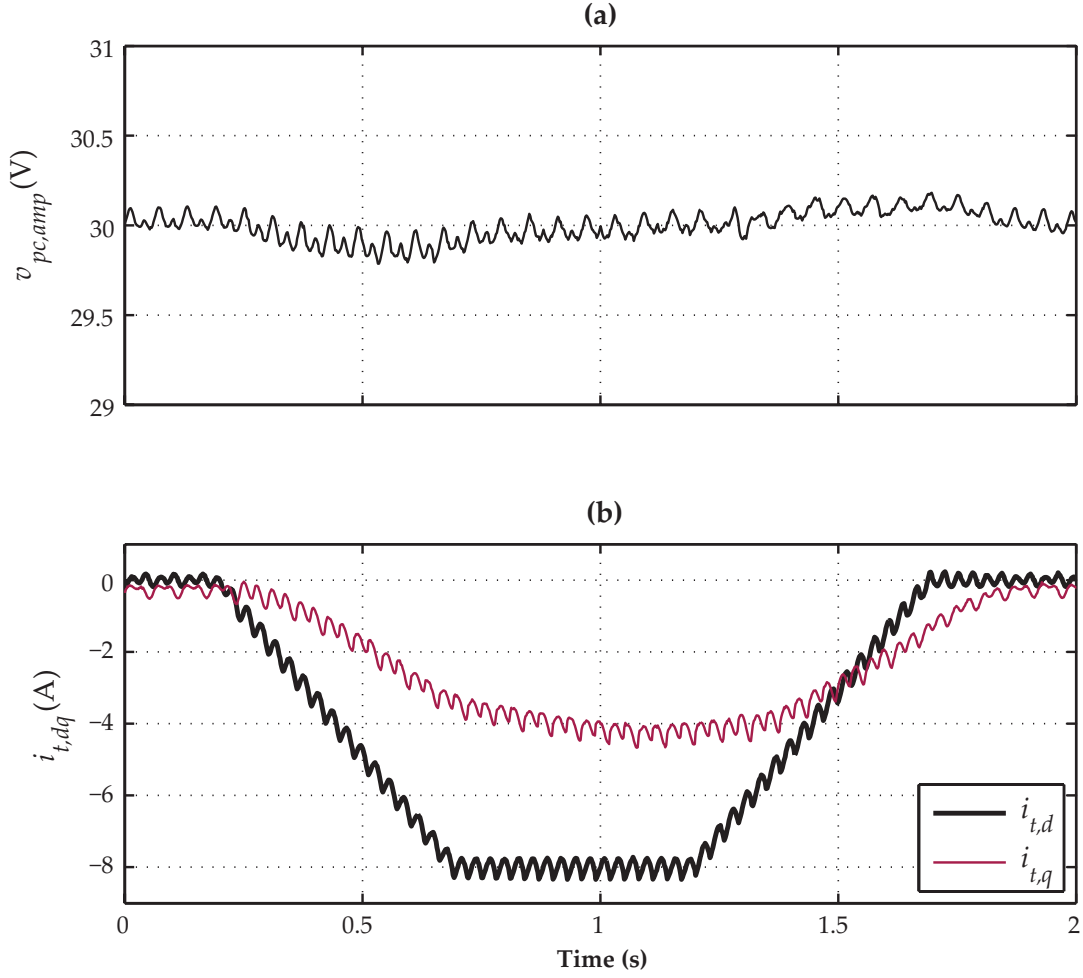
Figure 6.12: The experimental results of the system of Figure 6.11 during and subsequent to changes in the reference value of $i_{t,d}$ while the locomotive is close to the substation and the OVSS is in service: (a) the amplitude of the PC voltage and (b) the dq-components of the current

the OVSS injects the required reactive power. Figure 6.12 (a) shows the amplitude of the PC voltage, which is maintained at the rated value. Figure 6.12 (b) depicts the dq-currents of the locomotive.

Locomotive at the End of the Line   The locomotive is situated at the end of the catenary line, and the same test is conducted. The inductance between the PC and the substation is 80 mH. Figure 6.13 (a) shows the amplitude of the PC voltage that is regulated at its rated value. The dq-components of the locomotive current are also shown in Figure 6.13 (b). Note that the OVSS response time in this test is less than that of the previous test.

Figure 6.12 and Figure 6.13 show that the OVSS is able to regulate the PC voltage at the rated value for various locations of the locomotive. However, the response time of the controller for
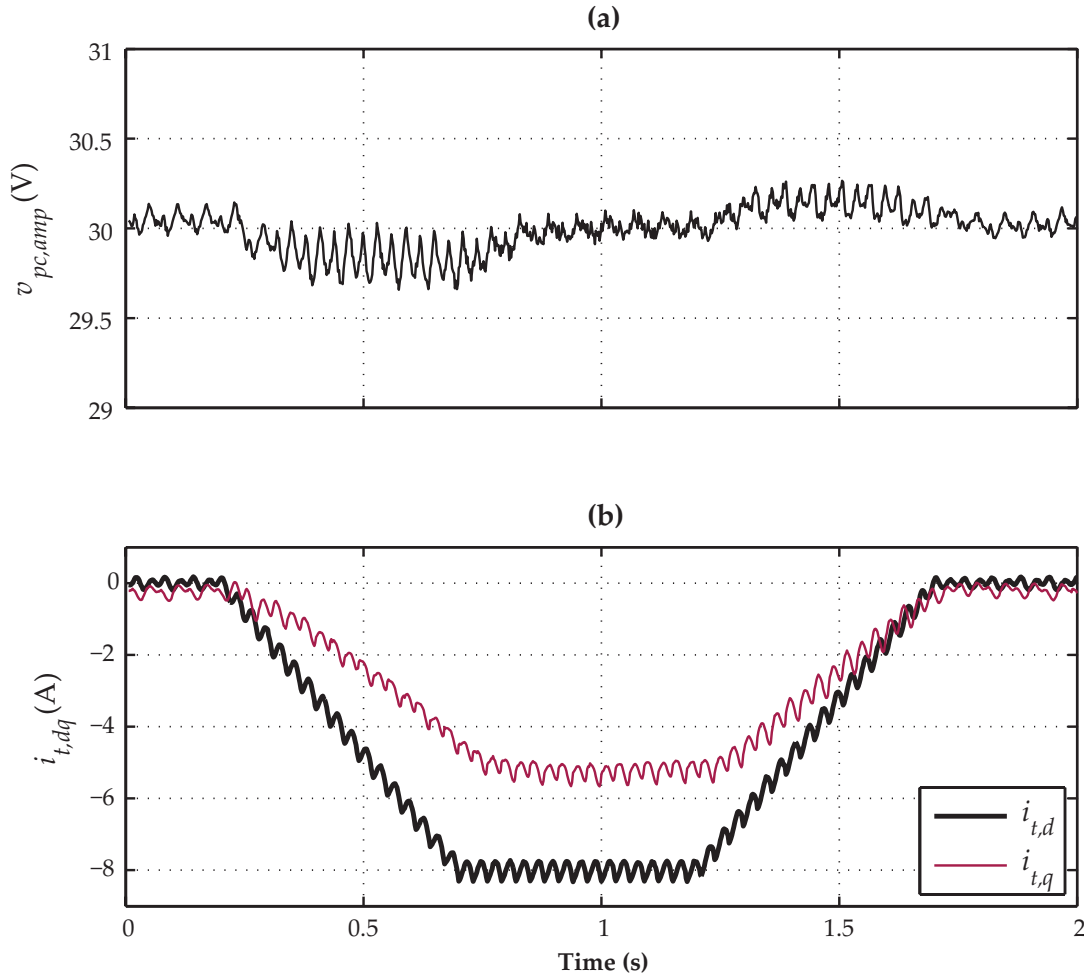
Figure 6.13: The experimental results of the system of Figure 6.11 during and subsequent to changes in the reference value of $i_{t,d}$ while the locomotive is far from the substation and the OVSS is in service: (a) the amplitude of the PC voltage and (b) the dq-components of the current

various locations, i.e., various line inductance amounts, differs.

6.4.2.2 Substation Voltage Drop

In this test, the performance of the OVSS in terms of maintaining the voltage subsequent to sudden drop in the substation voltage is evaluated. The test is conducted for two locomotive positions in the network: (i) close to the substation and (ii) at the end of the line. Note that for both tests, the amount of the voltage drop is selected such that the required amount of reactive power for compensation is -120 var.
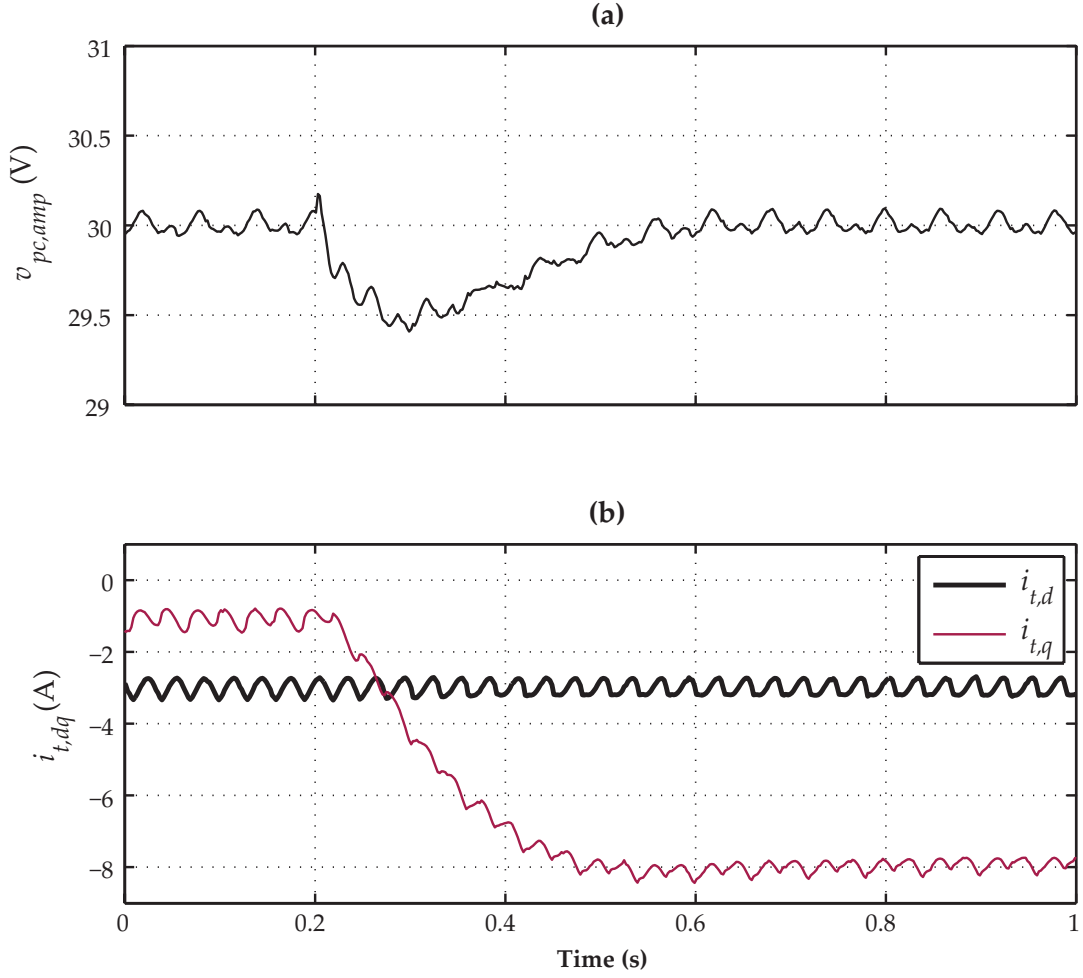
Figure 6.14: The experimental results of the system of Figure 6.11 during and subsequent to drop in the substation voltage while the locomotive is close to the substation and the OVSS is in service: (a) the amplitude of the PC voltage and (b) the dq-components of the current

Locomotive Close to the Substation   The locomotive is initially close to the substation and absorbs -3 A of $i_{t,d}$. The line inductance, which represents the internal inductance of the substation, is 8 mH. The substation voltage drops to 29.2 V at $t = 200\ ms$. The controller injects -120 var of reactive power to maintain the PC voltage at its rated value, i.e., 30 V, in almost 300 ms. Figure 6.14 (a) shows the amplitude of the PC voltage. The dq-components of the locomotive current are shown in Figure 6.14 (b). The d-component is fixed at -3 A, while the q-component changes to compensate for the substation voltage drop.

Locomotive at the End of the Line   In this test, the locomotive is at the end of the line, i.e., the inductance between the PC and the substation is 80 mH. The locomotive initially absorbs -3 A of $i_{t,d}$. At time instant $t = 200\ ms$, the substation voltage drops to 25.6 V. The OVSS changes

(a)

(b)
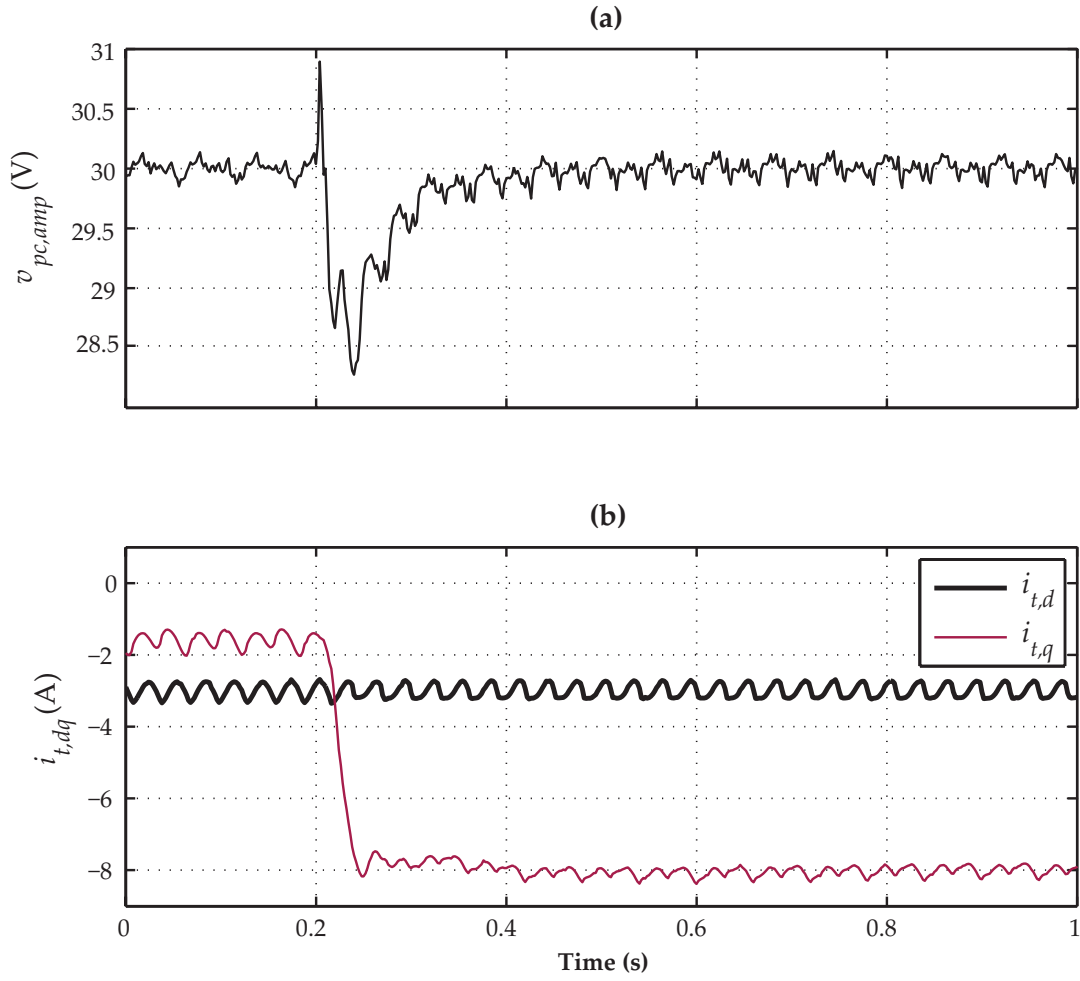
Figure 6.15: **The experimental results of the system of Figure 6.11 during and subsequent to drop in the substation voltage while the locomotive is far from the substation, and the OVSS is in service: (a) the amplitude of the PC voltage and (b) the** dq**-components of the current**

the reference value of $i_{t,q}$ to compensate for the voltage drop. The voltage is regulated at its rated value in almost 100 ms. Figure 6.15 (a) shows the amplitude of the PC voltage that is regulated at its rated value subsequent to the drop in the substation voltage. Figure 6.15 (b) depicts the dq-components of the locomotive current. The d-component is fixed, however, the q-component varies to compensate for the voltage drop.

Figures 6.14 and 6.15 depict that subsequent to the drop in the substation voltage, the OVSS can maintain the PC voltage provided the capacity of the ALC permits.

6.5   Conclusions

Adopting the active line-side converter of modern locomotives, a high-order catenary voltage support scheme is proposed. The compensation scheme is able to compensate for the voltage drop along the catenary line caused by locomotives real power absorption and/or substations voltage drop. Moreover, it can counteract the over-voltage caused by the active power regeneration of the locomotives during breaking. It injects reactive power to regulate the voltage at the connection point of the locomotive to the catenary. The injection of reactive power is performed through manipulation of the q-component of the locomotive current.

The taken design procedure is an optimization-based approach that relies on the nonparametric models of the system. The nonparametric models are achieved for several operating points in the network, and a controller is designed such that it stabilizes the system for all operating points while exhibits acceptable performance for each of them. The performance of the proposed compensation scheme is evaluated in MATLAB/PLECS environment. Moreover, the performance is experimentally evaluated, and it is concluded that the proposed voltage support scheme:

- is able to compensate for voltage drop and over-voltage along the catenary line provided the capacity of the line-side converter permits,

- stabilizes the system for various operating scenarios and exhibits acceptable performance for each of them,

- does not need any online tuning and is very simple to implement.

7 Conclusions

7.1 Summary and Conclusions

This thesis develops several control strategies for voltage source converters utilized in the context of microgrids and traction networks. For microgrids, a decoupled dq-currents control strategy is proposed, and its applicability is extended to single-phase systems. Then, assuming an islanded microgrid, three voltage control schemes are proposed: two single-stage controllers and a cascade controller. In the cascade control scheme the decoupled dq-currents control scheme is utilized to realize the inner loop. Moreover, for traction networks, inspiring from the cascade voltage control strategy, several voltage support schemes for traction networks, which are normally supplied by weak grids, are proposed. One of the proposed approaches for catenary voltage support requires the inductance of the catenary line at the connection point of the locomotive to the line to schedule its parameters. In this thesis, an identification scheme is also developed, which relies on the injection of harmonic current through the ALC of locomotives to identify the inductance.

7.1.1 Current Control of Grid-tied VSCs

A vector current control scheme for the three-phase grid-tied VSCs is introduced, which relies on an optimization-based loop shaping approach. To design the proposed controller, the second norm of the error between the nonparametric transfer function matrix of the system and a desired one is minimized. To ensure the stability and performance of the closed-loop system, the minimization problem is subject to constraints. Since the design procedure relies on nonparametric models, in contrast with the existing methods, it is immune to modeling mismatch and/or parametric errors. The performance of the proposed vector control scheme under various scenarios is evaluated. The studies conclude that the proposed method: (i) results in zero steady-state error, (ii) similar to its competitors, has fast dynamic response, and (iii) contrary to its competitors, fully decouples the dq-axes.

In order to benefit from the proposed decoupled vector control scheme in single-phase grid-tied VSCs, a countermeasure for obviating the need for a quarter of a cycle delay in conventional approaches is proposed. To create the dq-axes in single-phase system, imaginary components of the voltage and current orthogonal to the real ones are needed. In existing methods, a SOGI-based PLL is used for the generation of the orthogonal voltage, and the orthogonal current is created by phase-shifting the real current for a quarter of a fundamental period. However, the phase-shifting results in oscillatory dynamics and strongly coupled dq-axes. The proposed countermeasure generates the required orthogonal component of the current concurrently with the real one through a Fictive Axis Emulator (FAE). The feasibility of the proposed method in single-phase systems is verified through various simulation-based studies and experiments. The conducted studies show that the FAE-based approach (i) is much faster than conventional approaches, (ii) provides zero steady-state error, and (iii) results in fully decoupled dq-axes.

7.1.2 Voltage Control of Islanded Microgrids

Utilizing the generalized version of the optimization-based loop shaping approach, three control schemes for the voltage regulation of single-DG-unit microgrids and their dedicated loads are proposed. The adopted design procedure is based on minimizing the summation of the errors between the open-loop system transfer function matrices for several operating points of interest and a desired transfer function matrix. The minimization is subject to several constraints to ensure the stability and desired performance. The designed controllers are: (i) a Single-stage Multivariable-PI Controller (SMPC) (ii) a Single-stage Multivariable-PI-Resonant Controller (SMPRC), and (iii) a Cascade Multivariable-PI Controller (CMPC). According to the conducted time-domain simulations and experiments, it is concluded that:

- the proposed controllers show satisfactory dynamic performance in terms of load voltages regulation and robustness, upon various step changes in linear loads,

- compared to the SMPC, the SMPRC and the CMPC provide superior performance in the presence of nonlinear loads as they eliminate/minimize the adverse impacts of the low-order harmonics on the load voltages and system operation.

7.1.3 Catenary Parameters Identification

To estimate the catenary line parameters at the connection point of the locomotive to the line, a catenary line parameters identifier (CLPI), based on recursive least squares algorithms, is developed. The CLPI relies on the injection of harmonic current through the ALC of locomotives and monitoring its impact on the PC voltage. Using a simulation-based test bench, several test scenarios are conducted, and it is concluded that:

- the injected current can be of any frequency, provided the frequency is within the viable

range of the ALC,

- several factors, e.g., the choice of the identification sampling time and the forgetting factor, determine the quality of the estimated inductance. Such factors can be selected according to the system specifications, e.g., the number of locomotives in the system, their speeds, the distance between substations, etc.,

- to adopt the CLPI in multi-locomotive networks, the frequency of the adopted harmonic current for each locomotive must be unique and must be outside of the frequency range used for signaling systems.

7.1.4   Catenary Voltage Support

To support the catenary voltage, benefiting from the unused power capacity of ALCs, several secondary control schemes are proposed. The proposed schemes dictate the set-point of the reactive power through manipulating the set point of the q-component of the locomotive current. Three PI-based solutions are proposed: (i) a Proportional-based Voltage Support Scheme (PVSS), (ii) a Proportional-Integral-based Voltage Support Scheme (PIVSS), and (iii) a Gain-scheduled Voltage Support Scheme (GVSS). The gain-scheduling is performed through the developed catenary parameters identification scheme based on harmonic current injection. The performance of the proposed voltage support schemes are evaluated based on several simulation case studies. The studies conclude that:

- the PVSS is subject to steady-state error,

- the PIVSS can not provide satisfactory dynamic performance for all operating scenarios,

- among the proposed approaches, the GVSS shows the best performance.

Despite the acceptable performance of the GVSS, due to its deficiencies, e.g., the pollution of the network with harmonic currents, its susceptibility to erroneous catenary parameters identification, and implementation difficulties, an Optimization-based Voltage Support Scheme (OVSS) is also proposed. The OVSS relies on high-order controllers to realize the secondary control loop. Adopting the optimization-based loop-shaping approach for SISO systems, a high-order controller is designed that guarantees the excellent performance of the closed-loop system for various operating points of interest. The performance of the OVSS is evaluated in MATLAB/PLECS environment and also based on experiments. It is concluded that the proposed voltage support scheme:

- is able to compensate for voltage drop and/or over-voltage along the catenary line provided the capacity of the line-side converter permits,

- is able to support the catenary voltage in both single and multi-locomotive systems,

Table 7.1: Summary of the Results

	Controller	Applications	Advantages	Disadvantages
General Purpose Controllers	**OMCC**	Various Types of Grid-tied VSCs, e.g., Active Filters, STATCOMs, Drive Systems, etc.	Decoupled dq-Axes, Very Fast Dynamics, and Zero Steady-State Error	Complex Design
	FAE	Vector Control of Single-phase VSCs in Active Filters, STATCOMs, Drive Systems, etc.	Very Fast Dynamics, Zero Steady-Sstate Error, and Decoupled dq-Axes	—
	SMPC	Voltage Regulation of Islanded Systems, e.g., Islanded Microgrids, UPS, etc.	Large Robustness Margin and Zero Steady-State Error	Imperfect for Multi-DG Systems, Inability to Reject Harmonic Distortions, and Complex Design
	SMPRC	Voltage Regulation of Islanded Systems, e.g., Islanded Microgrids, UPS, etc.	Large Robustness Margin, Zero Steady-State Error, and Harmonic Distortion Rejection	Imperfect for Multi-DG Systems and Complex Design
	CMPC	Voltage Regulation of Islanded Systems, e.g., Islanded Microgrids, UPS, etc.	Large Robustness Margin, Zero Steady-State Error, and Harmonic Distortion Rejection	Imperfect for Multi-DG Systems, Needs Extra Current Sensors, and Complex Design
Traction-Related Controllers	**CLPI**	Identification of the Inductance of the Catenary in Traction Networks	Information for Designing Controllers Providing Ancillary Services	Network Pollution and Extra Signal Processing
	PVSS	Catenary Voltage Support in Traction Networks	Simple to Design and Implement	Steady-State Error
	PIVSS	Catenary Voltage Support in Traction Networks	Simple to Design and Implement, and Zero Steady-State Error	Slow Dynamics
	GVSS	Catenary Voltage Support in Traction Networks	Acceptable Dynamics and Zero Steady-State Error	Requires Identification and Susceptible to Identification Errors
	OVSS	Catenary Voltage Support in Traction Networks	Acceptable Dynamics and Zero Steady-State Error	Complex Design

- stabilizes the system for various operating points and exhibits acceptable performance for each of them,

- does not need any online tuning and is very simple to implement.

Table 7.1 summarizes the applications, advantages, and disadvantages of the proposed controllers of this thesis.

7.2 Contributions

The main contributions of this thesis are as follows:

- A vector control strategy for the current control of three-phase grid-tied voltage source converters is proposed. Contrary to existing methods, the proposed approach fully decouples the d- and q-components of the current.

- Using a Fictive Axis Emulator, the applicability of the proposed decoupled dq-currents control method is extended to single-phase systems. Contrary to existing methods, in order to generate the dq-components, the proposed control strategy generates the required imaginary orthogonal component of the current concurrent with the real one. This countermeasure obviates the need for a quarter of a cycle delay that is the source of oscillatory dynamic response of the existing methods.

- Three voltage control strategies for single-DG-unit microgrids are proposed, which have large robustness margins. The main advantage of the proposed controllers over the existing ones is their capability to guarantee given robustness margins. Moreover, one of the controllers is specifically designed to cancel the effects of the low-order harmonic currents and voltages generated by nonlinear loads.

- An identification scheme is proposed for catenary parameters identification in traction networks.

- A gain-scheduled voltage support scheme for traction networks is proposed, which is able to compensate for catenary voltage variations. The gain scheduling is performed through the developed catenary parameters identification scheme.

- A high-order controller that does not need any online modification and/or adaptation is introduced, which is able to compensate for voltage fluctuations in various operating points in traction networks.

7.3   Industrial Implementation

The proposed control strategies of this thesis may be utilized in various industrial applications. In the following, some of their possible application fields are presented:

- Current regulation schemes are extensively utilized in industry. Since the proposed current control scheme of this thesis provides superior performance compared with the existing ones, its chance to be exploited in various applications is high. For example, ABB, one of the worldwide leaders in power engineering, has shown interest in the proposed current regulation method.

- Due to the increasing concerns regarding energy and also greenhouse gases, renewable energy resources will be more and more utilized in the future. The islanded operation of microgrids operating based on renewable energy resources will also gain more attention. The proposed approaches of this thesis can be excellent solutions for designing controllers with given robustness margins for maintaining the voltage of islanded microgrids.

- The proposed voltage support schemes for traction networks, and specially the high-order voltage support scheme, have been already pretty much appreciated by SBB, the

Swiss Federal Railways company. It is very likely that in the near future, SBB will ask its locomotive suppliers to equip the future and also the existing locomotives with such voltage support strategies.

7.4 Future Works

In the continuation of this work, the following topics are suggested for future possible research:

- The performance of the high-order secondary control scheme for supporting the catenary voltage can be evaluated in a real traction network. To do so, adopting a modern locomotive equipped with an ALC, e.g., a FLIRT, one can inject a PRBS for identifying the network nonparametric model for various operating scenarios, i.e., for various traction network architectures and locomotive positions. Adopting the identified nonparametric models and the proposed control design procedure of this thesis, one can design high-order controllers as the secondary controller. Then, equipping the ALC with the designed controller, one can experimentally evaluate the performance of the proposed method in a real case.

- The proposed voltage control schemes for the islanded single-DG-unit microgrids can be extended to multi-DG-unit microgrids. Adopting a master/slave philosophy, one can validate the effectiveness of the proposed voltage regulation approaches in multi-DG-unit microgrids.

- The proposed vector control strategy for grid-tied VSCs, the OMCC, can be tested for some other conditions in which the switching frequency of the VSC is very low, e.g., in very high power applications. Moreover, by choosing other higher-order controllers instead of the PI-controllers of the OMCC, its performance in terms of axis-decoupling in the presence of uncertainties in the filter resistance may be evaluated.

- In this thesis, two-level VSCs are adopted to design and evaluate the performance of the proposed controllers. As a future research topic, the applicability of the proposed control strategies, i.e., the decoupled current control scheme for grid-tied three phase and single-phase VSCs, and the voltage regulation approaches for the islanded operation of microgrids, can be extended to other converter topologies.

- In this thesis, the H_∞ control design method [62, 63] has been utilized to design controllers for the discussed applications. One can use other control design approaches to design the controllers and compare their dynamic performance with the proposed ones.

Bibliography

[1] R. Lasseter, J. Eto, B. Schenkman, J. Stevens, H. Vollkommer, D. Klapp, E. Linton, H. Hurtado, and J. Roy, "CERTS Microgrid Laboratory Test Bed," *IEEE Transactions on Power Delivery*, vol. 26, pp. 325–332, Jan. 2011.

[2] P. Piagi and R. Lasseter, "Autonomous Control of Microgrids," in *IEEE Power Engineering Society General Meeting, Montreal, (PES'06)*, 2006.

[3] B. Bahrani, S. Kenzelmann, and A. Rufer, "Multivariable-PI-Based dq Current Control of Voltage Source Converters With Superior Axis Decoupling Capability," *IEEE Transactions on Industrial Electronics*, vol. 58, pp. 3016–3026, Jul. 2011.

[4] M. Liserre, R. Teodorescu, and F. Blaabjerg, "Multiple Harmonics Control for Three-phase Grid Converter Systems with the Use of PI-RES Current Controller in a Rotating Frame," *IEEE Transactions on Power Electronics*, vol. 21, pp. 836–841, May 2006.

[5] H.-S. Song and K. Nam, "Dual Current Control Scheme for PWM Converter Under Unbalanced Input Voltage Conditions," *IEEE Transactions on Industrial Electronics*, vol. 46, pp. 953–959, Oct. 1999.

[6] B. Bahrani, A. Rufer, S. Kenzelmann, and L. Lopes, "Vector Control of Single-Phase Voltage-Source Converters Based on Fictive-Axis Emulation," *IEEE Transactions on Industry Applications*, vol. 47, pp. 831–840, Mar./Apr. 2011.

[7] B. Blyden and W.-J. Lee, "Modified Microgrid Concept for Rural Electrification in Africa," in *IEEE Power Engineering Society General Meeting, Montreal, (PES'06)*, 2006.

[8] J. Balakrishnan, "Renewable Energy and Distributed Generation in Rural Villages," in *1st International Conference on Industrial and Information Systems, Sri Lanka, (ICIIS'06)*, pp. 190–195, 2006.

[9] A. Steimel, *Electric Traction - Motive Power and Energy Supply.* Germany: Oldenbourg Industrieverlag GmbH, 2008.

[10] B. Bahrani, H. Karimi, and R. Iravani, "Nondetection Zone Assessment of an Active Islanding Detection Method and its Experimental Evaluation," *IEEE Transactions on Power Delivery*, vol. 26, pp. 517 –525, Apr. 2011.

[11] R. Morrison, "Power Quality Issues on AC Traction Systems," in *9th International Conference on Harmonics and Quality of Power, Orlando, (ICHQP'00)*, vol. 2, pp. 709–714, 2000.

[12] C. Abbate, G. Busatto, and F. Iannuzzo, "High-Voltage, High-Performance Switch Using Series-Connected IGBTs," *IEEE Transactions on Power Electronics*, vol. 25, pp. 2450–2459, Sep. 2010.

[13] M. Rahimo and S. Klaka, "High Voltage Semiconductor Technologies," in *13th European Conference on Power Electronics and Applications, Barcelona, (EPE'09)*, 2009.

[14] C. Abbate, G. Busatto, L. Fratelli, F. Iannuzzo, B. Cascone, and G. Giannini, "Series Connection of High Power IGBT Modules for Traction Applications," in *11th European Conference on Power Electronics and Applications, Dresden, (EPE'05)*, 2005.

[15] R. Grunbaum, "FACTS for Dynamic Load Balancing and Voltage Support in Rail Traction," in *12th European Conference on Power Electronics and Applications, Aalborg, (EPE'07)*, 2007.

[16] R. Mastromauro, M. Liserre, and A. Dell'Aquila, "Control issues in single-stage photovoltaic systems: Mppt, current and voltage control," *IEEE Transactions on Industrial Informatics*, vol. 8, pp. 241 –254, May 2012.

[17] F. Blaabjerg, R. Teodorescu, M. Liserre, and A. Timbus, "Overview of Control and Grid Synchronization for Distributed Power Generation Systems," *IEEE Transactions on Industrial Electronics*, vol. 53, pp. 1398 –1409, Oct. 2006.

[18] H. Bühler, *Réglage de système d'électronique de puissance.* Switzerland: Presses Polytechniques et Universitaires Romandes, 1997.

[19] R. Teodorescu, F. Blaabjerg, M. Liserre, and P. Loh, "Proportional-resonant Controllers and Filters for Grid-connected Voltage-Source Converters," *Electric Power Applications, IEE Proceedings*, vol. 153, pp. 750–762, Sep. 2006.

[20] A. Timbus, M. Liserre, R. Teodorescu, P. Rodriguez, and F. Blaabjerg, "Evaluation of Current Controllers for Distributed Power Generation Systems," *IEEE Transactions on Power Electronics*, vol. 24, pp. 654–664, Mar. 2009.

[21] M. Kazmierkowski and L. Malesani, "Current Control Techniques for Three-Phase Voltage-Source PWM Converters: A Survey," *IEEE Transactions on Industrial Electronics*, vol. 45, pp. 691–703, Oct. 1998.

[22] E. Song, A. Lynch, and V. Dinavahi, "Experimental Validation of Nonlinear Control for a Voltage Source Converter," *IEEE Transactions on Control Systems Technology*, vol. 17, pp. 1135–1144, Sep. 2009.

[23] A. Gensior, H. Sira-Ramirez, J. Rudolph, and H. Guldner, "On Some Nonlinear Current Controllers for Three-Phase Boost Rectifiers," *IEEE Transactions on Industrial Electronics*, vol. 56, pp. 360–370, Feb. 2009.

[24] C. Schauder and H. Mehta, "Vector Analysis and Control of Advanced Static VAR Compensators," *Generation, Transmission and Distribution, IEE Proceedings C*, vol. 140, pp. 299 –306, Jul. 1993.

[25] D. Zmood and D. Holmes, "Stationary Frame Current Regulation of PWM Inverters with Zero Steady-State Error," *IEEE Transactions on Power Electronics*, vol. 18, pp. 814–822, May 2003.

[26] G. Shen, X. Zhu, J. Zhang, and D. Xu, "A New Feedback Method for PR Current Control of LCL-Filter-Based Grid-Connected Inverter," *IEEE Transactions on Industrial Electronics*, vol. 57, pp. 2033–2041, Jun. 2010.

[27] J. Espi, J. Castello, R. Garcia-Gil, G. Garcera, and E. Figueres, "An Adaptive Robust Predictive Current Control for Three-Phase Grid-Connected Inverters," *IEEE Transactions on Industrial Electronics*, vol. 58, pp. 3537–3546, Aug. 2011.

[28] O. Kukrer, H. Komurcugil, and A. Doganalp, "A Three-Level Hysteresis Function Approach to the Sliding-Mode Control of Single-Phase UPS Inverters," *IEEE Transactions on Industrial Electronics*, vol. 56, pp. 3477–3486, Sep. 2009.

[29] S. Zhang, K.-J. Tseng, D. Vilathgamuwa, T. Nguyen, and X.-Y. Wang, "Design of a Robust Grid Interface System for PMSG-Based Wind Turbine Generators," *IEEE Transactions on Industrial Electronics*, vol. 58, pp. 316–328, Jan. 2011.

[30] H. Komurcugil, "Steady-State Analysis and Passivity-Based Control of Single-Phase PWM Current-Source Inverters," *IEEE Transactions on Industrial Electronics*, vol. 57, pp. 1026–1030, Mar. 2010.

[31] M. Castilla, J. Miret, J. Matas, L. Garcia de Vicuna, and J. Guerrero, "Control Design Guidelines for Single-Phase Grid-Connected Photovoltaic Inverters With Damped Resonant Harmonic Compensators," *IEEE Transactions on Industrial Electronics*, vol. 56, pp. 4492–4501, Nov. 2009.

[32] E. Villanueva, P. Correa, J. Rodriguez, and M. Pacas, "Control of a Single-Phase Cascaded H-Bridge Multilevel Inverter for Grid-Connected Photovoltaic Systems," *IEEE Transactions on Industrial Electronics*, vol. 56, pp. 4399–4406, Nov. 2009.

[33] M. Saitou, N. Matsui, and T. Shimizu, "A Control Strategy of Single-phase Active Filter Using a Novel d-q Transformation," in *38th IAS Annual Meeting, Industry Applications Conference, Salt Lake City*, vol. 2, pp. 1222 – 1227 vol.2, 2003.

[34] U. Miranda, M. Aredes, and L. Rolim, "A DQ Synchronous Reference Frame Current Control for Single-Phase Converters," in *36th IEEE Power Electronics Specialists Conference, Recife, (PESC'05)*, pp. 1377 –1381, 2005.

[35] I. Balaguer, Q. Lei, S. Yang, U. Supatti, and F. Z. Peng, "Control for Grid-Connected and Intentional Islanding Operations of Distributed Power Generation," *IEEE Transactions on Industrial Electronics*, vol. 58, pp. 147 –157, Jan. 2011.

[36] F. Katiraei and M. Iravani, "Power Management Strategies for a Microgrid With Multiple Distributed Generation Units," *IEEE Transactions on Power Systems*, vol. 21, pp. 1821–1831, Nov. 2006.

[37] J. Vasquez, R. Mastromauro, J. Guerrero, and M. Liserre, "Voltage Support Provided by a Droop-Controlled Multifunctional Inverter," *IEEE Transactions on Industrial Electronics*, vol. 56, pp. 4510–4519, Nov. 2009.

[38] J. Guerrero, J. Vasquez, J. Matas, L. de Vicuna, and M. Castilla, "Hierarchical Control of Droop-Controlled AC and DC Microgrids - A General Approach Toward Standardization," *IEEE Transactions on Industrial Electronics*, vol. 58, pp. 158–172, Jan. 2011.

[39] J. Guerrero, J. Matas, L. G. de Vicuna, M. Castilla, and J. Miret, "Decentralized Control for Parallel Operation of Distributed Generation Inverters Using Resistive Output Impedance," *IEEE Transactions on Industrial Electronics*, vol. 54, pp. 994–1004, Apr. 2007.

[40] I. Hiskens and E. Fleming, "Control of Inverter-Connected Sources in Autonomous Microgrids," in *American Control Conference, Seattle, (ACC'08)*, pp. 586–590, 2008.

[41] J. Guerrero, L. Hang, and J. Uceda, "Control of Distributed Uninterruptible Power Supply Systems," *IEEE Transactions on Industrial Electronics*, vol. 55, pp. 2845–2859, Aug. 2008.

[42] J. Vasquez, J. Guerrero, A. Luna, P. Rodriguez, and R. Teodorescu, "Adaptive Droop Control Applied to Voltage-Source Inverters Operating in Grid-Connected and Islanded Modes," *IEEE Transactions on Industrial Electronics*, vol. 56, pp. 4088–4096, Oct. 2009.

[43] R. Majumder, G. Ledwich, A. Ghosh, S. Chakrabarti, and F. Zare, "Droop Control of Converter-Interfaced Microsources in Rural Distributed Generation," *IEEE Transactions on Power Delivery*, vol. 25, pp. 2768–2778, Oct. 2010.

[44] J. Guerrero, L. de Vicuna, J. Matas, M. Castilla, and J. Miret, "A Wireless Controller to Enhance Dynamic Performance of Parallel Inverters in Distributed Generation Systems," *IEEE Transactions on Power Electronics*, vol. 19, pp. 1205– 1213, Sep. 2004.

[45] J. Guerrero, L. GarciadeVicuna, J. Matas, M. Castilla, and J. Miret, "Output Impedance Design of Parallel-Connected UPS Inverters With Wireless Load-Sharing Control," *IEEE Transactions on Industrial Electronics*, vol. 52, pp. 1126–1135, Aug. 2005.

[46] J. Guerrero, J. Matas, L. de Vicuna, M. Castilla, and J. Miret, "Wireless-Control Strategy for Parallel Operation of Distributed-Generation Inverters," *IEEE Transactions on Industrial Electronics*, vol. 53, pp. 1461–1470, Oct. 2006.

[47] A. Mehrizi-Sani and R. Iravani, "Potential-Function Based Control of a Microgrid in Islanded and Grid-Connected Modes," *IEEE Transactions on Power Systems*, vol. 25, pp. 1883–1891, Nov. 2010.

[48] C. Sao and P. Lehn, "Intentional Islanded Operation of Converter Fed Microgrids," in *IEEE Power Engineering Society General Meeting, Montreal, (PES'06)*, 2006.

[49] M. Delghavi and A. Yazdani, "Islanded-Mode Control of Electronically Coupled Distributed-Resource Units Under Unbalanced and Nonlinear Load Conditions," *IEEE Transactions on Power Delivery*, vol. 26, pp. 661–673, Apr. 2011.

[50] H. Karimi, H. Nikkhajoei, and R. Iravani, "Control of an Electronically-Coupled Distributed Resource Unit Subsequent to an Islanding Event," *IEEE Transactions on Power Delivery*, vol. 23, pp. 493–501, Jan. 2008.

[51] H. Karimi, H. Nikkhajoei, and R. Iravani, "A Linear Quadratic Gaussian Controller for a Stand-alone Distributed Resource Unit-Simulation Case Studies," in *Power Engineering Society General Meeting, Tampa, (PES'07)*, Jun. 2007.

[52] H. Karimi, E. Davison, and R. Iravani, "Multivariable Servomechanism Controller for Autonomous Operation of a Distributed Generation Unit: Design and Performance Evaluation," *IEEE Transactions on Power Systems*, vol. 25, pp. 853–865, May 2010.

[53] H. Karimi, A. Yazdani, and R. Iravani, "Robust Control of an Autonomous Four-Wire Electronically-Coupled Distributed Generation Unit," *IEEE Transactions on Power Delivery*, vol. 26, pp. 455 –466, Jan. 2011.

[54] W. Guo, R. Enen, and T. Mingxing, "Analysis and Identification of Active Compensation Topology for Electrified Railway Load," in *International Conference on Intelligent Computation Technology and Automation, Changsha, (ICICTA'8)*, vol. 1, pp. 978–981, 2008.

[55] G. Celli, F. Pilo, and S. Tennakoon, "Voltage Regulation on 25 kV AC Railway Systems by Using Thyristor Switched Capacitor," in *9th International Conference on Harmonics and Quality of Power, Orlando, (ICHQP'00)*, vol. 2, pp. 633 –638 vol.2, 2000.

[56] P.-C. Tan, P. C. Loh, and D. Holmes, "Optimal Impedance Termination of 25-kV Electrified Railway Systems for Improved Power Quality," *IEEE Transactions on Power Delivery*, vol. 20, pp. 1703–1710, Apr. 2005.

[57] P.-C. Tan, P. C. Loh, and D. Holmes, "A Robust Multilevel Hybrid Compensation System for 25-kV Electrified Railway Applications," *IEEE Transactions on Power Electronics*, vol. 19, pp. 1043–1052, Jul. 2004.

[58] L. Battistelli, D. Lauria, and D. Proto, "Two-Phase Controlled Compensator for Alternating-Current Quality Improvement of Electrified Railway Systems," *Electric Power Applications, IEE Proceedings*, vol. 153, pp. 177–183, Mar. 2006.

[59] J. Dixon, L. Moran, J. Rodriguez, and R. Domke, "Reactive Power Compensation Technologies: State-of-the-Art Review," *Proceedings of the IEEE*, vol. 93, pp. 2144–2164, Dec. 2005.

[60] Z. Shu, S. Xie, and Q. Li, "Single-Phase Back-To-Back Converter for Active Power Balancing, Reactive Power Compensation, and Harmonic Filtering in Traction Power System," *IEEE Transactions on Power Electronics*, vol. 26, pp. 334–343, Feb. 2011.

[61] A. Rufer, D. Hotellier, and P. Barrade, "A Supercapacitor-Based Energy Storage Substation for Voltage Compensation in Weak Transportation Networks," *IEEE Transactions on Power Delivery*, vol. 19, pp. 629–636, Apr. 2004.

[62] G. Galdos, A. Karimi, and R. Longchamp, "H∞ Controller design for spectral MIMO models by convex optimization," *Journal of Process Control*, vol. 20, no. 10, pp. 1175–1182, 2010.

[63] A. Karimi and G. Galdos, "Fixed-order H-infinity Controller Design for Nonparametric Models by Convex Optimization," *Automatica*, vol. 46, no. 8, pp. 1388–1394, 2010.

[64] V. Blahnik, J. Zak, and Z. Peroutka, "Vector Control of Primary Active Rectifiers in Traction Converter with Medium-frequency Transformer," in *14th European Conference on Power Electronics and Applications, Birmingham, (EPE 2011)*, Sep. 2011.

[65] M. Meyer and A. Sonnenmoser, "A Hysteresis Current Control for Parallel Connected Line-side Converters of an Inverter Locomotive," in *5th European Conference on Power Electronics and Applications, Brighton, (EPE'93)*, pp. 102 –109 vol.4, sep 1993.

[66] W. de Jager and G. Tubbing, "A Vector Oriented Control Strategy for a 4-quadrant Line Side Converter," in *5th European Conference on Power Electronics and Applications, Brighton, (EPE'93)*, vol. 5, pp. 213 –218, Sep. 1993.

[67] S. Bertini, T. Ghiara, and M. Marchesoni, "AC/DC/AC High Voltage Traction Drives with Quasi-zero Reactive Power Demand," *IEEE Transactions on Power Electronics*, vol. 8, pp. 632 –639, oct 1993.

[68] H.-S. Song, R. Keil, P. Mutschler, J. van der Weem, and K. Nam, "Advanced Control Scheme for a Single-Phase PWM Rectifier in Traction Applications," in *38th IAS Annual Meeting, Industry Applications Conference, Salt Lake City, (IAS'03)*, pp. 1558–1565, 2003.

[69] C. Heising, M. Oettmeier, R. Bartelt, V. Staudt, and A. Steimel, "Multivariable Pole-placement Control Design for a Single-phase 50-kW, 16.7-Hz Railway Traction Line-side Converter," in *International Conference on Power Engineering, Energy and Electrical Drives, Lisbon, (POWERENG '09)*, pp. 273 –278, Mar. 2009.

[70] C. Heising, R. Bartelt, V. Staudt, and A. Steimel, "Single-phase 50-kW 16.7-Hz Four-quadrant Line-side Converter for Railway Traction Application," in *13th Power Electronics and Motion Control Conference, Proznan, (EPE-PEMC'08)*, pp. 521 –527, Sep. 2008.

[71] B. Busco, P. Marino, M. Porzio, R. Schiavo, and F. Vasca, "Digital Control and Simulation for Power Electronic Apparatus in Dual Voltage Railway Locomotive," *IEEE Transactions on Power Electronics*, vol. 18, pp. 1146 – 1157, Sep. 2003.

[72] I. D. Landau, R. Lozano, M. M'Saad, and A. Karimi, *Adaptive Control, Algorithms, Analysis and Applications.* Springer-Verlag Inc., USA, 2011.

[73] J. Doyle, B. Francis, and A. Tannenbaum, *Feedback Control Theory.* Macmillan Publishing Co., 1992.

[74] J. F. Strum, "Using SeDuMi 1.02, a Matlab toolbox for optimization over symmetric cones," in *Optimization Methods and Software*, vol. 11, pp. 625–653, 1999.

[75] A. V. Oppenheim and R. W. Schafer, *Discrete-Time Signal Processing.* NJ: Prentice Hall, 1999.

[76] Y. Murai, T. Watanabe, and H. Iwasaki, "Waveform distortion and correction circuit for pwm inverters with switching lag-times," *Industry Applications, IEEE Transactions on*, vol. IA-23, pp. 881 –886, sept. 1987.

[77] M. Ciobotaru, R. Teodorescu, and F. Blaabjerg, "A New Single-Phase PLL Structure Based on Second Order Generalized Integrator," in *37th IEEE Power Electronics Specialists Conference, Jeju, (PESC'06)*, 2006.

[78] P. C. Loh, M. Newman, D. Zmood, and D. Holmes, "A Comparative Analysis of Multiloop Voltage Regulation Strategies for Single and Three-Phase UPS Systems," *IEEE Transactions on Power Electronics*, vol. 18, pp. 1176 – 1185, Sep. 2003.

[79] H.-S. Kim, H.-T. Moon, and M.-J. Youn, "On-line Dead-time Compensation Method Using Disturbance Observer," *IEEE Transactions on Power Electronics*, vol. 18, pp. 1336–1345, Nov. 2003.

[80] J. Taufiq, "Power Electronics Technologies for Railway Vehicles," in *4th Power Conversion Conference, Nagoya, (PCC'07)*, pp. 1388–1393, 2007.

[81] G. Celli, F. Pilo, and S. Tennakoon, "Voltage Regulation on 25 kV AC Railway Systems by Using Thyristor Switched Capacitor," in *9th International Conference on Harmonics and Quality of Power, Orlando, (ICHQP'00)*, vol. 2, pp. 633–638, 2000.

[82] P.-C. Tan, R. Morrison, and D. Holmes, "Voltage Form Factor Control and Reactive Power Compensation in a 25-Kv Electrified Railway System Using a Shunt Active Filter Based on Voltage Detection," *IEEE Transactions on Industry Applications*, vol. 39, pp. 575–581, Mar./Apr. 2003.

[83] T. Söderström and P. Stoica, *System Identification.* UK: Prentice Hall International, 1989.

[84] A. Cagnano, E. De Tuglie, M. Liserre, and R. Mastromauro, "Online optimal reactive power control strategy of pv inverters," *IEEE Transactions on Industrial Electronics,* vol. 58, pp. 4549 –4558, oct. 2011.

[85] R. Mastromauro, M. Liserre, T. Kerekes, and A. Dell'Aquila, "A single-phase voltage-controlled grid-connected photovoltaic system with power quality conditioner functionality," *IEEE Transactions on Industrial Electronics,* vol. 56, pp. 4436 –4444, Nov. 2009.

[86] E. Demirok, P. Casado González, K. Frederiksen, D. Sera, P. Rodriguez, and R. Teodorescu, "Local reactive power control methods for overvoltage prevention of distributed solar inverters in low-voltage grids," *IEEE Journal of Photovoltaics,* vol. 1, pp. 174 –182, Oct. 2011.

[87] S. Kincic, X. Wan, D. McGillis, A. Chandra, B.-T. Ooi, F. Galiana, and G. Joos, "Voltage support by distributed static var systems (svs)," *IEEE Transactions on Power Delivery,* vol. 20, pp. 1541 – 1549, Apr. 2005.

[88] N. Ullah, K. Bhattacharya, and T. Thiringer, "Wind farms as reactive power ancillary service providers -technical and economic issues," *IEEE Transactions on Energy Conversion,* vol. 24, pp. 661 –672, Sep. 2009.

[89] P. Appun and W. Lienau, "Der Vierquadrantensteller bei Induktivem und Kapazitivem Betrieb," in *etzArchiv, Bd.6 H.1,* pp. 3–8, 1984.

[90] T. K. Kiong, W. Qing-Guo, H. C. Chieh, and T. J. Hägglund, *Advances in PID Control.* UK: Springer, 1999.

[91] M. Ciobotaru, R. Teodorescu, and V. Agelidis, "Offset Rejection for PLL based Synchronization in Grid-connected Converters," in *Applied Power Electronics Conference and Exposition, Austin, (APEC'08),* pp. 1611 –1617, Feb. 2008.

[92] Y. W. Li, "Control and Resonance Damping of Voltage-Source and Current-Source Converters With LC Filters," *IEEE Transactions on Industrial Electronics,* vol. 56, pp. 1511–1521, May 2009.

Behrooz Bahrani

Curriculum Vitae

Born in July 1984, Shiraz, Iran
Nationality: Iranian
✉ *behrooz.bahrani@a3.epfl.ch*

Education

03.2009-Present — **Ph.D., Electrical Engineering**, *Swiss Federal Institute of Technology (EPFL)*, Lausanne, Switzerland, Supervisor : **Prof. Alfred Rufer**.
Thesis Title : Advanced Control Strategies for Voltage Source Converters in Microgrids and Traction Networks

11.2006-11.2008 — **M.Sc., Electrical Engineering**, *University of Toronto*, Toronto, Canada, Supervisor : **Prof. Reza Iravani**.
Thesis Title : Islanding Detection and Control of Islanded Single and Two-Parallel Distributed Generation Units

11.2002-11.2006 — **B.Sc., Electrical Engineering**, *Sharif University of Technology*, Tehran, Iran.

Research Interests

– Power Electronics Converters and Their Applications in Power Systems
– Control of Power Electronics Converters
– Advanced Control Strategies for Renewable Energy Resources
– Advanced Control Strategies for Traction Networks

Research Experience

03.2009-Present — **Research Assistant**, *Industrial Electronics Laboratory*, EPFL, Lausanne, Switzerland.
Detailed achievements :
– Proposing Advanced Current Control Schemes for Single-phase and Three-phase Voltage Source Converters (VSCs)
  – Fictive Axes Emulation-based Current Controller for Single-phase VSCs
  – Optimization-based dq-Currents Control Strategy for Single- and Three-phase VSCs
– Proposing Advanced Voltage Control Schemes for Single-phase and Three-phase Voltage Source Converters
  – Voltage Support Schemes for Railways Catenary Lines
  – Voltage Regulation Schemes for Islanded Microgrids

11.2006-11.2008	**Research Assistant**, *Center of Applied Power Electronics*, University of Toronto, Toronto, Canada.

Detailed achievements :
– Islanding Detection of Distributed Generation Systems
– Non-Detection Zone Analysis of Islanding Detection Methods
– Control of Islanded Distributed Generation Systems
– Ride-Through Capability of Distributed Generation System

05.2008-11.2008	**Research Intern**, *Power Electronics Research Group (S1)*, ABB Corporate Research Ltd., Dättwil-Baden, Switzerland.

Detailed achievements :
– Hybrid Filtering Solutions for Power Quality Improvement

07.2005-11.2005	**Research Intern**, *Niroo Research Institute (NRI)*, Tehran, Iran.

Detailed achievements :
– Voltage and Current Measuring Insulators for Overhead lines

Publications

Journal Papers

[J8] **Bahrani, B.** ; Saeedifard M. ; Karimi, A. ; and Rufer, A. ; "*A Multivariable Design Methodology for Voltage Control of a Single-DG-Unit Microgrid*," Accepted for Publication in IEEE Transactions on Industrial Informatics, 2012.

[J7] **Bahrani, B.** and Rufer, A. ; "*Optimization-based Voltage Support in Traction Networks Using Active Line-side Converters*," Accepted for Publication in IEEE Transactions on Power Electronics, 2012.

[J6] **Bahrani, B.** ; Karimi, A. ; Rey, B. ; and Rufer, A. ; "*Decoupled DQ-Current Control of Grid-tied Voltage Source Converters Using Nonparametric Models*," Accepted for Publication in IEEE Transactions on Industrial Electronics, 2012.

[J5] **Bahrani, B.** ; Rufer, A. ; and Aeberhard, M. ; "*Catenary Voltage Support : Adopting Modern Locomotives with Active Line-side Converters*," IEEE Transactions on Smart Grid, Vol.3, No.1, pp.377-387, March 2012.

[J4] **Bahrani, B.** ; Karimi, H. ; and Iravani R. ; "*Stability Analysis and Experimental Evaluation of a Control Strategy for Islanded Operation of Distributed Generation Units*," IEEJ Transactions on Industry Applications, Vol.131, No.8, 2011.

[J3] **Bahrani, B.** ; Kenzelmann, S. ; and Rufer, A. ; "*Multivariable-PI-Based dq Current Control of Voltage Source Converters With Superior Axis Decoupling Capability*," IEEE Transactions on Industrial Electronics, Vol.58, No.7, pp.3016-3026, July 2011.

[J2] **Bahrani, B.** ; Karimi, H. ; and Iravani, R. ; "*Non-detection Zone Assessment of an Active Islanding Detection Method and its Experimental Evaluation*," IEEE Transactions on Power Delivery, Vol.26, No.2, pp.517-525, April 2011.

[J1]   **Bahrani, B. ;** Rufer, A. ; Kenzelmann, S. ; and Lopes, L.A.C. ; "*Vector Control of Single-Phase Voltage-Source Converters Based on Fictive-Axis Emulation*," IEEE Transactions on Industry Applications, Vol.47, No.2, pp.831-840, March-April 2011.

Conference Papers

[C6]   **Bahrani, B.** and Rufer, A. ; "*Model Predictive-based Voltage Regulation of an Islanded Distributed Generation Unit*," IEEE Energy Conversion Congress and Exposition (ECCE), 2011, Phoenix, USA.

[C5]   **Bahrani, B.** ; Rufer, A. ; and Aeberhard, M. ; "*Railway Catenary Parameters Identification based on Harmonic Current Injection*," European Power Electronics Conference (EPE), 2011, Birmingham, UK.

[C4]   **Bahrani, B.** ; Karimi, H. ; and Iravani, R. ; "*Stability Analysis and Experimental Validation of a Control Strategy for Autonomous Operation of Distributed Generation Units*," International Power Electronics Conference (IPEC), 2010 , Sapporo, Japan.

[C3]   **Bahrani, B.** ; Karimi, H. ; and Iravani, R. ; "*Decentralized Control of Parallel Connection of Two Distributed Generation Units*," 35th Annual Conference of the IEEE Industrial Electronics Society (IECON), 2009, Porto, Portugal.

[C2]   Rufer, A. ; **Bahrani, B.** ; Kenzelmann, S. ; and Lopes, L. ; "*Vector Control of Single-phase Voltage Source Converters based on Fictive Axis Emulation*," IEEE Energy Conversion Congress and Exposition (ECCE), 2009, San Jose, USA.

[C1]   **Bahrani, B.** and Grinberg, R. ; "*Investigation of Harmonic Filtering for the State-of-the-art Variable Speed Drives*," European Power Electronics Conference (EPE), 2009, Barcelona, Spain.

Languages

English   **C2, Advanced**
French   **B1, Intermediate**
Persian   **Mother Tongue**